Microfluidic Transport Studies on Lipid Vesicles

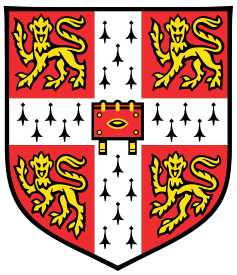

Michael Alexander Schaich

Department of Physics
University of Cambridge

This dissertation is submitted for the degree of
Doctor of Philosophy

Jesus College

March 2020

Declaration

I hereby declare that except where specific reference is made to the work of others, the contents of this dissertation are original and have not been submitted in whole or in part for consideration for any other degree or qualification in this, or any other university. This dissertation is my own work and contains nothing which is the outcome of work done in collaboration with others, except as specified in the text and Acknowledgements. This dissertation contains fewer than 60,000 words including summary/abstract, tables, footnotes and appendices.

Michael Alexander Schaich
March 2020

Abstract

Microfluidic Transport Studies on Lipid Vesicles

Michael Schaich

The plasma membrane is the outermost layer of a cell and separates it from the extracellular environment. The membrane, as well as the proteins that are anchored in it, plays a crucial role in the uptake and efflux of molecules. Lipid bilayers are therefore an important object of research in many fields of science, such as biophysics, pharmacology and synthetic biology. In this thesis, we develop new microfluidic methods that allow us to study the laws that govern the transport processes through lipid bilayers.

We use the novel microfluidic Octanol-Assisted Liposome Assembly (OLA) technique to obtain lipid vesicles which serve as model membrane for our studies. We perform a literature review, where we discuss OLA and other techniques to obtain liposomes in detail, before we provide a biophysical analysis of liposomes generated with OLA and compare them to vesicles obtained via traditional techniques. The biophysical analysis represents the first systematic evaluation of the properties of GUVs produced with the OLA technique to date. Using a fluorescence intensity assay, we show that OLA allows for the production of GUVs with binary lipid mixtures of DOPC-DOPG and DOPC-DOPE in the 1:3, 2:2 and 3:1 lipid ratio. GUVs with binary lipid mixtures of DOPG-DOPE are only stable in the 1:3 and 2:2 mixing ratio, but not in the 3:1 ratio. We attribute this behaviour to the high charge density of this mixture and the lipid polymorphism which makes it energetically unfavourable for certain lipid compositions to form lamellar structures. We furthermore investigate the lateral lipid diffusivity of DOPC and POPC vesicles produced with OLA using fluorescence recovery after photobleaching (FRAP) and compare it to that of vesicles obtained via the established electroformation technique. We find the lateral diffusion coefficients to be quantitatively similar and in the range of 1 $\mu m^2/s$ for the different lipid systems and techniques tested. Finally, using a dithionite bleaching assay, we quantitatively show the unilamellarity of OLA vesicles, confirming previous results.

After examining OLA vesicles for their suitability for transport measurements, we expand the OLA technique and develop a platform that allows for the on-chip fabrication and controlled exposure of liposomes to a solute of interest. This novel microfluidic platform combines OLA with a flow through system that enables us to measure transport and other membrane-active processes that occur in time scales of tens of seconds on chip. In this platform, we either use fluorescent labels or exploit the solute molecule's autofluorescence to visualise the transport across the vesicle membrane. Using this new method, we investigate the permeability of small antibiotic molecules of the fluoroquinolone family and quantify the transport of the drugs ciprofloxacin and norfloxacin through liposome membranes. For PGPC membranes, we measure median permeability coefficients of 3.57×10^{-6} cm/s for norfloxacin and 4.83×10^{-6} cm/s for ciprofloxacin in a PBS buffer at pH 7.4. These values correlate with the partition coefficients of the drugs, as well as previous studies on their permeation into lipid vesicles.

In a second series of experiments, we investigate whether or not DNA nanostructures can act as ion channels and increase the membrane's permeability towards protons. For these studies, we use a microfluidic perfusion assay that was previously developed by the Keyser group. In this assay, OLA-generated vesicles are immobilised on chip via vesicle traps and are either incubated with DNA nanopores or a buffer control, before being perfused with a low pH solution. By means of the fluorescent pH indicator HPTS, encapsulated inside the GUVs, the intravesicular proton concentration is monitored throughout this exposure. Our results do not suggest substantial enhancement of proton flux as a result of the incubation with the DNA nanopore. We attribute this behaviour to the low insertion efficiency of the DNA nanopore and the temporal resolution of the assay, which might be too low when put in context with the timescale of passive proton permeation to show a potentially flux enhancing effect of the DNA nanostructure.

Finally, we widen the scope of our technique by taking the first steps towards a new visualisation method based on the deep UV absorbance of molecules rather than fluorescence. Our results indicate that this new visualisation method can in principle be incorporated into a microfluidic assay and used to measure membrane permeability, however this imaging mode features a substantially lower signal to noise ratio compared to the design based on fluorescence, limiting its capabilities. The issue of low signal to noise ratio must be overcome before the absorbance assay can provide a true alternative to fluorescence-based microfluidic assays as a means to study membrane permeation.

All in all, our studies show that GUVs obtained with the novel OLA technique are viable alternative to vesicles generated with established methods such as electroformation. We successfully use OLA-generated vesicles to study a series of biophysical membrane parameters and conduct measurements on membrane permeability. We also demonstrate the versatility of the OLA technique by successfully incorporating it into complex microfluidic assays, exemplifying its potential for the investigation of membrane properties and its use in transport studies.

Acknowledgements

My first and foremost thanks go to my supervisor Prof. Ulrich F. Keyser. Ulrich accepted me as a visiting Master's student in 2015 and took me up in his group again one year later in 2016, this time as a PhD student. Needless to say, it would have not been possible for me to complete my PhD successfully without his guidance and support. I am truly grateful for the opportunity to work with him and the other members of the Keyser Lab.

A very special thank you also goes to Dr. Jehangir Cama. Jehangir supervised me during my master's project, when I first joined the Keyser group and he taught me the fundamentals of microfluidics and working with lipid vesicles. However, it is the deep friendship that we developed over the years that I am most grateful for. I enjoyed our countless discussions about politics, or our visits to classical concerts and our work on scientific projects.

I also owe a very special thanks to Kareem Al Nahas. We both joined the Keyser Lab together as visiting students in 2015 and both returned in 2016 to pursue our postgraduate degrees. Over the years, we spent countless hours together in the lab, worked on various projects together and discovered the secrets of the OLA technique. Naturally, we became close friends during this period which I am very grateful for.

My thanks also go to the rest of the Keyser Lab, namely Nik, Adrian, Raj, Jeff, Ran, Nikki, Diana, Alice, Stuart, Marcus, Alex, Elisa, Jinbo, Kaikai, Kerstin and Karolis. The Keyser group is a great community and I could have not wished for a better group to work in for my PhD.

I would also like to thank my Master's students Kevin Jahnke and Hannah Sleath who worked with me on the microfluidic transport projects. Furthermore, I would like to thank Siddharth Deshpande and Cees Dekker for letting me visit their lab in Delft and teaching the OLA technique to me.

Throughout my studies, I have had many mentors and people who supported and inspired me. I would like to point out and thank Prof. Dr. med. Dr.-Ing Erich Wintermantel. During my time at TUM, he sparked my passion for medical technology and biomedical engineering. Without him, I would not have chosen this field of study for my Master's and would ultimately not have ended up going to ETH Zurich and the University of Cambridge. I would also like to thank my mentor from the Friedrich-Naumann Stiftung, Dr. Florian Stork, for the many meetings, emails and his support.

It would not have been possible for me to complete my PhD without funding. I owe a special thanks to the Friedrich-Naumann Stiftung für die Freiheit, who granted me a 3-year PhD scholarship that allowed me to pursue my studies in Cambridge. I also thank the Cambridge Philosophocal Society and Jesus College Cambridge, who supported me with a research studentship and a stipend from the Jane Bourque-Driscoll Fund, for the final months of my PhD.

I would like to thank my best friends Lukas and Sebastian for always being there for me.

My final thanks go to my family. Knowing I have their support gave me the strength to go abroad and pursue my goals.

List of Publications

M. Schaich, D. Sobota, H. Sleath, J. Cama, and U. F. Keyser. 'Characterization of lipid composition and diffusivity in OLA generated vesicles.' *Biochimica et Biophysica Acta - Biomembranes*, 183359, 2020.

M. Schaich, J. Cama, K. Al Nahas, D. Sobota, H. Sleath, K. Jahnke, S. Deshpande, C. Dekker, and U. F. Keyser. 'An integrated microfluidic platform for quantifying drug permeation across biomimetic vesicle membranes.' *Molecular Pharmaceutics*, 16(6), 2494–2501, 2019.

K. Al Nahas, J. Cama, **M. Schaich**, K. Hammond, S. Deshpande, C. Dekker, M. G. Ryadnov, and U. F. Keyser. 'A microfluidic platform for the characterisation of membrane active antimicrobials.' *Lab Chip*, 19(5), 837–844, 2019.

J. Cama, **M. Schaich**, K. Al Nahas, S. Hernández-Ainsa, S. Pagliara, and U. F. Keyser. 'Direct optofluidic measurement of the lipid permeability of fluoroquinolones.' *Scientific Reports*, 6, 32824, 2016.

Table of contents

List of figures

List of tables

Chapter 1

Introduction

> *By the means of Telescopes, there is nothing so far distant but may be represented to our view; and by the help of Microscopes, there is nothing so small as to escape our inquiry.*
>
> Robert Hooke, 1665 (in the preface of *Micrographia*)

The British philosopher and polymath Robert Hooke was the first human to observe a living microorganism under a microscope when he described the fungus *Mucor* on a piece of leather in his 1665 published *Micrographia* as "microscopical mushrooms" [1]. It was also Hooke who coined the term "cell" in his *Micrographia*, as the honeycomb-like structures he observed when looking at cork under his microscope reminded him of the cells of monks in a monastery [2]. At the time, Hooke did not realise that what he was seeing were the remaining cell walls of dead cork cells. It wasn't for almost another 200 years, until the cell as the fundamental unit of life was recognised with the works of Schleiden, Schwann and Virchow in the mid 19th century [3]. Naturally, the envelope surrounding the cells was of particular interest from early on, as it sets the boundary of the cell and controls what goes into and out of the cell [4]. The theories regarding the function of the cell envelope go back to the 19th century. One of the earliest theories was proposed by the German botanist and plant physiologist Wilhelm Pfeffer in 1877. He conducted studies on the osmotic pressure within cells and concluded that the protoplasm of cells is surrounded by a thin layer that he called the "plasma membrane" [5, 6]. Pfeffer was not able to deduce the makeup of the plasma membrane from his experiments. However, he did speculate that the membrane is at least partially made up of proteins [5]. Due to his early work on cell membranes, he is sometimes referred to as father of membrane theory [6].

Gaining a better understanding of molecule transport through biological membranes is also the aim of the research presented in this thesis. However, before we begin to lay out our own research, let us briefly look into the past and see how our understanding of cell membranes has evolved since the days of Wilhelm Pfeffer.

The next crucial figure for the refinement of our understanding of cell membranes was the British biologist Ernest Overton. In his permeability measurements, 1899 published, Overton observed that ether soluble (nonpolar) substances can enter cells. In contrast, water soluble (polar) substances caused shrinking of cells [7]. Moreover, he recognised that the permeation of molecules correlates to their partition coefficient between water and oil [6] and concluded that the membrane is made from phospholipids and cholesterol [6, 7]. Phospholipids were known to Overton, as the French chemist Theodore Gobley had extracted phosphatidylcholine from several organic tissues and identified their chemical structure some 50 years earlier [8]. The structure of a phospholipid molecule is displayed in Figure 1.1. Phosphatidylcholines consist of two fatty acid chains, glycerophosphoric acid and choline. The remarkable feature of these molecules is their amphiphilic nature. Whereas the two fatty acid tail groups are hydrophobic, the glycerophosphocholine forms a hydrophilic head group [4]. From works by Langmuir in 1917, it was also known that phospholipids could form molecular layers [6].

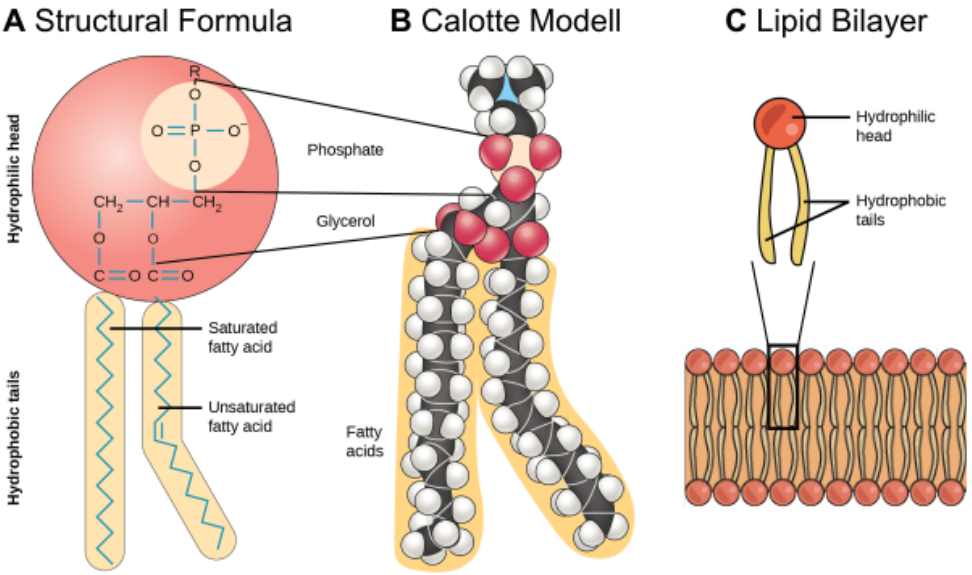

Fig. 1.1. (A) Structural formula of a phospholipid molecule. The combination of a hydrophilic head group and two hydrophobic tail groups give rise to the amphiphilic nature of the molecule. (B) Calotte modell of a phospholipid molecule. The hydrophobic tails consist of two fatty acid chains. The head group is made up of a glycero-3-phosphate to which other moieties such as choline can attach to. (C) Lipid molecules can form bilayers where the hydrophobic tails face each other and the headgroups face outwards. Image adapted from [9].

All these findings led Gorter and Grendel to propose the first membrane model of cells in 1925, according to which a single lipid bilayer covers the cell surface [6, 10]. The arrangement of lipid molecules in such a bilayer is depicted in Figure 1.1C. The phospholipid molecules are oriented in a way that the hydrophobic tail groups face each other, whereas the hydrophilic head groups face outwards [11]. This model was developed further in 1935, when Danelli and Davidson proposed that a protein layer is absorbed to each side of the bilayer [6]. Early electron microscopy studies by Robinson seemed to confirm this picture of biomembranes. In his 1959 review, he concluded that all membranes of biological cells follow a similar construction principle. According to him, they form a 7.5 nm thick three-layered structure where two protein layers are adsorbed to each side of the bilayer [12]. He called this structure the unit membrane [7]. Today, we believe that the triple layered structure observed by Robinson was likely an artefact stemming from the preparatory techniques of the time [11]. These caused extensive denaturing of the proteins and led to the structure that Robinson observed [11]. Robinson's unit membrane was also not universally accepted in the field at the time and throughout the 1960s, several other membrane models were discussed [7, 11].

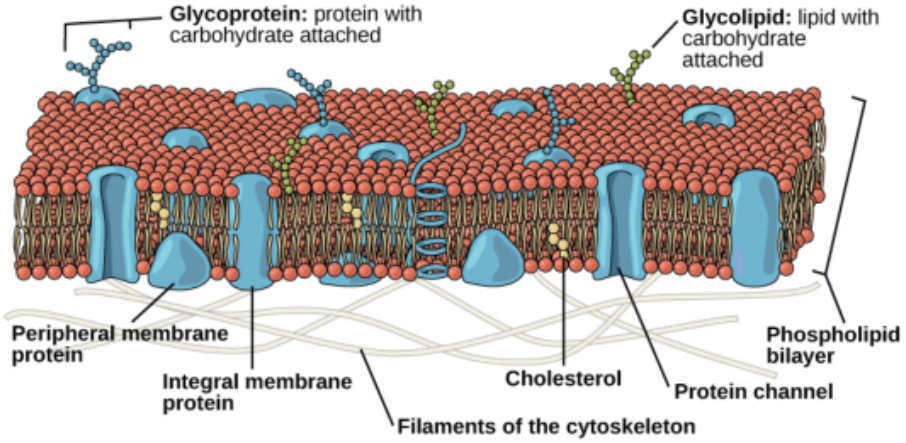

Fig. 1.2. Schematic of the fluid mosaic model. The backbone of the cell membrane is a lipid bilayer. Membrane proteins can be adsorbed to either side of the membrane, or span through the entire lipid bilayer. The proteins can freely diffuse laterally within the lipid membrane. Image from [9].

The next major refinement of the membrane model came from two scientists called Nicolson and Singer. Work on proteins throughout the 1960s let them to believe that proteins can also span through membranes. Furthermore, they observed labelled proteins as isolated spots on electron microscopy images [6]. In 1972 they proposed their highly influential membrane model called the fluid mosaic model, schematically drawn in Figure 1.2 [13]. According

to this model, the structure forming unit of the membrane is a single lipid bilayer. Proteins may be either adsorbed to the membrane, or span through it. The lipids are predominantly in their fluid state, allowing the proteins to freely diffuse laterally in the membrane [6]. Although this model has seen some refinement in the years since, the fluid mosaic model is still a widely accepted and highly useful model of biological membranes [6, 14]. Singer and Nicolson's picture of the fluid mosaic is also the underlying model that our theories of membrane transport are based on.

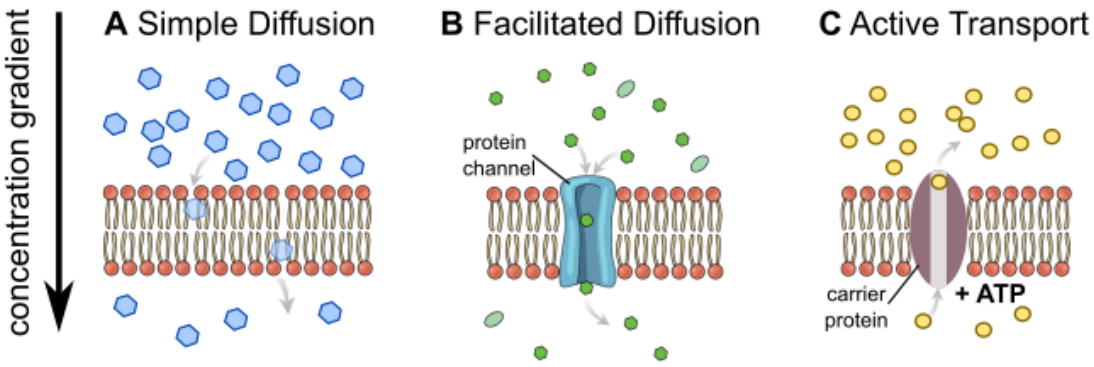

Fig. 1.3. Schematic of membrane transport mechanisms. (A) Driven by a concentration gradient, small nonpolar molecules can cross the membrane via passive diffusion. (B) Larger molecules or ions cannot permeate the membrane direcly, but require channel proteins that allow them to cross the lipid bilayer. (C) With consumption of ATP, active transporters can move molecules against an existing concentration gradient. Image modified from [9].

Understanding transport across biomembranes is crucial and a very active field of research [15]. The main motivations for this type of research are to improve our understanding of drug delivery [16], cell signalling [17], cell homeostasis [18] and diseases such as channelopathies [19]. As it is the outer boundary of the cell, every substance that enters or leaves the cell must pass the membrane. Schematically drawn in Figure 1.3, there are several mechanisms by which transport can occur. The simplest mechanism is passive diffusion. The driving force for the transport is a concentration or charge gradient between the two sides of the membrane. However, the permeability of membranes towards different molecules varies enormously depending on the polarity and size of the molecule [4, 15]. Whereas small nonpolar molecules such as oxygen transverse the membrane almost unhindered, the permeability of larger molecules is many orders of magnitude below that of oxygen [15]. Ions and most large molecules cross the membrane via different mechanisms and do not rely on passive diffusion. Instead, they require transporter proteins to pass the membrane [4, 15]. The two major classes of membrane transport proteins are channels and carriers. Channel proteins form aqueous pores that allow specific molecules to cross the membrane [4] via a process called facilitated diffusion. Carrier proteins on the other hand convey active transport.

They bind the specific solute and transfer it to the other side of the bilayer via a series of conformational changes, typically requiring ATP or other sources of energy to do so [4, 15]. Furthermore, there are several endocytic pathways that allow for molecules to enter and leave cells [15]. Today we know that many molecules in fact pass the membrane via more than just one pathway [20].

The work presented in this thesis aims to develop a better understanding of passive membrane transport. In the first part of the thesis, we will develop the necessary tools to measure membrane transport, before we look at the transport of small antibiotic molecules and protons in detail. However, we will not use cells to conduct our experiments, but instead use objects known as lipid vesicles, or liposomes. Lipid vesicles are small aqueous droplets that are encapsulated by a lipid bilayer. By stripping the membrane of proteins and using a simple bilayer with a well-defined lipid composition as our model membrane, we reduce the possible pathways of molecules to pass the membrane to simple diffusion. This reductionist approach allows us to precisely measure the membrane's permeability to the molecules in question without the interference of proteins or active processes that might occur in living cells. In a bottom up approach, the complexity of the membrane can then be expanded, for instance by inserting proteins or DNA structures into the liposome membrane and studying the effect of this inserted structure on transport [21].

We will use a recently developed technique called Octanol-Assisted Liposome Assembly (OLA) as the main source of liposomes in this thesis. We will perform a literature review, where we discuss OLA and other techniques to obtain liposomes in detail, before we provide a biophysical analysis of liposomes generated with OLA and compare them to vesicles obtained via traditional techniques. After examining OLA vesicles for their suitability for transport measurements, we expand the OLA technique and develop a platform that allows for the fabrication and controlled exposure of liposomes to the molecule whose transport is to be investigated. The methods we use to visualise the transport and determine the permeability rates can be summarised under the term optofluidics. Optofluidics is an approach which combines microfluidic methods with optical systems [22]. In our case, we will either use fluorescent labels and indicators or exploit the molecule's autofluorescence to visualise the transport. As pointed out above, we will then go on to investigate membrane transport with our newly developed methods. First, we will look at the permeability of small antibiotic molecules of the fluoroquinolone family. After that we expand our model membrane by inserting DNA structures into the bilayer to investigate whether or not this increases the membrane's permeability towards protons. Finally, we widen the scope of our technique by developing a new visualisation method based on the deep UV absorbance of molecules rather than fluorescence.

The thesis is structured as follows[1]

In **Chapter 2**, we provide a literature review of liposome formation techniques. Specifically, we will look at the traditional electroformation method, as well as the newly developed Octanol-Assisted Liposome Assembly (OLA) technique. We will lay specific emphasis of the solute composition necessary to form liposomes with OLA and investigate how the chemical environment might affect membrane properties.

In **Chapter 3**, we perform a biophysical analysis of vesicles derived from OLA and compare them to liposomes obtained via the traditional electroformation method. By demonstrating the quantitative similarity of the membrane properties, we show that OLA vesicles qualify for use in transport studies.

In **Chapter 4**, we develop the OLA technique further to obtain an integrated platform that allows for the formation and controlled exposure of lipid vesicles to an aqueous solute containing the molecule whose transport is to be investigated. Using this platform, we measure the permeability coefficient of two antibiotics of the fluoroquinolone family.

In **Chapter 5**, we use a novel microfluidic perfusion assay to study the transport of protons through lipid membranes. Furthermore, we modify our model membrane by incorporating DNA nanostructures into the bilayer and investigate whether or not these can act as ion channels, enhancing proton permeation.

In **Chapter 6**, we expand the scope of our technique to non-fluorescent molecules. We design and construct a new optical setup that exploits deep UV absorbance to visualise and measure the membrane transport and perform preliminary transport measurements.

In **Chapter 7**, we summarise our findings and provide an outlook on future studies with the microfluidic tools we developed in this thesis.

[1] In this thesis, I have consistently used the first-person plural ("we") when describing the work I performed. I opted for this style in order to be consistent with my journal publications and improve readability. Despite using "we" consistently in this thesis, all results described here are product of my own work and I designed, conducted and analysed all the experimental data myself, unless it is indicated by a footnote.

Chapter 2

Review of Lipid Vesicle Formation Techniques

2.1 Introduction

In this chapter, we will introduce lipid systems called lipid vesicles. Lipid vesicles are small aqueous droplets that are encapsulated by a lipid bilayer. Over the past decades, these structures have been an important tool in studying the properties of lipid membranes and have contributed fundamentally to our knowledge of these structures.

In the following sections we will first discuss the origins of vesicle-based research and introduce two traditional fabrication techniques. Subsequently, we will focus on a novel method to generate lipid vesicles called Octanol-Assisted Liposome Assembly (OLA). This technique is the main source of lipid vesicles in the studies presented in this thesis.

2.2 Classification and History

Lipid vesicles come in many shapes and sizes. Figure 2.1 illustrates their most common classification [23]. Vesicles are generally classified by their lamellarity and their size. If the membrane is made up of a single bilayer, the vesicle is called unilamellar. Membranes consisting of several bilayers are called multilamellar [24]. Unilamellar vesicles of up to 100 nm are typically called small unilamellar vesicles (SUVs), whereas vesicles of several hundred nanometres up to a micron are termed large unilamellar vesicles (LUVs). If the

diameter is greater than 1 micron, the term giant unilamellar vesicles (GUV) is used. [23, 24]. Vesicles can furthermore encapsulate other, smaller vesicles, in which case they are called multivesicular [23].

In the scientific literature, lipid vesicles are also often referred to as liposomes. Throughout this thesis, we will use the two terms interchangeably. Moreover, we will primarily focus on giant unilamellar vesicles (GUVs) in our studies. GUVs have several advantages associated with them, which we will look at in more detail later. First, we present a short overview of the origins of liposomes, and vesicle research.

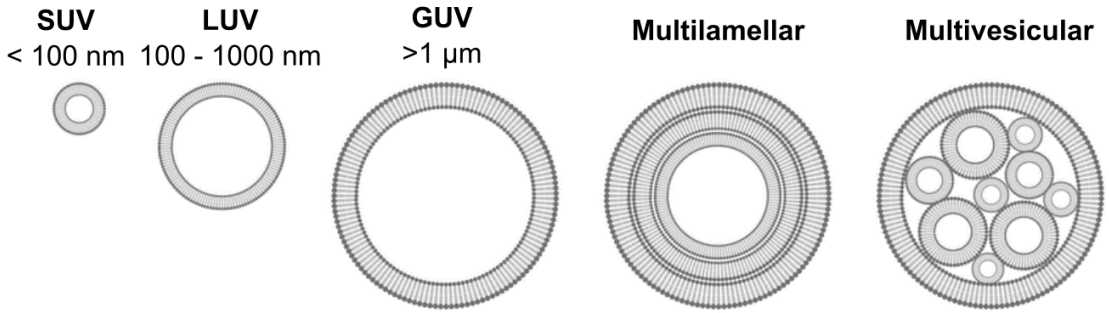

Fig. 2.1. Classification of lipid vesicles. Vesicles are classified as unilamellar if the liposome consists of a single bilayer, and multilamellar if several bilayers make up the membrane. Unilamellar vesicles are further classified according to their size. Unilamellar vesicles with a diameter under 100 nm are denoted as small unilamellar vesicles (SUVs), whereas vesicles with diameters ranging from several hundred nanometres up to a micron are called large unilamellar vesicles (LUVs). Vesicles of more than 1 micron in diameter are called giant unilamellar vesicles (GUVs). Vesicles that encapsulate other smaller vesicles are termed multivesicular. Image adapted from [23].

The story of liposomes begins in Cambridge in the year 1964. At the Babraham Institute, a partner facility of the University of Cambridge, Bangham and Horne recorded the first electron microscope images of multilamellar lipid vesicles [25, 26]. Bangham and Horne called the structures they observed "multilamellar smectic mesophases" and stated the extreme similarities to previous studies on nerve myelin in their original paper [25]. In the following years, Bangham *et al.* performed more ground breaking research on membranes, for instance, when they showed that bilayers could maintain ion concentration gradients and that detergents disrupt the bilayer [27, 28]. Bangham's research therefore provided important evidence for the theory that lipid bilayers are the primary permeability barrier of cell membranes, a finding that has been called "the membrane equivalent of finding the double helix structure of DNA" [26]. We must not forget that Bangham and Horne published their findings before there was consensus on the structure of biological membranes, and eight

years before Singer and Nelson proposed the fluid mosaic model [13]. Research in the years following the 1964 paper often referred to the structures observed by Bangham and Horne as “Banghasomes” or “lipid spherules” [26]. These names stuck until 1968, when Sessa and Weissmann published their influential paper “Phospholipid spherules (liposomes) as a model for biological membranes”, which led to the establishment of term “liposome” for these structures [26, 29].

Over the past decades, liposomes have found widespread use in many branches of science. They provide an ideal model membrane and allow for the systematic measurement of membrane properties [30]. This is especially the case for giant unilamellar vesicles, as their large size allows us to observe them using optical microscopy techniques and manipulate them individually, for instance using micro pipettes or optical tweezers [30, 31]. Unlike cells, vesicles are formed from a well-defined lipid mixture in a controlled environment. This reductionist approach enables us to deconvolute the myriad effects that happen at a natural cell membrane and study them individually. In fact, in the first paper describing GUVs in 1969, the authors stated that their motivation was to create a controlled system to study membrane permeation [32]. Since then, other model techniques such as supported lipid bilayers, black lipid membranes, lipid stacks and monolayers at the water-air interface have emerged [30]. However, GUVs remain a widely used model. One of the main advantages of GUVs over other techniques is their curvature resulting from their size, which is similar to that of cells [30]. Moreover, GUV membranes are typically free standing bilayers, and are not hindered sterically by a support or mechanical contraption [30].

2.3 Traditional Fabrication Techniques

Due to their widespread use as model membrane, many different techniques to form GUVs have emerged. These can be broadly classified into two categories and either form GUVs via swelling from a solid substrate, or are assembled from fluid interfaces, usually an oil phase [30]. Of the swelling approaches, a technique called electroformation has found especially widespread use. We will look at this technique in more detail below, as it is one of the techniques we use in this thesis to generate liposomes. Of the second category, many make use of microfluidics to form GUVs [23, 30]. We will have a short look at a previously published microfluidic technique, before we turn to Octanol-Assisted Liposome Assembly (OLA), the microfluidic method we used throughout this thesis to create GUVs on chip.

2.3.1 Electroformation

In the swelling approaches to form GUVs, the liposomes form spontaneously and bud off a lipid film in an aqueous environment. For this to happen, the lipids are dissolved in a volatile solvent, usually chloroform, and spread onto a solid substrate. The solvent is then evaporated and the lipid films hydrated. The liquid solution runs between the lipid lamellae on the substrate, which leads to the budding off of vesicles [30, 32].

This process, first published by Reeves and Dowben in 1969, occurs naturally without any external forces applied to the system [32]. However, this process is very slow and GUV formation protocols can last up to 1-2 days [30]. Strongly related to this method is the electroformation method, which is also often called electroswelling [30]. This technique was presented by Angelova and Dimitrov in 1986 [33]. They observed that external electric fields can influence the swelling of lipid films by exerting attraction and bending forces on the membrane. Applied to the lipid films when forming GUVs, this proved to drastically increase the yield and decrease the preparation time to several hours [30, 33]. The widespread use of this technique has even led to the development of a commercial bench-top device (Vesicle Prep Pro, Nanion Technologies GmbH, Germany), which facilitates GUV production via electroformation; this was also used in the studies presented in this thesis.

For the electroformation method, depicted in Figure 2.2, the lipid film needs to be spread on a conducting surface, in our case Indium Tin Oxide (ITO) coated glass slides. After the organic solvent (chloroform) has been evaporated away, the liquid solution is added on top of the lipid film and held in place by a rubber O-ring. Another ITO coated slide is placed on top of that and alternating current (AC) electric fields are applied to the lipid film via the conductive coatings [33].

GUVs formed via electroformation have been used for numerous studies and drastically increased our knowledge of lipid membranes. For instance, the method proved very useful to investigate membrane phase behaviour [35] and the mechanical properties [36] of lipid bilayers. Electroformed GUVs have also been a tool for drug permeation studies [37]. In addition, electroformation has been used for the creation of liposomes with complex binary and ternary lipid mixtures [35, 38]. However, there are drawbacks associated with this technique. Electroformation suffers from large batch-to-batch variation, as the spreading of the lipid film is crucial to the quality of the liposomes produced. Yet, the way the lipid film is deposited on the substrate is not easily reproducible [39]. Furthermore, the presence of ions in the solution interferes with the electric fields, which is why electroformation buffers usually require low ionic strengths [39]. Similarly, the method poses restrictions on the

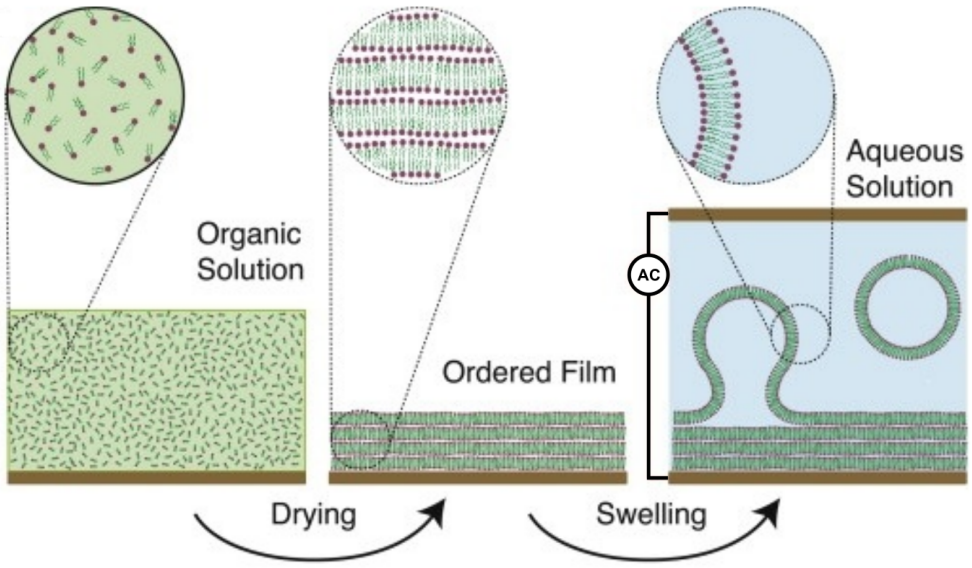

Fig. 2.2. Schematic of the electroformation process. After evaporating the lipid-carrying organic solvent, the lipids form structured films on the conducing surface substrate. The lipid films are hydrated and sandwiched by another coating surface from the top. The application of alternating currents via the conducting surfaces leads to lipid swelling and the eventually budding off of vesicles. Image adapted from [34].

choice of lipids, as it can promote oxidation in poly-unsaturated lipids [40] and has to be adapted for the use of charged lipids [39, 41]. A 2012 study even found that demixing of lipid mixtures can occur in the dried form, leading to heterogeneity in lipid composition of the resulting liposomes [42]. The nature of the method, furthermore, makes it hard to exert control over the size of the created liposomes [39], although a recently published protocol to swell the vesicles from a 2D-patterned surface seems to enhance control over the GUV size [43]. Finally, the electroformation method does not allow for the easy encapsulation of an aqueous solution inside the vesicle that is different from the surrounding fluid [44].

Notwithstanding these limitations, electroformation remains a useful technique for the formation and study of lipid vesicles. Yet, some of the limitations listed above can be overcome by novel microfluidic techniques, which we will discuss next.

2.3.2 Microfluidic Techniques

As the name implies, microfluidics is a field that deals with fluid systems in which the channels are scaled down to the micro domain [23]. The decrease of the characteristic dimensions to the micro and nano scale leads to an environment that is drastically different to the macro world. As the characteristic lengths decrease, the different physical forces do not decrease proportionally, leading to some effects of the macro world becoming negligible in the microchannels, whereas others dominate and vice versa [45]. In the testing of engineering models, the effects resulting from miniaturisation are often summarised under the term scaling laws [45, 46]. For us, what is important is that fluid flows in the micro world occur in a low Reynolds number regime [23, 45, 46]. The Reynolds number describes the relationship between viscous forces and inertial forces [47]. This means that fluid flows in a microfluidic chip are dominated by viscous forces and are therefore characterised by stable hydrodynamics and laminar flows [45, 46]. These conditions allow for precise process control and the use of smaller reagent volumes, shorter reaction times and the possibility of parallel operation [48, 49]. Many microfluidic applications aim to achieve a so called lab-on-a-chip, meaning the miniaturisation and integration of an entire experiment on a single micro device [48, 49]. We have done this ourselves, when we developed our own microfluidic platform to study membrane permeability. We will deal with the theoretical background of microfluidics in more detail in Chapter 4, when we discuss the development of this platform. For now, we describe a prominent microfluidic method that has been developed to obtain GUVs.

Figure 2.3 shows an example of a microfluidic device used to produce GUVs on chip following the double-emulsion approach. In these microfluidic systems, the GUVs are assembled stepwise. First, the microfluidic chip is used to create water in oil droplets. Typically, this occurs at a 4-way junction, where an inner aqueous phase is flanked by two oil carrying channels and the water-oil-immersion flows along the remaining channel. The lipids are dissolved in the oil phase and assemble into a monolayer at the water-oil interface [39]. In a second step, the outer lipid monolayer is assembled. This is done by flanking the W/O immersion again, this time by two channels carrying the external aqueous phase. What results is a W/O/W double emulsion, with a lipid monolayer on each side of the water interface [39]. In a final step, the residual solvent is removed to obtain GUVs [23, 39]. Different organic phases have been used to carry the oil, namely oleic acid [50, 51], squalene oil [52] or dodecane [53].

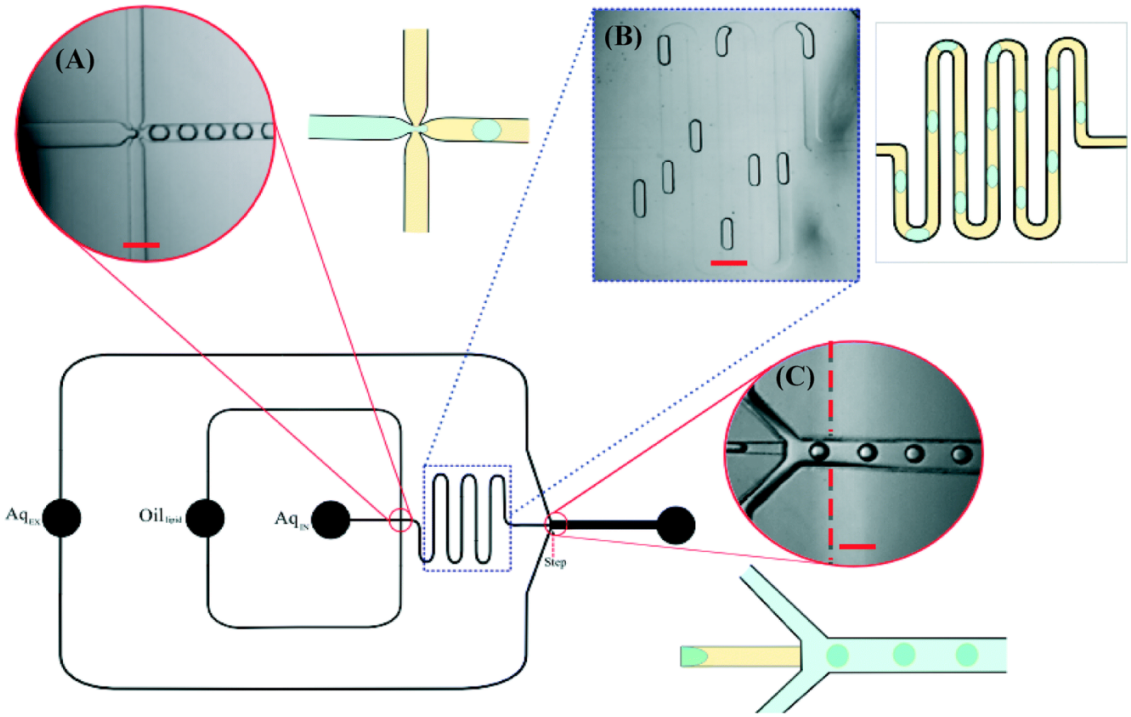

Fig. 2.3. Schematic and images of microfluidic chip to form double emulsion vesicles. (A) Formation of monodisperse water in oil (W/O) droplets. The internal aqueous phase (Aq_{in}) is flanked by two oil carrying channels (scale = 70 µm). (B) Delay line allowing for the lipid dissolved in the oil to assemble into a monolayer at the water-oil interface (scale = 80 µm). (C) Transfer of W/O droplets into external aquesous (Aq_{ex}) phase. The lipids dissolved in the oil phase form the second leaflet of the bilayer at the exterial oil-water interface (scale = 100 µm). Image from [52].

To date, different techniques have been developed to aid the removal of the residual oil phase from the GUV [23]. Whereas the first published methods still extracted the GUVs to remove the residual solvent off chip [54], later publications incorporated the removal procedure on chip [51]. The GUVs were immersed in a solution of water and ethanol, whereby the ethanol dissolved the organic compound. It is also possible to remove excess solvent via non-chemical methods, as is shown by a 2016 publication that was able to remove 93% of a fluorinated oil from a double emulsion via controlled mechanical squeezing inside a microfluidic chip [55].

The vesicles produced via this double emulsion approach have the advantage that they are monodisperse, unilamellar and can be formed in chemical environments that are difficult for other techniques such as electroformation [23]. Furthermore, since the aqueous substance that makes up the inside of the GUV is separated from the outer aqueous solution as of formation, these techniques allow for the selective encapsulation of an "inner" phase inside the liposomes [23]. On the other hand, these methods require extensive washing of the obtained liposomes, to remove the residual solvent from the double emulsion and form a true bilayer liposome [23, 54, 56].

In 2016, a novel method was presented that found a very elegant solution to the problem of residual oil removal. This microfluidic method, called Octanol-Assisted Liposome Assembly (OLA) is discussed in the next section.

2.4 Octanol-Assisted Liposome Assembly

In this section, we take a closer look at the Octanol-Assisted Liposome Assembly (OLA) technique. Introduced by Deshpande *et al.* in 2016 [56], we adapted this technique and it will prove to be our primary method for obtaining GUVs in the experiments to come. As we pointed out above, this method found a very elegant solution to the problem of residual oil in the GUV via modifications of the junction design and the choice of solvent.

2.4.1 Chip Design and Vesicle Formation

A schematic of the basic chip design is shown in Figure 2.4A. The chip has three fluid inlets and one outlet. OLA allows for the precise control of the solutions in the inside and outside of the vesicle. The aqueous substance which is to be encapsulated in the inside of the vesicle's lumen enters the chip via the inner aqueous (IA) inlet. The outside solution is flushed in via the outer aqueous (OA) inlet. The lipid making up the GUV's membrane is dissolved in 1-octanol and enters the chip via the Lipid-Octanol (LO) inlet. The channels leading towards the OLA junction are artificially elongated, running in spirals before reaching the junction. These long channel lines act as low-pass filters in the fluid system. They buffer spontaneous pressure peaks and slow down flows in general by increasing fluid resistance, thereby increasing pressure and flow control.

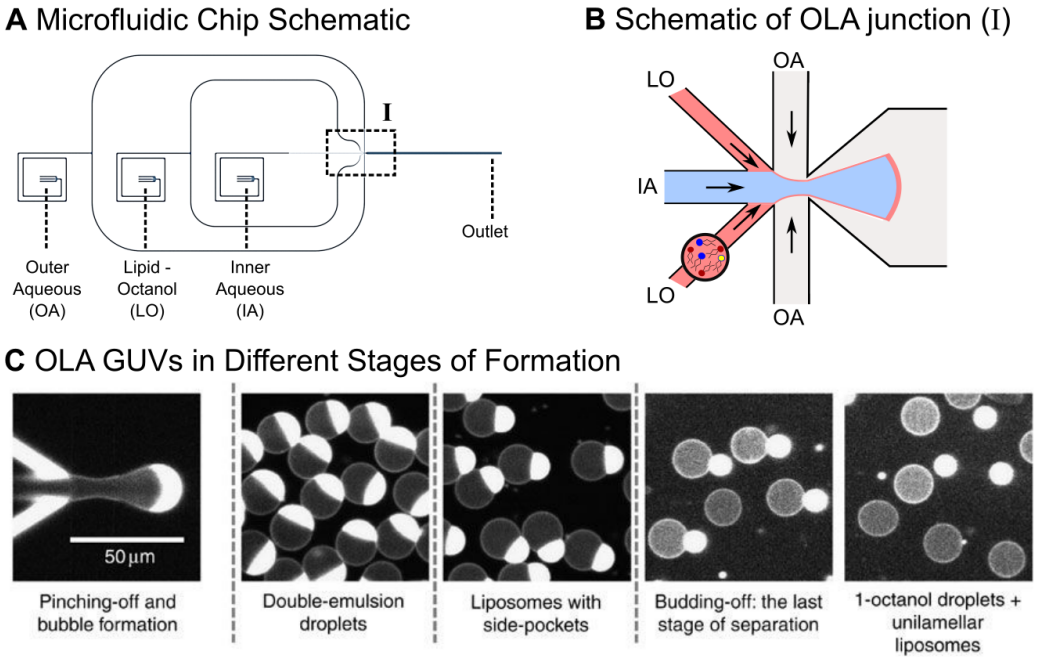

Fig. 2.4. (A) Schematic of the microfluidic chip used to produce the liposomes. The chip has three inlets for the inner (IA) and outer aqueous (OA) and the lipid-octanol (LO) phases, respectively. The vesicles are formed at a six-way junction (I) and flow along a long channel to the outlet where they can be extracted or imaged directly. (B) Schematic of the OLA junction, where liposome formation occurs. The IA fluid stream is flanked by two channels with the lipid-carrying LO phase. The OA flows pinch off double emulsion droplets. Different lipid types, as well as fluorescent lipids can be dissolved in the octanol. (C) Fluorescent OLA GUVs in different stages after formation. A double emulsion droplet is formed at the OLA junction in a process similar to blowing soap bubbles. Further downstream, the double emulsion self-assembles into a vesicle with a 1-octanol pocket attached to it. Seconds to minutes after formation. The octanol pocket completely buds off the vesicle, resulting in separate GUV and an octanol droplet. Subfigure (C) modified from [56].

The first innovation introduced by this technique is the junction design. In contrast to the previous double emulsion techniques, OLA does not use two 4-way junctions to assemble the inner and outer lipid leaflet in distinct and separate steps. Instead, these two junctions were combined into a single six-way junction, where the formation of the double emulsion occurs [56]. This junction design allows for the production of double emulsions using substantially less solvent, resembling some glass capillary approaches which, similarly, allow the formation of ultra-thin shelled double emulsions [57]. The six-way junction is schematically depicted in Figure 2.4B. By jetting a stream of inner aqueous (IA) solution into a meniscus of the lipid-octanol (LO) phase and pinching it off by the streams of the outer aqueous (OA) solution, the process of double emulsion formation is similar to blowing a soap bubble [56].

After the double emulsion is formed, the second innovation introduced by OLA comes into play. Unlike the other double emulsion techniques, OLA does not use oil or alkanes as the lipid carrying organic phase, but the aliphatic alcohol 1-octanol [56]. Deshpande *et al.* observed that this substance does not form stable long lasting double emulsions. Instead, the droplets quickly form an intermediate complex of an aqueous compartment surrounded by a lipid bilayer and a 1-octanol pocket attached to it [56]. As the liposome flows along the channel, the octanol pocket separates from the structure, resulting in a seemingly solvent-free liposome and a separate octanol pocket. Several effects must come together to result in this remarkable effect. One element is surely the chemical structure of octanol itself, shown in Figure 2.9. Unlike the previously used alkanes, octanol is amphiphilic by nature, resembling lipid molecules in this respect, although, unlike lipids, octanol cannot form bilayers [58]. The inventors furthermore attribute the separation to a combined effect of surface energy minimisation, shear stress induced by the surrounding fluid streams as well as contact with the channel wall [56]. We will discuss the properties of octanol in more detail below.

Figure 2.4C shows microscopy images of OLA vesicles in different stages after formation at the junction. In their original paper, Deshpande *et al.* state that after 5 minutes, 85% of the double-emulsion droplets separated into GUVs and octanol droplets, respectively [56]. As we will see later, the process of octanol separation depends on several elements, namely the speed of the fluid streams and the channel height. After separation, the GUVs and octanol droplets flow further downstream, towards the outlet. From the outlet, the GUVs can either be extracted or imaged directly. In Chapters 4 and 5, we will describe how we altered this basic OLA design and included downstream operations to handle the GUVs within the microfluidic chip.

In the next section, we will discuss the process of OLA chip production, preparation and GUV formation using microfluidic pumps.

2.4.2 Chip Fabrication and Flow Control

Photo and Soft Lithography

Since its emergence in the early 1990s, many different techniques and materials have been developed for use in microfluidic chips [59]. For instance, different groups have used various etching techniques, injection moulding or in situ construction for chip fabrication [48, 60]. However, for use with biological systems, most groups rely on a two-step process of photo and soft lithography [61]. Their material of choice for the soft lithography part is poly-

dimethylsiloxane (PDMS). Its main advantages are its transparency, its oxygen permeability and its relatively cheap price [62]. Similarly, we used the combination of photo and soft lithography for the production of the OLA chips.

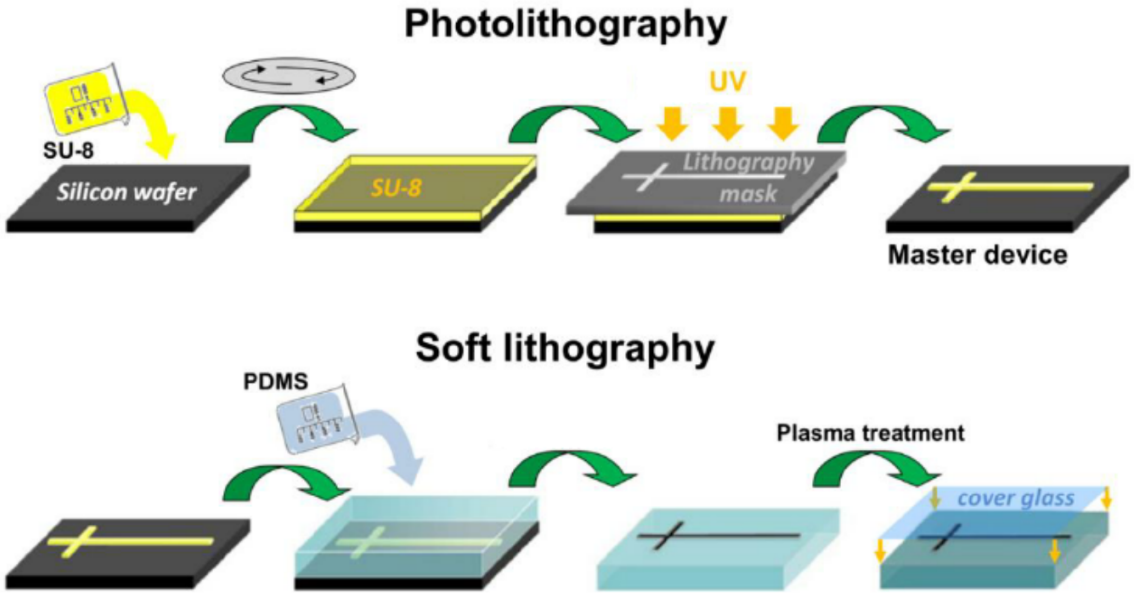

Fig. 2.5. Schematic of the fabrication of microfluidic chips. In the photo lithography step, photoresist is spin coated onto a silicon wafer. The resist is then selectively exposed with UV light. The exposed structures crosslink and solidify, whereas the unexposed structures are washed by a subsequent developer bath. This leaves the desired structures imprinted on the substrate. In the soft lithography step, liquid PDMS is poured onto the silicon master. After curing, the PDMS with the structures embossed in it is removed from the mold. The PDMS chip is bonded to a glass coverslip after plasma treatment. Image modified from [63].

In a first step, standard photo lithography is used to deposit a negative of the desired structures on a silicon wafer. To obtain this, negative photoresist such as SU-8 is spin-coated onto a silicon wafer and baked on a hot plate. The photo resist is then selectively exposed to UV radiation. Selective exposure is either achieved by shining the UV light through a mask blocking parts of the light, or by direct exposure systems, which focus UV light on the desired spots on the wafer. In the case of a negative photo resist, such as SU-8, the exposed parts crosslink and solidify thereby becoming insoluble to a developer solution. After another baking step, the wafer is washed in the developer, removing the unexposed SU-8 and leaving the UV-exposed structures remaining on the wafer.

In the soft lithography step, the wafer is used as a mold for liquid PDMS. The liquid PDMS adapts the structures that are deposited on the wafer and maintains these, as it sets. Once the PDMS has hardened, the structures are embossed in it and the chip is removed from the mold. In most cases, the final microfluidic device is obtained by bonding the PDMS chip to a glass coverslip. This is achieved by exposing both the surface of the coverslip and the PDMS to air plasma. The plasma causes silanol groups (Si-OH) to form on both surfaces. When the two surfaces are brought in contact with each other, the silanol condenses and forms an Si-O-Si bond, which fuses the PDMS and the glass slide together [62]. As we will see below, parts of the OLA chip have to undergo a coating procedure, which requires all channel walls to be made of PDMS, rather than having one side of glass. For this reason, OLA chips are made by bonding a PDMS coated coverslip on the PDMS chip, rather than a glass coverslip directly onto the chip.

PDMS coated coverslips and PVA treatment

To this end, a coverslip is coated with a thin film of PDMS before it is plasma bonded to the chip. This provides a homogeneous all-PDMS surface which is necessary for the coating procedure that is described below. The PDMS coated coverslips are obtained by pouring liquid PDMS onto a silanised wafer. The glass slides are placed on top of the PDMS and then pressed down to the surface of the wafer until they are completely immersed in PDMS. A thin layer of PDMS remains between the wafer and the glass slide. After curing, the excess PDMS can be peeled off the topside of the wafer, leaving the glass slides on the wafer, with the thin PDMS layer sandwiched between the two. Using a blade, the glass slide with the PDMS layer attached to it can carefully be removed from the wafer [64].

As shown in Figure 2.6B, the hydrophobic nature of PDMS typically leads to non-polar substances adhering to the glass and PDMS surfaces and spreading out on them [65, 66]. However, in the OLA system this has to be prevented in order to allow for the formation of double emulsion droplets. For this reason, the PDMS chip is flushed with a PVA solution via the OA channel, thereby rendering both the OA and the outlet channel hydrophilic [56, 66]. Importantly, as shown in Figure 2.6A, it is crucial not to render the IA and LO channels hydrophilic. Entering of PVA into these channels likewise impedes complete encapsulation of the inner aqueous phase by the non-polar LO phase; this is why the PVA is prevented from entering these channels by applying air pressure via the IA and LO inlets. After flushing the PVA through the chip, the PVA is removed by applying suction with a vacuum pump. The chip is then baked in the oven to cristallise and immobilise the PVA [67].

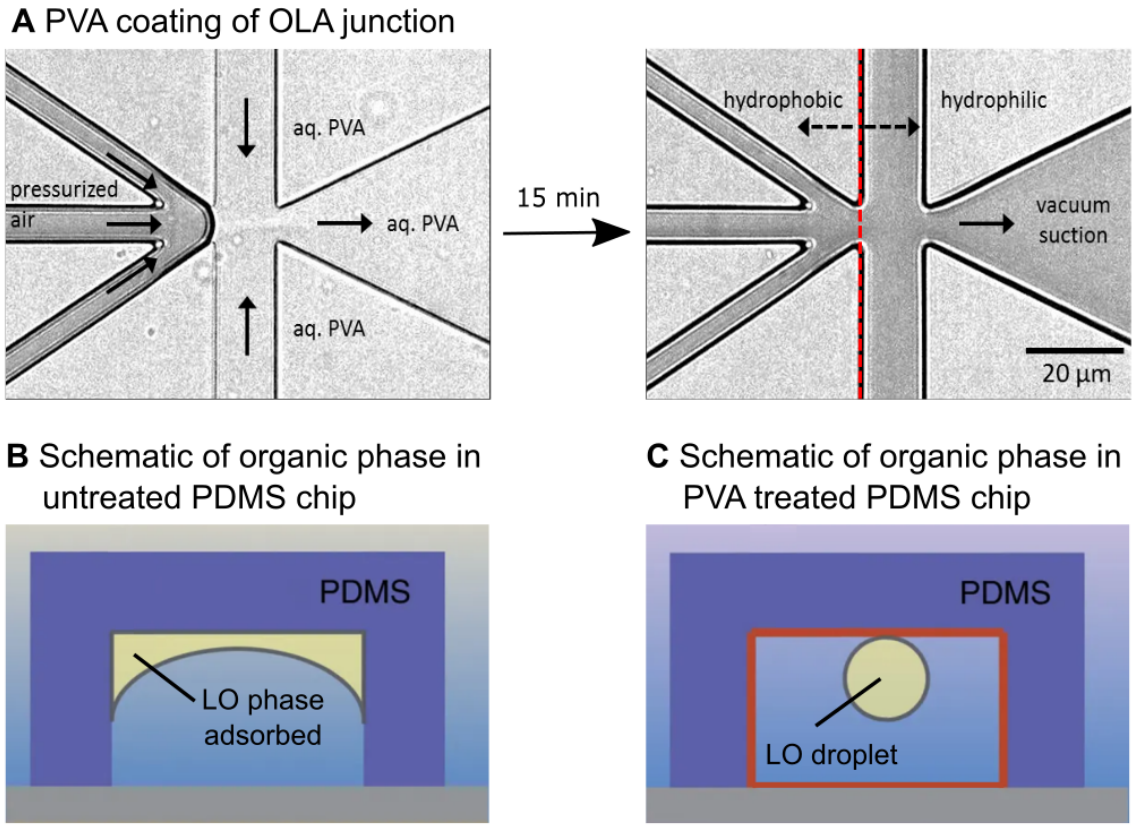

Fig. 2.6. (A) PVA coating of the OLA junction. A PVA solution is flushed through the channel via the OA inlet for approximately 15 minutes. The PVA is stopped from entering the IA and LO channels by applying air pressure via these two inlets. The PVA renders the OA and outlet channels hydrophilic. (B) Schematic of LO phase in untreated PDMS chip. Due to its hydrophobic nature, the LO phase adheres to the PDMS surface. (C) LO phase in PVA treated channel. The hydrophilic coating, shown in red, prevents octanol adhesion to the surface and enables the formation of double emulsion droplets which later self-assemble into the GUVs. Figure modified from [56] and [66].

Microfluidic Pumps

The flows in the OLA chip are controlled by pressure-driven microfluidic pumps. The microfluidic flow control system (MFCS-EZ) in combination with the Fluiwell-4C (both Fluigent SA, France) has proven very successful for the operation of the OLA chip [64, 68, 69]. In this system, the IA, LO and OA flows can individually be adjusted to create the necessary flow environment at the OLA junction, to form vesicles. The solutes are kept in a Fluiwell liquid reservoir and enter the microfluidic chip via polymer tubing and metal connector tips. Holes that are punched into the PDMS chip act as access ports for the

fluids. The individual pressures are adjusted using the MAESFLO 3.3.1 software. Figure 2.7 exemplarily shows an OLA chip as well as the Fluiwell system.

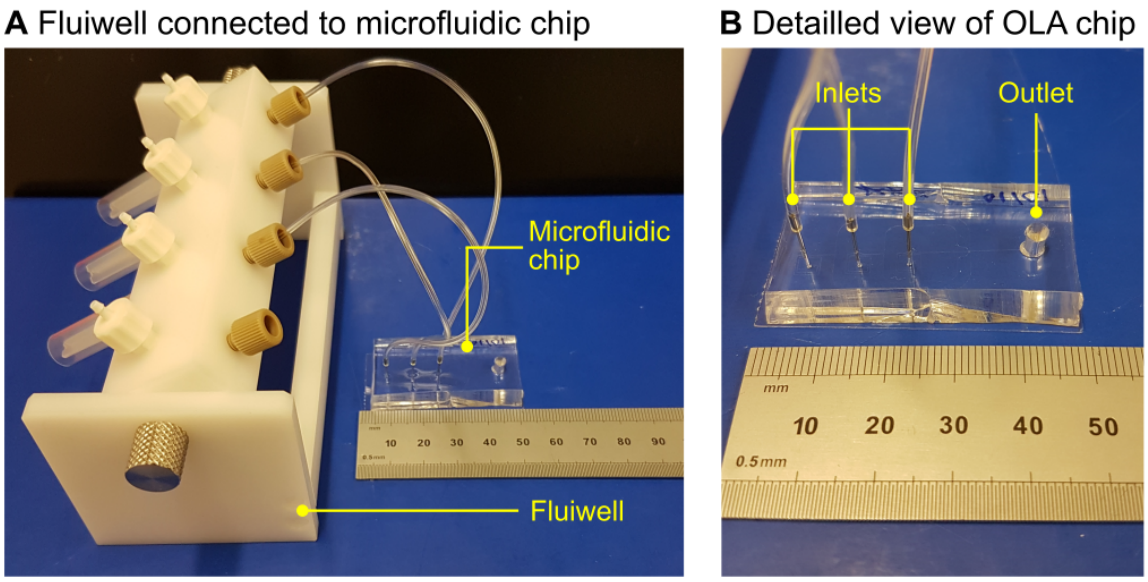

Fig. 2.7. (A) Photo of OLA chip connected to Fluiwell system. The Fluiwell is connected to the microfluidic pump which drives the flows via the polymer tubings and metal connectors into the microfluidic chip. (B) Detailed view of the OLA chip. The OA, LO and IA solutions (from left to right) enter the chip via the inlets and meet at the 6-way junction where the liposomes are formed. The large hole on the right serves as outlet reservoir, where the GUVs can be extracted or imaged directly.

The right pressure settings to achieve stable vesicle formation depend on several factors; namely the width of the junction, the height of the channels, the downstream chip design and the viscosity of the fluids. As a rule of thumb, the IA and LO pressures are roughly the same magnitude, and lower by a factor of 2-5 than the OA flows. Increased channel height and width of the OLA junction generally decreases the fluid resistance within the chip and leads to higher flow and vesicle production rates [68]. Furthermore, a larger gap at the junction generally leads to larger vesicles. The size of the vesicles can furthermore be fine-tuned by adjustment of the individual fluid streams, whereby an increase of the OA flow with respect to the IA and LO flows lead to smaller liposomes [56].

2.4.3 Solution Composition

In the following section, we take a closer look at the solution composition of the inner and outer aqueous, as well as the lipid-octanol phases that are used in OLA. Deshpande *et al.* presented several different solution compositions in their original and subsequent papers, mostly varying in the content of glycerol and poloxamer P-188 [56, 70, 71]. However, the following components turned out to be the basis necessary for robust GUV formation.

- **Inner Aqueous:** 15% glycerol in milli-Q water
- **Outer Aqueous:** 15% glycerol, 50 mg/mL P-188 in milli-Q water
- **Lipid-Octanol:** 2-4 mg/mL lipid in 1-octanol (lipid stock 100 mg/mL dissolved in EtOH)

One of the great advantages of OLA that sets it apart from many bulk techniques like electroformation is its capability to form GUVs in complex buffer solutions and at high salt concentrations [68, 69]. While most protocols for electroformation require ionic strenghts below 50 mM, we were able to successfully use OLA with in different chemical environments and at physiological ionic strength (>140 mM) [72]. The solutions we used include HEPES, PIPES, TRIS, acetic acid and potassium buffers, PBS as well as sucrose and glucose solutions. Before we finish our brief review of OLA and come to our own biophysical analysis of OLA vesicles, we describe what the existing literature says about the crucial components of OLA: Glycerol, Octanol and the Poloxamer P-188, with respect to liposome and microfluidic systems.

Poloxamer P-188

Poloxamers are a class of block co-polymers first developed by the Wyandotte Chemical Corporation in the early 1950s [73, 74]. These non-ionic detergents found widespread use in different industries, such as the textile, paper and cosmetics industries, where they are mainly used as emulsifiers [75]. What we now know as Poloxamer P-188 was originally named Pluronic F-68, and is sometimes still found under this or its other trademark names: Synperonics®, Lutrol®, or Kolliphor® [73–75]. The chemical structure of P-188 is shown in Figure 2.8A. It consists of a hydrophobic polypropylene oxide (PPO) block centred around two hydrophilic polyethylene oxide (PEO) blocks. The different poloxamers vary in the length of the respective PPO and PEO block chains. In the case of P-188 (MW $\approx$ 8400 Da), the PEO blocks make up around 80% of the molecule's weight [74, 75] which corresponds to

approximately 31 PPO groups and 75 PEO blocks on either side [76]. Since its introduction, P-188 also found several applications in medicine. For instance, it is used as an emulsifier for contrasting agents in biomedical imaging [75], and received FDA approval as a therapeutic to reduce the viscosity of blood before transfusions nearly 50 years ago [74]. Among other diseases, purified P-188 even underwent clinical trials for the treatment of sickle cell disease [77–79]. However, P-188 ultimately failed to meet its primary endpoint in a phase III study in 2016 (trial NCT01737814).

More important for us though, was the observation of P-188's effect on membranes. In the early 1990s and 2000s, it was found that P-188 aids the sealing of membranes that were electroporated or damaged by ionising radiation [80, 81]. The origin of the membrane sealing property of P-188 has since been the field of study of several groups. In 2002, Mascarinec *et al.* investigated the effect of P-188 on DMPC and DMPG monolayers using a Langmuir–Blodgett trough [82]. They measured P-188 insertion into the monolayer at low surface pressures (< 22 mN/m), but not at higher pressures. From this they concluded that the membrane healing property of P-188 stems from the insertion of the hydrophobic midsection into damaged parts of the membrane where the lipid packing density is reduced [82]. They interpret the fact that the P-188 cannot remain inserted in the membrane under the surface pressure equivalent of a normal membrane, in a way that suggests that the P-188 is "squeezed out" [82] once membrane integrity is restored. It is noteworthy that the ejection of P-188 from the monolayer has previously also been observed by another group [83].

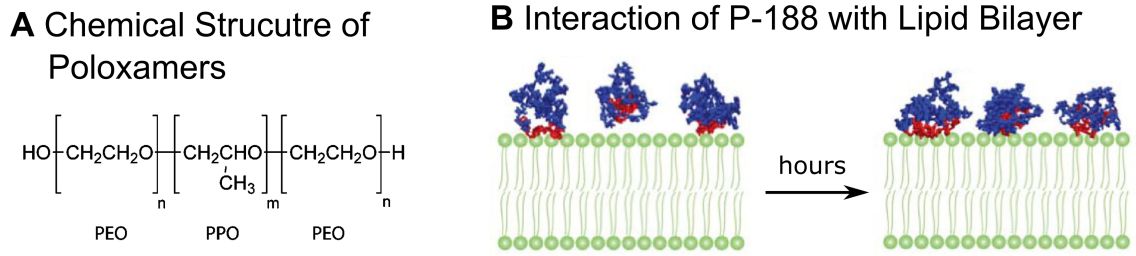

Fig. 2.8. (A) Chemical structure of poloxamers. A hydrophobic polypropylene oxide (PPO) core is attached to two hydrophilic polyethylene oxide (PEO) side chains. For P-188, the PEO chains make up about 80% of the molecule's mass (n ≈ 75 and m ≈ 31). (B) Proposed mechanism of interaction between P-188 and a lipid bilayer. P-188 adheres to the membrane, however the long PEO chains prevent the P-188 from entering the lipid bilayer. Image adapted from [83].

More recently, the effect of P-188 on DOPC LUVs was investigated by Cheng *et al.* by observing the hydration dynamics close to the bilayer using a newly developed NMR

technique [83]. They conclude that "poloxamer–membrane interaction is of subtle and weak nature" [83]. Their study furthermore implies "that the polymer–lipid interactions is (sic) too weak to cause measurable changes in lipid dynamics" [83]. Their proposed mechanism of membrane interaction is schematically drawn in Figure 2.8B. Like the previous studies, they also found that P-188 adsorbs to the membrane, but does not enter the bilayer within the time scale of their experiment, which lasted up to 45 hours [83].

Due to their emulsifying and membrane sealing properties, poloxamers are increasingly being adapted in the microfluidics community, especially by groups working with droplets, double emulsions and liposomes [51, 84, 85]. The emulsifying and membrane sealing properties of P-188 are also required for GUV formation with OLA. Attempts to form OLA vesicles both by us and Deshpande *et al.* without the presence of P-188 failed due to droplet fusion and immediate vesicle bursting [64]. In Chapter 3 we investigate the effect of P-188 on membrane properties ourselves, by studying the lipid lateral diffusion of GUVs in the presence of P-188 and without it.

Glycerol

Glycerol, also known as glycerine, is depicted in Figure 2.9. It is the simplest 3-carbon sugar alcohol. It is used for a myriad of purposes in different fields of science and can be found in everyday household items such as food additives, cosmetics and antifreeze [86]. In the field of microfluidics, glycerol has previously been used to modulate solution viscosities [87] and it found several applications in the microfluidic production of droplets [87–89]. The viscosity modulating property is also the main reason for the use of glycerol in OLA [64]. At room temperature, the addition of 15% glycerol increases the dynamic viscosity of water by over 60% from 1.005 mNs/m^2 to 1.6458 mNs/m^2 [90]. The higher viscosity of the OA improves shearing on the LO phase and thereby facilitates the separation of the octanol pocket from the liposome [64, 91, 92]. Furthermore, more viscous fluids reduce the Reynolds number, leading to more laminar flows and thus facilitating encapsulation [47, 92].

In addition, glycerol has also been found to have a stabilising effect on lipid membranes [92]. The increase in membrane stability is attributed to an increased membrane hydration caused by the glycerol [93, 94]. Since glycerol is membrane permeable, we can also expect it to balance potential differences in osmotic pressure between the GUVs inside and outside upon formation. Deshpande *et al.* have reported that the removal of glycerol from the solution composition impacts liposome formation [64] which is the reason why it is contained in our standard OLA protocol.

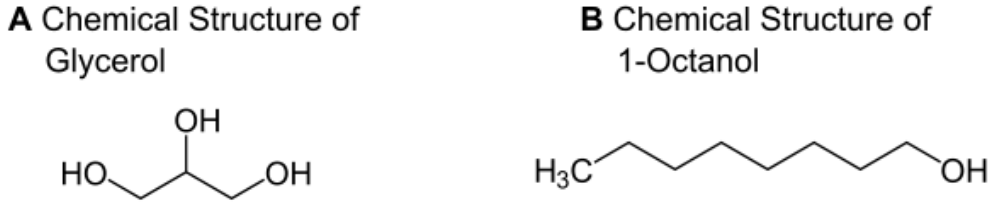

Fig. 2.9. Chemical structures of (A) glycerol and (B) 1-octanol.

Octanol

Finally, we take a look at the eponymous element of OLA, the octanol itself. Note that throughout this thesis, when we are speaking of octanol, we always mean 1-octanol and do not speak of its isomers (2-octanol, 3-octanol, etc.).

The chemical structure of octanol is shown in Figure 2.9B. Octanol is an aliphatic 8-carbon alcohol. Its most prominent application is its use in the determination of a metric known as the water-octanol partition coefficient [95]. The partition coefficient, described by Equation 2.1, is the ratio of equilibrium concentrations of a solute in a mixture of two immiscible solvents, in this case water and octanol [95].

$$P = \frac{[solute]_{orgphase}}{[solute]_{aqphase}} \tag{2.1}$$

As such, the partition coefficient is a metric for the lipophilicity of a substance. Interestingly, the partition coefficient is used by the pharmaceutical industry to estimate the membrane permeability of drugs. The hydrophobicity of the octanol is used as a model to approximate the non-polar hydrophobic layer of a lipid membrane which is the main barrier for drugs or other compounds entering a cell [37]. Importantly, the partition coefficient only takes the equilibrium of un-ionised compounds into consideration [96]. The value is therefore a constant and independent of properties like the pH [96]. However, as we will see later, many compounds dissociate in water and the degree of ionisation depends on the pH and the pKa [97]. Furthermore, we wish to point out that this method of estimating membrane permeability disregards elements such as the lipid composition, a crucial factor determining the actual flux of molecules across the lipid membrane [98]. We will describe better methods and measures to describe the permeability of membranes in Chapter 4.

In OLA, the octanol is the carrier phase for the lipid molecules and the solvent in which they are presented to the aqueous streams within the microfluidic chip. To the best of our knowledge, there is no study to date that investigates the conformation of the lipid

molecules in the octanol phase in detail. Moreover, the exact structure of the individual molecules in bulk octanol itself is topic of a debate [99, 100]. In the past, several groups have investigated the structure of alkanol molecules in the liquid phase by means of X-ray diffraction. Repeatedly, these experiments have shown a peak in diffraction stemming from the lateral separation of the fatty acid chains. This main peak corresponds to that observed for an alkane with the same chain length, indicating that the fatty acid separation of octanol is similar to that of octane [100]. However, next to the main peak, alkanols additionally express a side peak stemming from correlations between H-bonded molecules [99]. This side peak has been interpreted differently by several groups. A 1993 study came to the conclusion that the individual octanol molecules aggregate into spherical clusters resembling reverse micelles with the hydrocarbon chains pointing outward [101]. Other groups interpreted the data as octanol forming linear chains of about 10 molecules [102]. More recent studies conclude that the structure of the molecules depends on the degree of hydration of the octanol, neat octanol forming long and thin chains and hydrated octanol forming more spherical clusters, resembling inverse micelles [58, 100]. A recent publication even proposes that hydrated octanol forms nanostructures [99]. In any case, there are regions within the octanol bulk that are more polar and others that are more non-polar. Since they are amphiphilic by nature, the lipid molecules are not too different in structure from the octanol itself, having a hydrophilic head group and two fatty acid chains. One can therefore assume that the lipid molecules align with the general structure of the surrounding octanol, placing their hydrophilic head group in the more polar domains and aligning the fatty acid chains with that of the octanol in the more non-polar regions. However, this is just a theory based on the structure of the surrounding medium. It is clear that more research, specifically addressing the question of the conformation of lipid molecules in octanol needs to be performed in order to be able to give a more definite answer.

While the structure of lipids dissolved in alkanols such as octanol is not researched very well, the effect of alkanols on lipid membranes has been an intensively debated and researched topic [103, 104]. The larger interest of the scientific community in this question stems from the fact that alkanols have an anaesthetic effect on organisms [103]. We should not forget that the 2-carbon cousin of the 8-carbon octanol is simple ethanol whose anaesthetic effect has been known for millennia [105]. One of the earliest theories of general anaesthetics links the potency of an anaesthetic to its lipophilicity, a theory known as the Meyer-Overton rule [106]. Interestingly, this brings us back to the partition coefficient we discussed earlier, since the partition coefficient is a measure of lipophilicity. We will discuss the Meyer-Overton rule in more detail in Chapter 4, as it provides a helpful tool to interpret and predict the membrane permeability of drugs and other small molecules [106].

One of the most important effects that alkanols have on lipid membranes is their effect on the phase transition temperature of the lipids. The phase transition temperature determines the fluidity of a membrane thereby strongly influencing the mechanical properties of the bilayer [107] and the functionality of membrane proteins [108]. Early research on lecithin and DPPC lipids revealed that shorter chain alkanols decrease the phase transition temperature, whereas longer chain alkanols increase the phase transition temperature of lipid membranes [109–112]. However, these early studies disagreed in the chain length where the shift from increasing to decreasing starts, with values varying from 8 to 12 carbons [103, 110, 112]. Interestingly, this behaviour coincides with the so called cutoff effect, which describes the sudden decrease in anaesthetic potency of long chained alkanols, after the potency initially increased with growing chain length [103]. As before, the cutoff length seems to change from investigated system to system. For instance, experiments on Xenopus oocytes showed a cutoff as low as 4-carbon butanol [113], whereas tadpoles showed a cutoff after 12-carbon dodecanol [103].

More recent research sheds light on this phenomenon and showed that not only the chain length of the alkanol, but also of the investigated lipid influences the cutoff length [104, 114, 115]. Numerous studies suggest that the observed behaviour is rooted in a trade-off between bilayer disordering and ordering effects of the alkanols. At short chain lengths, the disordering effect dominates, as the alkanol molecules perturb the bilayer-solution interface. However, with increasing chain length of the alkanol, its fatty acids reach further into the hydrocarbon layer of the membrane where they interact with the acyl chains of the lipids thereby stabilising the membrane [103, 109]. A recent study by Ingolfsson *et al.* concluded that the cutoff effect appears when the alkanol reaches about half the chain length of the bilayer forming lipid, which is in accordance with previous works [104, 114, 115].

The effect of the phase transition temperature should always be considered, especially when studying transport processes across the membrane, as numerous studies suggest enhanced permeability of membranes to ions and small molecules close to the phase transition temperature of lipids [116]. Blicher *et al.* provide a nice example for this in their experiments with SUVs and BLMs [117]. In their work, Blicher *et al.* directly measured a change in permeability towards ions and fluorophores by shifting the phase transition temperature closer or further away from their operating temperature via the addition of octanol [117]. One has to keep this effect of octanol in mind when using OLA and depending on the desired experiment, should consider choosing lipids which are far away from the phase transition regime to avoid any undue influence of octanol on membrane transport.

2.5 Conclusion

In this chapter we briefly discussed the classification and history of liposomes. Furthermore, we looked at electroformation, perhaps the most widespread technique used to obtain GUVs, and discussed its drawbacks. We saw how microfluidic double emulsion techniques have the potential to overcome some of these drawbacks. Nonetheless, microfluidic techniques have their own downsides, namely the presence of organic solvents in the membrane, which need to be removed in extensive protocols.

We introduced Octanol-Assisted Liposome Assembly (OLA), a novel microfluidic technique that seemingly solves this problem by using the aliphatic alcohol 1-octanol as the lipid carrying organic phase, instead of alkanes. Octanol has the property of separating from the GUVs inside the microfluidic chip and does not require a separate cleaning protocol, making it ideal for lab-on-chip applications. However, the OLA technique has its own unique requirements that potentially influence membrane properties. First, although OLA GUVs do not have a visible octanol residue, it cannot be ruled out that traces of octanol are still present in the membrane. This is especially important, as our literature review revealed that octanol is known to influence the phase transition temperature of lipids. Furthermore, the technique requires the addition of glycerol and the poloxamer P-188, both of which potentially influence lipid behaviour.

In the next chapter, we will perform a biophysical characterisation of OLA vesicles and compare a selection of its membrane properties to that obtained by the established electroformation technique. We perform this to quantify whether OLA GUVs are suitable for membrane permeation studies.

Chapter 3

Biophysical Characterisation of OLA Vesicles [1]

3.1 Introduction

In Chapter 2, we looked at GUVs as model systems for membranes and introduced OLA as a novel method for GUV production. We saw that this new microfluidic method of GUV generation has many advantages associated with it, which makes it a great candidate for implementation in lab-on-chip applications. As pointed out in the outline of this thesis, our overall aim is to develop a microfluidic platform that allows us to study membrane permeation using GUVs. However, before we begin to modify and expand OLA for this purpose, we want to investigate several biophysical properties of OLA derived GUVs, to ensure they are suitable for membrane permeation studies. Since OLA was only presented in 2016, no such detailed biophysical characterisation was performed on OLA vesicles to date.

In some of the studies in the following chapter, we compare the properties of OLA derived GUVs to that of GUVs made with the established electroformation method. The reason for this lies in the fact that vesicles obtained via electroformation have been successfully used for permeability measurements, both in our group and elsewhere [37, 119]. Quantitatively similar characteristics of vesicles obtained from the two techniques thus provide a strong argument for the feasibility of OLA vesicles for this purpose.

[1] Elements of this chapter have previously been published in Schaich et al., *Mol. Pharmaceutics*, 16(6), 2494-2501, 2019 [68] and Schaich et al., *BBA-Biomembranes*, 183359, 2020 [118].

The experiments described in the following sections were predominantly performed on a confocal microscope using extracted GUVs. Before we report the outcomes of the individual experiments, we briefly describe the protocols for chip design and fabrication, as well as GUV formation and extractions, since they are similar or identical for each of the experiments. An exact list of solution composition is given in Appendix Tables A.4 and A.5.

3.1.1 Materials and Methods

Chip Design and Fabrication

The microfluidic chip design used to create the liposomes is depicted in Figure 2.4A. We modified the original design geometry published by Deshpande *et al.* [56]; we scaled up the channel dimensions by a factor of ~2. Whereas the original chip design has a junction width and a channel height of 10 µm, our design has a channel width of 20 µm and a height of approximately 16 µm. By scaling up the dimensions, we were able to obtain larger liposomes than typically possible with the originally published chip design [56]. The scaled-up channels furthermore lead to higher flow rates and higher liposome production rates than the original device [68]. However, if operated in a high flow rate regime, the vesicles often only have approximately 30-40 seconds from their production until they reach the outlet of the microfluidic chip, compared to up to several minutes in the original design. The vesicles in our chip design are therefore exposed to the shear stress from the PDMS channel wall as well as the fluid streams for a much shorter period of time. Importantly, Deshpande *et al.* found that these two effects are at least partially responsible for the separation of the octanol pocket [56]. Depending on the flow conditions, as well as the size of the octanol pocket attached to the GUV upon production, the time period that the vesicles are exposed to the shear stress does not suffice for every single vesicle to separate from its octanol pocket until it reaches the outlet. The number of resulting vesicles with octanol pocket attached can vary drastically and ranges from as little as 5% up to well over 50%, depending on the flow speed. We always attempted to obtain as little vesicles connected to their octanol pocket as possible with an estimate 85% of the vesicles being octanol free in the studies in this chapter.

The microfluidic chips were fabricated from polydimethylsiloxane (PDMS) using established photo- and soft lithography techniques as described in Section 2.4.2. A master mold with the structures of the microfluidic chip was produced by spin coating a thin layer of SU-8 2025 (MicroChem, USA) on a 4-inch silicon wafer (University Wafer, USA). The wafer was spun at 1800 rpm for 60 s with a ramp of 100 rpm/s in a spin coater (WS-650-23NPP, Laurell

Technologies, USA) to obtain features of 16 µm height. The wafer was then pre-baked on a hot plate at 65°C for 1 min and at 95°C for 6 min and placed in a table-top laser direct imaging (LDI) system (LPKF ProtoLaser LDI, Germany). The LDI system exposes the structures specified in the software directly to UV light, causing the photoresist to crosslink and solidify. Following the exposure, the wafer was post-baked for 1 min at 65°C and for 6 min at 95°C. By rinsing the wafer with propylene glycol monomethyl ether acetate (PGMEA), the unexposed photoresist was flushed away leaving the desired structures imprinted on the substrate. Finally, the wafer was hard baked for 15 min at 120°C.

The silicon wafer was then used as a mold to fabricate the microfluidic devices. A 9:1 ratio mixture of liquid elastomer (Sylgard 184, DowSil) and curing agent was desiccated to remove air bubbles and cast into the mold. After curing for 60 min at 60°C, the PDMS was removed from the mold. Biopsy punches (0.7 mm diameter, WPI, UK) were used to cut fluid access ports into the chip at the position of the inlets. Larger biopsy punches (4 mm diameter, WPI, UK) were used to cut the outlet reservoir. The PDMS chip was then plasma-bonded to PDMS-coated coverslips using a standard plasma bonding protocol (100 W, 10 s exposure, 25 sccm, plasma oven from Diener Electric, Germany).

We note that the liposome formation for the subsequent experiments were generated on microfluidic chips made from two different molds. The chip designs are depicted in Appenix Figure A.1 and Figure B.1. The latter design contains downstream features to handle the vesicles which we will discuss in the next chapter. By placing the outlet punch before the vesicles reach this part of the chip, the two chip designs are functionally identical, consisting of an OLA junction with a straight outlet channel leading the outlet reservoir.

Vesicle Formation and Extraction with OLA

The microfluidic chip was set up on a commercial epifluorescence microscope (either Nikon TE 2000U or Olympus IX 73) equipped with an EMCCD camera (Evolve 512 Delta, Photometrics). The liquid flows were controlled with a pressure-driven microfluidic pump (MFCS-EZ, Fluigent) equipped with a Fluiwell-4C reservoir kit. Polymer tubes (Micrewtube 0.5 mL, Simport) containing the OLA solutions were screwed into the Fluiwell-4C. The solutions entered the microfluidic chip via tygon tubing (microbore tubing, 0.020” x 0.060” OD, Cole Parmer). Cut dispensing tips (Gauge 23 blunt end, Intertronics) were used as metal connectors between the tubing and the chip. Liposome formation was performed by adjusting the respective fluid pressures. Typically, pressures of 40 mbar for the inner aqueous, lipid-octanol and 70 mbar for the outer aqueous phases lead to a stable production

of liposomes. However, the pressures that lead to a stable GUV production can vary from chip to chip. Either 15 µL or 20 µL of the aqueous stock were added to the outlet reservoir after the pressures were adjusted for stable vesicle formation. The larger volume in the outlet allows for the easier separation of octanol droplets and vesicles, as the droplets rise to the surface, due to their lower density of 0.827 g/l [64]. After approximately 1-3 hours of vesicle formation, the GUVs could be extracted from the outlet using a wide bore pipette tip.

Electroformation [2]

The GUVs were formed using the Vesicle Prep Pro (Nanion Technologies GmbH, Germany) using an established electroformation protocol [33]. 80 µL of a 5 mg/mL lipid suspension (containing a fraction of fluorescently labelled lipid) in chloroform was spin coated (660 rpm for 2 min) on an Indium Tin Oxide (ITO) coated glass slide (Visiontek) and desiccated for 60 min to evaporate the solvent. 600 µL of the IA solution was added and held in place by a rubber O-ring and sandwiched by another ITO slide. An A/C voltage was applied via the conducting surfaces of the ITO slides inducing swelling of the lipid film and the formation of vesicles [33]. The electroformation process was performed at 37°C and ran through the following protocol: the A/C voltage linearly increased from 0 V to 3.2 V peak-to-peak (p-p) at 10 Hz over a time period of 1 hour. Then the voltage stayed at 3.2 V p-p and 10 Hz for 50 minutes. Finally, the frequency decreased linearly to 4 Hz over a time window of 10 min and was held at 4 Hz for another 20 min. The vesicle suspension was then removed and stored in an Eppendorf tube.

The exact solutions used for GUV formation with OLA and electroformation in the experiments discussed below are summarised in Appendix Table A.4. Unless otherwise specified, the chemicals were obtained from Sigma-Aldrich.

3.2 Validation of Membrane Unilamellarity

The first properties of OLA liposomes that we want to investigate are their lamellarity and vesicularity. As discussed in Chapter 2, bulk techniques such as electroformation suffer from polydispersity and often yield liposomes that are multilamellar or multivesicular [23]. We will compare the appearance of OLA GUVs to electroformed GUVs in order to assess if they suffer from a similar spread in composition.

[2] Electroformation performed for the experiments presented in this chapter were performed by D. Sobota

By observing fluorescently labelled vesicles in a confocal microscope, we can draw conclusions on the structure of the membranes. As shown by Figure 2.1 in the previous chapter, multilamellar vesicles consist of more than a single lipid bilayer. If these are present, one therefore expects to see vesicles with highly varying fluorescence and thicker membranes within the population of GUVs. The distinguishing feature of multivesicular liposomes is that they are not isolated GUVs, but have several GUVs encapsulated within each other. Since confocal microscopy allows us to image distinct slices, we can therefore easily identify whether there are vesicles encapsulated within other vesicles.

3.2.1 Comparison of Confocal Micrographs

The IA and OA solutions for this experiment consisted of 200 mM sucrose in milli-Q water with 15% v/v glycerol. The OA phase additionally contained 50 mg/mL P-188. The LO phase consisted of 4 mg/mL 1,2-dioleoyl-sn-glycero-3-phosphocholine (DOPC) lipid with 0.5% m/m 18:1 NBD-PC in octanol. The aqueous solution used for the electroformation protocol was identical to the IA stock. Additionally, we prepared a 200 mM glucose solution in milli-Q water with 15% v/v glycerol which we used as a low-density dilution stock. After a few hours of vesicle production with OLA, we extracted 20 µL of the vesicle stock from the outlet and mixed it with 50 µL of the low-density dilution stock in a microscopy chamber (Grace Bio-Labs FlexWell™, Sigma Aldrich) and incubated for an hour. The higher density of the sucrose-containing liposomes causes them to sink to the bottom of the imaging chamber. There, the GUVs can be imaged more easily with the confocal microscope. The same procedure was performed for the electroformed vesicles. The imaging chambers were glued to either a BSA-coated or a PDMS coated cover slip, to prevent adhesion and bursting of the liposomes on the glass surface. Imaging was performed on an Olympus FluoView FV1000 Confocal Laser Scanning Microscope equipped with a 60× oil immersion objective (Olympus PlanApo, N.A. 1.4).

Representative confocal scans of GUVs created via the two techniques are shown in Figure 3.1. The GUVs formed by electroformation show a wider spread in diameter, as well as a larger variety in appearance, compared to the OLA vesicles. While the latter show a diameter range of 27-36 µm, the diameters of the electroformed GUVs range from 2-30 µm. The heterogeneity of electroformed vesicles is displayed in Figure 3.2. While a large number of unilamellar vesicles can be obtained by this technique, it also yields multilamellar and multivesicular vesicles. Examples of these are shown in Figure 3.2B and 3.2C. In contrast to

that, OLA does not show clustering of vesicles, or GUVs engulfed inside others, as can be seen in the confocal scan in Figure 3.1B[3].

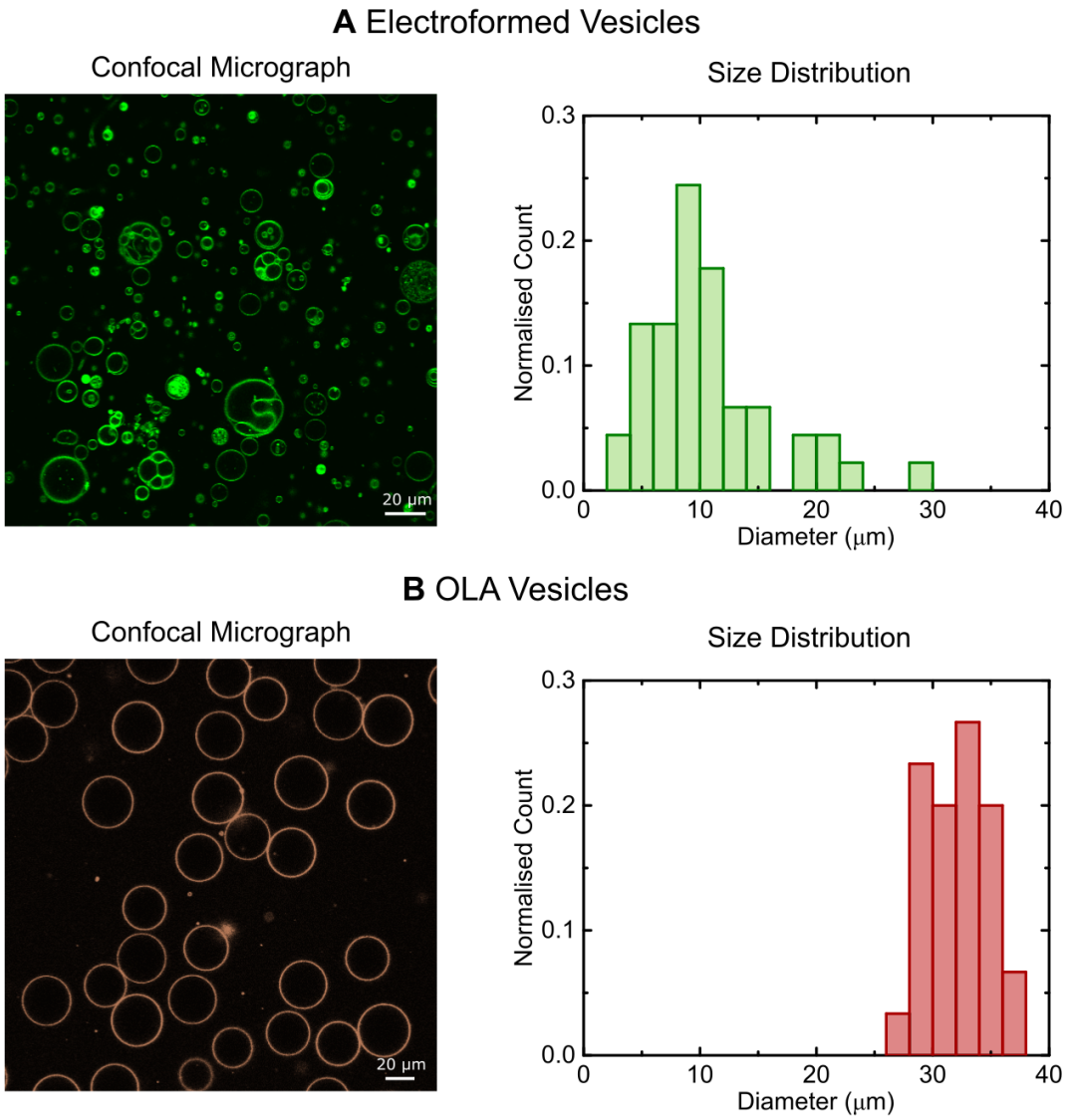

Fig. 3.1. Comparision of electroformed and OLA vesicles. (A) Electroformation results in heterogeneous vesicles and a wide range in vesicle sizes. The diameters of the electroformed vesicles range from 2 µm to 30 µm. (B) OLA results in more homogeneous vesicles with a smaller spread in liposome size. The diameters range from 27 µm to 36 µm.

[3]The confocal micrographs of electroformed and OLA-derived vesicles shown in this figure were obtained by D. Sobota and R. Tivony, respectively.

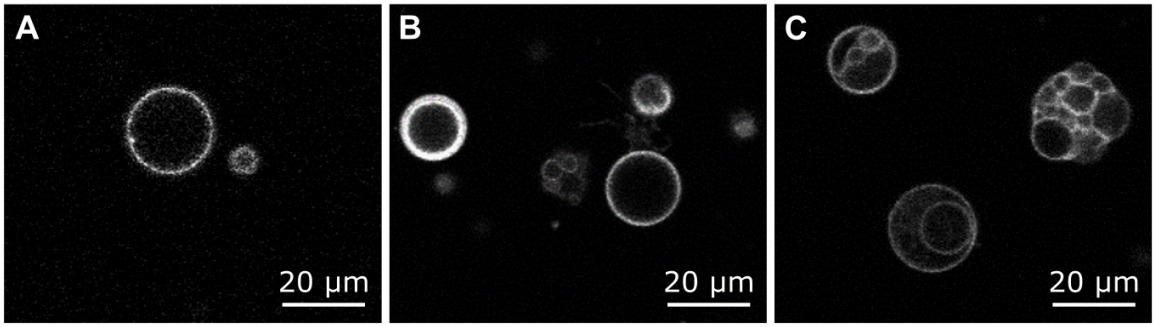

Fig. 3.2. Confocal images displaying the heterogeneity of electroformed vesicles. Image (A) shows a presumably unilamellar vesicle. The left vesicle in image (B) is clearly multilamellar, indicated by the thicker membrane and higher brightness, comapred to the other vesicles in the image. Picture (C) shows three multivesicular liposomes.

3.2.2 Dithionite Bleaching Assay

Although the images in Figure 3.1 suggest that the OLA-derived vesicles consist of a single bilayer, they do not provide quantitative evidence for the unilamellarity of these liposomes. For this reason, we subjected OLA vesicles to a dithionite bleaching assay. In this assay, the membrane impermeable anion dithionite is added to a population of vesicles which contain a fraction of nitrobenzoxadiazole (NBD) labelled lipids. It is assumed that the NBD labelled lipids are evenly distributed among the outer and inner leaflet of the bilayer. If brought in contact, the dithionite reduces and thereby irreversibly bleaches NBD. However, the dithionite cannot enter the inside of the vesicle and thereby only bleaches the outermost leaflet of the membrane. If the vesicles indeed consist of a single bilayer, the fluorescence is expected to drop to half of its original value, as the inner leaflet of the GUV remains fluorescent [120, 121]

The IA and OA for this experiment consisted of 200 mM sucrose and 15% v/v glycerol in PBS. Again, the OA contained 50 mg/mL P-188, whereas the IA had no P-188. The LO phase consisted of 2 mg/mL of a 3:1 DOPC-DOPG lipid mixture (1,2-dioleoyl-sn-glycero-3-phosphocholine and 1,2-dioleoyl-sn-glycero-3-phospho-1'-rac-glycerol) with 0.5% 16:0 NBD-PC in octanol. As before, the extracted vesicle stock was diluted with a low-density solution of 200 mM glucose with 15% v/v glycerol in PBS for imaging. We mixed 15 µL of the vesicle stock with 35 µL of the low-density dilution stock and similarly left the GUVs to settle on the surface of the imaging chamber. We prepared a dithionite stock solution of 1 M sodium dithionite in Tris pH 10 buffer. We then diluted the concentrated dithionite stock

solution further by mixing it with the glucose buffer to obtain a final dithionite concentration of 15 mM. After starting imaging, we added 30 µL of the 15 mM dithionite solution to the chamber containing the vesicles. Imaging was performed on a confocal microscope (Olympus IX83, FV10-MCPSU laser system, 20× objective UPLSAPO Olympus, 5 s frame interval). Image analysis was performed using the open source software Image J. The mean intensity of the fluorescent rings was extracted using the software's band tool, explained in more detail below.

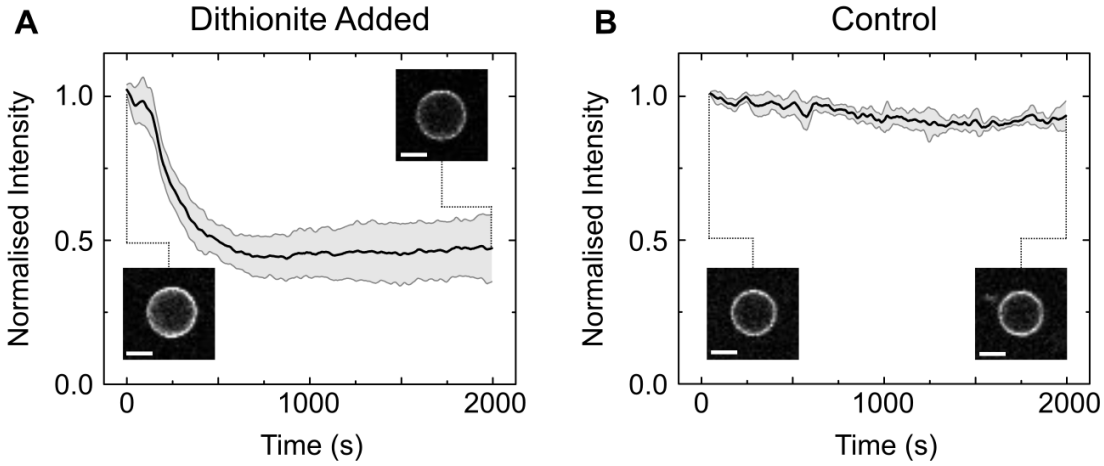

Fig. 3.3. Normalised intensity traces of the liposome membranes. (A) Intensity drop of the liposome membranes (N = 10) upon addition of dithionite. The mean intensity of the observed liposomes is shown in black with the standard deviations depicted in grey. The drop to half of the initial value is caused by the bleaching of the outer membrane leaflet by the dithionite. (B) Liposome intensity (N = 3) stays stable throughout the entire experiment upon addition of buffer without dithionite, suggesting a negligible effect of photo bleaching. The insets show a representative liposome at the beginning of the measurement and after 2000 s. Scale bars = 10 µm.

The intensity traces of the liposomes normalised to their initial intensity value are depicted in Figure 3.3. Figure 3.3A shows the intensity drop upon addition of dithionite, whereas Figure 3.3B shows the results of the bleaching control experiment upon the addition of buffer without dithionite. The mean intensity of the observed liposomes is shown as a black line with the standard deviations depicted in grey. The intensity of the liposomes subjected to dithionite (N = 10) drops to half of the initial intensity after about 500 seconds and then stays steady at that value. These results suggest that the liposomes indeed consist of a single lipid bilayer, whose outer leaflet is bleached by the dithionite [120]. Since the dithionite anion cannot penetrate the membrane, the inner leaflet of the membrane is not affected by the dithionite and remains fluorescent. The control experiment without dithionite in Figure 3.3B shows a stable intensity signal over the timespan of the entire experiment (N = 3). This

suggests that photo bleaching does not play a significant role in the observed drop in the intensity and that we are indeed observing the bleaching of the outer leaflet of a single bilayer.

Liposomes produced by OLA have previously been tested for their unilamellarity via the incorporation of the pore forming toxin α-hemolysin [56]. Additionally, the antimicrobial peptide cecropin B was found to permeabilise and lyse OLA-produced liposomes, again suggesting that the liposomes are unilamellar [69]. The dithionite assay performed by us provides an additional, quantitative proof that the liposomes formed with OLA are indeed unilamellar.

3.2.3 Conclusion on Membrane Lamellarity

To recapitulate, in this section we investigated the appearance of OLA vesicles using confocal microscopy in order to infer conclusions about their lamellarity and vesicularity. We compared the images of OLA vesicles to images of electroformed GUVs that we formed in the same solutions. While we found that both techniques yield unilamellar vesicles, electroformation also yielded multilamellar and multivesicular vesicles, whereas we did not observe these with OLA. Since the appearance alone does not suffice to safely claim the unilamellarity of the OLA GUVs, we also performed a dithionite bleaching assay on the vesicles, in order to assess the unilamellarity quantitatively. Our results support previous investigations that reported the unilamellarity of OLA liposomes [56, 69].

3.3 Investigating the Membrane Lipid Composition

In the previous section we tested OLA generated vesicles for unilamellarity and multivesicularity. In order to visualise the lipid membrane in these experiments, a fraction of the lipids we added to the LO phase was fluorescently labelled. Since we were able to observe the fluorescence in the resulting GUVs, it is clear that these fluorescently labelled lipids translate into the GUV membrane together with the unlabelled lipids. However, from the experiments above, we cannot deduce whether or not the lipid composition of the resulting GUVs actually matches the composition of the lipid mixture in the LO phase. Theoretical and experimental studies suggest different partition coefficients of octanol into bilayers of PG, PE and PC lipids, respectively [122, 123]. A lipid type with a higher affinity to octanol could therefore potentially remain in the LO phase during liposome formation. It is important to quantify that no such demixing occurs and that the membrane composition of the obtained liposome

matches the lipid mixture in the LO phase. The emergence of the field of lipidomics [124] highlights the increasing importance attributed to membrane composition. When using GUVs as a tool to study membrane transport or other membrane processes, knowledge of this property is therefore of great importance [98].

In the following section, we demonstrate comprehensively the feasibility of the OLA technique in forming GUVs of binary lipid mixtures of DOPC, DOPG and DOPE lipids in different lipid ratios. Via a mean intensity analysis performed on the OLA vesicles, we were able to assess the lipid composition of the liposomes.

3.3.1 Experimental Procedure

We tested whether or not the lipid composition of OLA liposomes matches the lipid mixture in the LO phase for three different binary lipid mixtures. This was done by doping one of the lipids of the binary lipid mixture with a fluorescent derivate and forming GUVs at different mixing ratios. By assessing the fluorescence of the resulting GUVs, we can deduce the makeup of the lipid bilayer, as we expect to observe the fluorescence of the resulting GUVs to scale according to the percentage of fluorescently tagged lipid in the mixture. Our proposed mechanism is schematically drawn in Figure 3.4.

The lipids used to form the lipid systems were 1,2-dioleoyl-sn-glycero-3-phospho-rac-(1-glycerol)sodium salt (DOPG), 1,2-dioleoyl-sn-glycero-3-phosphocholine (DOPC) and 1,2-dioleoyl-sn-glycero-3-phosphoethanolamine (DOPE). In each of the lipid systems, two of the lipids were combined in 2:2, 1:3 and 3:1 mixing ratio. One lipid contained a small proportion of a fluorescently labelled lipid (18:1-12:0 NBD PC or 16:1 Liss Rhod PE), causing the fluorescence of the GUVs to scale in a defined manner. Aliquots of the individual lipids were combined to form binary lipid systems in three different ratios. The lipids were dissolved in 1-octanol to a final concentration of 3.6 mg/mL to form the LO phase. The exact lipid mixing protocols can be found in Appendix A.3. The investigated binary lipid systems were as specified in Table 3.1.

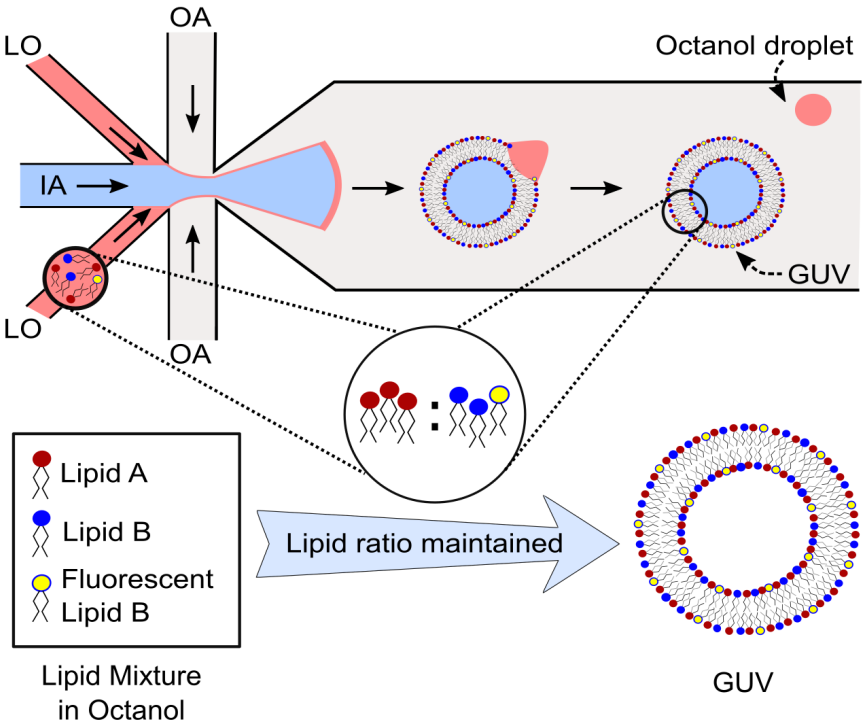

Fig. 3.4. Schematic of liposome production and proposed mechanism of lipid mixture conversion from the LO phase to the liposomes. A binary mixture of lipid A and lipid B is dissolved in the octanol phase, whereby a fixed proportion of lipid B is fluorescently labelled. The mixing ratio of lipid A to B is maintained from the LO phase to the resulting GUV. By changing the mixing ratio of lipid A to B, the fluorescence intensity of the resulting GUVs should scale proportionally to the content of lipid B in the mixture.

A mixture of 200 mM sucrose and 15% v/v glycerol in PBS buffer was used as the standard solution for the inner aqueous (IA) phase of the lipid mixture experiments. The base solution of the outer aqueous (OA) phase was identical to the IA but contained an additional 50 mg/mL poloxamer Kolliphor P-188. For all experiments containing DOPE lipid, P-188 was also added to the IA phase, as we found this increased liposome stability, confirming the membrane-stabilising properties of P-188 we discussed in Section 2.4.3. As in our previous experiments, a low-density solution with the same composition as the IA, but containing 200 mM glucose instead of sucrose was prepared. All solutions used are again summarised in Appendix Table A.4.

Table 3.1. Lipid stocks forming the binary lipid systems used to create GUVs with the OLA technique. Lipid A and Lipid B were combined in 1:3, 2:2, and 3:1 volume ratios each. Lipid B contains a small fraction of fluorescently labelled lipids. The membrane composition was evaluated by observing if the fluorescence intensity of the liposomes scales as expected from the lipid mixture.

Binary Lipid System	**Lipid A**	**Lipid B**
PGPC DOPG - DOPC	90 mg/mL DOPG	90 mg/mL DOPC with 0.1% m/m NBD-PC
PCPE DOPC - DOPE	90 mg/mL DOPC	90 mg/mL DOPE with 0.05% m/m Liss Rhod PE
PGPE DOPG - DOPE	90 mg/mL DOPG	90 mg/mL DOPE with 0.05% m/m Liss Rhod PE

We formed the GUVs as described in the sections above. However, the GUVs were not transferred into an imaging chamber. Instead, the outlet reservoir was used to both collect and image the created vesicles directly. After adjusting the pressure such that a stable vesicle formation was established, 15 µL of the low-density dilution stock was pipetted into the outlet. After 1-3 hours of vesicle formation, the microfluidic chip was disconnected from the microfluidic pump and the vesicles imaged on a confocal microscope.

3.3.2 Microscopy Parameters and Image Processing [4]

Standard epifluorescence microscopes (Nikon TE 2000U or Olympus IX 73) were used for imaging the microfluidic devices during vesicle production and the PVA treatment of the microfluidic chips [68]. The recording of the fluorescence data of the lipid mixtures was performed on commercial inverted confocal microscopes. Images were obtained with the focal plane of the microscope set to the centre of the vesicles in order to capture the fluorescence at the equator of the vesicles. A Leica TCS SP5 Confocal was used to image PGPC liposomes fluorescently labelled with nitrobenzoxadiazole (NBD), excited by a 488 nm laser. An Olympus FluoView FV1000 Confocal Laser Scanning Microscope was used to image PGPE and PCPE liposomes fluorescently labelled with Liss Rhod PE, which were excited by a 559 nm laser. Importantly, all optical parameters were kept the same for the measurement of each lipid system. The detailed imaging parameters can be found in Appendix A.3.

[4] The measurement of the PGPC lipid mixture, as well as the image analysis was performed by H. Sleath, as part of her Part III project supervised and instructed by M. Schaich.

The mean intensity values of the fluorescent ring of a vesicle were extracted using the open source software ImageJ as depicted in Figure 3.5. Using the software's band tool, the intensity of the fluorescent ring was extracted. The band width was 2 µm. Overlaps with other vesicles, or bright fluorescent spots stemming from residual octanol in the membrane, were excluded from the analysis using the software's brush tool.

We performed a linear regression for each lipid system (PGPC, PCPE and PGPE) with the fluorescence intensities of the liposomes on the y-axis and relative concentrations of the fluorescently tagged lipid in the LO phase on the x-axis. The y-intercept for the regression was fixed at zero. We then normalised the fluorescence intensities of each lipid system with the slope of the linear function we obtained from the regression. By normalising to the slope of the regression, the new values scale directly with the relative concentrations of the fluorescently doped lipid in the mixture. This results in expected values of 1, 2 and 3 for the 3:1, 2:2 and 1:3 (non-fluorescent: fluorescent lipid ratio) systems, which facilitates comparison of the fluorescence intensity ratios.

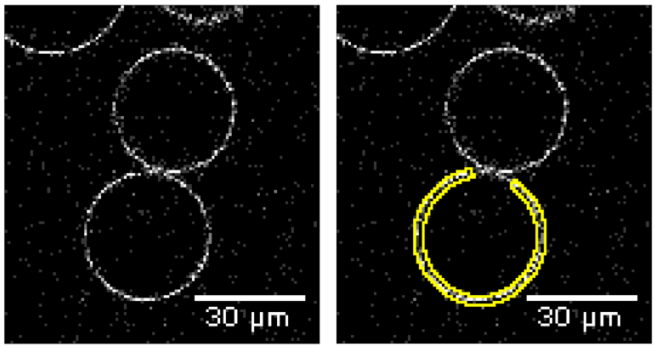

Fig. 3.5. Extraction of the mean average fluorescence of GUVs. A 2 µm thick band (shown in yellow) engulfing the fluorescent ring of the liposome was used as the region of interest. Areas of overlapping liposomes, or bright fluorescent spots stemming from residual octanol or lipid aggregates in the membrane were excluded.

Importantly, the images were acquired with identical optical parameters for all three volume ratios of the binary lipid systems. The difference in fluorescence is therefore not the result of a difference in excitation power or camera sensitivity, but of a higher number of the fluorescently labelled lipids in the GUV membranes. When choosing the microscope parameters, we were careful to eliminate the possibility of PMT saturation, which would have skewed our measurements. We always performed the measurement with the liposomes containing the largest amount of fluorescently labelled lipids first, which was expected to have the highest fluorescence intensity. After calibrating the microscope properties with this set and making sure no PMT saturation occurred, the GUVs with lower expected intensities were imaged.

3.3.3 Results of the Mean Intensity Analysis

Figure 3.6 shows representative images obtained for the lipid mixtures PCPE (DOPC – DOPE) in three different volume ratios. In this case, the DOPE stock contained 0.05% Liss Rhod PE lipids. As can be seen in the images, the fluorescence intensity of the liposomes increases with larger DOPE content in the LO phase, as expected. We also observed this behaviour for the other two lipid systems PGPE (DOPG – DOPE) and PGPC (DOPG – DOPC), where the DOPC phase was doped with 0.1% of the fluorescent NBD-PC. Representative images of all three binary lipid systems are shown in the Appendix Figures A.2, A.3 and A.4.

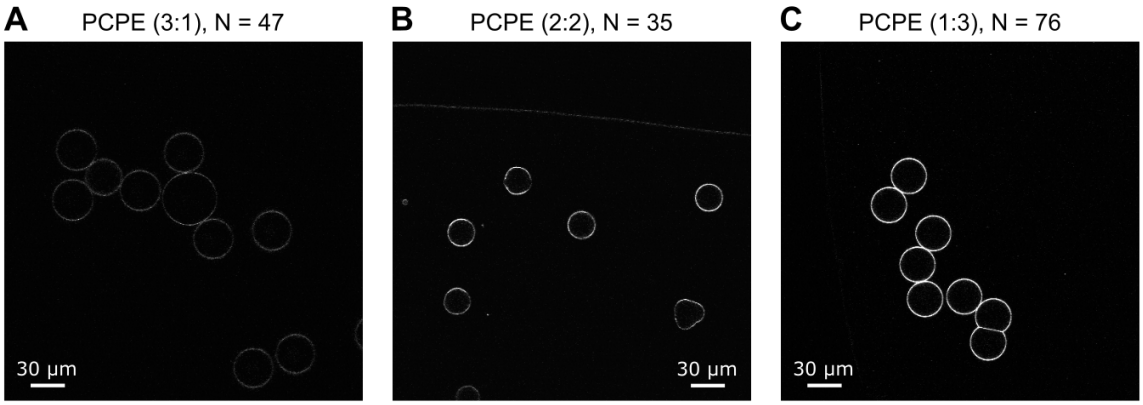

Fig. 3.6. Confocal images of the PCPE (DOPC-DOPE) lipid system in different volume ratios. The fluorescence intensity of the liposomes scales according to the content of fluorescently labelled DOPE in the lipid-octanol phase. PCPE 3:1 (A) vesicles with the least amount of DOPE show the lowest fluorescence intensities, whereas PCPE 1:3 (C) vesicles with the highest content of DOPE in the octanol expresses the strongest fluorescence. PCPE 2:2 (B) with equal amounts of DOPC and DOPE lies in between the two.

We performed a mean fluorescence intensity analysis on each of the binary lipid systems under investigation in order to quantify the shift in fluorescence between the different lipid mixing ratios. The results are depicted in Figure 3.7. We performed a linear regression on the fluorescence intensities of each lipid system and then normalised the fluorescence values to the slope of the linear function we obtained. This results in a gradient of +1 for the normalised intensity values with increasing relative concentrations of fluorescently doped lipid. For the 3:1, 2:2 and 1:3 lipid mixtures this translates into values of 1, 2 and 3, respectively, if the lipid composition of the LO phase is maintained in the vesicles produced. We observe the expected linear scaling in our experiments. The PCPE vesicles showed values (mean ± std. dev.) of 1.01 ± 0.1, 2.01 ± 0.68 and 2.98 ± 0.62 for the mixing ratios 3:1, 2:2 and 1:3, respectively. The PGPC vesicles yielded mean normalised intensities of 0.81 ± 0.13,

2.06 ± 0.25 and 3.02 ± 0.32 for the mixing ratios 3:1, 2:2 and 1:3, respectively. Note that we were not able to form stable PGPE liposomes in the 3:1 lipid ratio. However, we were able to form PGPE vesicles in the ratios 2:2 and 1:3, which followed the expected scaling with values of 1.99 ± 0.29 and 3.00 ± 0.33.

We attribute the small deviations we observed from a linear increase to pipetting error, photo bleaching as well as low signal-to-noise ratio. The latter affects primarily the vesicles with low amounts of fluorescent lipid, as we imaged all lipid systems with constant optical parameters and did not change the signal-to-noise ratio by adjusting the gain setting of the microscope.

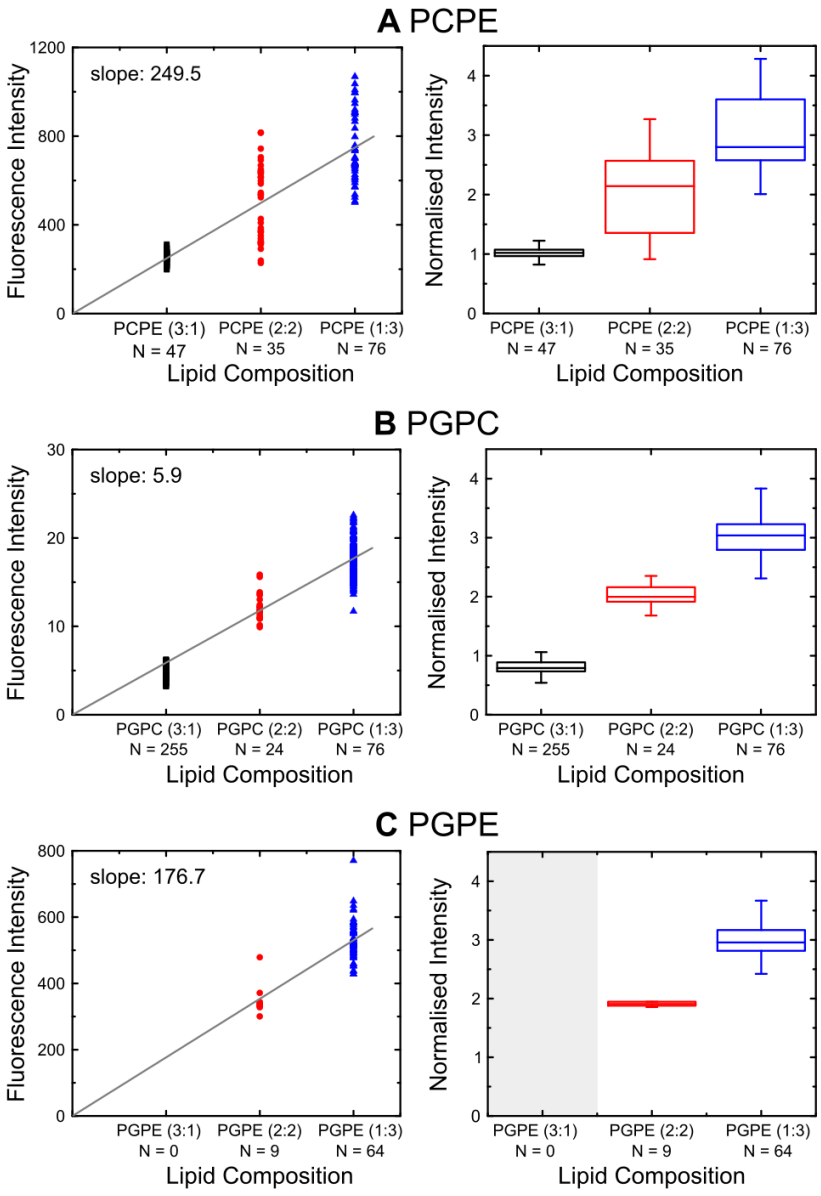

Fig. 3.7. Results of the mean fluorescence intensity analysis for the binary lipid mixtures studied. The scatter plots on the left show the raw intensities of the individual vesicles. In these graphs, the y-axis shows the average fluorescence intensity and the x-axis the relative amount of fluorescently doped lipid in the LO phase. The respective linear regression line for every lipid system is shown in grey with the gradient given inset. Boxplots of the mean normalised intensity for every lipid mixture are shown in the graphs on the right. For the boxplots, we normalised the fluorescence intensities of the individual vesicles to the slope of a the linear fit line. The normalised intensities of the lipid systems increase in accordance with their larger fraction of the fluorescently doped lipid. The increase in fluorescence for PCPE (A), PGPC (B) and PGPE (C) scales in a linear manner, as expected from the relative concentration of the fluorescently doped lipid in the LO phase. It was not possible to form PGPE lipid vesicles in a 3:1 mixing ratio. The upper and bottom ends of the box indicate the top and bottom quartile, whereas the upper and lower whiskers indicate the smallest and largest value of the set. Outliers ± 3/2 of the upper and lower quartiles are not shown in the plot but are included in the analysis. The line in the middle of the box indicates the median value.

3.3.4 Discussion

The electroformation technique is a widely used method in the biophysics community [125]. It has also been used for the creation of liposomes with complex binary and ternary lipid mixtures [35, 38]. Our experiments show that OLA is likewise able to form GUVs of different binary lipid mixtures. However, our experiments revealed that it is not possible to form PGPE vesicles of 3:1 lipid ratio with OLA. The issue impeding our measurements of these vesicles was their low stability. Although it was initially possible for us to form these vesicles at the OLA junction, they appeared to be less resistant to mechanical stress compared to the PCPE and PGPC vesicles. The vast majority of PGPE (3:1) vesicles that were created at the OLA junction burst as they flowed through the microfluidic chip towards the outlet reservoir. The likely reason is that these vesicles burst when subjected to shear stress from the PDMS channel walls [68]. Although occasionally individual vesicles survived to the end of the outlet channel in the reservoir, we noticed bursting events for these vesicles after several minutes as well.

We partially attribute this behavior to the lipid polymorphism of PGPE (3:1) vesicles. PE lipids are known to have a cone like shape which makes it energetically unfavourable for them to form lamellar structures [126]. If forced into a GUV forming bilayer, the acyl chains are pressed together, increasing the lateral pressure at the centre of the membrane, a state coined the ‘frustrated bilayer’ [127, 128]. In nature, this pressure can be balanced by the enrichment of the PE lipid in the inner leaflet of the membranes of cells [127, 129]. The fact that we

could produce PCPE liposomes in all three lipid ratios suggests that other effects in addition to the lipid shape are responsible for the low stability of PGPE (3:1) vesicles. Additionally, there are reports that PG stabilises PE membranes, which seemingly contradicts our findings [130]. However, these studies only looked at PG fractions of up to 30 mol% , whereas the PGPE (3:1) GUVs in our experiments predominantly consist of PG. MD simulations by Murzyn *et al.* on POPG-POPE (1:3) bilayers revealed that the prevailing interactions between lipid molecules are water bridges and H-bonds [131]. While PE predominantly forms all these bonds with PG lipids, PE also bonds to other PE molecules. PG on the other hand barely bonds with other PG molecules [131]. The low H-bonding capacity of PG lipids has also been observed in MD simulations on pure PG bilayers by Zhao *et al.*, who attribute this to the net negative charge and electrostatic repulsion of the individual molecules [132]. However, the two simulations diverge on the role of ion bridges between lipids. Whereas Murzyn *et al.* found that Na^+ ion bridges are only a minor contributor to membrane stability, Zhao *et al.* found strong ion-mediated interactions between the lipid molecules causing attractive forces that overcome the electrostatic repulsion between the negatively charged PG headgroups [132]. Our findings suggest that in addition to the effect of PE, the high content of charged PG in the PGPE (3:1) GUVs further destabilises the membrane. However, more research is needed to explain the low stability behaviour of the PGPE (3:1) vesicles that we observed.

3.3.5 Conclusion on Lipid Mixtures

Future experiments involving the use of lysolipids could provide further evidence to indicate whether the cone shape of PE lipids and the charge density of PG are responsible for the low stability of the PGPE (3:1) vesicles we observed. Lysolipids, such as LPC, only have one acyl chain and add a high positive curvature to the membrane. As such, they can counterbalance the negative curvature induced by the PE lipids (18, 19). A tertiary lipid mixture of LPC, DOPG and DOPE should therefore have a higher stability than binary PGPE mixtures. Other potential methods to yield GUVs of arbitrary compositions involve stabilising the membrane mechanically using nanostructures. Since OLA allows for the efficient encapsulation of substances in the interior of the vesicles, as well as coating from the exterior in well-defined conditions [69], an artificial cytoskeleton, for instance made of DNA [133], could be applied to the membrane.

3.4 Lateral Diffusion Coefficient

In the previous two sections, we validated the unilamellarity of OLA derived liposomes and furthermore tested OLA for its capability in forming GUVs of defined lipid mixtures. In the following section, we want to investigate the dynamics of the lipid molecules in the membrane itself. For this, we performed fluorescence recovery after photobleaching (FRAP) measurements on fluorescently labelled OLA and electroformed GUVs.

In the FRAP technique, depicted in Figure 3.8A, a small region of the GUV membrane, doped with fluorescent lipids, is irreversibly bleached using a confocal microscope. As the surrounding non-bleached lipid molecules diffuse into the area, the fluorescence of the previously bleached region of interest recovers. From the recording and analysis of this recovery, it is possible to calculate the lipid lateral diffusion coefficient of the lipids [134]. FRAP is a powerful biophysical technique and has been used on cells and GUVs in the past, for instance to investigate protein diffusion on cellular surfaces [135] or lipid rafts [136]. Using FRAP, we will directly compare the lipid lateral diffusion coefficients of OLA-derived GUVs to those obtained from vesicles generated by the established electroformation technique. By comparing the lateral diffusion coefficients in different chemical environments, we will assess whether or not the presence of the poloxamer P-188 or residual octanol affects lipid lateral diffusion. We thus provide an important biophysical characterisation of liposomes produced using microfluidics. Quantitative similarity of OLA derived GUVs and electroformed GUVs will encourage the wider uptake of this novel liposome production method in the field. Furthermore, quantitative similarity provides a strong argument for the use of microfluidic GUVs for the study of membrane properties such as permeability.

3.4.1 Experimental Procedure

We formed GUVs of two different PC lipid types by both electroformation and OLA to obtain and compare their lateral lipid diffusion coefficients. The tested lipids were 1,2-dioleoyl-sn-glycero-3-phosphocholine (DOPC) and 1-palmitoyl-2-oleoyl-glycero-3-phosphocholine (POPC). The LO phase consisted of 4 mg/mL PC lipid with 0.5% m/m NBD-PC in octanol. The aqueous solutions (200 mM sucrose, 15% glycerol) were prepared in milli-Q water, as the formation of GUVs using electroformation fails at high salt concentrations [23, 39]. We extracted the GUVs as described in Section 3.1.1 and imaged them on confocal imaging chambers, after mixing them with a low-density glucose stock.

Table 3.2. P-188 concentrations in the respective environments that the FRAP measurements were performed in. Vesicles of the high P-188 environment were formed in 50 mg/mL. For imaging, they were diluted in the low density stock devoid of P-188 lowering the outside concentration to 14 mg/mL. OLA vesicles could not be formed in a solutions completely devoid of P-188.

	Encapsulated P-188 concentration	**Outside P-188 Concentration**
Electroformation no P-188 environment	0 mg/mL	0 mg/mL
Electroformation high P-188 environment	50 mg/mL	14 mg/mL
OLA low P-188 environment	0 mg/mL	14 mg/mL
OLA high P-188 environment	50 mg/mL	14 mg/mL

Two sets of vesicles for each technique were investigated. The lateral diffusion coefficient of one set was measured in a high P-188 environment, the other set was measured in a low P-188 environment. The P-188 concentrations in the respective environments are given in Table 3.2. The solutions furthermore contained glycerol, sucrose and glucose; these were left out in Table 3.2 for the sake of clarity. The full solution compositions used for liposome formation and FRAP measurements are listed in Appendix Tables A.4 and A.5. Note that since OLA requires the addition of P-188 at least in the OA phase to form vesicles, we were not able to create an environment for OLA vesicles that was completely devoid of the poloxamer.

In a second series of experiments, we performed FRAP measurements on electroformed DOPC vesicles at varying levels of glycerol (0% vs 15% glycerol, each in the IA and OA) and different temperatures (approximately 20°C vs. 37°C). For these experiments, we used similar sucrose solutions, devoid of ions and P-188 as laid out in Appendix A.4 but with varying glycerol content.

3.4.2 Microscopy Parameters and Image Analysis

The FRAP measurements were performed on an Olympus FluoView FV1000 Confocal Laser Scanning Microscope equipped with a cellVivo Incubation System. The field of view was focused on the bottom of a GUV. By adjusting the pinhole diameter, the slice thickness was increased such that the lower part of a GUV was observed as a fluorescent disc. Using

the FRAP function of the microscope's software, a spot of Ø 4 µm was bleached and the fluorescence recovery observed. 8 images were collected pre-bleaching. Bleaching was performed over 0.1 s with 98% laser power and the fluorescence recovery was recorded for 100 frames (2 µs/pixel exposure).

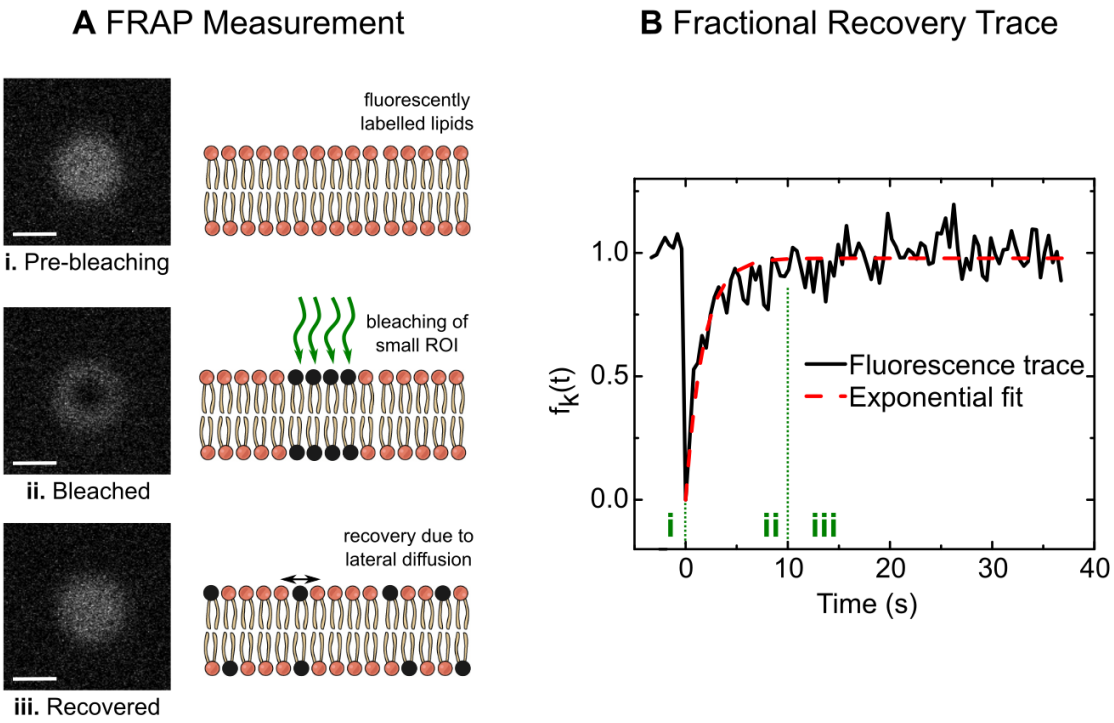

Fig. 3.8. (A) Example of a vesicle in the different stages of a FRAP measurement. The fluorescence intensity of a circular disk is recorded pre-bleaching (i), bleached (ii) and recovered (iii). The bleached region manifests itself as a dark circle on the vesicle membrane. (B) Fractional recovery trace of a vesicle. An exponential curve is fit to the trace from which the half-life recovery time $t_{1/2}$ is extracted. The lateral diffusion coefficient of the lipids is calculated using the extracted half-life time and the area of the bleaching spot. Scale bar 10 µm.

We calculated the fractional fluorescence recovery trace $f_K(t)$ for each vesicle, according to the formula below (30, 31):

$$f_K(t) = \frac{F_K(t) - F_K(0)}{F_K(\infty) - F_K(0)} \tag{3.1}$$

where $F_K(t)$ is the measured fluorescence intensity, $F_K(0)$ is the intensity just after bleaching and $F_K(\infty)$ is the recovered intensity. The recovered intensity was defined as the average of the last 8 frames of the fluorescence trace. Furthermore, the mobile fraction M of each vesicle was calculated:

$$M = \frac{F_K(\infty) - F_K(0)}{F_K(t<0) - F_K(0)} \tag{3.2}$$

The fluorescence intensity before bleaching $F_K(t < 0)$ is defined as the average of the 8 frames recorded pre-bleaching. An exponential function of the form $y = y_0 \times (1 - \exp(-at))$ was fit to the fractional recovery curve of each vesicle and the half-life recovery time $t_{1/2}$ was extracted, as shown in Figure 3.8. We calculated the lipid lateral diffusion coefficient of each vesicle, following the approach of Axelrod *et al.*[137] and Soumpasis [138]:

$$D = 0.224 \times \frac{w^2}{t_{1/2}} \tag{3.3}$$

where w is the radius of the bleaching spot.

3.4.3 Results of the FRAP Measurements

We followed the guidelines for FRAP analysis recommended by Chen *et al.* [139] and Tocanne *et al.* [140], only including diffusion measurements performed on vesicles where the radius of the bleached spot w was small compared to the diffusion area A ($\frac{A}{w} > 5$). Furthermore, we kept the bleaching pulse t_B short compared to half-life recovery time $t_{1/2}$ ($t_B < \frac{1}{10} t_{1/2}$) and used $t_B = 0.1s$, as recommended by Guo *et al.* [141]. Additionally, we excluded vesicles that moved during the FRAP measurement, as well as vesicles whose fluorescence did not recover to at least 75% of the pre-bleaching intensity (exclude mobile fraction of $M < 0.75$). For the latter, the assumption of an infinite lipid reservoir is not met, and the diffusion coefficient can be underestimated due to the bleaching of substantial parts of the membrane. The vesicles we excluded due to a mobile fraction $M < 0.75$ typically also did not meet the criterion of a small bleaching spot w compared to the diffusion area ($\frac{A}{w} > 5$).

The lateral lipid diffusion coefficients of DOPC vesicles obtained with the different formation techniques are compared in Figure 3.9A. Without the presence of P-188 in the IA, the FRAP experiments revealed values (mean ± std. dev.) of 1.0 ± 0.2 μm^2/s (N = 17) and 1.1 ± 0.2 μm^2/s (N = 34) for electroformed and OLA vesicles, respectively. Note that in the above case, the outside solution of the OLA vesicles contained 14 mg/mL P-188, whereas the outside solution of the electroformed vesicles was devoid of P-188. As pointed out above, the reason for this lies in the fact that GUV formation with OLA is not possible without the presence of P-188 in the OA phase. GUVs formed with 50 mg/mL P-188 encapsulated within the vesicle showed values of 1.2 ± 0.4 μm^2/s (N = 14) for electroformation and 1.0 ± 0.3 μm^2/s (N = 30) for OLA. The measurements on POPC vesicles yielded similar results as the DOPC measurements in the range of 1 μm^2/s. Electroformed and OLA vesicles without the presence of P-188 had lateral diffusion coefficients of 0.8 ± 0.2 μm^2/s (N = 28)

and 1.0 ± 0.3 μm^2/s (N = 49), respectively. With 50 mg/mL P-188 encapsulated in them, the GUVs yielded diffusion values of 1.3 ± 0.4 μm^2/s (N = 20) and 0.9 ± 0.3 μm^2/s (N = 27) for electroformation and OLA, respectively.

We furthermore conducted FRAP measurements on electroformed DOPC vesicles with varying glycerol content (0% vs. 15%) and temperatures (20°C vs. 37°C), shown in Figure 3.9B. We found a stronger difference between the lateral diffusion coefficients with varying glycerol and temperatures than between the different formation techniques or varying P-188 concentrations. The diffusion coefficient (mean ± std. dev) increases from 1.0 ± 0.2 μm^2/s (N = 17) at 20°C and 15% glycerol to 1.6 ± 0.2 μm^2/s (N = 12) without the presence of glycerol. At 37°C, the coefficients rise to 1.9 ± 0.6 μm^2/s (N = 19) with 15% glycerol and 2.2 ± 0.5 μm^2/s (N = 7) without glycerol.

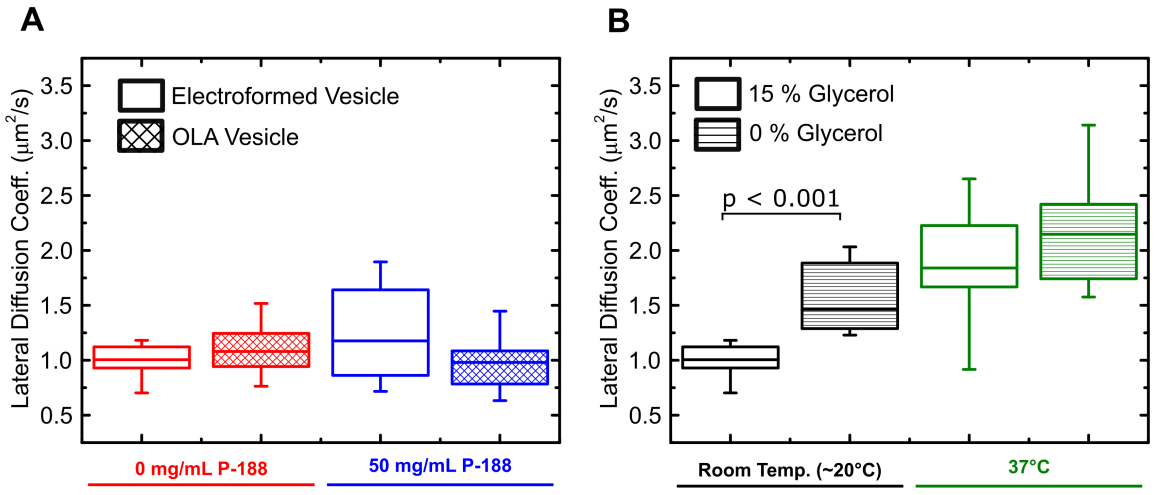

Fig. 3.9. Boxplots of the lipid lateral diffusion coefficients obtained via FRAP. (A) Comparison of DOPC vesicles produced by OLA and electroformation with varying concentrations of encapsulated P-188. The lateral diffusion coefficients are on the order of 1 μm^2/s for all investigated systems, irrespective of the production method or the presence of P-188. (B) Lipid lateral diffusion coefficients of electroformed DOPC vesicles at varying temperatures and glycerol concentrations. We found a significant ($p < 0.001$) increase in lateral diffusion with rising temperature and decreasing glycerol concentration, compared to the base line at room temperature (approximately 20°C) and 15% glycerol.

3.4.4 Discussion of the Results

Lateral lipid diffusion values reported in the literature vary greatly, as these are strongly affected not only by the chemical and physical environment [133], but also by the choice of measurement technique. Different techniques like Fluorescence Correlation Spectroscopy (FCS), FRAP and NMR have yielded different lateral diffusion coefficients [142]. For instance, Filippov *et al.* obtained values of 9.32 $\mu m^2/s$ for DOPC and 8.87 $\mu m^2/s$ for POPC with NMR [143], both higher than the values obtained by us. Furthermore, the choice of membrane platform, e.g. supported lipid bilayer (SLB) vs. GUV [144] can influence the measurement. Guo *et al.* report POPC lateral diffusion coefficients of 1.8 ± 0.2 $\mu m^2/s$ on supported lipid bilayers and 3.3 ± 0.2 $\mu m^2/s$ on GUVs [141] while Pincet *et al.* measured DOPC lateral diffusion coefficients of 1.9 ± 0.4 $\mu m^2/s$ on supported lipid bilayers and 3.4 ± 0.7 $\mu m^2/s$ on GUVs [144]. All values are again summarised in Table 3.3. The values above are in good agreement with the values we obtained for OLA vesicles, albeit still significantly elevated. We explain this by the presence of 15% v/v glycerol in the OLA solution, as both previous research and our control experiments reveal that glycerol lowers the lateral diffusion coefficient [145]. Our FRAP measurements at elevated temperatures and without the presence of glycerol match the above-mentioned values more closely. Furthermore, differences in the exact shape of the bleaching profiles, the imaging parameters and data analysis can skew the obtained diffusion values [146]. Interestingly, our control experiments also reveal that varying the glycerol concentration and temperature both have a stronger effect on the lateral diffusion coefficient of lipids in electroformed DOPC vesicles than variations in the P-188 concentration or the formation technique.

Table 3.3. Lateral diffusion coefficients measured with different techniques and lipid systems. NMR measurements were performed on multivesicular vesicles. The GUV and supported lipid bilayer (SLB) values were obtained via FRAP.

	NMR	**GUV**	**SLB**
DOPC	9.32 $\mu m^2/s$ [143]	3.4 ± 0.7 $\mu m^2/s$ [144]	1.9 ± 0.4 $\mu m^2/s$ [144]
POPC	8.87 $\mu m^2/s$ [143]	3.3 ± 0.2 $\mu m^2/s$ [141]	1.8 ± 0.2 $\mu m^2/s$ [141]

3.4.5 Confocal Imaging of Octanol Pocket

Interestingly, we were able to find vesicles with and without an attached octanol pocket amongst the population of extracted OLA vesicles for both DOPC and POPC. Figure 3.10 shows isometric and confocal sliced views of GUVs with and without the octanol attached.

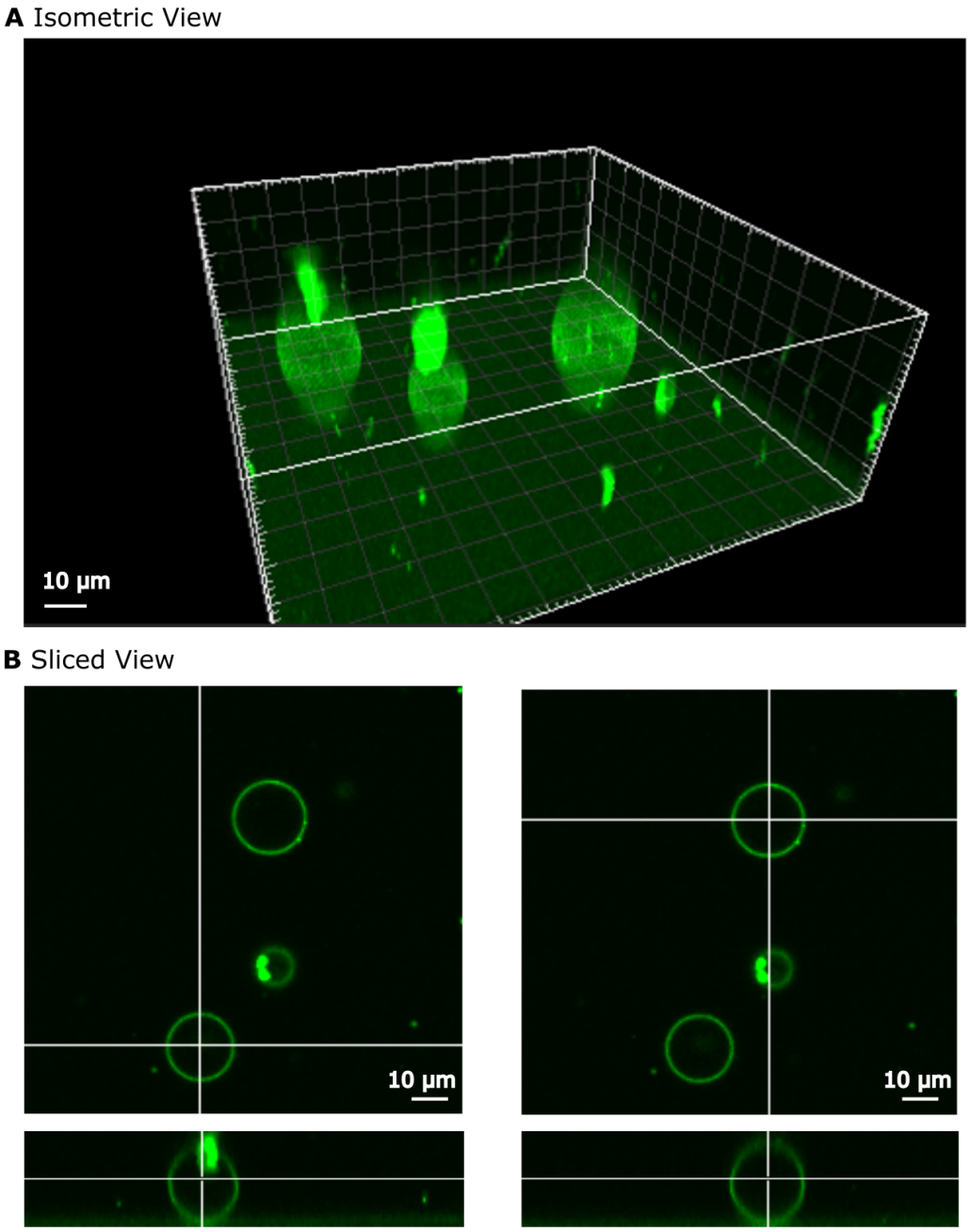

Fig. 3.10. (A) Isometric view of three GUVs produced with OLA. Two vesicles have a bright octanol pocket attached to their surface. (B) Sliced view of two of the vesicles. The white lines indicate the slice planes. The upper image shows the top view, whereas the bottom image shows the vesicle from the side. A bright octanol pocket can be seen on the side view of the left vesicle. It is not visible in the top view, as it is not within the slice plane. The view on the right shows a vesicle without a visible bright octanol pocket attached to it.

The octanol typically manifests itself as a bright spot on the top side of the vesicle. We did not observe a significant ($p < 0.01$) difference between the lateral diffusion coefficients of vesicles with and without octanol pockets attached. The FRAP measurements of both DOPC and POPC, as well as the measurements with varying temperature and glycerol content are summarised again in Appendix Tables A.6 and A.7. Statistical analyses for the FRAP measurements are reported in Appendix Tables A.8-A.17.

In the confocal scan of a vesicle, the octanol pocket manifests itself as a bright spot at the top side of a GUV. This location is plausible, due to the lower density of octanol compared to the surrounding aqueous solution. The higher brightness can be explained by the large number of lipid molecules in the bulk of the octanol droplet, compared to the single bilayer of the vesicle membrane. 3D reconstructions of confocal scans of both types of vesicles are depicted in Figure 3.10. Remarkably, we found no significant differences ($p < 0.01$) in lateral lipid diffusion coefficients between vesicles with or without an octanol pocket. This is an interesting parallel to research by Karamdad *et al.* who compared the bending rigidity of vesicles obtained with a microfluidic technique (using squalene oil) to electroformed vesicles. They also found that the presence of residual oil in the membrane did not alter the biophysical properties of the membrane [52].

While most studies report octanol having a lowering effect on the phase transition temperature of lipids [104, 117, 147], conflicting reports exist on its effect on lateral lipid diffusion coefficients. Molecular Dynamics simulations by Griepernau *et al.* on DMPC membranes showed a decrease in lateral diffusion of the lipids in presence of 1-octanol [104], whereas NMR experiments by Rifici *et al.* on the same lipid revealed an increase in lateral diffusion [147]. They furthermore reported sudden changes in lateral diffusion near the phase transition temperature T_m [147]. A possible explanation for why we did not observe a strong shift in lateral diffusion coefficients between OLA vesicles containing octanol vs. electroformed vesicles without octanol might lie in the phase transition temperature of the lipids used in our experiment. According to the manufacturer, DMPC lipids investigated by the previously mentioned groups have a melting temperature of 24°C, whereas the DOPC and POPC lipids we investigated have melting temperatures of -17°C and -2°C, respectively. Since we performed our experiments at room temperature (approximately 20°C), the lipids are well in the fluid phase and the effect of altered phase transition temperature due to the octanol might have diminished. Furthermore, it is possible that the diffusion lowering effect of the glycerol dominates our system. In addition, the cutoff effect of anesthetics, described in Section 2.4.3, could play a role in modulating membrane properties. The cutoff effect describes the phenomenon of the increasing anesthetic potency of alcohols with increasing chain length, which

suddenly levels off and even reverses for much longer chain lengths [104, 115, 147]. Since the investigated DOPC and POPC lipids have 18:1c9 and 16:0-18:1 acyl chains, respectively, octanol with a chain length of 8 might reach into the domain where membrane modulation changes from a destabilising to a stabilising effect. However, in this case, the effect should have also been observed in the 14:0 DMPC system.

3.4.6 Conclusion on Lateral Diffusion

Overall, our experiments suggest that neither the formation technique, nor the presence of P-188 changes the lateral diffusion coefficients in a substantial manner (see Appendix Table A.6). However, we did find a significant effect of glycerol and temperature on the lipid lateral diffusion. Future experiments to characterise OLA produced vesicles could involve the quantification of the actual content of octanol left in the membrane (if any) after the budding off process, for instance by mass or Raman spectroscopy. A follow up investigation would involve OLA vesicles of different lipid types with higher chain melting temperatures, as they are likely to show more pronounced changes in membrane properties due to the presence of any residual octanol.

3.5 Conclusion

In this chapter, we conducted a biophysical analysis of lipid vesicles generated by the novel Octanol-Assisted Liposome Assembly (OLA) technique. The comparison of confocal images showed the homogeneity of the GUVs obtained with this technique. In comparison to other techniques, OLA yields a narrower size distribution and does not produce multivesicular or multilamellar GUVs. We furthermore showed the unilamellarity of the OLA GUVs by conducting a dithionite bleaching assay.

Using the fluorescence recovery after photobleaching (FRAP) technique, as well as a mean fluorescence analysis, we investigated the membrane composition and the lateral diffusion of lipid molecules of GUVs generated by OLA. In recent years, we have gained a better understanding of the importance of both parameters on cellular processes. For instance, simulations by Duncan *et al.* show that clustering of certain channel proteins is modulated by the compositional complexity as well as the lateral diffusion coefficient of the lipids in the membrane [148]. Other studies have revealed that lateral lipid diffusion is rate limiting for many cellular processes [149]. The proposition of different modes of lateral mobility [150],

as well as the emergence of the field of lipidomics [124], furthermore highlight the increasing importance attributed to membrane composition and the lateral mobility of lipids in the membrane. When using GUVs as a tool to study proteins, precise knowledge and control of these two parameters is therefore of great importance.

Our fluorescence analysis revealed that the lipid composition of OLA-generated vesicles matches the composition of the lipids in the LO phase. We did not observe any demixing effects, or cases with one element preferentially remaining in the octanol phase upon liposome production, showing that the technique reliably produces vesicles of desired lipid compositions. In addition, our lipid composition experiments revealed the stable vesicle production of binary lipid mixtures of DOPG-DOPC as well was DOPC-DOPE in 1:3, 2:2 and 3:1 ratios. However, DOPG-DOPE lipid mixtures could only be formed in 2:2 and 3:1 ratios. We hypothesise that the low stability of PGPE vesicles with high (>50%) PG content is due to the polymorphism and charge density of the PE and PG lipids, respectively.

The FRAP measurement showed lateral diffusion coefficients of approximately 1 $\mu m^2/s$ for all the chemical compositions and formation protocols studied. The lateral lipid diffusion coefficients of the vesicles generated by the two techniques, OLA and electroformation, showed relatively minor deviations from one another, and additionally most of these differences were found to be statistically insignificant (Appendix Tables A.8-A.17). In contrast, an increase in temperature and the removal of glycerol from the vesicle solution resulted in a more than two fold increase in the lateral lipid diffusion coefficient ($p < 0.001$). Moreover, we were able to compare the lateral lipid diffusion coefficients of OLA vesicles with and without octanol pockets and found that the octanol pocket does not alter the lateral diffusion properties in a statistically significant manner (at the $p < 0.01$ significance level).

Overall, this set of biophysical characterisations demonstrates the similarities in membrane properties for vesicles produced using OLA and electroformation, suggesting that the added functionality of the OLA platform does not involve any compromise in membrane quality.

Chapter 4

Development of a Microfluidic Platform to Measure Membrane Permeation [1]

4.1 Introduction

In the previous chapters, we reviewed different methods to obtain GUVs and conducted a biophysical analysis of GUV membranes obtained from the microfluidic Octanol-Assisted Liposome Assembly method. In this chapter, we want to develop the OLA chip design further. Our aim is to obtain an integrated total analysis platform that will allow GUV production and membrane permeability measurements on the same chip. In the sections below, we explain how we adapted the microfluidic chip design to allow handling and controlled exposure of the OLA GUVs to a drug solute. Furthermore, we introduce the optical setup used to visualise drug transport.

However, before we go into the details of the platform, we must introduce the metric that we use to describe transport through the membrane, the so-called permeability coefficient P. It is the phenomenological expression for the flux of molecules J, across a unit area per unit time [106, 151, 152]. With c_{in} and c_{out} being the concentrations of solute in the inside and outside of the vesicle, we obtain:

$$J = P \times (c_{out} - c_{in}) \tag{4.1}$$

[1] Elements of this chapter have previously been published in Schaich et al., *Mol. Pharmaceutics* 2019, 16, 6, 2494-2501 [68]

The permeability coefficient is a quantity that depends on both the properties of the membrane and on the solute molecules. When we speak about the permeability coefficient, we therefore always refer to a value of a specific molecule for a specific membrane in a certain chemical environment [151].

In order for a molecule to passively cross the membrane, it first needs to dissolve in the membrane from one side, diffuse through the hydrocarbon layer and leave the membrane on the other side again. The permeability is thus determined by both the predisposition of the molecule to dissolve in the hydrocarbon phase of the bilayer and the actual diffusion through the thickness of the membrane. We already discussed a quantity that describes the tendency of a molecule to dissolve in an organic phase in Chapter 2. It is the partition coefficient K. The permeability coefficient P is thus defined as

$$P \equiv \frac{KD}{d} \tag{4.2}$$

which relates the permeability coefficient to the partition coefficient via the diffusion coefficient of the solute in the hydrocarbon phase D and the thickness of the membrane d [151, 152].

This definition relates directly to the observations by Ernest Overton that nonpolar substances cross biomembranes more easily than polar molecules. Research has shown that this correlation holds true for many molecules, such as the small antibiotic molecules we will be focussing on below [37, 106, 153]. Due to this correlation, the partition coefficient is often used as a metric to assess the permeability of a compound. However, as we already discussed previously, the partition coefficient cannot be more than a rough estimate of the permeability. First of all, we can see from the definition of P that a focus solely on the partition coefficient K neglects the factor $\frac{D}{d}$ of the equation. Yet, the diffusion coefficients are not the same for all compounds and should not be neglected [154]. Second, the partition coefficient only looks at the equilibrium of un-ionised molecules. However, the charge state of a molecule is strongly affected by the chemical environment such as presence of other ions and the pH [37, 153]. Also, the partition coefficient is typically measured in octanol and not a lipid system that respects the lipid composition of the membrane. The lipid composition, however, has been shown to have a strong effect on the permeability [98]. Finally, for complete crossing, the compound must dissociate from the membrane into the aqueous phase on the other side of the bilayer. However, compounds with high partition coefficients often express low aqueous solubility, which can limit the dissociation process. Certain long-chained free fatty acids, for instance, have lower permeability coefficients than their shorter chained counterparts, despite having a higher partition coefficient. This behaviour is at least partially explained

by the decreasing aqueous solubility for longer chained fatty acids, which remain in the hydrocarbon part of the bilayer rather than to dissociate and enter the aqueous phase on the other side of the membrane [155–157].

We are not the first to see the need for platforms that allow the measurement of membrane permeation directly. Several other attempts to create such methods have been made. The earliest studies go back to the 1960s and 1970s and were performed on black lipid membranes (BLM) [158, 159].

In these experiments, two static aqueous reservoirs are separated by a lipid bilayer. The transport can be quantified by adding the target molecule in one reservoir and observing the increase in concentration on the other side of the bilayer. Though generally regarded as good model to study membranes and especially membrane proteins [158, 160], BLMs did not meet the demands for passive permeation studies. Researchers observed a region depleted of solute molecules close to the planar bilayer in transport studies. This depleted region, referred to as the unstirred water layer, forms an additional diffusion barrier for the molecules [159, 161]. As a result, the bulk concentrations of the permeant in the reservoirs are believed to substantially differ from the actual transmembrane concentration difference, skewing the permeation measurement [106, 159].

Modern techniques such the parallel artificial membrane permeability assay (PAMPA) found workarounds to this problem. PAMPA still relies on the separation of two aqueous reservoirs by a membrane, however, the assay can be equipped with a stirrer that corrects for the additional diffusion barrier. Yet, PAMPA comes with its own drawbacks. In this assay, the reservoir of microtiter plates is separated by a porous filter material, which is impregnated by a lipid solution [162]. The lipid solution is typically an alkane such as dodecane or hexadecane that only contains 1-20% lipid and some researchers argue that residual solvent influences the permeation kinetics [163]. A review of the technique concluded in 2007 that PAMPA "may be a very limited asset to a drug discovery effort" [164].

An alternative approach was developed by Cama *et al.* in 2014. They presented a microfluidic, label-free method to study drug permeation using GUVs as model membranes [37]. In their system, a stream of liposomes is mixed with a stream of drug solute, engulfing the GUV in a bath of the molecules. The GUVs are observed as they flow through a channel surrounded by the solute molecule. The transport across the membrane is visualised label-free by exploiting the target molecule's autofluorescence upon excitation in the UV. The permeability coefficient of the membrane is determined by analysing the increase of a vesicle's intensity, as fluorescing molecules diffuse through the bilayer into the GUV.

Importantly, confocal studies by Cama *et al.* found no evidence of a micron scale unstirred water layer in this assay [37]. Moreover, since the method of Cama *et al.* is a flow through system, one would expect the effect of an unstirred water layer on membrane permeation to be dependent on the vesicle's velocity. However, no correlation between permeability and vesicle speed has been found [37]. We used the method ourselves, to show that the permeability of different drugs from the fluoroquinolone family can span over 2 orders of magnitude at different pH levels [153]. Before that, Purushothaman *et al.* used the assay to show that the liposome lipid composition influences fluoroquinolone transport [98]. These results further strengthen the argument that the rate limiting element in this assay is indeed the permeation through the lipid membrane and not the diffusion through an unstirred water layer. In 2015, Cama *et al.* managed to study the transport behaviour of proteoliposomes containing the *E.coli* outer membrane protein OmpF [21], which shows the potential of this method to study flux through porins. However, the technique still relied on the electroformation method for GUV production with all its associated drawbacks that we discussed earlier.

In the following sections, we describe how we combined the fluorescence based approach of the optofluidic permeability assay with OLA to develop a lab-on-chip total analysis platform that enables the continuous production and screening of drug transport into vesicles on the same device. We will first discuss the microfluidic chip design, before we turn towards the optical methods and the diffusion model used to calculate the permeability.

4.2 Development of the Chip Design

As a robust, on-chip method to form liposomes, there are many potential ways to integrate OLA into a molecule transport assay. One seemingly obvious idea is to add the substance of interest to the IA phase and encapsulate it with a lipid bilayer upon the vesicle's formation. The molecule transport across the membrane could then be studied as the drug molecules diffuse from the inside of the vesicle, to the outside. However, we previously showed that this approach is not feasible to study drug transport [68]. The reason for this is the 1-octanol pocket that is initially attached to the liposome. Instead of moving through the membrane, the drug molecules partition into the octanol, distorting the measurement. The octanol pockets must hence be separated from the GUVs before the measurement. Another element to consider is the exposure of the vesicle to the drug itself. Ideally, the vesicles are exposed to the substance of interest in a well-defined manner to enable a precise permeability measurement that is not diffusion limited or skewed by a slow exposure of the substance with relation to the transport rate of the molecule. In the section below, we will discuss two

possible methods for octanol droplet separation as well as our design of controlled exposure to drug solutes, before we discuss the final chip design and our validation experiments.

4.2.1 On-Chip Liposome Purification

Density-based Purification of Liposomes

The problem of residual octanol was also identified by Deshpande *et al.* shortly after their initial presentation of the OLA technique. A purification protocol for OLA vesicles was therefore one of the first published follow-ups to the original OLA paper [70]. The separation method is based on the lower density of the octanol compared to the surrounding water. With a density of $\rho = 0.817$ g/cm^3, octanol will rise to the surface in an aqueous environment ($\rho = 1$ g/cm^3) [70]. A water filled punch in the microfluidic chip can therefore act as a shunt for the octanol droplets, as schematically drawn in Figure 4.1A. This separation hole must be placed far enough away from the formation junction for the GUVs to have lost their octanol droplets before they reach the separation hole. Within the separation hole, the octanol droplets will rise to the surface, whereas the liquid filled GUVs remain at the bottom. Figure 4.1B and 4.1C show micrographs of vesicles pre-separation that have their octanol pockets attached to them, as well as vesicles after the density-based purification occurred [70].

However, the purified vesicles at the bottom of the separation hole do not continue to flow into the post-hole channel automatically. In order for the GUVs to keep moving and be available for downstream operations, they have to be driven into the post-hole channel. This can occur by suction via the outlet, for instance with syringe pumps, or by using pressure driven pumps with a suction function [70]. The flow control after the separation hole is decoupled from the pressures that are used for liposome formation. Depending on the application and the downstream operation this can be either advantageous or an impediment for microfluidic handling. In any case, it has to be kept in mind that this mechanism of liposome purification changes the mode of operation from pushing the vesicles through the microfluidic chip to sucking them through via the outlet.

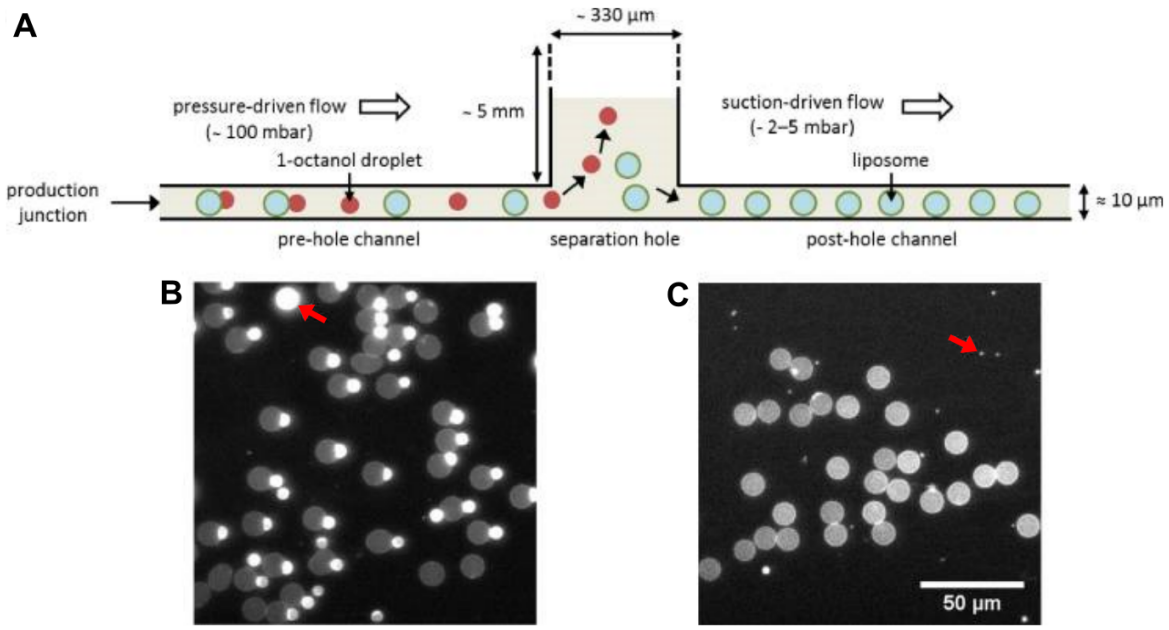

Fig. 4.1. Density based separation of OLA vesicles. (A) Schematic of the separation principle. After production, the GUVs have an octanol pocket attached to them which separates as the vesicles flow down the pre-hole channel. After separation, both the GUVs and the separated octanol droplets enter a separation hole. Due to their lower density, the droplets rise to the surface, whereas the GUVs remain at the bottom of the separation hole. By applying suction via the outlet, the octanol-free GUVs can be driven back into the microfluidic chip and are available for operations in the post-hole channel. (B) Micrograph of fluorescently labelled GUVs before octanol separation. The octanol pocket can be identified as bright fluorescing spot. A large octanol droplet is indicated by the red arrow. (C) Octanol-free GUVs sucked in from the separation hole. The vesicles do not contain visible octanol pockets attached to them. However, small residual octanol droplets are also sucked into the chip, indicated by an arrow. Image modified from [70].

Speed-based Purification of Liposomes

In addition to the difference in density between octanol droplets and GUVs, the two populations can also be separated by flow speed. As demonstrated in Figure 4.2A, the vesicles are generally much larger than the octanol droplets. The GUVs are therefore subjected to substantially more shear from the PDMS channel walls compared to the smaller octanol droplets. The latter hence travel through the microfluidic chip with a much higher speed than the liposomes. An existing population of GUVs in the outlet channel can thus be purified by simply lowering the IA and OA pressures and stopping the LO flow completely. By halting the vesicle production this way, no new octanol droplets are added to the existing

population of vesicles. The lower IA and OA pressures lead to generally slower flow speeds, ensuring that the octanol droplets have sufficient time to completely bud off the vesicles. After the octanol droplets separate from the GUV, they are automatically flushed through the chip towards the outlet, while the GUVs are kept back due to the shear-induced mechanism. The GUVs are hence available for downstream operations in the chip. After the purified GUVs have been used or flushed through the chip, the vesicle production can be restarted by increasing the fluid pressures again.

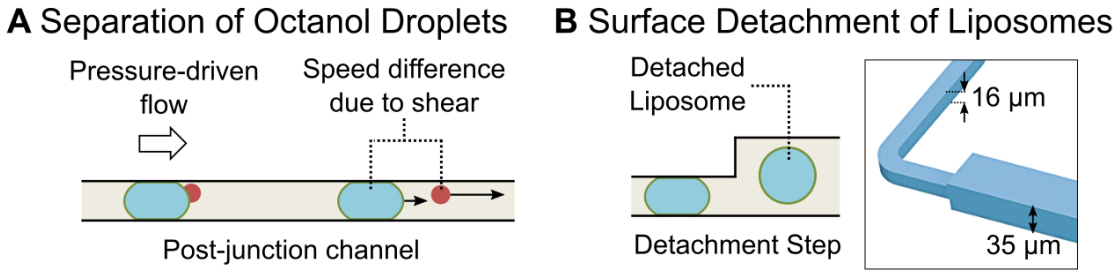

Fig. 4.2. Principle of liposome purification based on flow speed. (A) Upon formation the GUVs are subjected to shear with the PDMS channel walls which slows down the GUVs considerably. Since the octanol droplets are much smaller than the GUVs, they can flow through the microfluidic chip without interacting with the channel wall, which can be exploited to separate a population of GUVs present in the post-junction channel. (B) An increase in channel height allows the purified GUVs to detach from the PDMS channel wall in order to ensure that downstream operations are not impeded by the shear stress applied to the liposome membranes.

However, for the downstream transport measurements, we want to ensure that the vesicle membrane is not impeded by shear, as this could lead to membrane damage and leakage, which would skew the transport measurement. To avoid this, an increase in height in the microfluidic chip can be introduced to detach the vesicle from the PDMS channel wall, as illustrated in Figure 4.2B. After the step in channel height, the vesicles are no longer in contact with the channel walls and can be handled without PDMS-induced shear.

One side effect of this technique of liposome purification is the loss of the monodispersity of the GUV population, as demonstrated in Figure 4.3. Upon formation, the GUVs are typically all equal in size, as can be seen in the micrograph that shows GUVs 9 mm away from the formation junction. 4 mm further downstream from that position, the octanol pockets are seen to have bud off and were flushed through the microfluidic chip. However, some of the remaining vesicles have split into two or have partially burst, indicated by the rising presence of vesicles that are 50% of the initial diameter. Further downstream, the GUVs have lost even more of their homogeneity with GUV diameters ranging down to 25% of the original diameter.

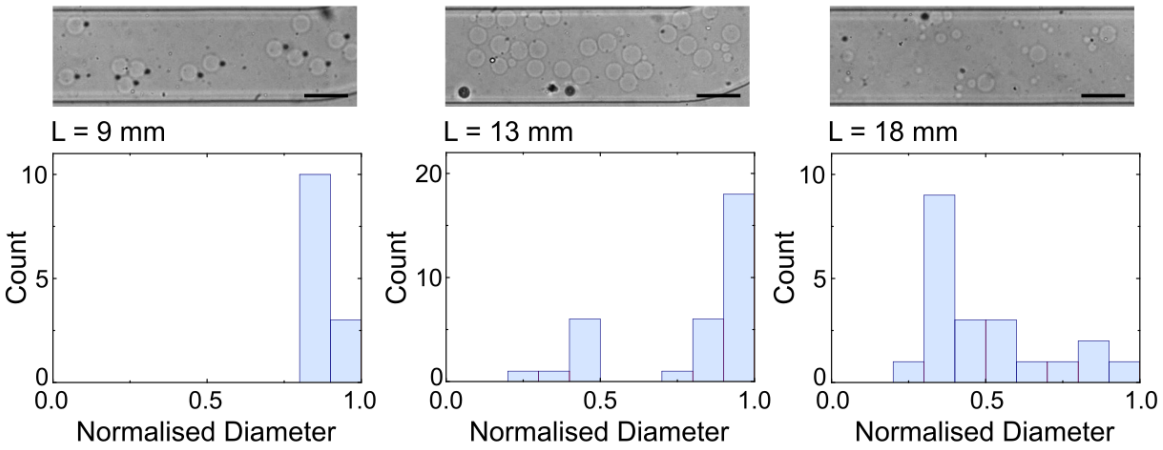

Fig. 4.3. Size distribution of liposomes in different parts of the channel. The GUVs are geometrically confined by the PDMS channel which causes shearing of the membrane. The shearing leads to the splitting of the vesicles into smaller diameter GUVs, as they flow downstream. The bright field images in the top row show liposomes at the indicated distances from the formation junction. The histograms below the micrographs show the diameter distribution of the vesicles at that position. The diameters in all histograms are normalised to the maximum diameter present in the leftmost image in order to highlight the increase in size dispersity. Scale bar 50 µm.

Both methods of liposome purification have advantages and disadvantages and should be chosen depending on the application. The purification by flow speed has the advantage that it maintains the modus of operation. The flows remain pressure-driven and the vesicles are pushed through the chip, rather than being pulled through via suction. Furthermore, it does not require additional modifications of the microfluidic chip, like the hole punch, needed for the separation based on density. The shear-induced purification is also easier and faster to implement. On the downside, the GUVs lose their monodispersity when separated by speed and the vesicle production must be stopped for the purification, as continuous liposome formation introduces new octanol droplets into the system. One is therefore required to work with the number of vesicles that are present in the channel after the GUV formation has stopped. In the case of density-based GUV formation, the liposome formation can be maintained because the flows downstream of the separation hole are decoupled from the GUV formation. Another factor to consider is the fact that the density-based purification requires additional pumps capable of applying suction, such as syringe pumps, whereas the speed-based purification does not require additional equipment.

4.2.2 Controlled Exposure to the Drug

The second design choice we must make concerns the exposure of the vesicles to the drug. Figure 4.4 shows the T-junction design we opted for to expose the GUVs to a drug solute in a controlled manner.

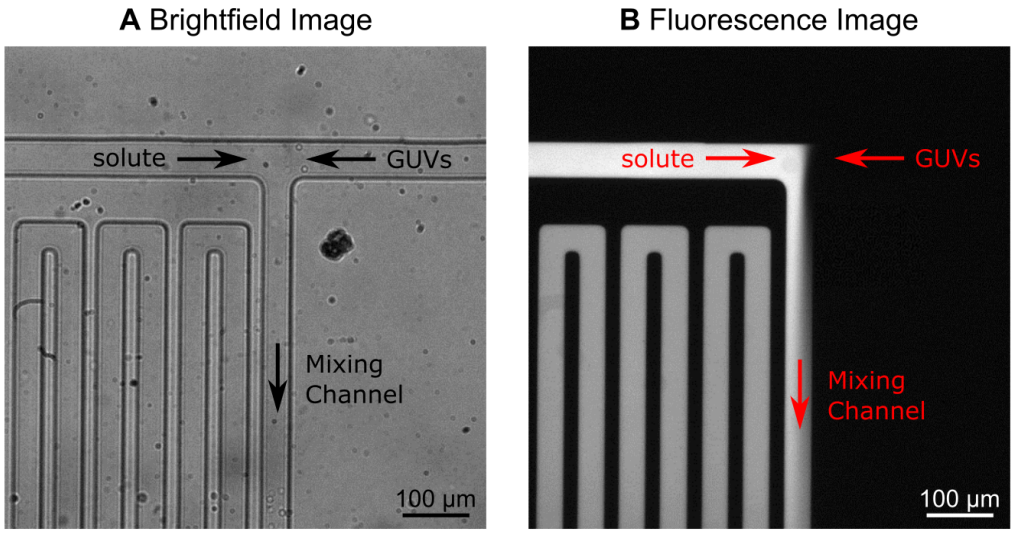

Fig. 4.4. Controlled exposure of the vesicles to the substance of interest. (A) Brighfield image of T-junction design. Two flows, one containing the GUVs and the other the drug, face each other head on and mix in a common channel leading to the outlet. (B) Fluorescence micrograph showing a fluorophore flushed in via the drug inlet channel and the equal mixing in the outlet channel.

The original T-junction design stems from the GUV permeability assay designed by Cama *et al.* in 2014 [37]. In this design, the stream of vesicles and a stream of the substance which is to be investigated encounter head on and then flow sideways along a common channel towards the outlet. Immersed in a bath of the compound, the individual vesicles and the interaction of the membrane with the added solute can be observed. The advantage of this design is the immediate exposure of the GUV to the drug stream. Due to the small dimensions of the channel heading to the outlet, the drug diffuses across the entire width of the channel, completely engulfing the GUV within several hundred milliseconds. The fast exposure to the drug makes this kind design suitable for the investigation of permeation studies that occur within seconds up to minutes [37]. Cama *et al.* previously showed that the fluid streams which the vesicles are exposed to, do not affect the permeability measurement [37]. The drawback of this design is the restrictions it sets on flow control, particularly if it is to be combined with OLA. The stream containing the vesicles and the stream from the drug inlet have to be precisely matched to ensure equal mixing at the T-junction. This limits the degrees of freedom involved in adjusting the pressure at the OLA junction to form the liposomes and

poses limits on the frequency of GUV production and vesicle size. The pressures cannot be increased at will without running the risk of pushing the vesicles into the drug inlet channel. This factor makes it harder to adjust the correct pressure regime for stable vesicle production. However, we have observed that increasing the fluidic resistance of the drug inlet channel by elongating it, improves the flow environment at the OLA junction and allows for a greater freedom to adjust the pressures. We explain this with more closely matching fluidic resistances from the channels as well as a generally higher resistive preload, which has been shown to lead to hydrodynamic flow stabilisation in microfluidic chips [165]. All in all, it is possible to balance the pressures such that vesicle production is possible without impeding the mixing of the flows at the T-junction.

4.2.3 Integration into the Final Transport Assay and Chip Operation

A schematic of the final chip design is shown in Figure 4.5. For our transport assay, we have chosen to work with the octanol separation based on flow speed and exposure to the drug via a T-junction.

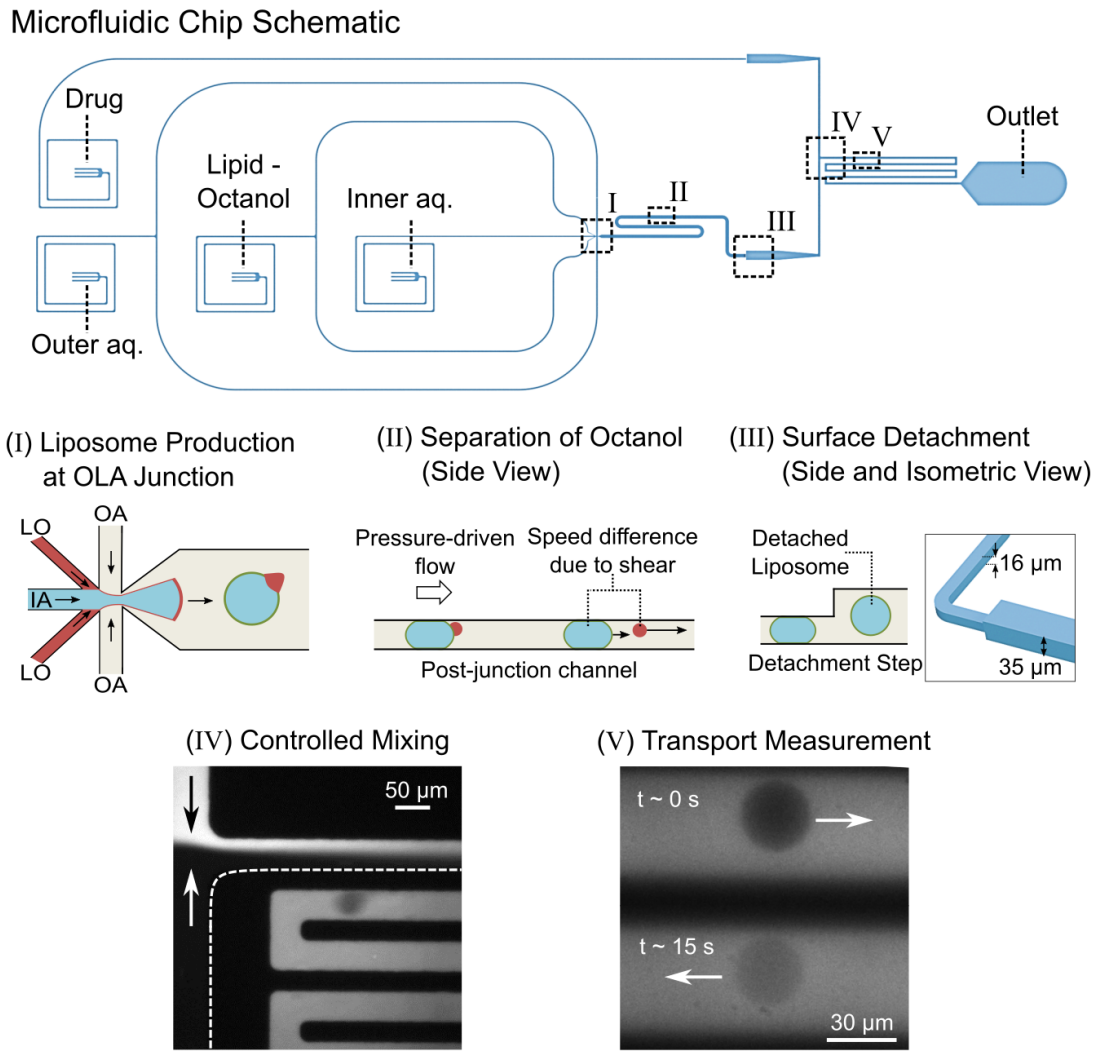

Fig. 4.5. Microfluidic total analysis system for quantifying drug permeability across liposome membranes. The microfluidic chip features four inlets, one outlet and two different channel heights. The outer aqueous, inner aqueous and lipid-octanol inlets are needed for liposome production on chip. The fourth inlet is used to flush in the drug whose permeability is to be measured. The liposome production occurs at a 6-way junction, where the aqueous flows meet the lipid-octanol phase (I). The 1-octanol pocket which is initially attached to the liposome separates from it in the post-junction channel (II) within minutes after production. In the post junction channel, the GUVs are separated from the octanol droplets. Due to their larger diameters, the GUVs are subjected to shear from the PDMS channel walls which slows them down and keep them in the microfluidic chip, whereas the smaller octanol droplets are flushed through towards the outlet. The purified liposomes then encounter a step in the chip (III), where the channel height is increased from 16 µm to 35 µm. The increase in channel height frees the liposomes from the geometric confinement and enables transport measurements across the membrane without the risk of shear-induced leakage. The GUVs continue to flow downstream without shearing against the PDMS channel walls. The liposomes are then mixed with the drug solute at a T-junction (IV) and flow along a common outlet channel. The transport measurement takes place as the liposomes flow towards the outlet, immersed in a bath of the drug (V).

As in the previous chapters, we use pressure-driven microfluidic pumps and the Fluiwell system to control the liquid flows within the microfluidic chip. The microfluidic device has four inlets and one outlet. In addition to the traditional inlets for the inner aqueous (IA), lipid-octanol (LO) and outer aqueous (OA) flows, the transport assay features a drug inlet. However, the operation principle is identical to the chips we used in the previous chapters.

The vesicles are created at the OLA junction with a width of 20 µm. This width allows us to form liposomes in a size range suitable for our application. In our case, we typically aim to form liposomes with radii between 15-18 µm. The necessary pressures for GUV formation vary from chip to chip, however, we have experience that pressures around 40 mbar for the IA, LO and drug inlets and 70 mbar for the OA phase have a high success rate [68]. The height of the chip at the OLA junction and the subsequent channel is 16 µm. We designed and fabricated two different versions of the chip with varying lengths of the channel after the junction. The two versions feature channel lengths of 13.5 mm and 34 mm respectively. In both chips, the width of the channel is approximately 200 µm. Both designs are shown in Appendix Figure B.1.

When operating the chip, we fill the large channel after the OLA junction with GUVs. Both versions of the chip are equivalent in their working principle, however, the chip version with the longer channel provides a larger reservoir for the GUVs and is therefore able to hold more vesicles than the shorter chip. After we filled the post-junction channel with GUVs, we

set the LO pressure to 0 mbar and lower the IA, OA and drug inlet pressures to 15 mbar. This stopps new generation of GUVs at the OLA junction and considerably slows down the flows in the remaining chip. At this pressure regime, the liposomes present in the large channel typically move with speeds of 0.05 mm/s, whereas the octanol droplets move at 0.2 mm/s in this region of the chip. The GUVs are separated from the octanol droplets, as explained above.

After the octanol pockets have split off the GUVs and separated from the population of GUVs, the purified GUVs reach a step in the microfluidic chip where the channel height increases from 16 µm to 35 µm. Here, the GUVs detach from the PDMS channel walls and continue to flow downstream without being subject to shear from the PDMS surface. As the vesicles reach the T-junction, they are mixed with a stream of a drug solute. The vesicles and drug solute flow along the common outlet channel. The channel winds in a serpentine-like manner towards the outlet. The overall length of the common outlet channel is 28 mm. As we will see below, the GUVs are typically driven through the channel with a speed of 0.4 - 1.0 mm/s, so that the interaction between the GUV and drug solute can be observed for time scales up to a 70 s, before the liposomes reach the outlet.

We use fluorescence video microscopy to record the GUVs passing through the channel towards the outlet using the optical setup explained below. Since the outlet channel winds back and forth, we can set the field of view in our optical setup in such a way that we can observe two parts of the channel at the same time. Typically, we observed the GUVs immediately after they were exposed to the drug solute and at a second point in the channel where the vesicle has been exposed to the solute for several seconds. From this we can work out the permeability coefficient according to a diffusion model, which we discuss in Section 4.3.3.

Importantly, while recording the videos, no new GUVs are generated. We are still operating the chip with the pressures we used for the separation of the octanol pockets (0 mbar for the LO and 15 mbar for the remaining inlets). The vesicles we are screening are the ones that were present in the long outlet channel before we lowered the flow rate. The chip with the longer channel allows us to screen over 400 vesicles, whereas the shorter version typically allows us to screen up to approximately 150 vesicles per vesicle production run. Once all vesicles have run through towards the oulet, the vesicle production with OLA can be restarted and the process repeated.

We were not able to perform transport measurements while we maintained continuous vesicle production with OLA. The reasons are the high pressures necessary to form GUVs and the resulting high flow rates. During vesicle formation, the GUVs move too fast to be precisely

captured with our EMCCD camera, as it can only operate with a maximum of 100 fps. Furthermore, maintaining GUV production with OLA continuously introduces new octanol droplets to the system. However, we want to minimise the amount of octanol during our experiment. By stopping the vesicle production, the octanol droplets can be flushed through the chip and effectively separated from the population of GUVs, as explained in Section 4.2.1.

4.3 Optical Methods and Permeability Calculation

In the previous section we have spoken about liposome handling and exposure to the drug solute. In this section we will explain the method we use to visualise the transport itself, perform our measurements and calculate the permeability coefficient.

4.3.1 Drug Molecule Visualisation

Our assay relies on fluorescence to visualise the solute molecules, whose permeability we want to study. We used fluoroquinolone antibiotics for the validation experiments of the platform we present below. Fluoroquinolones are an ideal candidate for this purpose, due to their autofluorescence [37]. The solute molecules themselves fluoresce upon excitation in the UV and they do not have to be conjugated to a fluorescent dye to visualise their presence. Using the optical setup explained below, the microfluidic device is illuminated with UV light (λ_{ex} = 350 nm) and the induced fluorescence (λ_{em} = 440 nm) is detected. Importantly, the fluorescence signal scales linearly with the concentration up to 2 mM, as has been shown before [37]. The mixing of the vesicle and the drug flow at the T-junction is shown in Figure 4.6A, with the drug flow appearing bright and the vesicle flow dark. When we mix the GUVs with the stream of autofluorescent drug molecules at the T-junction, the liposomes initially appear dark on a bright background, as shown in Figure 4.6B. The reason for this is the lack of fluorescent molecules in the inside of the vesicles. As the fluorescent drug molecules diffuse through the membrane, the liposomes get brighter. We record and analyse the increase in fluorescence intensity using the MATLAB routine explained below. From the increase in fluorescence, we can quantify the permeability coefficient of the drug molecule for the specific lipid composition under investigation.

4.3.2 Optical Setup

The microfluidic chips for our validation measurement are operated on a custom-built UV epifluorescence setup, to induce autofluorescence in the drug molecules and to capture the experimental video data. In this setup, white light from a broadband light source (EQ99FC, Energetiq, USA) enters a monochromator (Monoscan 2000, OceanOptics, USA) where the excitation wavelength (λ_{ex} = 350 nm) for the target drug molecule is selected. The UV light passes through a Köhler illumination pathway and illuminates the microfluidic device via a quad band dichroic mirror (BrightLine full-multiband filter set, Semrock, USA) and a microscope objective. The fluorescence signal is detected by an EMCCD camera (Evolve 512 Delta, Photometrics). The camera and recording settings (exposure 10 ms, bin 2, gain 150) are controlled using the open source software µManager 1.4 [166]. A 60× water immersion objective (UPLSAPO NA 1.2, Olympus) is used for data recording, whereas lower magnifications (4×, 10×, 20×, Plan Achromat, Olympus) are used for optimising the vesicle formation and PVA treatment of the chip.

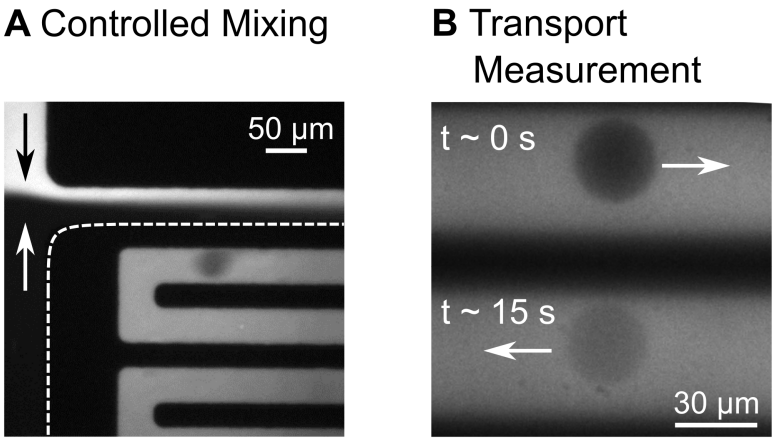

Fig. 4.6. Liposomes at different positions in the microfluidic chip. (A) Liposomes experience a controlled exposure to a drug solute at a T-junction where the two flows mix. Note that the image shows the T-junction at higher flow rates than typically used for in the experiments, resulting in a homogenous mixing of the drug and vesicle flows further downstream. (B) Liposomes, surrounded by the autofluorescing drug (λ_{ex} = 350 nm), can be monitored at different parts of the channel, corresponding to different times that the liposome has been exposed to the drug. The increase in liposome intensity as the fluorescing drug diffuses across the membrane is used to determine the permeability coefficient of the drug across the lipid membrane under investigation.

Alternatively, the microfluidic devices can also be run on commercial epifluorescence microscopes if they are equipped with filter sets suitable to induce fluorescence in the target molecule.

4.3.3 Diffusion Model

Our transport platform uses the same liposome-based principle for the measurement of membrane permeability as the original microfluidic platform, published by Cama *et al.* in 2014 [37]. Since the fundamental transport principle is identical, we can use the diffusion model Cama *et al.* developed for small fluorescent molecules for our platform [68].

The starting point for the permeability model is Fick's law of diffusion. We know that the flux of molecules across a membrane J is described by the equation

$$J = 4\pi R^2 \times P \times \Delta c = 4\pi R^2 \times P \times (c_{out} - c_{in}(t)) \tag{4.3}$$

Where P is the permeability coefficient, our desired quantity, which is defined as $P \equiv \frac{KD}{d}$ [151].

Furthermore, the flux across a spherical vesicle's membrane is equivalent to the change of drug concentration within a vesicle over time.

$$J = \frac{dc_{in}}{dt} \times \frac{4}{3}\pi R^3 \tag{4.4}$$

$$\Leftrightarrow -\frac{3P}{R} = \frac{1}{c_{out} - c_{in}(t)} \times \frac{dc_{in}}{dt} \tag{4.5}$$

And upon integration:

$$-\frac{3Pt}{R} = \ln(c_{out} - c_{in}(t)) + C \tag{4.6}$$

We know that the initial concentration inside the vesicle is zero. Our boundary condition is therefore $c_{in}(t = 0) = 0$.

$$0 = \ln(c_{out} - 0) + C \Leftrightarrow C = -\ln(c_{out}) \tag{4.7}$$

$$\Rightarrow -\frac{3Pt}{R} = \ln\left(\frac{c_{out} - c_{in}(t)}{c_{out}}\right) \tag{4.8}$$

Which we can easily solve for the permeability coefficient P

$$P = -\frac{R}{3t} \times \left(\frac{c_{out} - c_{in}(t)}{c_{out}} \right) \tag{4.9}$$

For our data analysis, it is necessary to link the concentration values $c_{in}(t)$ and c_{out} to the autofluorescence light intensities, which is the quantity we capture with our camera. Without a vesicle present and the fluorescent drug filling the entire channel, the case is simply $c_{out} \propto I_{out}$. For the case of a vesicle in the channel, we cannot simply assume direct proportionality as we are not obtaining a confocal measurement. We have to consider the background intensity I_0 from the fluorescing drug surrounding the vesicle and subtract this from the intensity of the vesicle $c_{in}(t) \propto (I(t) - I_0)$.

For the expression in brackets in Equation 4.8, we thus receive

$$\frac{c_{out} - c_{in}(t)}{c_{out}} = \frac{I_{out} - (I(t) - I_0)}{I_{out}} \tag{4.10}$$

With our setup, we measure the intensity inside a vesicle (I_{in}) and outside (I_{out}) at two distinct time points. The first measurement is always immediately after exposure of the vesicle to the drug ($t = 0$) and we assume that there are no fluorescent molecules in the inside of the vesicle at this time point. The fluorescent signal I_{in} we obtain at this timepoint is therefore equivalent to the signal coming from the fluorescent drug surrounding the vesicle I_0. The second measurement of the inside and outside intensities occurs at a later timepoint t_f.

If we normalise the intensities at the two time points to the outside fluorescence, we obtain.

$$\Delta I_1(t = 0) = \frac{I_{out} - I_{in}}{I_{out}} = \frac{I_{out} - I_0}{I_{out}} \tag{4.11}$$

and

$$\Delta I_2(t = t_f) = \frac{I_{out} - I_{in}}{I_{out}} = \frac{I_{out} - I(t)}{I_{out}} \tag{4.12}$$

We can now reshape the expression in the brackets of Equation 4.10. By adding and subtracting $\pm I_{out}$, in the numerator we do not change the validity of the expression, but attain

$$\frac{I_{out} - I(t) + I_{out} + I_{out}}{I_{out}} = \frac{I_{out} - I(t)}{I_{out}} - \frac{I_{out} - I_0}{I_{out}} + \frac{I_{out}}{I_{out}} = \Delta I_2 - \Delta I_1 + 1 \tag{4.13}$$

We finally receive our equation for the permeability coefficient expressed by autofluorescence intensity as

$$P = -\frac{R}{3t} \times \ln(\Delta I_2 - \Delta I_1 + 1) \tag{4.14}$$

The acquired videos are analysed using a newly developed MATLAB script. It extracts the relevant vesicle data from the images and calculates the permeability coefficient according to the diffusion model explained above. In the next section we will briefly explain the analysis routine and debug features of the code.

4.3.4 Data Processing and Permeability Calculation

The MATLAB script is optimised for video files in the TIFF format. In every experiment, we typically record 15-30 movies of 5000 frames each. With a frame rate of 100 fps, each movie is 50 seconds long. The analysis explained below is performed for each video. If problems occurred during data recording, such as exposure to stray light or obstructions in the flow, the respective videos can be identified from the debugging files and excluded from further analysis.

The video files must show two channels, as depicted in Figure 4.6B. The code will automatically recognise the channel and define each as a specific region of interest (ROI). The vesicles passing in each of the respective channels represent two different time points that the vesicle has been exposed to the drug. Next, the frames with vesicles present in the channel are identified. This is achieved by observing the mean fluorescence intensity over time. As a vesicle enters the ROI, the mean fluorescence intensity decreases, since the vesicle is darker compared to the background, due to the lack of fluorescent antibiotic molecules in the inside of the vesicle. When the vesicle leaves the field of view, the fluorescence is restored to the initial level.

From the frames we identified as a vesicle event, all the necessary information required for the diffusion model is extracted. Using MATLAB's *imbinarize* function, we identify the contour of the vesicle and extract the radius, the coordinates of the centre point, and the circularity using the *regionprops* function. Most importantly, we identify a 5×5 pixel box around the GUV centre and measure the mean intensity of this square for every frame of the vesicle event. The average intensity over all the frames is the quantity I_{in} from the diffusion model above. In order to extract the outside intensity I_{out}, the frames before and after the vesicle event are merged into one image. The GUV is not present in this image. The same 5×5 pixel boxes used to obtain the I_{in} signal are now measured in the frame without the GUV

present, to obtain I_{out}. To avoid errors in the extraction of the intensity values, we introduced a debugging option in this part of the code. A debugging proof, as seen in Figure 4.7, is generated for every vesicle event. It shows the background image that was generated to extract I_{out}. Furthermore, it shows one of the frames of the vesicle event and the contour identified which is used for the *regionprops* function. Obvious sources of error, for instance two vesicles that are clustered together and are identified as one single vesicle, can easily be detected and excluded from the analysis with the debugging option. Note that we subtract the camera's dark noise from all intensity values, as this baseline intensity is not a fluorescent signal of the molecule.

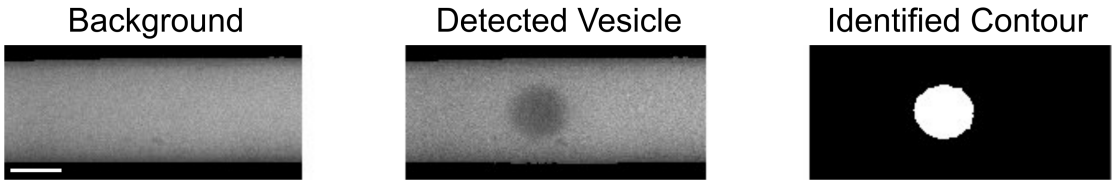

Fig. 4.7. Debugging panel exported for every vesicle event. The panel consists of three images. The left image shows the background which is used to determine I_{out} in the diffusion model. The middle image shows the detected vesicle as it is recorded. The right frame shows the vesicle after binarisation. The binarised image is used to identify the contour of the vesicle and extract parameters such as radius and intensity. The exported panel allows for a fast screening for errors, for instance when two vesicles clustered together are identified as one. The scale bar 20 µm.

We extract the speed of the vesicle by its movement through the field of view. Since we set the position of our detection points, we know the distance the GUV has travelled when it reaches the second ROI and thereby the time t_f it has been exposed to the drug.

We place the first t_0 time point, where the drug had diffused across the entire channel width. This was typically 200 microns downstream of T-junction point. The vesicles measured in the second ROI have been exposed to the drug throughout their path towards the outlet. The chip geometry is designed in such a way that the second ROI lies 7.5 mm after the first ROI. With speeds between 0.4 mm/s and 1.0 mm/s, the vesicles have therefore been engulfed in the bath of drug molecules for between 7.5 and 19 seconds when they are screened for the second time to obtain ΔI_2.

Figure 4.8 shows a typical scatter plot, as obtained from a permeability measurement. The normalised intensity values ΔI on the y-axis and the vesicle radius on the x-axis make up the coordinate plane. Every data point represents a single vesicle measurement. The dark data points are ΔI_1 measurements taken just after the vesicle encountered the drug at the

T-junction. The coloured data points are the ΔI_2 measurements obtained after the GUV has been exposed to the drug for the time specified in the inset. The spread in liposome radius is an effect of the method we used to purify the liposomes, as we pointed out above.

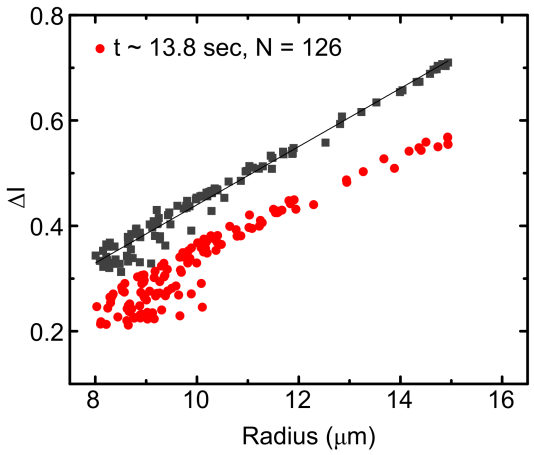

Fig. 4.8. Scatter plot of permeability measurements. The normalised intensity difference is given on the y-axis, the radius on the x-axis. Every data point represents a single vesicle measurement. The dark data points are taken at the first measurement point immediately after the vesicle was exposed to the drug (t ~0 s). The coloured data points are vesicles measured at the second position. The timespan between the two measurements as well as the total number of data points at the second position is noted. The normalised intensity is lower at the second time point, as fluorescing molecules diffused across the membrane reducing the vesicle's contrast to the outside.

If we remember our definition $\Delta I = \frac{I_{out}-I_{in}}{I_{out}}$, the distinct shape with two linear bands of values becomes evident to us. ΔI_1 is higher than ΔI_2 since no fluorescing molecules have crossed the membrane at the first measurement point. The normalised intensity difference between the vesicle inside I_{in} and outside I_{out} is therefore larger than at the second time point, when autofluorescing drug molecules have crossed the membrane and decreased the difference $I_{out} - I_{in}$. We can also understand the linear increase of ΔI as a function of the radius when we consider the design of the optical setup. Since we do not perform a confocal measurement, the fluorescent drug molecules on top and below a vesicle on its vertical axis (the optical axis) contribute to the I_{in} value we measure. With increasing radius, there are fewer fluorescent molecules present surrounding the vesicle in the channel that contribute to I_{in}. The difference $I_{out} - I_{in}$ and therefore ΔI is hence higher for larger vesicles. In other words, since the concentration of the drug solute is constant, the fluorescence is directly proportional to the volume of the solute. As we always measure a 5×5 pixel area in the centre of the vesicle, the volume occupied by the solute, and therefore the fluorescence, scales directly with the distance between the channel ceiling/floor and the vesicle.

The field of view we obtain using the 60× objective allows us to observe two channel segments at the same time. The two channels segments correspond to two time periods which the vesicle has been exposed to the drug. One crucial measurement according to our diffusion model is the ΔI_1 value taken the t_0 time point. However, when the field of view is set to this position, the second channel segment, where we measure ΔI_2, is always 7.5 mm downstream from the T-junction, due to the geometry of the chip. If we want to shift the field of view down to positions in the channel that correspond to longer exposure times, we can no longer obtain the corresponding ΔI_1 for that individual vesicle.

We solved this restriction set to us by the chip geometry, by not comparing one and the same vesicle at two time points directly. Instead, we exploit the linear relationship between ΔI_1 and the radius R. We first measure a sufficient number of vesicles at the t_0 position such that we can fit a linear function to the values of $\Delta I_1(R)$. The fitted linear function is depicted as a solid black line in Figure 4.8. We then use this function to recalculate ΔI_1 for any vesicle we measure at a later timepoint. By recalculating ΔI_1, can shift the field of view to any position in the chip.

4.4 Permeability Measurement of Fluoroquinolone Antibiotics

After we introduced the chip design in the previous sections, we want to turn to the actual measurement of small drug molecule permeation across defined lipid bilayers. We will perform validation experiments using the fluoroquinolone drug norfloxacin and measure the permeability of this drug in two chemical environments - one measurement in an acetic acid buffer at pH 5 and one in a pH 7.4 phosphate buffered saline (PBS) solution. Next, we compare the permeability values obtained with our assay to similar experiments which were performed on electroformed vesicles to validate that permeability measurements using OLA vesicles are quantitatively similar to those performed using electroformed GUVs. Furthermore, we determine the permeability coefficient of a second drug, ciprofloxacin, at pH 7.4 and physiological salt concentrations.

Before we begin, we want to briefly explain the relevance of antibiotic permeability measurements using GUVs as model membranes.

4.4.1 Motivation

Over the past decades, multidrug resistance (MDR) in microbial pathogens has developed into a serious threat for public health, leading to a global medical crisis [167]. In 2016, more than half (58.6%) of clinical *Escherichia coli* isolates in the European Union showed resistance to at least one of the antimicrobial groups under regular surveillance [168]. One of the major biochemical causes of antibiotic resistance is the reduced membrane permeability of drug molecules [169–172].

This problem is especially apparent for Gram-negative bacteria, as their cell envelope consists of a double membrane; drugs require seemingly contradictory chemical properties to overcome these two barriers to reach their cytoplasmic targets [20, 170, 172]. The outer bilayer is equipped with a highly charged layer of lipopolysaccharides (LPS), effectively preventing the permeation of both hydrophilic and hydrophobic compounds [170]. Most compounds therefore need to pass the outer membrane via water filled β-barrel channels (porins) such as OmpF [21]. Many of these porins favour the passage of hydrophilic or charged compounds [170, 173]. Once a compound crossed the outer membrane, it still needs to penetrate the inner membrane. This membrane, however, behaves like a standard phospholipid bilayer and provides a strong barrier for charged or hydrophilic molecules. The properties that allow a molecule to pass the first membrane are hence what prevents it from permeating through the second membrane. We see that the passive uptake of molecules is not trivial. A deeper understanding of the mechanisms that govern passive drug transport across lipid membranes is therefore of great importance in the context of solving the antibiotic resistance challenge.

Bacterial cell membranes are very complex systems that are involved in numerous cellular processes [174]. Drug permeability studies have not only proven very difficult due to the small size of the bacteria, but also due to the convolution of active and passive effects that simultaneously take place in the membranes of living bacteria [172, 175]. We therefore use OLA derived GUVs as model membranes [175]. The GUVs offer the advantages of having well-defined lipid compositions, being easy to image and also being more controlled systems for studying transport processes than a living bacterium.

The lab-on-chip total analysis platform we presented above enables the continuous production and screening of liposomes on the same device. This enabled us to efficiently screen an order of magnitude more liposomes than the earlier platforms we discussed above. Importantly, it also enables us to explore transport using physiological salt concentrations which was challenging using electroformed GUVs [176]. We investigate the transport using biomimetic

membranes, using a lipid mixture of DOPG-DOPC (1:3 ratio) to form the GUVs. The net negative charge carried by this membrane mimics bacterial membranes more closely than simple bilayers consisting of pure PC lipids and is often used to mimic bacterial membranes [69, 177–179].

4.4.2 Material and Methods

Chip Fabrication

The microfluidic chips are made of polydimethylsiloxane (PDMS) following the protocol we explained previously in Section 2.4.2. The generation of the master mold requires an additional fabrication step, due to the multi-height (16 µm and 35 µm) features in this chip design. The 16 µm features are obtained by spin coating a layer of SU-8 2025 photoresist (MicroChem, USA) on a 4-inch Silicon wafer (University Wafer, USA). The wafer is pre-baked on a hot plate at 65°C for 1 min and at 95°C for 6 min. The structures are imprinted on the substrate using a table-top laser direct imaging (LDI) system (LPKF ProtoLaser LDI, Germany). The LDI system exposes the structures specified in the software directly with UV light, causing the photoresist to crosslink and solidify. After exposure, the wafer is post-baked for 1 min at 65°C and for 6 min at 95°C. The substrate is developed by rinsing the wafer with propylene glycol monomethyl ether acetate (PGMEA), which removes the unexposed photoresist and leaves the desired UV-exposed structures on the substrate. The wafer is then hard baked for 15 min at 120°C. The multi-height feature is achieved by performing this photo-lithography process again on the same silicon wafer with different layers of photoresist with varying heights. Feature heights of 16 µm and 35 µm respectively were obtained by spinning the photoresist at 3800 rpm and 1800 rpm respectively (WS-650-23NPP, Laurell Technologies, USA) for 60 s with a ramp of 100 rpm/s. The anchoring tool of the direct laser writer is used for aligning the features in the two designs.

Solution Composition

The base solutions for the OLA aqueous phases consist of 200 mM sucrose and 15% v/v glycerol in buffer. In accordance to previously published protocols, the outer aqueous phase additionally contains 50 mg/mL poloxamer Kolliphor P-188, which facilitates the initial double-emulsion formation [64]. We performed experiments on the fluoroquinolone drugs norfloxacin and ciprofloxacin. Transport of both drugs is measured in phosphate-buffered saline (pH 7.4) which mimics physiological pH and salt concentrations. Additionally,

experiments using a 5 mM acetic acid buffer (pH 5) are performed for norfloxacin as controls for membrane stability. At pH 5, norfloxacin molecules are primarily in their positively charged form and hence show low permeability through lipid bilayers [37, 153]. The drug solutes are prepared by diluting 48.5 mM norfloxacin and 49.5 mM ciprofloxacin stock solutions, respectively, to a final concentration of 2 mM with the aqueous base stock. All pH levels were adjusted and checked using a digital pH meter (Hanna Instruments, UK). The lipid-octanol phase is obtained by dissolving a 100 mg/mL lipid stock mixture with 1-octanol to reach a final concentration of 2 mg/mL. The lipid stock is a 3:1 mixture of DOPC (1,2-dioleoyl-sn-glycero-3-phosphocholine) and DOPG (1,2-Dioleoyl-sn-glycero-3-phosphorac-(1-glycerol) sodium salt) in 100% Ethanol. DOPG is an anionic lipid with a net charge of -1. Lipid mixtures of DOPG with the net-charge neutral lipid DOPC roughly mimic the negative charge density of bacterial lipid extracts and are typically used when modelling bacterial membranes with GUVs [69, 177–179]. All chemicals are obtained from Sigma-Aldrich, unless stated otherwise.

Optical Setup

The microfluidic chips for the norfloxacin measurements were run on the custom-built UV epifluorescence setup we explained above. The ciprofloxacin measurements were obtained on a commercial epifluorescence microscope (Nikon TE 2000U). The Nikon epifluorescence microscope is equipped with a pE-1 LED lamp (λ_{ex} = 365 nm (DAPI), Cool LED, UK). We used the same water immersion objective (60×, UPLSAPO NA 1.2, Olympus), dichroic mirror (BrightLine full-multiband filter set, Semrock, USA) and camera (Evolve 512 Delta, Photometrics; exposure 15 ms, bin 2, gain 250) as in the custom built setup for the ciprofloxacin measurements.

4.4.3 Results and Discussion

Norfloxacin transport measurements were performed in two different chemical environments. One set of measurements was performed in PBS at physiological pH and salt concentrations. The second set was taken as a control in an acetic acid buffer at pH 5. The scatter plots in Figure 4.9A and 4.9B show representative results from our norfloxacin experiments. The dark data points mark the normalised intensity difference levels ΔI_1 of individual liposomes at the first measurement point, when the liposomes have just encountered the drug flow and hence do not contain any drug molecules within them. The coloured data points mark the

normalised intensity difference ΔI_2 of the individual liposomes after they have been exposed to the drug for the time indicated inset. As we explained in Section 4.3.4, the drop in ΔI is a direct result of the influx of fluorescent molecules into the GUV.

In Figure 4.9A, we can see no drop in ΔI for the vesicles at pH 5 between the two measurement points. The technical repeats of this experiment shown in Appendix Figure B.2 report similar results. Since the drop in ΔI is a direct result of the influx of fluorescent molecules, we can conclude that no significant transport occurs at pH 5 over the observed timespans. Expanding the exposure and observation time for the pH 5 measurement to 40 seconds yields the same result of no significant transport, in line with our previous observations. This also confirms that the liposome membranes are not being compromised due to shear or any other interactions in our device.

In contrast to the pH 5 measurements, we observe a substantial decrease in ΔI for the vesicles in PBS shown in Figure 4.9B. From these scatter plots, we can conclude that there exists effective norfloxacin transport across the bilayer at physiological pH and salt concentrations. Comparing the two measurements taken in PBS, we also observe a larger drop in ΔI in the right scatter plot compared to the left scatter plot. We can explain this when we look at the timespan that lies between the two measurement points for ΔI_1 and ΔI_2, which are given inset. Approximately 14 seconds lie between the two measurement points in the scatter plot on the left, which shows the smaller gap. In contrast to that, approximately 18 seconds lie between the two measurement points in the scatter plot on the right, which displays the larger gap between ΔI_1 and ΔI_2. The larger gap between ΔI_1 and ΔI_2 hence stems from the fact that more autofluorescing drug molecules could diffuse across the bilayer in the additional time, lowering ΔI_2, as expected.

Figure 4.9C shows two representative scatter plots obtained for the fluoroquinolone drug ciprofloxacin. Again, we observe a substantial decrease in ΔI between the two time points, visualising the passive transport of this drug across the bilayer in the PBS environment. Note that the ΔI scale is different in these scatter plots compared to the measurements taken for norfloxacin. This is due to the fact that the ciprofloxacin measurements were obtained on a different optical setup which required different gain and exposure settings.

Additional scatter plots with technical repeats for all measurements are shown in Appendix Figures B.2 to B.5.

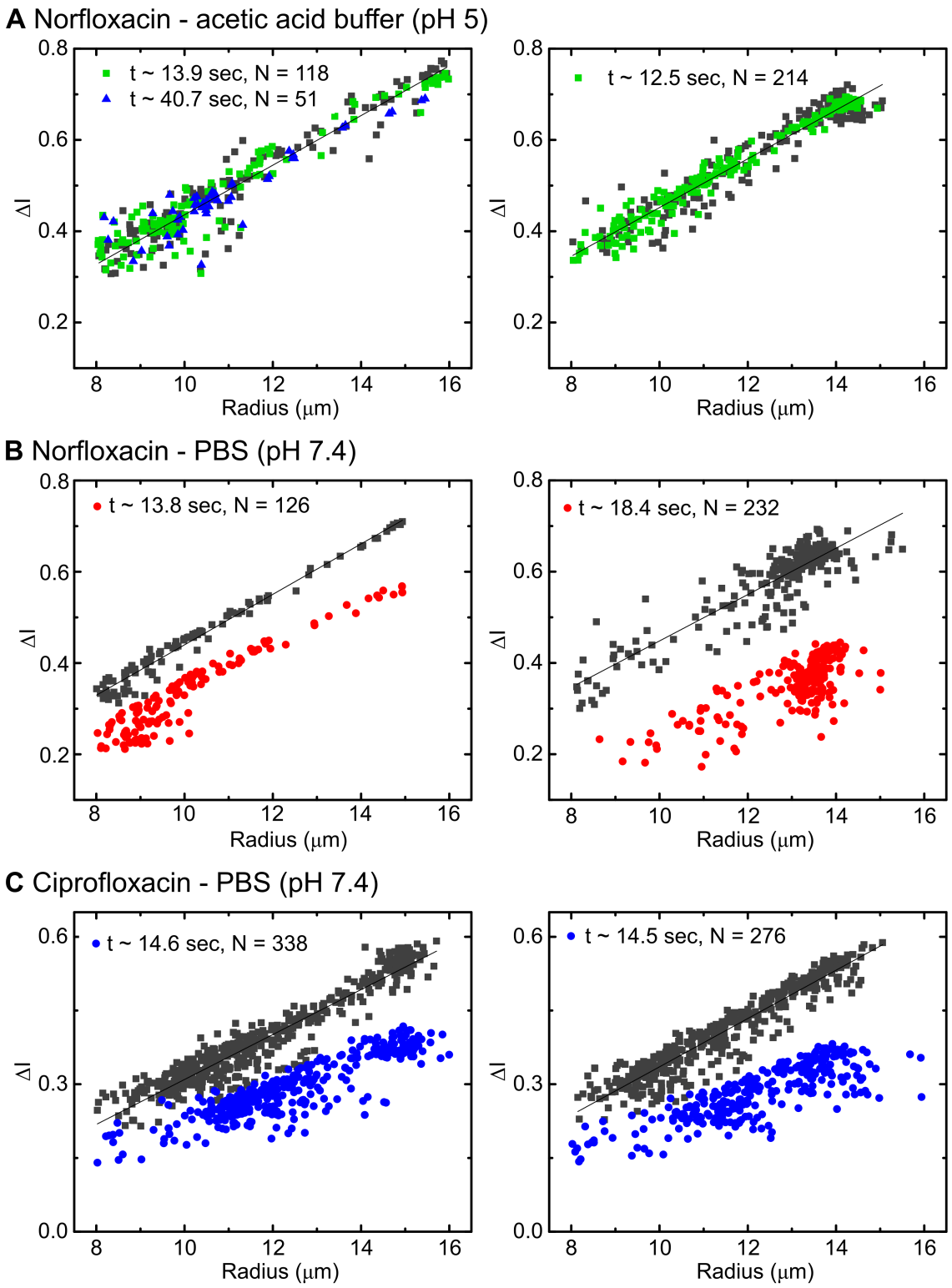
A Norfloxacin - acetic acid buffer (pH 5)
t ~ 13.9 sec, N = 118
t ~ 40.7 sec, N = 51
t ~ 12.5 sec, N = 214
B Norfloxacin - PBS (pH 7.4)
t ~ 13.8 sec, N = 126
t ~ 18.4 sec, N = 232
C Ciprofloxacin - PBS (pH 7.4)
t ~ 14.6 sec, N = 338
t ~ 14.5 sec, N = 276
ΔI
Radius (μm)

Fig. 4.9. Representative scatter plots of permeability measurements. Every scatter point represents a single vesicle measurement. The dark scatter points are taken at the first measurement position at t $\approx$ 0 s, just after the vesicles encountered the drug. The coloured scatter points are vesicle measurements taken at the second position, after the vesicles have been exposed to the drug for the time given inset. (A) Norfloxacin measurement in acetic acid buffer at pH 5. The dark and the coloured scatter points overlap, indicating that there is no substantial drug perfusion into the vesicle in the given time frame. In the left scatter plot, the field of view was moved to a position later in the chip that corresponds to a drug exposure of the vesicles of over 40 seconds. (B) Norfloxacin measurements in PBS and at a physiological pH level. The gap in ΔI between the two measurement positions reveal that substantial transport occurred between the two measurement time points. The gap between ΔI_1 and ΔI_2 is larger for the scatter plot on the right, where 18 seconds have passed between the two measurement points, compared to 14 seconds for the scatter plot on the left. (C) Ciprofloxacin measurements in PBS and at physiological pH level. The gap in ΔI, again, reveals substantial transport via passive diffusion. Note that the ΔI levels in these measurements are marginally different from the norfloxacin measurements, as they were obtained on a different optical setup which required different gain settings.

The observed transport behaviour for the drugs at pH 5 and pH 7.4 is as we expect and is a result of the charge state of the molecules in the different chemical environments. The majority of norfloxacin molecules are positively charged at pH 5 whereas the proportion of uncharged molecules is highest at pH 7.4 [153, 180, 181]. Lipid membranes are generally regarded as largely impermeable to ions and highly charged molecules, since these cannot cross the hydrocarbon section of the lipid bilayer easily. In nature, these transport processes are governed by transmembrane proteins such as porins or ion channels [15]. The observed behaviour is therefore perfectly in line with what the theory predicts.

The histograms showing the permeability coefficients of all the norfloxacin and ciprofloxacin experiments performed in PBS are given in Figure 4.10. The total number of liposomes for the norfloxacin histogram is 1620 and results in an overall average permeability coefficient of $4.13 \pm 0.05 \times 10^{-6}$ cm/s (mean ± std. error of mean) and a median value of 3.57×10^{-6} cm/s. The values were obtained from 12 experiments in 5 technical repeats. The mean (± std. error of mean) permeability coefficient obtained for ciprofloxacin is $4.99 \pm 0.07 \times 10^{-6}$ cm/s and the median value is 4.83×10^{-6} cm/s. The values are obtained from 4 experiments (4 technical repeats) and a total of 960 vesicles. For the pH 5 measurement, five experiments on two technical repeats were performed. An experiment is defined as a continuously acquired dataset measured from one batch of liposomes produced on the microfluidic device. As described above, up to four experiments were performed on one microfluidic device, by restarting the liposome production after completion of one

measurement. Each set of experiments performed on an individual device is defined as a technical repeat.

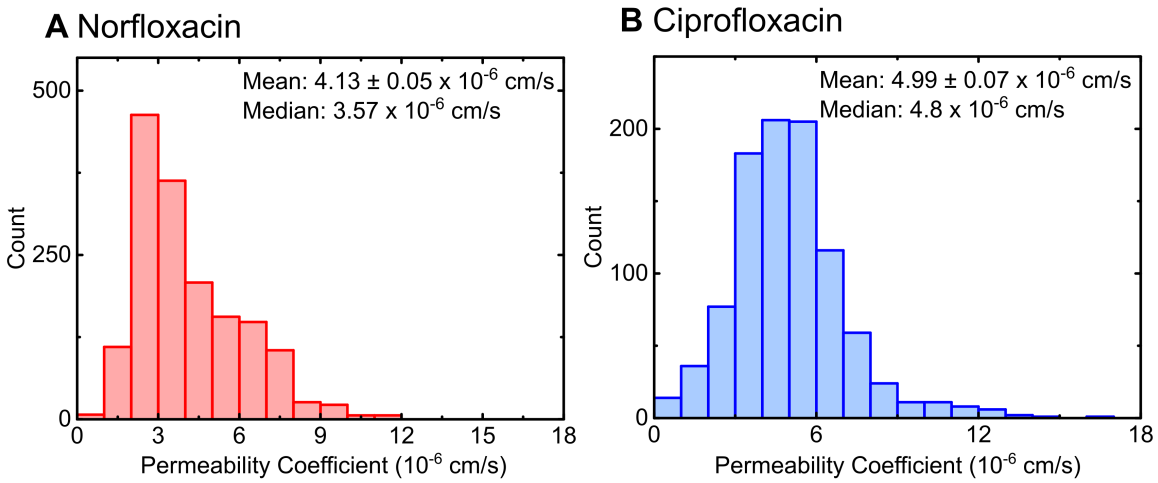

Fig. 4.10. Histograms of the permeability coefficients for norfloxacin (N = 1620) and ciprofloxacin (N = 960). The mean ± std. error of mean, as well as the median values are noted. The permeability of ciprofloxacin is significantly higher than the permeability of norfloxacin (two sample t-test, $p < 0.001$). The values for norfloxacin were obtained in 12 experiments performed on 5 different microfluidic chips (5 technical repeats). The values for ciprofloxacin were obtained in 4 experiments on 4 different microfluidic chips.

The value obtained from the transport measurements matches the values previously obtained in our group using the established electroformation liposome production technique. Purushothaman *et al.* measured the permeability coefficient of norfloxacin through PGPC liposomes (30:70 ratio) in a 5 mM phosphate buffer solution at pH 7.0 to be $4.3 \pm 0.2 \times 10^{-6}$cm/s [98]. The main advantages of the on-chip OLA technique over electroformation are the high-throughput liposome production and its compatibility with physiological salt concentrations. The higher liposome production efficiency allows us to perform tests on 1620 liposomes here compared to the 138 liposomes in previous experiments using electroformation. Due to the greater efficiency of vesicle formation under these conditions and the correspondingly higher number of data points, we can provide a more precise estimate of the permeability coefficient than before, with the standard error of the mean lowered by over an order of magnitude compared to the results previously reported [98] using electroformed vesicles. Furthermore, the possibility of producing liposomes at physiological salt concentrations allows us to mimic the natural environment of a bacterial cell more closely. Any possible remaining traces of solvent (1-octanol, poloxamer P-188) do not seem to alter the transport properties of the membrane, as seen by the similarity to the previously acquired result.

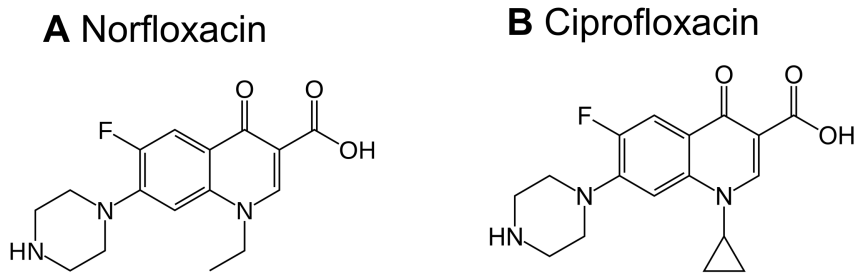

Fig. 4.11. Chemical structures of norfloxacin and ciprofloxacin. Norfloxacin carries an ethyl group at the N-1 position, whereas ciprofloxacin has a cyclopropyl group at this position.

The higher permeability coefficient of ciprofloxacin compared with norfloxacin is to be expected based on the chemical structures of the respective molecules, drawn in Figure 4.11. We see that norfloxacin carries an ethyl group at the N-1 position, where ciprofloxacin has a cyclopropyl group. This functional group increases the lipophilicity of the compound as compared to the corresponding ethyl group in norfloxacin, and therefore results in a higher permeability coefficient [153].

According to the DrugBank database, calculated partition coefficient (log P) values for norfloxacin lie between -0.47 and -0.92, while experiments show a log P of -1.03 [182]. For ciprofloxacin, the calculated log P values lie between -0.57 and -0.81 with an experimental value of 0.28 [182]. A positive partition coefficient indicates a larger lipophilicity of a compound, whereas a more negative partition coefficient suggests a higher hydrophilicity. The higher permeability coefficient we obtained for ciprofloxacin is therefore also in line with the experimental and predicted partition coefficients of the two drugs.

Overall, our experiments demonstrated that our fluorescence-based assay can be effectively used for the measurement of fluoroquinolone permeability. In the next section, we will discuss the use of the platform with fluorescently labelled compounds.

4.5 Fluorescently Labelled Drug Molecules

4.5.1 Motivation

Aside from a few individual exceptions, the only other class of antibiotics aside from fluoroquinolones that expresses intrinsic fluorescence in the UV, is the tetracycline family [183]. In its current form, the setup can therefore only be used to obtain the permeabilities of these

two classes of antibiotic molecules. Although it should be noted that there are applications in other fields of drug discovery such as in chemotherapy where a number of compounds show intrinsic fluorescence [184]. Further, as we demonstrated in [153], permeabilities within the same group of antibiotics can span orders of magnitude, and hence this technique allows us to study the effect of specific functional groups on lipid permeability. For instance, we showed that a tertiary amine within a quinolone's piperazine group significantly enhances membrane permeability compared to secondary amines at the same position and were able to quantify this using the microfluidic assay [153].

One seemingly obvious possibility to expand the technique is by using fluorescent derivates of drug molecules, which have found much attention in biomedical research recently [183]. The limited number of fluorescent drugs that are available to date have been used successfully in numerous studies and helped us gain a deeper insight into various aspects of the drugs, such as their mode of action, localisation or biological targets [183–187].

However, a major concern when working with fluorescently tagged molecules is the influence of the fluorophore on target binding and membrane permeation. Recently, Stone *et al.* reported a procedure to fluorescently tag drug molecules using an azide-handle which links the drug molecule and the fluorophore. This handle is placed at a position that is believed not to inhibit the binding of the drug to the intracellular target, thereby maintaining the tagged-molecule's antimicrobial activity [188]. Stone *et al.* furthermore used 7-nitrobenz-2-oxa-1,3-diazol-4-yl (NBD) to tag the drug molecules. This fluorophore has a low molecular weight compared to other fluorescent tags commonly used and is therefore expected to influence the membrane and cytosol permeation of the drug in bacterial cells to a lesser extent [188].

Importantly for us, Stone *et al.* synthesised an NBD-tagged version of ciprofloxacin. Although the new fluorescent version required higher minimal inhibitory concentrations (MIC) than the native form of the drug, the developers concluded that it could be used for bacterial penetration and efflux studies [188]. The fluorescent version of ciprofloxacin provides the opportunity for us to directly compare the permeabilities of the native version of the drug to the fluorescent derivate. Using our assay, we should be able to characterise and quantify the influence of the fluorophore on drug permeability - knowledge of which is important for the interpretation of studies using fluorescently tagged antibiotics. The developers of the NBD-ciprofloxacin supplied us with a stock of the said drug, which we investigated with our microfluidic permeability assay.

4.5.2 Results and Discussion

We conducted the experiment following the same experimental procedure as we did for the native ciprofloxacin. The IA, OA and LO phases were identical to the experiments above. To obtain the drug solute, we diluted a NBD-ciprofloxacin stock (10 mM in DMSO) with IA buffer to a final concentration of 100 µM. Due to the stronger fluorescence of the NBD-tag compared to the native autofluorescence, we were able to work with lower drug concentrations compared to the 2 mM drug concentrations we used in the experiments above. The microfluidic device was operated on the same commercial epifluorescence microscope (Nikon TE 2000U) as the native ciprofloxacin measurements.

To our surprise, exposing the vesicles to the NBD-ciprofloxacin did not yield the typical images we observed in our assay using autofluorescence. Instead, we saw a bright ring appear around the vesicles, as shown in Figure 4.12. We have not seen such a fluorescent ring appear, using native fluoroquinolones, excited in the UV. The ring around the vesicle using NBD-ciprofloxacin is already formed at the first measurement position, immediately after exposure to the drug. We furthermore observed that if we flushed octanol droplets through the chip, the droplets increase drastically in fluorescence.

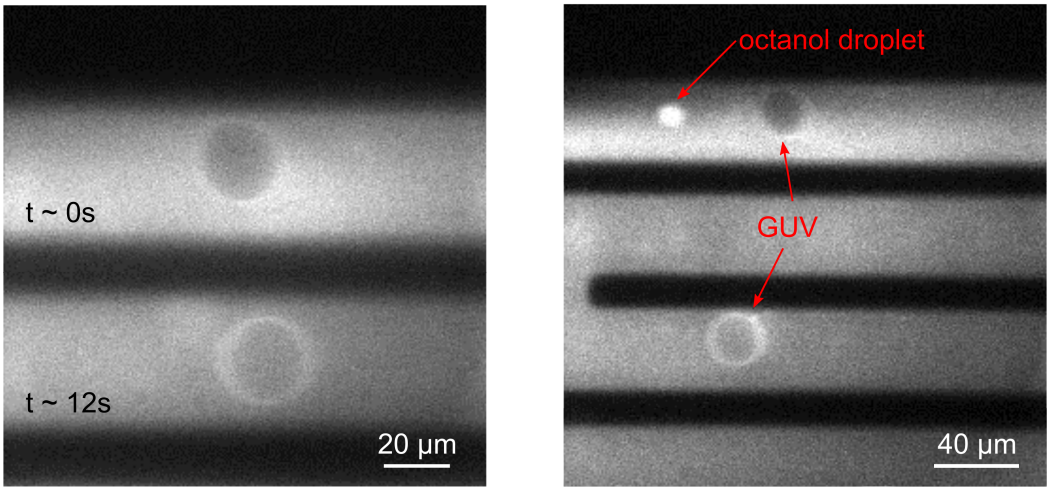

Fig. 4.12. PGPC vesicles exposed to NBD-ciprofloxacin. (A) Two vesicles in different parts of the channel. The vesicle in the upper ROI is recorded immediately after exposure to the drug. The GUV in the bottom ROI has been exposed to the drug for approximately 12 seconds. The fluorescence is induced by excitation at λ_{ex} = 460 nm. A fluorescent ring around the GUV starts to form as soon it is exposed to the drug. (B) Microfluidic chip at lower magnification. A bright octanol droplet as well as two GUVs are indicated by arrows.

These observations led us to believe that the fluorescence of the NBD-ciprofloxacin is dependent on the chemical environment and increases when it changes from an aqueous phase to an organic phase. To validate this, we measured the fluorescence of 50 µM NBD-ciprofloxacin samples in a fluorimeter (slit size 5 µm, Varian Eclipse), both in millipore water and in 1-octanol. The emission spectra of the two samples upon excitation at 460 nm and at 360 mm are shown in Figure 4.13A and 4.13B, respectively. We see that the fluorescence of NBD increases more than 12-fold when it is dissolved in an organic compound, compared to when it is dissolved in water. Indeed, this behaviour of NBD is known and has been investigated in the past. NBD is a so called solvatochromic dye. These fluorophores exhibit strong shifts in their emission spectra as a function of environment hydration and polarity [189], which explains our observation.

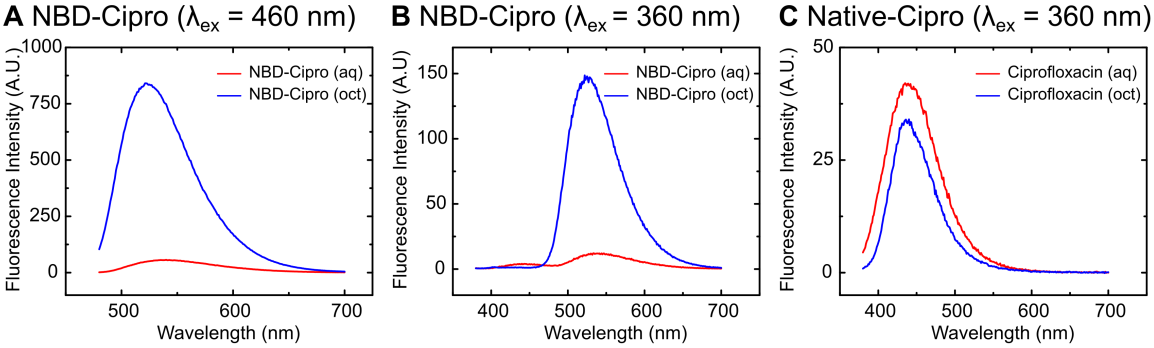

Fig. 4.13. Emission spectra of NBD-ciprofloxacin in different chemical environments and different excitation wavelengths. (A) Emission spectra upon excitation at 460 nm. NBD-ciprofloxacin yields a more than 12-fold higher fluorescence when it is dissolved in octanol compared to water. (B) Emission spectra of NBD-ciprofloxacin upon excitation in the UV. A similar 12-fold increase in fluorescence in the organic environment can be observed. A small peak stemming from the natural autofluorescence of the drug can be observed at 440 nm in an aqueous environment. (C) Native ciprofloxacin shows comparable emission spectra in the two solvents.

As we see in Figure 4.13B, the NBD-ciprofloxacin mainly emits at the fluorophore's emission wavelength at λ_{em} ~530 nm, even if it is excited in the UV. Furthermore, the drug also maintains the 12-fold increase in fluorescence when it is excited at this wavelength. Interestingly, we do observe a small emission peak at λ ~440 nm, the autofluorescence wavelength, in an aqueous environment for NBD-ciprofloxacin. However, it is not clear if this peak stems from the labelled drug, or remaining ciprofloxacin that did not conjugate to the dye.

We furthermore measured the fluorescence of native ciprofloxacin (100 µM, slit size 5 nm) in water and octanol, shown in Figure 4.13C. As we see, the native ciprofloxacin shows comparable fluorescence emission in the two solvents.

The fluorescent ring appearing around the vesicles made it impossible for us to analyse the obtained video data with the previously developed MATLAB routine. Our code is capable of automatically detecting GUVs that appear dark on a bright background, as shown in Figure 4.7. However, due to the bright ring around the vesicles, these were either not identified as GUVs at all, or detected with an incorrect radius. Instead, we therefore extracted the necessary parameters (GUV radius, speed and intensity values) of 38 vesicles manually from the videos using the imaging software ImageJ.

A scatter plot generated from the manually extracted data is shown in Figure 4.14A. The scatter plot has the same general appearance as the scatter plots for our measurements on unlabelled fluoroquinolones. Again, we obtain two bands of scatter points for the two measurement positions, and a linear dependence of ΔI on the radius R. However, we notice that the scatter points for ΔI_2 show values of around 0 or are even negative for small radii. Since we obtain ΔI from $\Delta I = \frac{I_{out} - I_{in}}{I_{out}}$, negative ΔI values appear when the vesicle fluorescence (I_{in}) is higher than that of the background (I_{out}). This is a result of the measurement technique and the strong contribution of the fluorescent ring. As we laid out in Section 4.3.4, we do not perform a confocal measurement in our setup. The I_{in} we obtain is the signal stemming from the fluorescent molecules along the optical axis, so the sum of the NBD-ciprofloxacin inside and outside of the GUV, as well as in the hydrocarbon layer of the membrane. Unlike in our previous measurements, the enhanced fluorescence of the NBD-ciprofloxacin in the hydrocarbon layer contributes substantially to the I_{in} value explaining the negative values.

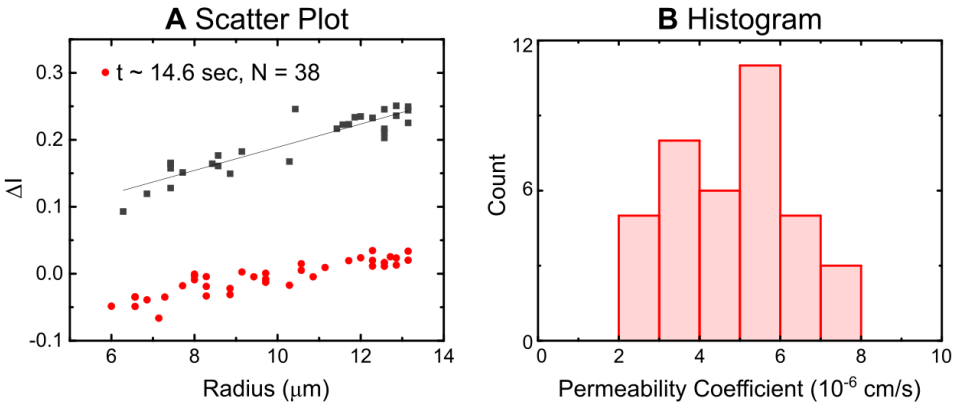

Fig. 4.14. (A) Scatter plot of NBD-ciprofloxacin experiment. The dark data points show the ΔI_1 measurements taken at the t_0 time point. The red points visualise ΔI_2 taken after the time given inset (B) Histogram of obtained permeability coefficients. The average (mean ± standard error) permeability coefficient of NBD-ciprofloxacin is $4.9 \pm 0.2 \times 10^{-6}$ cm/s.

We proceeded to calculate the permeability coefficient of the NBD-ciprofoxacin as before, using Equation 4.14. The histogram of the measued values is shown in Figure 4.14B. We obtained a mean ± standard error of 4.9 ± 0.2 $\times$ 10^{-6} cm/s and a median value of 5.0 $\times$ 10^{-6} cm/s. These values are very close to the ones we obtained for native ciprofloxacin. Given in Table 4.1, we obtained a mean ± standard error of 4.99 ± 0.07 $\times$ 10^{-6} cm/s and a median of 4.8 $\times$ 10^{-6} cm/s for the latter.

Table 4.1. Permeability coefficients of NBD-ciprofloxacin and native ciprofloxacin obtained with the permeability platform.

	NBD- Ciprofloxacin (N=38)	**Ciprofloxacin (N=960)**
Mean ± S.E.	4.9 ± 0.2 $\times$ 10^{-6} cm/s	4.99 ± 0.07 $\times$ 10^{-6} cm/s
Median	5.0 $\times$ 10^{-6} cm/s	4.8 $\times$ 10^{-6} cm/s

The close permeability values are a very promising result. They indicate that the NBD label does, in fact, not alter the transport properties to an extent that it drastically changes the permeability coefficient. A low influence of the NBD fluorophore on the transport properties is also claimed by the developpers of the NBD-ciprofloxacin [188]. However, the solvatochromic behaviour of the NBD label is a potential source of error that must be accounted for and further investigated. The permeability coefficient, was obtained under the assumption that the fluorescent ring is fully developed at the t_0 measurement position and does not change its intenstiy over time. If this assumption holds true, the change in vesicle intensity that we observe is indeed only due to the fluorescing drug that diffused across the membrane into the inside of the GUV. However, if the fluorescence of the membrane is not fully saturated at the t_0 time point, the increase in signal from the membrane adds to that of the diffusing drug leading to the overestimation of the fluorescent signal at the second measurement position. The elevated fluorescence at the second measurement position would in return lead to an overestimation of the permeability coefficient.

All in all, our experiments with the NBD-labelled ciprofloxacin show very promising, albeit preliminary results. The permeability coefficient we obtained with the tagged molecule is very close to what we measured for the native version. However, our experiments also revealed that in addition to potential effects of the fluorescent label on the transport properties, one also has to be concerned about the sensitivity of the fluorophore to environmental changes. More experiments are necessary to determine definitely whether or not the NBD label affects the transport properties of the drug. Potential next experiments should be performed using fluorescent tags that do not express solvatochromic behaviour in order to ensure that our measurement was not skewed by the fluorescence properties of the NBD-ciprofloxacin. A change in optical technique could further improve our understanding of the fluorescent label

on the transport. By introducing confocal detection, for instance, the fluorescence of a slice in the centre of the vesicle could be viewed without the effects of the fluorescent membrane.

4.6 Conclusion

In this chapter, we presented an integrated microfluidic platform for quantifying drug permeation across biomimetic membranes. We combined an on-chip liposome formation technique OLA with a downstream T-junction for the controlled exposure of liposomes to a drug solute. Norfloxacin and ciprofloxacin transport through biomimetic PGPC (1:3 ratio) liposomes was measured at physiological pH and salt concentrations. The measurements yielded permeability coefficients of $4.13 \pm 0.05 \times 10^{-6}$ cm/s (mean ± std. error of mean) with a median value of 3.57×10^{-6} cm/s for norfloxacin and $4.99 \pm 0.07 \times 10^{-6}$ cm/s (mean ± std. error of mean) and a median value of 4.8×10^{-6} cm/s for ciprofloxacin. These values are in good agreement with previous measurements by Purushothaman *et al.* who obtained a permeability coefficient of $4.3 \pm 0.2 \times 10^{-6}$ cm/s for norfloxacin in a similar lipid mixture [98, 153]. We produced PGPC (1:3) liposomes to mimic the anionic charge density typically associated with bacterial membranes [69, 177–179], and used this as a model system to quantify passive drug transport through the lipid bilayer component of the Gram-negative cell envelope.

Since our method directly quantifies the permeability coefficient of the drug across the specific membrane of interest, our technique offers an alternative to traditional drug transport assays such as octanol-partition coefficients, or the parallel artificial membrane permeability assay (PAMPA) which suffer from multiple drawbacks [164, 190]. Thanks to the microfluidic character of our method, we require only very small reagent volumes in the microliter range for our measurements [191]. Specifically, we only require approximately 70 µg of each fluoroquinoline drug for each run of the microfluidic chip. Another advantage of the integrated on-chip technique presented here over previously published optofluidic permeability assays lies in the benefits of controlling liposome formation with OLA. OLA allows the formation of large numbers of liposomes with physiological salt concentrations and with complex lipid mixtures. Other techniques such as electroformation suffer from very low yields in this environment [23], or in the case of other microfluidic techniques, require extensive procedures to remove oil remnants associated with the production [56]. Moreover, OLA allows for the efficient encapsulation of desired solutes inside the vesicles upon production [56, 69]. This makes it an interesting technique for biosensor-based approaches to detect drug molecules. The encapsulation approach has successfully been performed by Kuhn *et al.* to measure tetracycline transport across lipid bilayers [163]. However, their

experiments were performed using populations of small unilamellar vesicles (SUVs) of under 200 nm in radius, whereas we can work with GUVs and analyse drug transport on the single vesicle level. We will present such an encapsulation approach to measure membrane permeability in the next chapter.

We performed transport studies on an NBD-labelled derivative of ciprofloxacin and compared the permeability coefficient we obtained to that of the native version of the drug. We measured a permeability coefficient for NBD-ciprofloxacin (mean ± S.E.) of $4.9 \pm 0.2 \times 10^{-6}$ cm/s which lies within the error of the value we obtained previously for the unlabelled ciprofloxacin. However, we also found that our measurements were affected by the solvatochromic behaviour of the NBD-label. This dye increases its fluorescence drastically in the hydrocarbon phase of the bilayer, leading to the formation of a fluorescent ring around the vesicles. More studies are necessary to conclude wether or not these fluorescence properties skew the obtained permeability coefficients to higher numbers. For future permeability studies with labelled molecules, it is advisable to use other, environmentally non-sensitive, fluorophores. Furthermore, the introduction of a different imaging technique, such as confocal detection could provide better means to study the permeation of fluorescently labelled compounds.

The microfluidic platform presented here is not bound to a specific form of visualisation such as fluorescence. Since the optics and the microfluidics are decoupled from one another, the platform can be combined with different approaches of label-free drug visualisation, which is a field in its own right with various different methods published [192–195]. In Chapter 6, we will explore other forms to visualise solute molecules in order to study non-fluorescent molecules in the future.

While passive diffusion across lipids is an important element in bacterial drug uptake, it is known that porin-mediated uptake plays a crucial role in drug permeation across the outer membrane [20, 21]. Mutations of membrane proteins have furthermore been associated with antibiotic resistance [21, 196]. The incorporation of these protein channels into liposomal membranes is an attractive target for the study of drug uptake [20]. However, to integrate this with on-chip liposome formation requires the development of on-chip protein reconstitution techniques, which are still pending. The successful insertion of the pore forming toxin α-hemolysin into the membrane of OLA generated liposomes [56] suggests that the microfluidic platform can be extended to form and study more complex lipid compositions and even proteoliposomes on chip, potentially offering an alternative to current reconstitution techniques [197].

Chapter 5

Towards Ion Transport through DNA Nanopores [1]

5.1 Motivation

After quantifying the transport of small antibiotic molecules across lipid membranes in the previous chapter, we will turn to a different kind of membrane transport in the following sections. In the work presented below, we will use microfluidic tools to investigate the transport of ions, specifically, if novel DNA nanostructures are capable of forming channels for hydrogen ions (protons) to cross the membrane.

As we discussed before, lipid membranes are generally considered to be impermeable to charged molecules and ions [4]. We provided an illustration of this in the previous chapter, when we showed that norfloxacin molecules cannot penetrate the membrane in their charged form. In nature, charged molecules and ions cross biomembranes either via facilitated diffusion or active transporters. Salts typically cross the membrane via bilayer spanning proteins called ion channels [4, 21, 15]. Cells use these transporter proteins to regulate the flux of ions into and out of the cell and maintain their salt homeostasis [4]. The precise balance of salts is crucial for the survival of the cell and is highly regulated. The malfunction of these processes can give rise to a number of diseases, which are called channelopathies [19, 198]. One example of a well-known channelopathy is cystic fibrosis (CF). Patients with this disease suffer from an abnormal production of mucus, which leads to further complications in other

[1] Elements of this chapter have previously been published in Al Nahas et al., *Lab Chip*, 2019, 19, 837-844 [69]

organs, typically the lung and the pancreas [199]. However, it has been shown that the underlying cause of CF is the mutation of a regulator gene, leading to an altered expression of epithelial chloride channels [199, 200]. In other diseases, different ion channels are affected. Patients of Dravet's syndrome, for instance, carry a mutation that leads to the development of dysfunctional sodium channels [201]. This disease manifests itself via severe epilepsy and seizures [202]. For many channelophaties there exists no cure to date [203]. Ion channels for salts like sodium or chloride are therefore an interesting field of study with important medical implications.

Ion channels do not only exist for physiological salts like sodium, potassium or chloride, but also for protons. Postulated in 1972, proton channels were found in 1982 by voltage-clamp measurements on snail neurons [204–206]. However they are also present in the human body [204, 207]. The role of proton channels has been a topic of intensive debate in the scientific literature. Based on the findings that proton channels are highly selective and regulated by pH gradients [208], DeCoursey *et al.* argue that their main functions are the modulation of the membrane potential, regulation of internal and external pH and osmotic balancing [209]. In the human body, malfunctions of proton channels are believed to be linked to neurological diseases and cancer [207].

However, channel proteins are not the only mechanism of facilitated diffusion for protons and other ions. Other ways for ions to cross the membrane include using ionophores. Ionophores are typically lipid soluble molecules that bind to the ion on one side of the bilayer, carry it across the bilayer and release it on the other side [210]. Ionophores that carry protons are termed protonophores. They can, for instance, effectively short circuit the proton pump mechanism in cells. One example of a protonophore is the small organic molecule indole [211]. It has been shown to stop bacterial cell division by dissipating the membrane potential [212]. The membrane dissipating property of protonophores makes them potential candidates for novel antimicrobial agents. In fact, some protonophores are being tested for the treatment of methicillin-resistant *Staphylococcus aureus* [213].

Other intensively studied channel proteins are proton pumps. These transmembrane proteins are active systems and regulate the proton flux across membranes against a chemical gradient, typically requiring an energy source like ATP to do so [4, 214]. An example for a proton pump is the H^+/K^+-ATPase system, which is found in cells of the inner stomach lining. This pump uses ATP to actively pumps cytoplasmic hydronium into the intestine, thereby lowering the pH of the stomach contents [214]. However, proton pumps can also generate ATP from existing proton gradients. A prominent example of this is found in the cell respiration process of eukaryotes. The mitochondria inside these cells contain a double membrane that separate

the mitochondria's inside, called the mitochondrial matrix, from the cytosol. Within the mitochondria, there exists a proton gradient between the mitochondrial matrix and the inner membrane. This proton gradient gives rise to a proton-motive force. The protons flowing back into the mitochondrial matrix drive the transmembrane protein ATP synthase which catalyses the generation of ATP [215, 216].

The examples we listed above show that electrochemical proton gradients across lipid membranes play an important role in biological systems. Furthermore, they exemplify that the modulation of ion gradients across the membrane has many potential applications, especially in the field of medicine. As a crucial element of natural cell membranes, ion channels are also of interest to other fields of science, such as synthetic biology. This field aims to (re)create biological systems via the synthesis or assembly of artificial or natural components [217].

One interesting approach that is used in synthetic biology for the *de novo* assembly of biological structures is DNA nanotechnology [218]. First conceptualised by Nadrian Seeman in the early 1980s, DNA nanotechnology enables the design and assembly of nanoscale structures using DNA as building material [219]. Several techniques are summarised under the term DNA nanotechnology and almost all of them make use of the strict Watson-Crick base pairing rules of DNA to assemble the structures [220]. The structure of DNA and the base pairing rules are depicted in Figure 5.1A. The backbone of the DNA molecule consists of two single strands which are connected by pairs of nucleotide bases to form a double helix [220]. The four nucleotide bases are adenine, thymine, guanine and cytosine. Importantly, adenine binds to thymine and guanine to cytosine. Two single strands of DNA hence need to possess complementary base sequences to bind together [4]. A prominent technique that exploits this property of DNA for the construction of arbitrary shapes is called DNA origami [221]. Schematically shown in Figure 5.1B, DNA origami uses short single DNA strands, called "staple" strands, to fold a long single DNA strand, called a "scaffold" strand, into the desired structure [221, 222].

DNA origami structures in solid state nanopores have been presented by Bell *et al.* in 2012 [223]. Shortly after, Langecker *et al.* successfully inserted a DNA origami nanopore into a lipid bilayer and showed that it can act as a membrane channel [224]. In the following years, bilayer-spanning DNA pores have been presented by several other groups [225, 226]. In 2015, Göpfrich *et al.* introduced a DNA structure with dimensions comparable to those of naturally occurring ion channels [227]. The nanopore used by Langecker *et al.* was assembled via DNA origami and required a kilobase long scaffold and ≈200 staple strands [224]. In contrast to that, the DNA pore by Göpfrich *et al.* was a so called non-scaffolded DNA

structure, where the scaffold strand is omitted and the short single DNA strands bind directly to each other to form the nanopore. The advantage of non-scaffolded structures is a greatly simplified assembly process compared to classical DNA origami. In our studies below, we used a modification of the non-scaffolded DNA pore [227], which was presented by Ohmann *et al.* in 2018 [121].

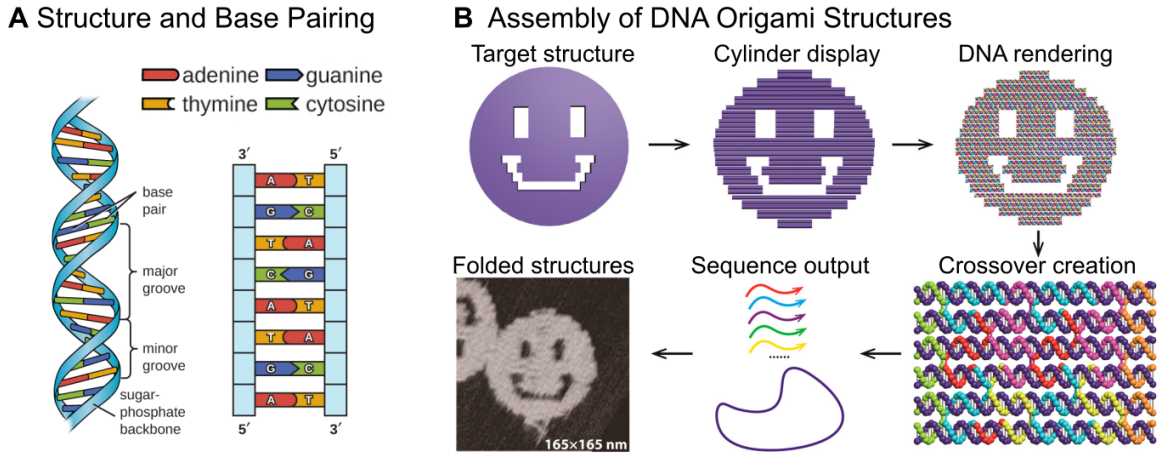

Fig. 5.1. (A) Structure of the DNA molecule. Two single strands of a phosphate-sugar backbone are connected via nucleotide base pairs. The base pairing follows strict rules with adenine only pairing with thymine and guanine binding to cytosine. (B) A target structure like a smiley face can be assembled via DNA origami. The technique makes use of the strict base pairing rules according to which two single DNA strands bind together if they possess complementary base sequences. Short single DNA strands called staple strands can therefore be used to fold a long single DNA strand called a scaffold strand into the desired shape. Images adapted from [9] and [222].

In the following sections we will explore proton transport into GUVs using DNA nanopores as channels. Before we discuss our own experiments, we will first briefly present the DNA nanostructure that we use in our experiments, followed by the introduction of a new microfluidic perfusion platform which we use to carry out our measurements.

5.2 DNA Nanostructures

5.2.1 Nanopore Design

The nanopore we use for the experiments is a non-scaffolded DNA structure designed by A. Ohmann [228]. The pore consists of eight single DNA strands which assemble into four interconnected DNA duplexes. Similar to the square packing of four cylinders, the DNA duplexes have an opening at the centre point of the structure, as seen in Figure 5.2A. The entire structure has a length of approximately 13.1 nm and a width of 5 nm. The hole in the middle of the structure is approximately 0.8 nm in diameter [228]. The DNA structure can furthermore be functionalised with up to two fluorescent labels as well as up to two cholesterol anchors. The cholesterol anchors are consciously placed in the middle section of the DNA structure so that the pore effectively spans the entire bilayer if both cholesterol anchors are inserted in the membrane [228]. The strand layout is depicted in Figure 5.2B. The DNA sequence of the individual strands is given in Appendix C1. A schematic of the bilayer inserted DNA pore can be seen in Figure 5.2C. Both cholesterol tags are necessary for the DNA pore to effectively insert into the membrane. DNA structures with only one cholesterol tag merely attach to the membrane but do not orient themselves in such a way that they span through the bilayer [228]. DNA pores without any cholesterol anchors neither insert into, nor attach onto the lipid membrane [229].

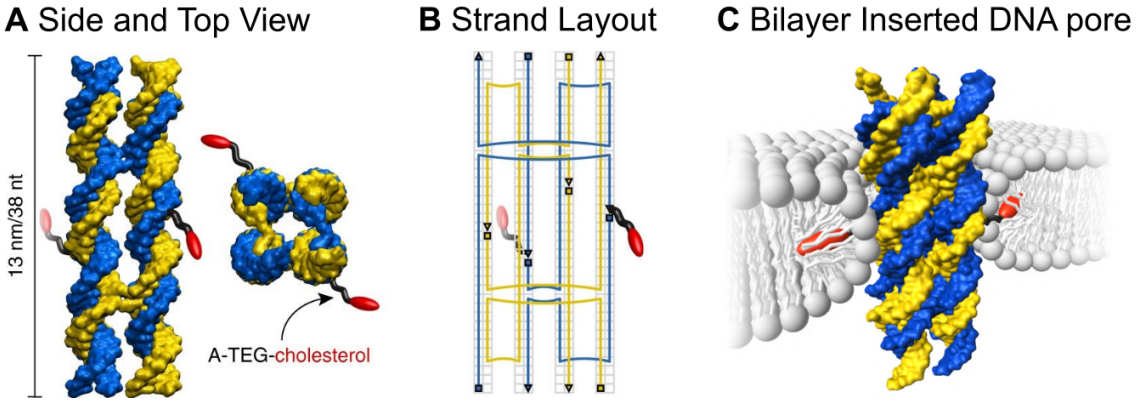

Fig. 5.2. (A) Side and top view of the DNA structure. The structure is made up of four double helix bundles linked together. The height of the structure is approximately 13 nm. It features two cholesterol anchors shown in red. Similar to four cylinders in a square packing, the structure has an opening in the middle spanning approximately 0.8 nm. (B) Layout of the strand design. The pore is made up of eight single DNA strands which bind together to form the structure. (C) Proposed position of the DNA pore inserted into a lipid bilayer. Image adapted from [121] and [228].

The pore design, depicted in Figure 5.2, has shown to promote lipid flipping between the two leaflets, when inserted into a bilayer [121]. Furthermore, it has been used to investigate the aggregation of cholesterol-tagged DNA structures [230]. Most importantly though, electrophysiological measurements with the DNA pore inserted into a lipid bilayer have successfully shown ion translocation through the pore [228].

5.2.2 Electrophysiological Measurements

The electrophysiological measurements on the DNA pores have been performed by A. Ohmann [228] using black lipid membranes (BLM), a technique which found widespread use in the investigation of ion channels and other transmembrane proteins [160]. The experimental setup for the black lipid membranes (BLM) is schematically depicted in Figure 5.3A. Two aqueous reservoirs are separated by a small aperture, which is covered by a lipid bilayer [160, 231]. The size of the aperture can range from several microns to millimetres [160]. Other methods such as pipette aspiration work in a similar fashion, however, here a bilayer is formed at the tip of a micro or nano pipette [231]. A voltage is applied across the bilayer via two electrodes that are immersed in the liquid reservoirs and the resulting current trace recorded. After the DNA structures are applied to one side of the aperture, the insertion of these structure into the bilayer, as seen in Figure 5.3B, leads to a distinct jump in ion conductance [232]. Interestingly, the current traces of the DNA pores also express short, discrete drops in conductance, resembling the gating of naturally occurring ion channels [4]. Göpfrich *et al.* explain this behaviour with the flipping of the DNA pore from a complete spanning of the bilayer to a mere attachment of the pore to the membrane. While the pore spans the entire bilayer, ions can be conducted through the membrane, whereas the conductance drops once the DNA pore is no longer in this configuration [227]. An example current trace showing both the insertion of the DNA structure into the membrane, as well as the gating-like behaviour of the pore is shown in Figure 5.3C.

In the experiments below, we want to use microfluidically assembled GUVs and fluorescent ion tracers instead of electrophysiological methods to show the translocation of ions through the nanopore. While we do not apply a constant electric potential in these experiments, we should be aware of the fact that electric fields are still present in this system. Concentration differences of ions between the inside and outside of the membrane give rise to electrochemical gradients and therefore an electric potential [4]. Nevertheless, the optical detection of ion transport into GUVs is a different approach to previous methods and can therefore provide further evidence for the function of DNA nanopores.

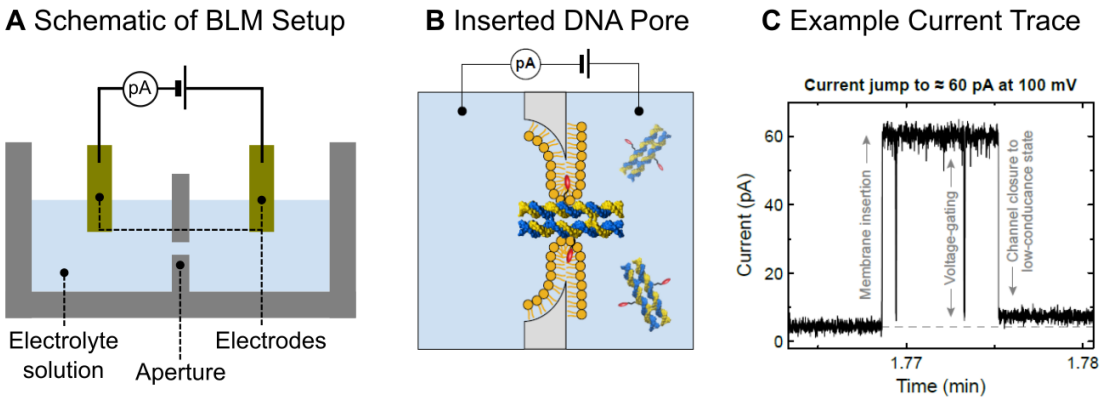

Fig. 5.3. Electrophysiological experiments conducted on a DNA nanopores. (A) Schematic of Black Lipid Membrane (BLM) experimental setup. Two aqueous reservoirs are separated by an aperture, which is sealed by a lipid bilayer. A voltage is applied via two electrodes immersed in the aqueous reservoirs and the resulting current recorded. (B) Schematic of aperture with DNA pore inserted into the lipid bilayer. (C) Example current trace showing a discrete jump in current as the DNA pore inserts into the membrane, and a drop, as the DNA pore returns to a low-conducting state. Short drops in conductance resemble gating as also observed in natural ion channels [4]. It is believed that the conducting behaviour is linked to the arrangement of the DNA pore in the membrane and the high conducting state reached when the pore is configured such that it fully spans the bilayer. Images (B) and (C) adapted from [228].

5.3 Microfluidic Perfusion Assay

5.3.1 The Need for a Different Microfluidic Assay

As discussed above, the DNA pore has been successfully used for a number of experimental studies, including electrophysiology [228] and scramblase experiments on lipid vesicles [121]. A result of these experiments was the observation that the DNA pores suffer from low insertion efficiency in GUV membranes. This behaviour has also been observed by other groups working with DNA origami pores [233]. For instance, Langecker *et al.* report that voltage pulses were necessary for pore insertion in their electrophysiology experiments [224]. The high activation barrier likely stems from the significant rearrangement of the lipid bilayer that is necessary to insert the negatively charged pore in it [233]. Established protocols to insert the DNA pores in GUVs therefore require incubation periods of 1 hour or more [121, 228].

Attempts to use the permeability platform from Chapter 4 in conjunction with DNA pores to study sodium transport were trialled by K. Jahnke [229]. In his experiments, K. Jahnke encapsulated DNA pores inside OLA GUVs and mixed them with a sodium solution at the T-junction. Visualisation of the sodium occurred via a fluorescent sodium indicator [234]. However, he was ultimately not able to observe transport of the ions into the GUVs. He attributed this to the short period of time that the vesicles were incubated with the DNA pores. After production, the vesicles in the permeability platform typically reach the T-junction in less than 5 minutes, much shorter than the incubation times used by Ohmann *et al.* in their successful experiments [121]. Furthermore, his experiments were impeded by the low fluorescence signal and photo bleaching of the sodium indicator [229].

The investigation of the ion transport through DNA nanopores therefore requires a platform that allows us to incubate the GUVs with the nanostructures for time scales of hours. Another prerequisite is the use of very photo stable ion indicators, to avoid the issues of photo bleaching.

In 2019, Al Nahas *et al.* presented a microfluidic perfusion platform that allows the on-chip formation of GUVs with OLA and their subsequent immobilisation using vesicle traps. The trapped vesicles can be perfused with a substance of interest and observed over time scales of many hours. In their original publication, Al Nahas *et al.* perfused trapped GUVs for time scales of up to 10 hours which can even be extended if needed [69]. Furthermore, the microfluidic protocol uses the fluorescent dye HPTS. HPTS is not just a fluorescent pH indicator [235], it is also a dye known for its high photo stability. For instance, HPTS is the basis for several “super-photoacids” [236] that are used in ultrasensitive fluorescence spectroscopy.

The assay therefore fulfils the requirements we set to the experiments in respect to photo stability and incubation time of the vesicles. In the following section we will explain the principle of the perfusion assay, before we discuss how we will use the platform to test for proton transport through DNA nanopores.

5.3.2 Principle of the Perfusion Assay

Microfluidic Chip Design

The working principle of the chip is illustrated in Figure 5.4. The chip features a two level design. The OLA junction for vesicles production as well as the perfusion part, which features the vesicle traps, are located on the bottom layer. This bottom layer is drawn in blue

in Figure 5.4. In contrast to the design that we have used previously, the OLA part does not feed the GUVs directly into the perfusion part. Although the OLA junction and the perfusion part are both located on the bottom layer, they are not directly connected. Instead, the two are coupled via a second-level connector chip located on top of the first PDMS chip. The second-level connector is indicated in red in Figure 5.4.

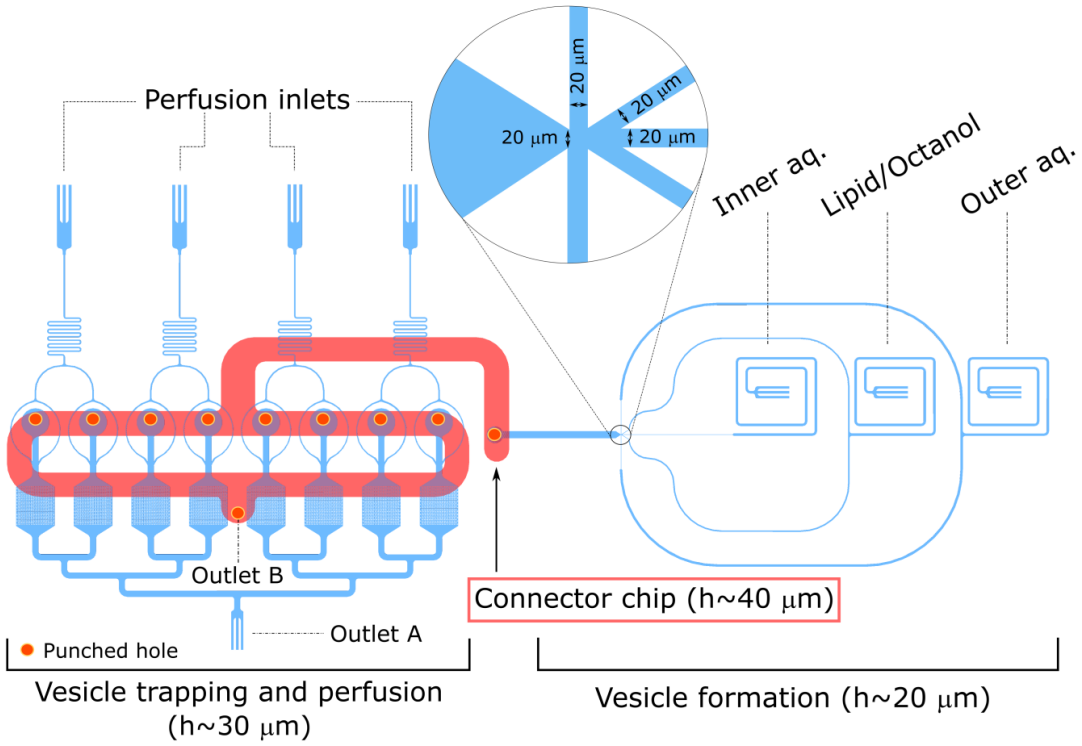

Fig. 5.4. Principle of the microfluidic perfusion platform. The microfluidic device has a two-level design. The bottom layer, drawn in blue, features the OLA design, as well as a perfusion design consisting of 8 chambers with 372 vesicle traps each. The OLA part and the trapping part are connected by a second-level connector chip, drawn in red. The chip is operated in a two-step process. The first step consists of the production and trapping of vesicles. The liposomes are produced at the OLA junction. From there, the vesicles travel upwards into the second-level connector chip via a vertical channel. From the connector chip, the vesicles enter the perfusion part of the chip, by applying suction via outlet A. The octanol droplets, which are present in the fluid stream as a by-product of liposome formation, remain in the connector chip due to their lower density compared to the water-filled GUVs. The octanol droplets leave the chip via outlet B, while the GUVs are immobilised in the vesicle traps located in the perfusion chambers. After a sufficient number of vesicles has been trapped, the GUVs are perfused with a substance of interest in a second step. For this, outlet B is blocked and the substance is flushed in via the perfusion inlets. The interaction with the immobilised vesicle can be observed in the trapping chamber. Image modified from [69].

Al Nahas *et al.* filled the perfusion chambers with a trap design that has previously been presented by Kazayama *et al.* [237]. A schematic of the trap design is shown in Figure 5.5A. The traps have a semicircle shape with a gap in the middle. The basket-like design allows for the effective immobilisation of the vesicle once it has entered the trap. The gap between the two trap components is necessary to allow sufficient liquid flow through the centre of the trap to let a vesicle move into a trap. The traps are optimised to capture vesicles of diameters 20-25 µm, which we can obtain with OLA. Figure 5.5B shows an image obtained from a fluorescence microscope featuring immobilised vesicles with the HPTS dye encapsulated inside the GUVs.

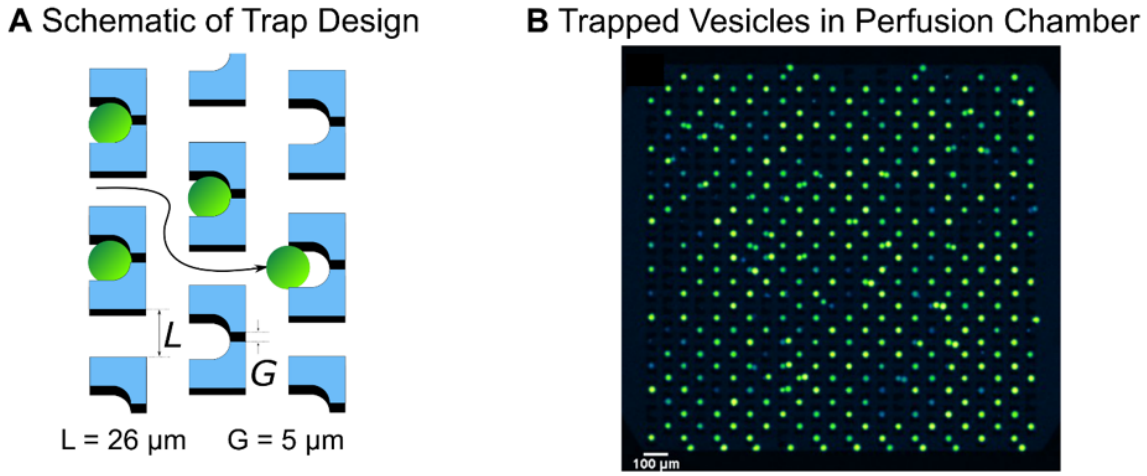

Fig. 5.5. (A) Schematic of trap design. The basket-shaped vesicle traps are designed such that vesicles of diameters ranging between 20 – 25 µm are immobilised in them. The spacing of the traps is approximately 26 µm, whereas the gap size between the two trap components measures approximately 5 µm. The values are optimised such that the vesicles cannot squeeze through the gap, but enough flow is present to allow vesicles to enter the trap. (B) Image of the perfusion chamber with immobilised GUVs in the traps. The fluorescent dye HPTS is encapsulated inside the vesicles (λ_{ex} = 488 nm). Images adapted from [69].

5.3.3 Chip Operation

The operation of the microfluidic device consists of two steps. In the first step, the vesicle traps are filled with GUVs. Vesicle production occurs in the OLA part of the microfluidic device. This happens in a similar fashion to that described in Chapter 3 using pressure driven Fluigent pumps. After production at the OLA junction, the vesicles flow downstream and enter a hole which was punched into the microfluidic chip at the end of the channel.

The punch serves as a vertical channel and allows the vesicles to flow upward into the connector chip. Among other functions, which are explained in more detail below, the connector chip serves as a reservoir for the GUVs. From the connector chip, the GUVs can enter the perfusion/trapping part of the microfluidic device. This part of the chip is likewise connected to the connector chip via punches serving as vertical channels for the GUVs. Suction is applied via outlet A using a flow-driven syringe pump (neMESYS, Cetoni GmbH). This forces the vesicles down into the perfusion part of the chip which is made up of 8 perfusion chambers containing 372 vesicle traps each. After a sufficient number of GUVs have been trapped (in our case we aimed for approximately 80% of the traps filled), the vesicle production is stopped and the syringe pump is disconnected from outlet A. This marks the beginning of the second step of the experimental protocol.

In the second step, the vesicles are flushed with a substance of interest via the perfusion inlets. However, before perfusion of the trapping chamber is started, the second-level outlet B is blocked. This is achieved by setting a microfluidic switch that is connected to this outlet to the "closed" mode. The switch system (2-Switch, Fluigent SA, France) has two states. In the "open" state, the switch allows a fluid stream to pass through unhindered. In the "closed" state, the switch effectively blocks all fluid streams. The blocking of outlet B ensures that the substance entering through the perfusion inlets in fact continues to flow into the trapping chambers and does not flow upwards into the connector chip towards that exit. The perfusion flows are again controlled using a pressure-driven Fluigent pump. There exist four different perfusion inlets. The channel of each perfusion inlet bifurcates and flushes two chambers and the trapped vesicles within them. Up to four different substances can hence be tested on the same batch of vesicles, by using a different solution in each individual perfusion inlet. After the perfusion has been initiated, the interaction between the solute and the immobilised vesicles can be observed in the trapping chambers [69].

Note that we used two versions of the microfluidic chip in the experiments below. They are identical in basic design and operation procedure. However, one design features 8 chambers with 372 vesicle traps each, whereas the second design features 8 chambers with 744 traps. In the first design, the flow from one perfusion inlet bifurcates and perfuses two trapping chambers, while each trapping chamber has a separate perfusion inlet in the second design. Schematics of both chip designs can be found in Appendix C.6.

5.3.4 Advantages of the Two-Level Design

As indicated above, the use of a second-level connector chip has several advantages associated with it. One of the advantages is its use as reservoir from which the vesicles are drawn to fill the traps. This eliminates the need to extract the liposomes off chip and reintroduce them into a different device [69]. The connector chip approach furthermore simplifies the device fabrication, as the OLA junction must be treated with PVA in order to enable GUV formation. However, Al Nahas *et al.* found that PVA treatment can render the traps dysfunctional, if coating materials such as PVA solidify between the trapping microstructures [69]. By separating the perfusion part and the OLA part and linking them together with a separate connector chip later, the PVA treatment of the OLA section can be performed without PVA entering the trapping and perfusion system. Lastly, the use of a second-layer connector chip is also an effective way to separate the GUV population from the octanol droplets, which are present in the fluid streams as a by-product of vesicle formation with OLA [56]. Schematically drawn in Figure 5.6, the microfluidic device uses the density-based approach for GUV purification, which we already discussed in the previous chapter. As we see in Figure 5.6, both GUVs and octanol droplets enter the connector chip after generation at the OLA junction. However, when suction is applied via outlet A, only the water-filled GUVs are driven down into the trapping chambers, whereas the low-density octanol droplets remain in the top-level connector chip and leave the chip via outlet B.

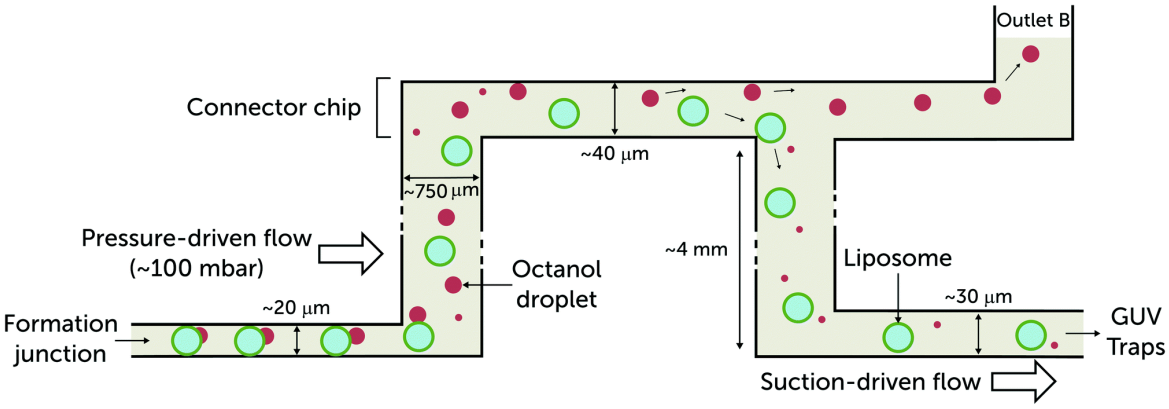

Fig. 5.6. Separation of GUVs and octanol droplets in second-level connector chip. GUVs as well as octanol droplets enter the connector chip via a 750 µm punch which serves as a vertical channel. By applying suction from the bottom-level outlet, the GUVs are pulled down into the chamber containing the vesicle traps, where the GUVs are immobilised. Due to the lower density of the octanol droplets compared to the water-filled GUVs, the droplets remain in the connector chip and flow towards a second outlet located on the connector chip. Image from [69].

5.3.5 Data Acquisition and Image Processing

The microfluidic chip is run on an epifluorescence microscope (Olympus IX 73) equipped with an EMCCD camera (Evolve 512, Photometrics), an LED light source (wLS LED, Q-Imaging) and a programmable piezo stage (ProScan III, Prior Scientific Instruments, UK). The chambers are imaged using a 10× objective (UPLFLN, Olympus). This setup allows for the systematic scanning of the perfusion chambers to observe the trapped vesicles using the microscope's epifluorescence capabilities.

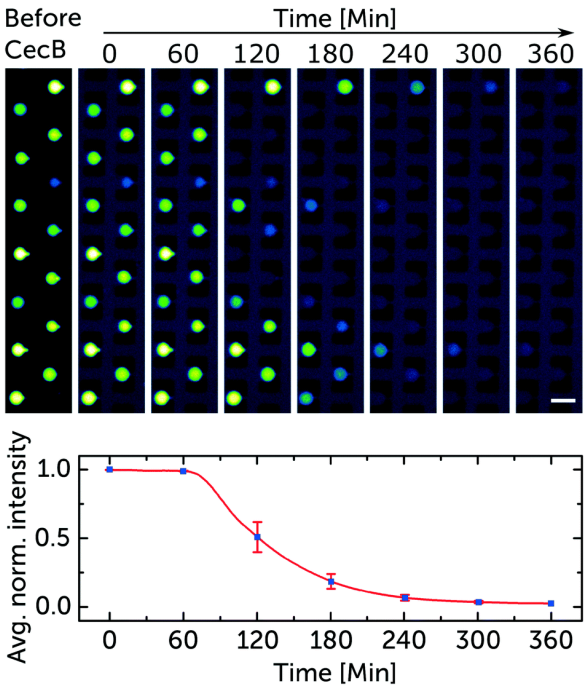

Fig. 5.7. Array of trapped vesicles, exemplifying the drop in fluorescence upon perfusion with a 5 µM solution of the pore forming peptide CecB. After approximately 60 minutes of exposure to the peptide, the dye begins to leak out from the vesicles, lowering their fluorescence intensity. The average normalised intensity of the trapped vesicles is drawn in the graph below. Scale bar 50 µm. Image from [69].

As stated before, Al Nahas *et al.* designed the platform for testing the efficacy of antimicrobial peptides. Pore forming peptides can be designed to specifically target bacterial membranes where they accumulate and lead to cell lysis [69]. The perfusion platform allows for the investigation of this behaviour of peptides. For this purpose, Al Nahas *et al.* encapsulate the fluorescent dye HPTS inside the vesicles upon production. When the peptides are flushed in via the perfusion inlets, they lead to the disintegration of the vesicle membrane causing leakage of the dye and ultimately bursting of the vesicle. An array of such trapped vesicles with the fluorescent dye inside can be seen in Figure 5.7. As the vesicles are perfused with

the peptide Cecropin B (CecB), they gradually lose their internal fluorescence. The drop in vesicle fluorescence that is associated with this process is recorded and analysed. The tracking of large numbers of vesicles in such a way provide a good metric to evaluate and compare the efficacy of antimicrobial peptides [69].

In the next section, we will discuss how we use the microfluidic perfusion assay to assess whether or not DNA nanopores can mediate proton transport across vesicle membranes.

5.4 Measurement of Proton Flux

5.4.1 Experimental Procedure

Upon production, we encapsulate the fluorescent and photo stable dye HPTS inside the vesicles. Using the perfusion platform, we fill the vesicle traps with the generated GUVs, as described above. The platform features four perfusion inlets, each of which flushes two trapping chambers. We can therefore perform both the DNA pore experiments and the control experiments on the same batch of vesicles. We perfuse half of the chambers with the DNA structure and flush the other half of the chambers with a buffer control void of the DNA pores. In a second perfusion step, we change the perfusion solute and expose the trapped vesicles to a solution of low pH. As we know, the pH is defined as the negative decadic logarithm of the proton concentration of a solution: $pH = -\log_{10}(c(H^+))$. Furthermore, we know that acids, with a low pH value, serve as proton donors [238]. We therefore obtain a concentration difference in protons between the vesicles outside, which is perfused by a low pH solution, and the vesicle's inside which encapsulates buffer of a higher pH. Proton flux across the membrane manifests itself via a pH shift inside the vesicles.

Under the assumption that the lipid bilayer provides an effective barrier for the protons, we only expect to see a shift in pH in the vesicles that have been incubated with the DNA pores, as the protons can use these as channels to cross the membrane. The control group would maintain the pH gradient or decrease at a much lower rate due to diminutive leakage of ions. As we will see later, protons represent a special case of ion movement across membranes and proton leakage plays a much larger role than we initially anticipated. However, for the design of the experiment we assumed that passive proton permeation through the bilayer is small compared to potential movement through DNA pores.

We make use of the properties of the HPTS dye which is encapsulated inside the GUVs to assess the flux of protons across the bilayer. This is possible because HPTS is a fluorescent pH indicator. A pH drop in a solution containing HPTS is associated with a decrease in fluorescence intensity [235, 239]. We confirmed this by measuring the fluorescence of a PBS buffer with 50 µM HPTS in a range from pH 5.9 to pH 7.4, shown in Figure 5.8. We can see that a drop of pH from 7.4 to 5.9 results in an approximately linear, 9-fold decrease in the fluorescence of HPTS. For the measurement, the pH of the buffer solution was adjusted by adding small amounts of hydrochloric acid (37%) to the solution and confirmed using a digital pH meter (Hanna Instruments, UK). The fluorescence signals were obtained using a fluorimeter (Eclipse, Varian; slit size 5 nm) and are the peak emission values (λ_{em} range 500–600 nm) upon excitation at λ_{em} = 488 nm.

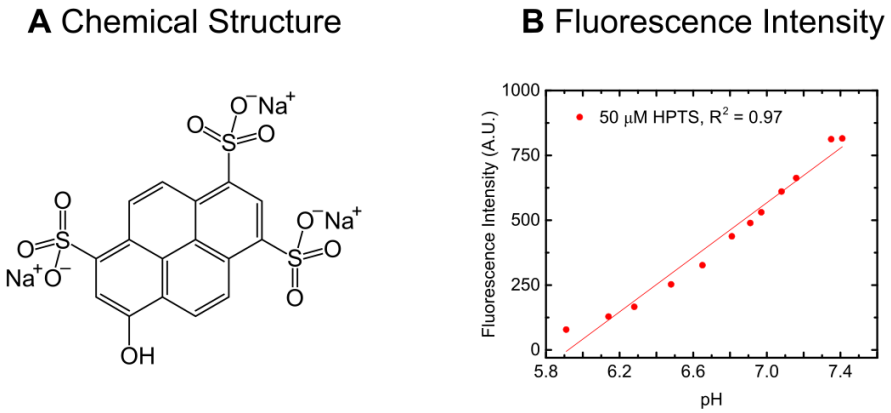

Fig. 5.8. (A) Chemical Structure of HPTS. (B) Fluorescence intensity curve for HPTS. The x-axis shows pH value of the solution, the y-axis the fluorescence intensity. The fluorescence of a 50 µM HPTS solution is highest for neutral pH and decreases for more acidic pH levels. At pH 5.9 the fluorescence intensity decreased to approximately 10% of the fluorescence at neutral levels (pH 7.4). The single data points are the peak emissions of individual measurements with λ_{ex} = 488 nm and an emission range from 500 – 650 nm.

This property of HPTS allows us to perform the proton transport experiments using the tools that were developed by Al Nahas *et al.* for the study of antimicrobial peptides. In the case of perfusion with peptides, a drop in fluorescence is the results of dye leakage due to peptide-induced membrane poration. In our experiments, we perfuse the vesicles with a low pH solution (pH 5.9) instead of peptides. A drop in fluorescence indicates a pH shift inside the vesicle as a result of proton flux.

5.4.2 Materials and Methods

Chip Fabrication and Preparation

The microfluidic chips were made of polydimethylsiloxane (PDMS) following the protocol presented in Sections 2.4.2 and 4.4.2. The silicon master chip was designed and fabricated by K. Al Nahas as previously described [69]. Note that we used two versions of the perfusion assay design, both of which can be found in Appendix section C.6. The two chip designs are identical in operating principle, but differ in the amount of vesicle traps per chamber. One design contains 372 vesicle traps per chamber, whereas the second design features enlarged perfusion chambers that hold 744 vesicle traps each. We performed one experiment on the version with the smaller perfusion chambers and two experiments using the chip with 744 vesicle traps.

The first level of the microfluidic chip was plasma bonded (100 W, 10 s exposure, 25 sccm, plasma oven from Diener Electric, Germany) onto a PDMS coated glass slide (76 mm × 39 mm and 1 mm thickness). The OLA junction of that chip was then PVA coated using a 5% PVA solution as described in section 2.4.2 using a Fluigent pump and baked in the oven at 120°C for 15 minutes. The connector chip was PVA coated by hand by spreading 10 µL of PVA (10 mg/mL) on the open channels using a pipette tip. The connector chip was then likewise baked in the oven for 1 hour at 60°C. After both, the first layer chip and connector chip have been PVA coated and cured in the oven, the connector chip is plasma bonded on top of the first layer such that it bridges the vertical channels from the OLA and the perfusion part.

Solution Composition

The DNA strands were sourced from Integrated DNA Technology (IDT) and assembled according to an established folding protocol [228] given in Appendix C.2. Folding occurred in TE20 buffer (10 mM Tris, pH 8.0, 0.1 mM EDTA) containing an additional 20 mM $MgCl_2$, which is necessary for the stability of the DNA structure. The folding process yielded a 1 µM stock of DNA structures which we diluted with the basic OLA stock solution to a final concentration of 50 nM. We validated the correct folding of the DNA structures prior to our experiments via gel electrophoresis. An example of this is given in Appendix Figure C.1.

We formed the GUVs using the same standard stock solution we also used in our drug transport experiments. The basic stock consisted of 200 mM sucrose and 15% v/v glycerol in PBS buffer (pH 7.4). The IA phase was made up of the base stock but contained an additional 50 µM HPTS dye. As before, the OA was made up of the base stock with 50 mg/mL P-188. The LO phase consisted of 4 mg/mL DOPC in 1-octanol.

The DNA perfusion solute was similarly made up of the base stock, but contained an additional 20 mM $MgCl_2$ and 50 nM of the DNA pores. The buffer control was identical to the DNA perfusion solute but contained 50 nM of the folding buffer without the DNA pores. Using the separate perfusion chambers, we always performed experiments on both the DNA pores and a buffer control on the same chip.

The low pH buffer to which we exposed the vesicles in the second perfusion step was similarly made up of the base stock with 20 mM $MgCl_2$. However, we lowered the pH of this solute to 5.9 by adding HCl (37%) to the solution. The pH of all solutions was checked and adjusted before every experiment using a digital pH meter (Hanna Instruments, UK). The low pH solution furthermore contained either 5 µM or 20 µM of HPTS as a fluorescent tracer. The slight background fluorescence marks the arrival of the low pH solution in the trapping chamber.

The exact solutions for all experiments are again listed in detail in Appendix C.4. All solutions were obtained from Sigma Aldrich, unless stated otherwise.

Pressure Control and Vesicle Perfusion

We formed and trapped GUVs using the perfusion assay as described in section 5.3.3. A detailed description of the experimental protocol including the necessary pressures and flow rates is given in Appendix section C.5.

The procedure for the two perfusion steps is depicted in Figure 5.9. In the first perfusion step, we flush the chambers with the DNA pore solution and a control solution, respectively. In the second perfusion step, we flush the chambers with a PBS solution that is adjusted to pH 5.9. Importantly, when we switch to the second perfusion step, we do not remove the tubing that is connected to the microfluidic device. Instead we exchange the vial carrying the fluid in the Fluiwell system. This allows us to change the perfusion liquid without unplugging the tubing from the microfluidic device. However, at this moment, the tubing that connects the fluid reservoir to the microfluidic chip is still filled with the DNA pore/buffer solution from the first perfusion step. The low pH solution does not arrive in the perfusion chamber until all the remaining DNA pore solution present in the tubing is pushed through the microfluidic chip.

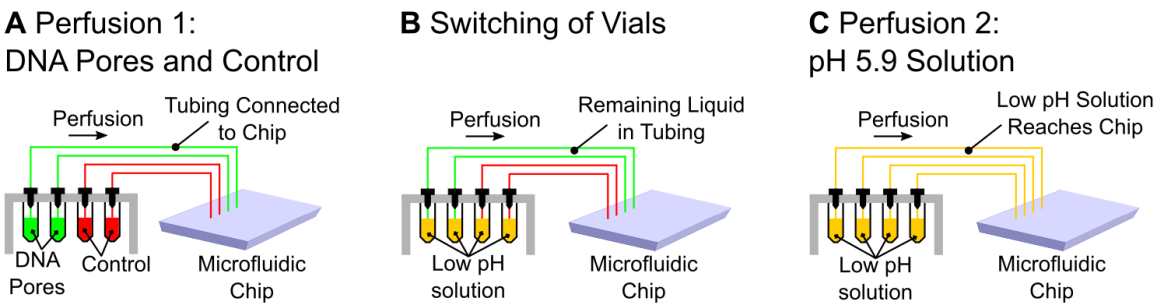

Fig. 5.9. Procedure of chip perfusion. (A) In the first perfusion step, we perfuse half of the chambers with the DNA pores and the other half with a buffer control solution. (B) The vials with the DNA/control are exchanged for vials containing the low pH solution. The tubing connecting the fluid reservoir to the chip is still filled with the initial DNA/control solutions which continues to be perfused through the chip. (C) The second perfusion step begins once all the remaining DNA/control solution has been flushed through and the low pH solution reaches the chambers with the immobilised vesicles. Since the low pH solution contains a small amount of fluorescence tracer, its arrival in the perfusion chambers is marked with a slight increase in background fluorescence.

We found the method shown in Figure 5.9 to be the only feasible way to change the perfusion liquid. Unplugging of the tubes causes movement of the liquid in the microfluidic chip and this perturbance is severe enough to flush out the vesicles from their traps. Furthermore, removal and reinsertion of tubing into the microfluidic chip can introduce air bubbles which disturb the flow patterns in the chip and can lead to heterogeneous perfusion of the chambers.

We always applied the same pressure for the first (DNA/buffer) and second (low pH) perfusion step. In total we conducted 3 experiments. Perfusion in the first two experiments occurred at 10 mbar and 8 mbar per chamber, respectively. The third experiment was perfused at 4 mbar. The effective perfusion times that resulted from these pressures are given in Table 5.1. We reduced the perfusion pressure with every experiment, as we observed that the higher perfusion rates caused the flushing out of vesicles from the traps, reducing the overall vesicle count. The small amount of HPTS that we added to the low pH solution allows us to determine the time point at which all remaining DNA solution from the tubing has been pushed through the chip and the low pH solution hits the vesicles. This moment is indicated by a slight increase of background fluorescence. After arrival of the low pH solution we observed the fluorescence of the vesicles in the individual chambers for another 400 minutes.

Note that within the individual experiments there are differences in the exact time point when the low pH solution arrives in the different chambers. The spread increases for the experiments with lower perfusion pressures. We observed the largest difference in Experiment 3, where the difference between the first and the last arrival of the low pH

solution was 100 minutes. The reason for the spread in arrival time is due to small differences in fluidic resistance in the different channels, which we attribute to variations in tubing length or the connection to the microfluidic chip. We tried to minimise this by using tubing with the same 5 cm length for all perfusion chambers. However, we cannot rule out the possibility of a partial blockage of one of the perfusion channels. Partial blockage would lead to an overall lower flow rate in the perfusion chamber that is fed by this particular channel. This might have been the case in one perfusion chamber in Experiment 3, leading to the late arrival time.

Table 5.1. Solution composition for confocal micrographs of OLA and electroformed vesicles.

Experiment	Perfusion 1 DNA pores/buffer control	Perfusion 2 pH 5.9 solution
Experiment 1	250 - 260 min	400 min
Experiment 2	240 - 300 min	400 min
Experiment 3	300 - 400 min	400 min

Data Acquisiton and Analysis

After switching the vials for the low pH solution, we started image acquisition. The microfluidic chip was operated on an epifluorescence microscope (Olympus IX 73) equipped with an EMCCD camera (Evolve 512, Photometrics), an LED light source (wLS LED, Q-Imaging) and a programmable piezo stage (ProScan III, Prior Scientific Instruments, UK). The chambers were imaged using a 10x objective (UPLFLN, Olympus). We programmed the piezo stage to systematically scan the perfusion chambers. Experiment 1 featured 40 recording positions; each position was recorded once every 30 seconds. Experiments 2 and 3, which were run on a device with larger perfusion chambers, featured 64 recording positions, each of which was recorded once every minute.

The intensity values of the individual vesicles were extracted using a python routine[2]. The basic algorithm is depicted in Figure 5.10. The script identifies the vesicles in the input video file and assigns unique labels to the individual vesicles. The intensity value of a 4×4 pixel box around the vesicle's centre is then averaged and extracted.

We smoothed the extracted intensity data with a Savitzky–Golay filter. Furthermore, we excluded vesicles that burst or escape the traps from the data. Burst or escaped vesicles manifest themselves via a sudden drop in fluorescence, rather than a steady decay. Finally,

[2]The python routine used for the data analysis was developed by M. Fletcher.

we excluded all vesicles in chambers that show an inhomogeneous background profile, which indicated unsteady perfusion with the low pH solution. An image of the desired background profile is shown in Figure 5.11 of the next section where we discuss the background signal in more detail.

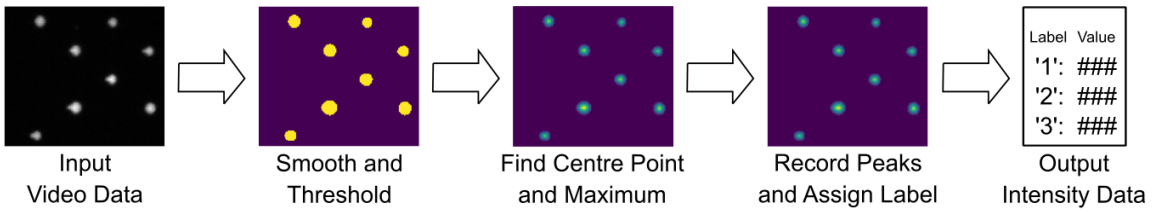

Fig. 5.10. Python routine to extract the vesicle intensity data. The video data is first smoothed and the vesicles are identified based on an intensity threshold. Subsequently, the location of the centre points and the maximum intensity values are used to assign a label to each individual vesicle. The intensity value of a 4x4 pixel box around the vesicle's centre is then averaged and extracted.

5.4.3 Results and Discussion

Overall, we conducted three experiments. Every experiment was run on an individual microfluidic device in which we perfused half of the chambers with the DNA pore solution and the other half with a buffer control. In Figure 5.11, we show typical intensity traces of two vesicles as well as of the background over the entire length of the experiment. Figure 5.11A shows the intensity and background curves of a vesicle incubated with the DNA pore, while Figure 5.11B shows the curves of a vesicle which was perfused with the buffer control.

The left curve in Figure 5.11A shows the intensity trace of the background signal over the entire length of the experiment. This curve provides us with information on the perfusion state and the pH environment in the chamber. In the first 400 minutes, the intensity signal is low while the trapping chamber is being perfused with the DNA pore solution which does not contain any fluorescent HPTS tracer. After 400 minutes, the low pH solution containing 5 µM HPTS as fluorescent tracer arrives in the chamber. At this time point, we observe an increase in background fluorescence. Interestingly, the intensity curve does not have a sigmoidal shape which Al Nahas *et al.* observed when the chamber was homogeneously filled with the solution [69], but a peak that drops off again and equilibrates at a value that lies between the maximum fluorescence and the baseline when no fluorescent tracer was present. We believe that our chambers are also homogeneously filled, and the distinct shape of the background fluorescence results from the pH dependent fluorescence of the HPTS

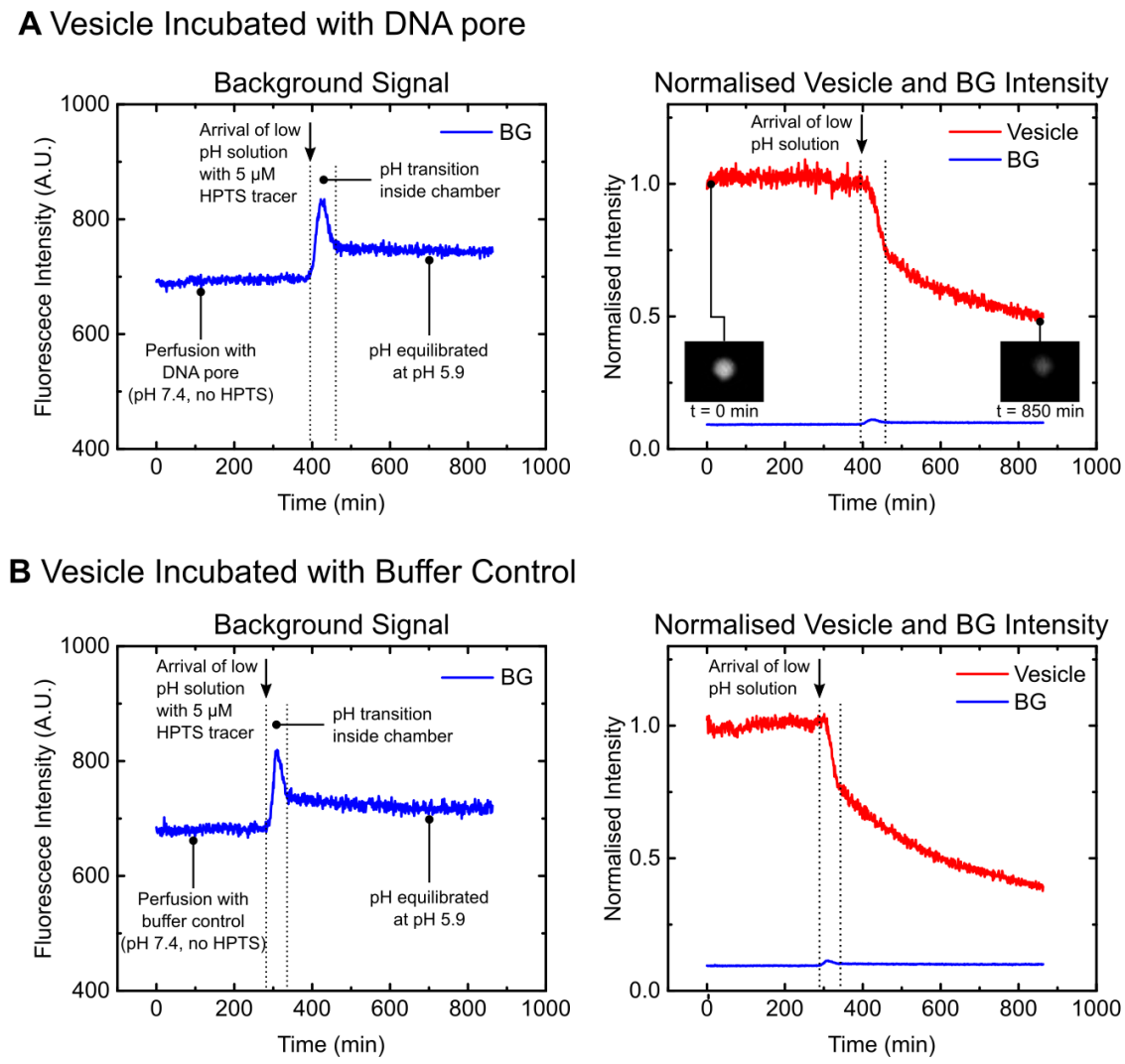

Fig. 5.11. Example intensity traces of vesicles and background. (A) Fluorescent traces from a chamber perfused with the DNA pore. The left curve shows the background signal in the perfusion chamber. The background goes through three individual phases. During the perfusion with the DNA pore or the buffer control, the BG signal is low, as no HPTS is present in the background. After about 400 minutes, the low pH solution arrives in the perfusion chamber, indicated by a spike in fluorescence signal. The pH inside the chamber goes through a transition phase. The fluorescence initially overshoots, as the pH adjusts, since HPTS shows stronger fluorescence at neutral pH values. In the third phase, the background remains steady, indicating a constant pH in the chamber. The right graph shows the intensity of a GUV overlaid with the background. Both intensities are normalised to the fluorescence of the vesicle before low pH arrival. During the perfusion of the chamber with the DNA pores, the fluorescent signal is constant. As the low pH solution arrives in the chamber, the inside fluorescence begins to decrease. The pH transition period coincides with a steep decline in fluorescence intensity, which tapers off after the pH in the chamber has fully adjusted. (B) Example traces from chamber perfused with buffer control. The background and the vesicle intensity go through similar phases as the vesicle that was perfused with the DNA pore. The low pH solution arrives earlier in this chamber, after roughly 300 minutes.

tracer. We observe the mixing of the low pH solution (pH 5.9) with the solution present in the perfusion chamber (pH 7.4). The pH in the perfusion chamber undergoes a transition which we can observe because the fluorescence of the HPTS tracer is higher at neutral pH than at acidic levels. Once the pH shift in the chamber to a value of pH 5.9 is complete, the background stays steady at one fluorescence level. The pH transition times necessary for the adjustment of the lie between 20 and 40 minutes in the different experiments. These time scales are typical for the perfusion assay and similar to the times that Al Nahas *et al.* require for the filling of the perfusion chambers in their experiments on antimicrobial peptides [69].

The right-hand side graph in Figure 5.11A shows the same background signal overlaid with the intensity trace of a vesicle in the chamber. We see that the fluorescence intensity of the GUV remains constant during the perfusion with the DNA pore and then expresses a two-stage decay in fluorescence with a steep, initial decay which then suddenly tapers off. The dashed lines indicate the two critical time points we identified before: the arrival of the low pH solution and the complete shift of pH in the perfusion chamber. The decrease in vesicle fluorescence begins with the arrival of the low pH solution, while the shift from the fast fluorescence decay to the slower decay matches the time point of pH equilibration in the outside chamber.

In Figure 5.11B, we look at the signal for a vesicle that has been perfused with a buffer control. From the background signal, we can again identify the two critical time points. The arrival of the low pH solution occurs after 300 minutes of perfusion with buffer. Approximately 30 minutes later, the pH in the perfusion chamber has adjusted to a pH 5.9 level. Surprisingly, the intensity trace of the vesicle that has been perfused with the control looks similar to the vesicle that has been perfused with the DNA pore. Again, we observe a steep, initial decay in fluorescence, which coincides with the pH transition in the chamber, followed by a steady decrease at a lower rate, once the pH in the chamber has adjusted.

In order to compare the intensity traces of the entire set of trapped vesicles, we created heatmaps which display the behaviour of all vesicles that were perfused with the same substance (DNA pore/buffer) in a single experiment. In the heatmaps, shown in Figure 5.12, every horizontal line originating from the y-axis shows the normalised intensity of the encapsulated HPTS in an individual vesicle. The intensity values are colour coded with the maximum value displayed in red and a complete loss of fluorescence shown in blue. The intensity traces are sorted by the time point the fluorescence decreases below 50% of the initial intensity. The x-axis denotes the time of exposure to the low pH solution. Note that the t_0 time point of the heat maps is set to the arrival of the low pH solution which is identified by the python code. We do not depict the perfusion step with the DNA pores/buffer control in the heatmaps.

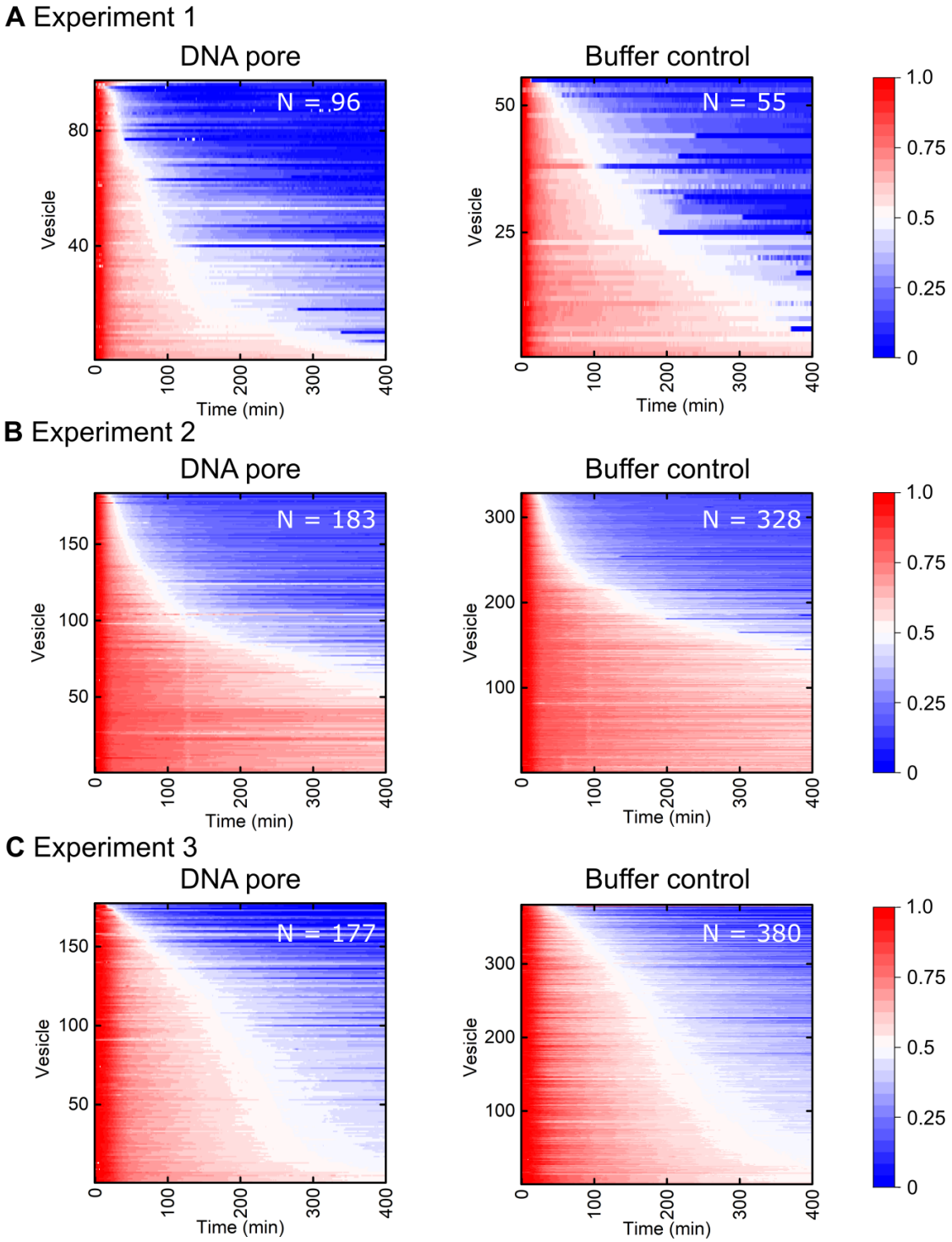

Fig. 5.12. Heatmaps of the perfusion experiments. The time of exposure to the low pH solution is given on the x-axis, the individual vesicle on the y-axis. Every horizontal line depicts the intensity decay curve of a single vesicle. The normalised vesicle intensities are colour coded with the maximum intensity depicted in bright red and a complete loss of fluorescence in dark blue. The vesicles are sorted by the time point at which the intensity drops to 50% of the initial value. Subfigure A, B and C show the results of experiments 1, 2 and 3, respectively. The respective number of vesicles is given inset.

The same fluorescence data as for the heatmaps is used in Figure 5.13. However, here we do not show the data of the individual vesicles, but a mean ± std. dev of all the vesicles in a single experiment over time. In each of the plots, the average intensity of the vesicles that were incubated with the DNA pore is shown in red and the buffer control is shown in blue. The decay traces give us a more quantitative view of what is shown in the heatmaps.

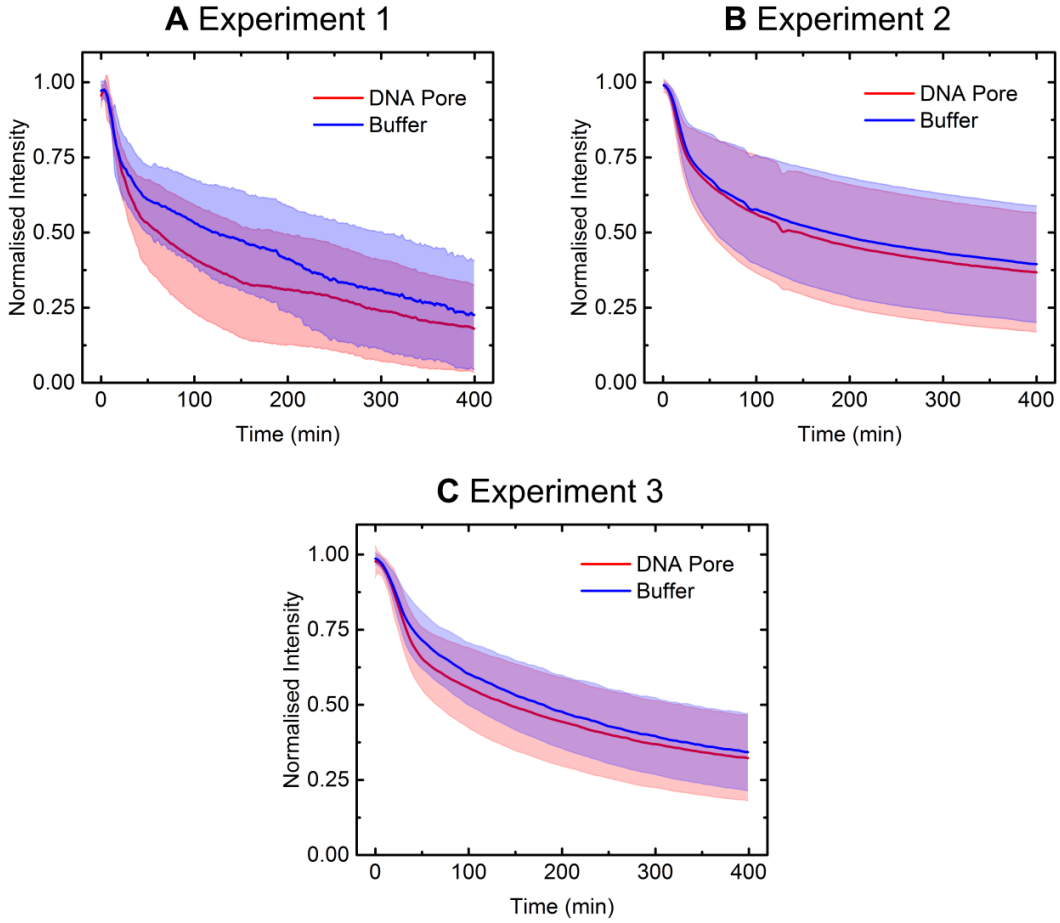

Fig. 5.13. Fluorescence decay curves of the different experiments. The solid line displays the mean intensity of all vesicles in the respective experiments. The shadowed region indicates the standard deviation. The vesicles incubated with the DNA pores are shown in red, the buffer control group is shown in blue. All experiments show a rapid increase in fluorescence to about 75% of the initial fluorescence in the first 30 minutes. After the initial, quick decay, the decrease continues for both sets of vesicles, albeit at a slower rate. Overall the vesicles incubated with the DNA pore show a slightly faster decay than the control group, however, this behaviour is most substantial in the first experiment.

Looking at the heatmaps of Experiment 1 in Figure 5.12A, we see an immediate shift from dark red to bright red within the first few minutes of the experiment in both vesicle populations. This decrease represents the initial drop in vesicle intensity during the pH transition period in the chamber. Initially, the decrease in both groups occurs in almost the same time period. From Figure 5.13A, we can see that a drop to 75% of the initial intensity occurs within 19 minutes in the pore-incubated vesicles and 20 minutes for the control group. After this time span, the intensity traces of the two vesicle populations noticeably diverge. After 50 minutes of exposure to the low pH solution, the vesicles with the DNA pores show an average fluorescence intensity of 53% ± 14% of the initial value, compared to 61% ± 11% of the control. This divergence can also be seen in the heat map, as we see a substantially faster shift from red to blue in the DNA vesicles than in the control. After the initial fast decrease in fluorescence, both groups steadily decay in fluorescence until the end of the experiment, albeit not at a rate as high as in the first 50 minutes of the experiment.

In Experiments 2 and 3 we similarly see the fast, initial decay for both the vesicles incubated with the pore and the control group. In Experiment 2, the drop to 75% of the initial fluorescence occurs within 26 minutes for the pore-incubated vesicles and 29 minutes for the control. In Experiment 3 these numbers are 33 minutes and 40 minutes, respectively. As in Experiment 1, the fast decay in Experiment 3 continues for the DNA-incubated vesicles, while it tapers off for the control group. Figure 5.13C shows us that after 50 minutes, the mean fluorescence (mean ± std. dev.) in the DNA incubated vesicle dropped to 65% ± 10% of the initial value, compared to 71% ± 11% in the control. Interestingly, we do not see such a pronounced divergence of the decay traces in Experiment 2, although the overall fluorescence decay is larger for the vesicles that were incubated with DNA pores here as well.

Overall, the total mean intensity decay in Experiments 2 and 3 is not as strong as in Experiment 1. The overall fluorescence (mean ± std. dev.) in the latter drops to 18% ± 16% and 23% ± 18% for the pore-incubated and control group, respectively. The DNA-incubated and control vesicles in Experiment 2 decay to a value of 37% ± 20% and 40% ± 19% after 400 minutes, respectively. These values are 32% ± 14% and 34 ± 13% for the DNA and control vesicles in Experiment 3.

The number of vesicles we were able to trap and observe throughout the entire length of the experiment differed between the technical repeats. In Experiment 1, we were able to trap 96 vesicles that were incubated with the DNA pore and 55 vesicles for the buffer control. In Experiments 2 these numbers were 183 for the DNA pore and 328 for the control, as well as 177 and 380, respectively for Experiment 3. The lower number of vesicles in Experiment 1

is due to the reason that we used the chip design with fewer vesicle traps compared to the chip in Experiments 2 and 3. In addition, not all vesicle traps were filled when we switched to the perfusion step and some vesicles escaped from the traps or burst, which we also excluded. Furthermore, we disregarded all vesicles in perfusion chambers that did not show a homogeneous background signal, as shown in Figure 5.11, reducing the overall number of vesicles again.

The fact that the initial drop in vesicle fluorescence coincides with the transition period that we identified in the background signal suggests that the intravesicular pH drops alongside the pH in the chamber. There is no substantial time delay between the arrival of the low pH solution and the drop in vesicle fluorescence, as we see in Figure 5.11. The protons seem to flow across the membrane and change the intravesicular pH as they arrive in the perfusion chamber. This is despite the fact that PBS buffer is encapsulated inside the GUVs, which should slow down a shift in pH due to its buffering capacity. The fast shift in pH suggests a low permeability barrier of the membrane to protons. We expected such a behaviour for the vesicles that were incubated with the DNA pore, since the protons can use these as channels. However, since we see a similar drop in pH in the vesicles that were incubated with a buffer solution, we must conclude the pure lipid bilayer of these vesicles likewise does not provide an effective barrier to the protons.

It is interesting that after the initial drop in fluorescence which coincides with the pH transition in the chamber, the fluorescence of the GUVs continues to decline. This indicates that the pH transition inside the vesicles is not complete after the initial drop in fluorescence and seemingly contradicts the observation of the fast proton transport that we witnessed during the first few minutes of the experiment. The continued decline in fluorescence over the time scale of hundreds of minutes suggest that the bilayer is indeed an effective barrier for the protons; the opposite conclusion that we drew from the first few minutes of the experiment.

We compared the steady decay that followed the initial drop in fluorescence, since the latter seems to be rate limited by the pH transition in the perfusion chamber. For this, we fitted an exponential function of the form $y = a \times \exp(-bt)$ to the decay of the final 350 minutes of every vesicle in the respective experiments. An example trace with the corresponding exponential fit is shown in Figure 5.14. Histograms of the decay parameter b are shown in Figure 5.15 for the vesicles incubated with the DNA pore, as well as for the buffer control. The median values are given inset. Note that outliers > 0.02 min^{-1} are not shown in the histograms, but are included in the calculation of the median.

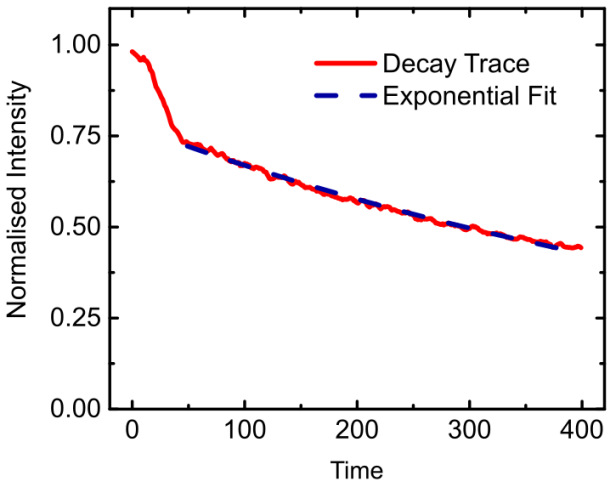

Fig. 5.14. Example trace of exponential decay trace. The displayed decay trace is a vesicle incubated with the DNA pore from Experiment 3. The normalised intensity of the vesicle is shown in red. An exponential trace is fitted to the secondary decay for the final 350 minutes of the experiment.

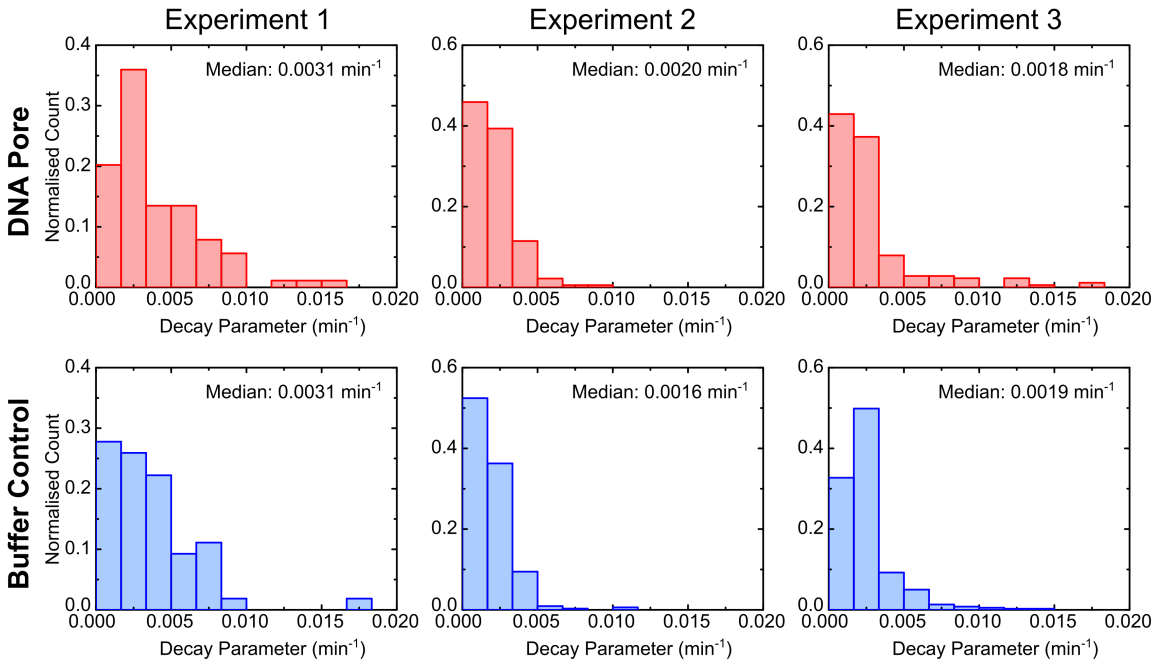

Fig. 5.15. Exponential decay parameters fitted to the steady state decay for the last 350 minutes of every experiment. The decay rates of the vesicles incubated with the DNA pore are shown in red, the control group in blue. The median value is given inset.

In line with our previous observations, Experiment 1 not only shows the greatest absolute rate constant, and hence the fastest decay, but also the greatest spread in decay parameters. However, there is remarkably little difference between the rate constants of vesicles that have been incubated with the DNA pore, compared to the control group. The median decay parameter of both sets of vesicles is 0.0031 min^{-1}. Compared to Experiment 1, the absolute decay rates are smaller in Experiments 2 and 3, in line with the smaller overall decay we see for these experiments in the heatmaps and decay traces. Like before, the decay parameters are similar for the DNA incubated vesicles and the control group. In Experiment 2 the median values are 0.0020 min^{-1} for the DNA incubated vesicles, and 0.0016 min^{-1} for the buffer control. These values are 0.0018 min^{-1} and 0.0019 min^{-1} for Experiment 3, respectively.

The analysis above shows that, overall, we cannot observe a notable enhancement of proton flux in the set of vesicles that have been incubated with the DNA pore, compared to the control group. This is somewhat surprising, considering the pH gradient between the bilayer and the size of the nanopore. In Appedix C.6, we perform a theoretical calculation, according to which a single DNA pore can mediate sufficient proton transport to equlibrate the pH within several minutes. Effects like the previously discussed low insertion efficiency of the pore as well as the possibility of the flushing away of the DNA pores can be explanations for this discreptancy. However, the most crucial cause for our inability to see enhanced transport is the passive permeation of the protons through the bilayer itself. We designed the experiment under the assumption that the bilayer provides an effective barrier for the protons. In that case, even a small enhancement of ion flux due to the DNA pore would accumulate over the entire span of the experiment and show a noticeable effect. Instead, we see a seemingly two-step process of pH adjustment of the vesicles irrespective of whether DNA pore are present or not. An initial drop in fluorescence of the vesicles coincides with the pH transition in the perfusion chamber, which suggests fast proton transport across the membrane. However, after the initial acidification, we observe a steady decrease in fluorescence over the remaining time span of hours, which suggests slow proton permeation.

The review of the literature on the membrane permeation of protons reveals that this transport process is indeed a non-trivial and highly debated phenomenon. There exist conflicting numbers on the actual membrane permeability coefficient of protons. Measurements range from 10^{-4} to 10^{-12} cm/s [159, 240–243]. Early measurements of proton permeability through lipid membranes were conducted by the group of David Deamer who have consistently found permeability values in the order of 10^{-4} – 10^{-5} cm/s [159, 241, 242]. This is surprising, as the permeabilities of other ions like potassium and sodium lie in the order of 10^{-12} to 10^{-14} cm/s [15, 241, 244]. We can put these numbers into perspective, when we compare

them to the permeability values we obtained for the passive diffusion of fluoroquinolones in the previous chapter. For the transport processes that occurred over time scales of tens of seconds, we obtained permeability values of 10^{-6} cm/s. The proton permeability coefficients measured by Deamer *et al.* lie two orders of magnitude above that, implying transport in the time scales of hundreds of milliseconds. Following this analogy, the transport of sodium and other ions occurs in the time scale of hundreds of hours, a number which is consistent with the observations by Hauser *et al.* [244].

The permeability coefficients measured by Deamer *et al.* have been questioned by other groups, due to their severe physiological implications [240]. For instance, it was argued that the high passive proton permeability can collapse the electrochemical H^+/OH^- gradient that drive the proton motive force that is necessary for processes like the synthesis of ATP which we discussed earlier in this chapter [240, 241]. Nozaki and Tanford measured the permeability values of H^+ ions to be in the order of 10^{-12} cm/s [240], while Gutknecht and Walther obtained 10^{-9} cm/s in a 1981 study [245]. In a later publication, Gutknecht reported various other values ranging from 10^{-5} to 10^{-7} [241, 243]. It turns out that the permeability values obtained depended strongly on the conditions in which the measurements were performed. A 1987 review concluded that proton permeability measurements only provide useful comparative information if they are obtained under the same conditions [241]. The same review also concluded that the high permeability values measured in vesicle systems or with black lipid membranes do not contradict the existence of proton gradients across membranes in biological systems. For instance, it has been shown that the proton conductance of mitochondrial membranes is in the order of 10^{-6} S/cm^2, similar to that of other ions [241]. However, because the concentration gradients of protons in this system is typically six orders of magnitude lower than that of other ions, the membrane function is not impeded by the high intrinsic membrane permeability [241].

Irrespective of the exact value for the permeability coefficient, most researchers agree that proton permeability is abnormally high compared to that of other ions and that protons have a unique mechanism via which they cross the bilayer [241, 243]. Two main theories are discussed in the literature. According to one model, proton permeation occurs along transient hydrogen-bonded chains. These chains act as "water wires" [243] and allow protons to cross the membrane similar to electrical conductance in an electrical wire [241]. The second model explains the unusually high proton permeability with the presence of contaminants that act as a protonophore. Gutknecht *et al.* have argued that even oxidized lipids can act as protonophores increasing proton permeability drastically [241, 243].

The large range of proton permeability and the strong dependence on the chemical environment could explain the biexponential shape that we see in our fluorescence decay curves. The environment of the experiment could be such that there initially exists a large proton flux across the membrane which then decreases. For instance, the fast, initial flow could be driven by the Nernst potential that arises due to the concentration difference of ions between the two sides of the membrane. The pH difference of 1.5 gives rise to a voltage of -88.5 mV [238], to which we have to add a potential of -14.5 mV stemming from the concentration difference in HPTS [246]. The initial high flux of protons could equalise the electrical potential difference which in return decreases the driving force for the protons. After the depletion of the electric potential, different transport mechanisms dominate the system.

Another effect that could lead to the distinct biexponential decay curve is the movement of counter ions. There exist several publications on cells where the external drop of pH leads to an intracellular pH profile of the distinct shape we also observe [247, 248]. An initial internal acidification originated from fast proton or undissociated acid transport across the membrane. A slower, passive efflux of anions then continues to lower the internal pH. In our case, (protonated) phosphate ions could passively diffuse out of the vesicle. The leakage of buffer ions can change the equilibrium reaction inside the vesicle and over prolonged periods of time lead to a lower pH inside the vesicle than outside [247].

Finally, it is possible that the subsequent drop in fluorescence is due to bleaching of the HPTS dye. We think this explanation is unlikely though, as Al Nahas *et al.* performed a bleaching control on HPTS encapsulated vesicles with the same exposure settings and did not observe any bleaching of the dye over the time span of at least 10 hours [69]. Similarly, the fluorescence trace shown in Figure 5.11 shows no sign of substantial bleaching in the 400 minutes before the arrival of the low pH solution. Studies on the solvent dependence of HPTS confirm that this stability also extends to the molecule in acidic environments [249].

Finally, we must conclude that we were not able to observe enhanced ion flux mediated by DNA nanpores in our microfluidic system. However, our assay allowed us to witness the anomaly of proton permeation through lipid bilayers and is a potential tool to study this phenomenon in more detail in future studies.

5.5 Conclusion

In this chapter we investigated the transport of hydrogen ions through GUV membranes. We introduced a DNA nanopore that can insert into lipid bilayers and has shown ion conductance in electrophysiological measurements. Using a novel microfluidic perfusion assay, we compared the proton flux across GUV membranes that were incubated with the DNA pore to untreated vesicle membranes. We exposed the two populations of vesicles to a low pH solution and compared the decay of the fluorescent pH indicator HPTS that is encapsulated inside the vesicles. The fluorescence intensity of the pH indicator decreases with lower pH and is therefore a readout of the proton concentration inside the GUVs. The fluorescence decay curves revealed a distinct biexponential shape with a steep initial decay that is followed by a slower decrease. We found this decay curve for both, the vesicles that were incubated with the DNA pores and the control group. On average, the vesicles with the DNA pore showed a steeper initial decline as well as a greater overall decrease in fluorescence. However, the means of the different decay curves all lie within the standard deviation of each other. Moreover, we also observed that the steep decay coincides with the pH transition in the perfusion chamber in which the vesicles are trapped. We can therefore not rule out that the steeper initial decrease is an artifact stemming from the different filling of the perfusion chamber with the low pH solution. The analysis of the exponential decay that follows the initial drop in fluorescence revealed similar decay rates for both sets of vesicles over the final 350 minutes of the experiment. Due to the passive diffusion of protons across the membrane, any potentially transport enhancing effect of the DNA pore is therefore not detectable with the current experimental procedure.

However, a series of experiments are possible that could clarify the behavior of the proton transport we observed. One measure to enhance the informative value of the assay in future experiments would be adding the same concentration of HPTS as we have inside the vesicles to the low pH solution with which we perfuse the vesicles. In the way we currently designed the experiment, the HPTS in the low pH solution only serves as a tracer to signal the arrival of the pH 5.9 solution in the chamber. By having the same concentration of HPTS in the background, we can use this signal as chip internal calibration, to determine which fluorescence intensity corresponds to that pH value. This would be an effective way to assess to which extent the initial drop in pH we observe equalises the proton gradient. Other possible experiments involve the use of ionophores such as valinomycin. Other groups have used this compound to modulate the membrane potential and study its effect on proton permeability [250]. It would be interesting to include valinomycin in our experiments and verify whether or not the steep decline of the biexpoential curve is indeed linked to the

Nernst potential that arises from the pH gradient. Furthermore, it would also be interesting to perfuse the vesicles with a known protonophore such as indole in order to have a side-by-side comparison of the proton flux across untreated GUV membranes, vesicles that have been incubated with a DNA pore and the proton transport in presence of an established protonophore.

Our experiments revealed that hydrogen ions are not the ideal choice of ions to study the flux through DNA nanopores due to their abnormally high passive permeation. Ions such as sodium or potassium might be more suited, as no substantial passive transport of these ions should occur over the time scales of the experiment. Any transport we observe in vesicles that are incubated with DNA pores would therefore most likely be conducted via the pore. However, as noted above, any fluorescent tracer used in the perfusion assay must be highly photo stable, in order to avoid severe photo bleaching over the long time scales of the experiment. Advances in the development of such indicators for other ions could open up the possibilities for further experiments in this direction.

Chapter 6

Towards a Deep UV Absorbance Assay to Determine Membrane Permeability

6.1 Motivation

In the previous chapters, we relied on the molecule's autofluorescence, or fluorescent indicators such as HPTS to visualise the molecule/ion whose transport we want to study. In this chapter we will look into a new potential way to expand the scope of our assay. One advantage of our microfluidic platform is the fact that it is not bound to fluorescent readouts but can be combined with other optical sensing mechanisms. By using a different optical effect to visualise the molecule of interest, we can improve our assay and obtain the permeability of compounds that we were unable to measure before.

The development of label-free methods to investigate membrane permeability and other membrane-molecule interactions is a field in its own right and several different methods have been published in the past [251]. For instance, Zeng *et al.* used a non-linear optical phenomenon called second-harmonic generation (SHG) to study the transport of Machalite green across *E.coli* membranes [192]. In this technique, two incident photons interact with the target molecule to create a second order polarisation in its assembly. Via an intermediate virtual state, the two photons are then converted into a single photon which can be detected. Since the resulting photon has double the initial frequency, the effect used for this imaging technique is also called frequency doubling [252, 253]. Other groups used confocal Raman spectroscopy to study drug-membrane interactions and the permeability of anti-inflammatory drugs [195, 251]. Raman spectroscopy relies on the inelastic scattering

of light in a medium to identify a molecule. An incident photon is absorbed and lifts an electron to a higher virtual energy state. As the electron returns to a lower energy state, it emits a photon. However, the electron does not return to the ground energy level, but to an excited state that corresponds to different vibrational and rotational modes of the molecule. This leads to a shift in the emission spectrum which can be recorded and used to study the molecule [195, 251]. There are also non-optical methods being developed to study molecule-membrane interactions. Ghatkesar *et al.* for instance developed a micro-cantilever assay that allows for the investigation of peptide adsorption to liposome membranes [254]. In their assay, lipid vesicles are immobilised on an oscillating cantilever and exposed to the peptide melittin. As the peptides insert into the membrane, the resonance frequency of the cantilever changes. The group exploits the change in resonance frequency to obtain the mass of inserted peptides and measure other micromechanical changes in the membrane [254].

A disadvantage of many of the label-free methods above is the fact that they cannot be coupled with microfluidic techniques or require extensive equipment such as pulsed femtosecond lasers to function. We want to maintain the microfluidic character of our permeability assay, as it offers advantages such as the precise control over the chemical environment, small reagent volumes and single vesicle resolution. For this reason, we opted for the use of a different technique to expand our assay. In the work below, we exploit the absorbance property of a molecule to visualise the transport through a vesicle membrane and determine its permeability coefficient. However, we will not conduct our experiments with visible light, but use ultraviolet (UV) radiation instead. As we will see below, we use light with a wavelength of 280 nm in the new optical setup. Electromagnetic radiation with wavelengths from 100 – 280 nm is defined as UV-C radiation by the International Organisation of Standardisation (ISO). UV-C radiation is commonly also called hard UV or deep UV [255], which is why we refer to the technique developed in this chapter as the Deep UV Absorbance Assay, or simply Absorbance Assay. The advantage of using UV radiation instead of visible light for the absorbance setup is the fact that many organic molecules show an absorbance peak in this part of the electromagnetic spectrum [256, 257]. A transport assay using the UV absorbance can therefore expand the scope of our transport studies to molecules we were unable to investigate previously, due to their lack of autofluorescence or fluorescent indicators.

Beer-Lambert's law describes the relationship of a molecule's absorbance to its concentration along a given optical path length [258–260]. The principle of this interaction is shown in Figure 6.1. Light with an initial intensity I_0 is attenuated as it traverses a medium containing the absorbing substance. The absorbance A is described by the product $A = \varepsilon \times c \times L$ where

L is the optical path length and c is the molar concentration of the absorbing substance. ε is a material property called the molar attenuation or extinction coefficient. Multi-component systems, or several absorbing layers in series behave additively, so we obtain $\sum_{i=1}^{N} = \varepsilon_i \times c_i \times L_i$. The absorbance of the light is likewise described by the equation $A = \log_{10}(\frac{I_T}{I_0})$ with the transmitted intensity I_T and the incident intensity I_0.

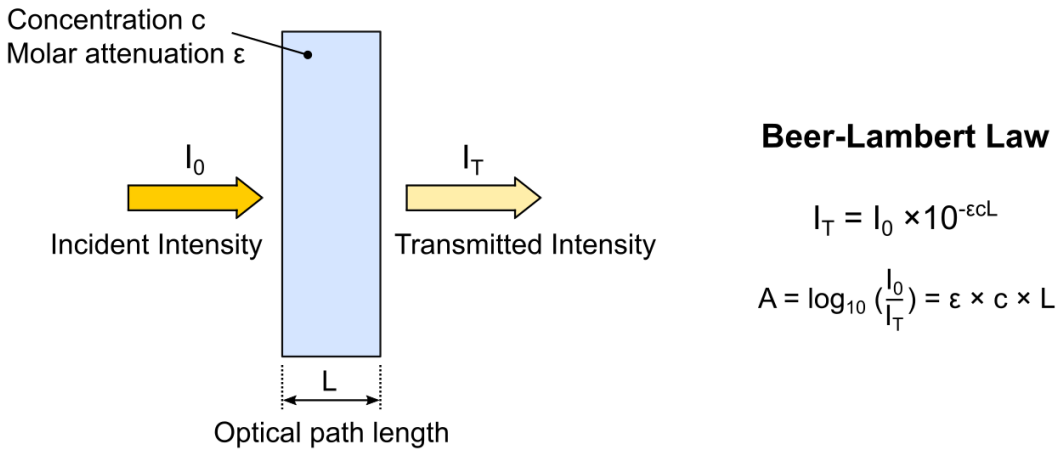

Fig. 6.1. Schematic explaining Beer-Lambert's law. Light with an incident intensity I_0 is attenuated as it traverses a medium containing an absorbing substance with concentration c and attenuation coefficient ε. The Absorbance A is described by the logarithm of the ratio of incident and transmitted intensities I_0 and I_T.

Beer-Lambert's law is used in interpreting data from UV-Vis spectrophotometers and other techniques to determine the concentration of a target compound [261]. Moreover, it is also used in medical imaging techniques like computed tomography (CT) to identify specific tissues [262].

In the following sections, we will show how we can use it in conjunction with our microfluidic techniques to measure the permeability coefficient of molecules traversing lipid membranes.

6.2 Design of Experiment

6.2.1 Fleroxacin as a Model Antibiotic

As before, we will use an antibiotic of the fluoroquinolone family as a model drug to test our assay. In this chapter, we will work with the antibiotic fleroxacin, whose chemical structure is depicted in Figure 6.2A. The advantage of this molecule is the fact that we can image it both using absorbance and autofluorescence. As we see in Figure 6.2B, the molecule expresses an absorbance peak at λ = 286 nm, but also a smaller peak at 340 nm. The latter can be used in our permeability assay in Chapter 4 to include autofluorescence. The absorbance maxima overlaps with the emission wavelength of our deep UV light source whose emission peak is stated as 275 – 285 nm by the manufacturer. These properties make fleroxacin an ideal candidate for our purpose, as we can compare the permeability value we obtain with our new technique as well as with the established technique. In Figure 6.2C, we show the calibration curve of fleroxacin showing that the absorbance at 280 nm scales linearly with the concentration, in line with Beer-Lambert's law. The absorbance spectrum, as well as the calibration curves were obtained in a NanoDrop UV-Vis Spectrometer (NanoDrop 2000, Thermo Scientific, UK) in a 5 mM acetic acid buffer.

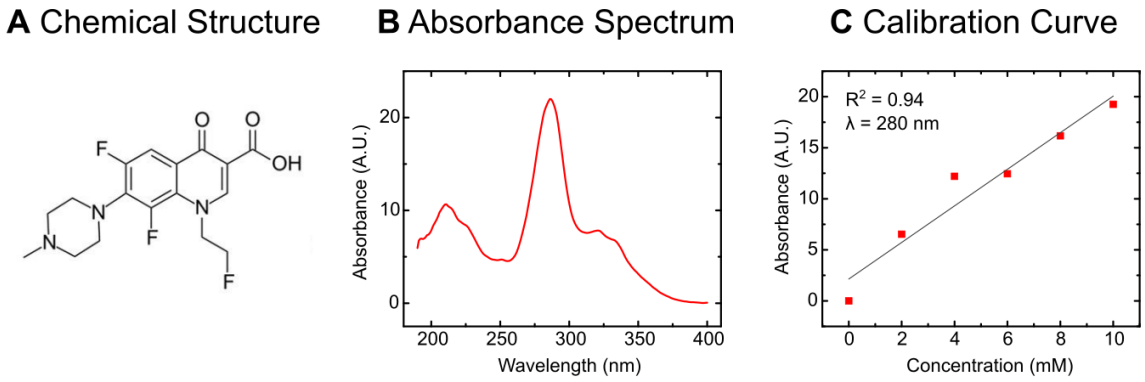

Fig. 6.2. (A) Chemical structure of fleroxacin. (B) Absorbance spectrum of 10 mM fleroxacin in a 5 mM acetic acid buffer. The absorbance peak at $\lambda \approx 286$ nm is exploited for the visualisation of the drug in the new optical setup. (C) Calibration curve showing the linear scaling of the absorbance in the relevant concentration range.

6.2.2 Optical Setup and Flow Control

We conducted the studies presented in this chapter before we developed the integrated vesicle production and permeability testing microfluidic platform introduced in Chapter 4. For this reason, we did not use our own microfluidic chip design for the experiments below. Instead, we used the original chip design presented by Cama *et al.* in 2014 that our own permeability platform is based on. We ran the old chip design with our altered optical train, suitable for absorbance measurements.

The optical setup is depicted in Figure 6.3A. An ultraviolet LED (M280L3, Thorlabs, Germany) generates light of 280 nm which is collimated and evenly illuminates a PDMS chip bonded to a PDMS coated quartz cover slip (Type 2, UQG Optics, UK). The signal passing through the chip is detected by a 40× UV objective (0.5 N.A. LMU- 40X-UVB, Thorlabs). Any autofluorescence is filtered out by a 280 nm bandpass filter (280/10 nm BrightLine single-band bandpass filter, Semrock). The signal is then focused into an EMCCD camera (Evolve 512 Delta, Photometrics). The camera is controlled using the open source software µ-Manager 1.4 [166]. Video recordings occurred at EM gain 25, bin 2 and 10 ms exposure time. All involved lenses and optics are either made of quartz or UV grade fused silica (Thorlabs, Germany).

The microfluidic chip design is shown in Figure 6.3B. The fluid flows are similar to that in our own permeability platform. Two channels, one containing lipid vesicles and one containing a drug solute, meet at a two-way T-junction where the flows mix equally. The field of view of the camera is set to an observation point indicated by the red box in Figure 6.3B that allows the recording of vesicles passing through two different parts of the channel. The liposomes in the different parts of the channel have been exposed to the drug for different amounts of time and therefore have different amounts of drug molecules within them. Comparison of the intensity levels of the vesicles allows the calculation of the permeability coefficient. Yet, the visualisation of the drug transport is achieved by a completely different principle as before. Instead of emitting light and therefore appearing bright, the drug absorbs the incoming wavelength in this assay and appears dark. The vesicles on the other hand are initially bright as they do not have absorbing drug molecules within them. The T-junction that shows the difference in transmitted light between the vesicles and the drug solute is shown inset in Figure 6.3B. The GUVs grow darker as the drug diffuses across the membrane. By comparing the transmitted light intensity of the vesicles at two different time points, the membrane's permeability to the drug of interest can be determined. We present a diffusion model that allows for the calculation of the permeability coefficient from the transmitted light intensities in Section 6.2.3.

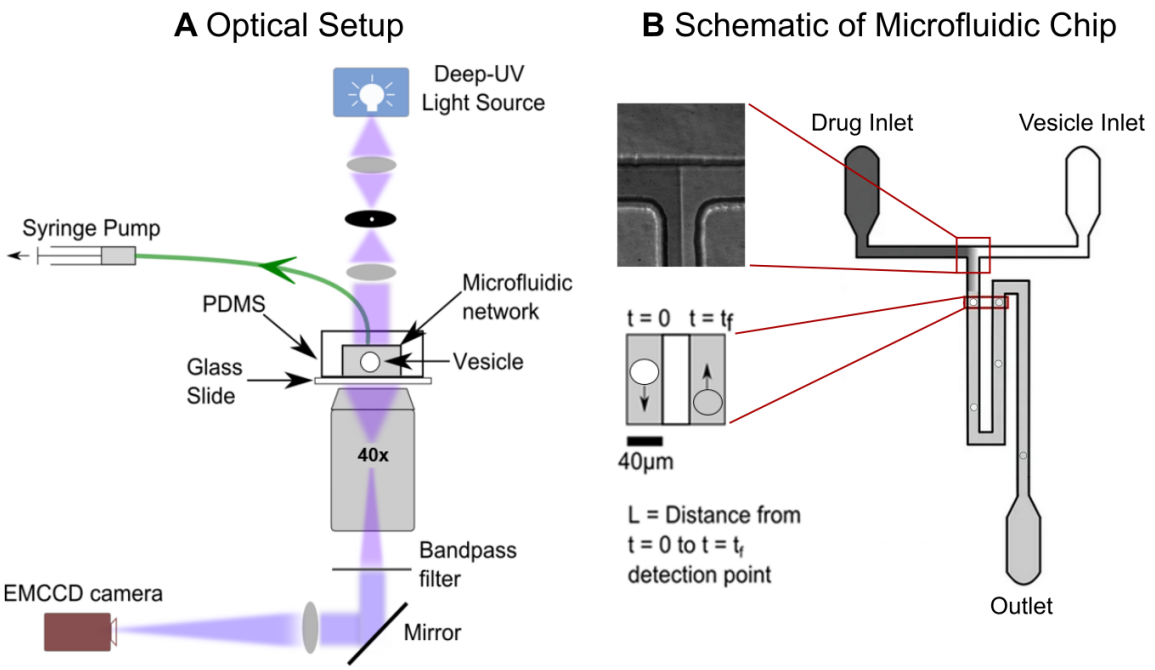

Fig. 6.3. Schematic of the absorbance assay. (A) Optical train of the setup. Light from a deep-UV LED is collimated and evenly illuminates a microfluidic chip on a quartz cover slip. The signal passes through a deep-UV transparent objective. Fluorescence artefacts are filtered out by a 280 nm bandpass filter and the signal is then focused into an EMCCD camera. (B) Design of the microfluidic chip. Two flows, one containing lipid vesicles, one containing a drug solute, equally mix at the junction. The flow containing the drug solute is dark as the drug molecules absorb the UV light, whereas the flow containing the vesicles remains bright. As the drug molecules diffuse across the membrane, the vesicles get darker due to the higher concentration of absorbing drug molecules within them. By analysing the light intensity of the vesicles at distinct time points, indicated by red boxes, the speed of drug transport across the membrane can be determined. Image modified from [37].

The fluid flow in the chip is driven by a neMESYS syringe pump (Cetoni GmbH, Germany) with a 250 µL Duran Borosilicate glass syringe (ILS, Germany) that is connected to the outlet of the microfluidic chip via an Upchurch 1520 G tubing with an inner diameter of 0.03”. Two pipette tips, one containing 40 µL of the drug solute and one containing 40 µL of the vesicle solution are placed into the inlet chambers of the microfluidic chip and serve as fluid reservoirs. Initial suction of 30 µL/h is applied for 30 minutes via the syringe pump. Over the time period of 20 minutes, the flow rate is reduced stepwise to 3 µL/h. After the flows settle, the field of view is set to the measurement position and image acquisition started.

6.2.3 Beer-Lambert Law and Diffusion Model

As mentioned above, the attenuation of light passing through a material is described by Beer-Lambert's law [258]. We can combine the diffusion model from Chapter 4 with this law to produce a model for the membrane's permeability based on the UV absorbance of the drug molecules within a vesicle. According to Beer-Lambert's law, the absorbance A of a material sample is directly proportional to the path length of the light travelling through a material, as well as to the individual concentrations of the attenuating substances [258].

$$A = \sum_{i=1}^{N} \varepsilon_i \times c_i \times L_i \tag{6.1}$$

Where ε_i is the attenuation coefficient, c_i the molar concentration of the substance and L_i the path length of the travelled light.

Furthermore, the overall absorbance is described by the equation

$$A = \log_{10}\left(\frac{I_0}{I_T}\right) \tag{6.2}$$

with I_0 the incident intensity and I_T the transmitted intensity.

In order to determine the permeability coefficient, we require three measurements of the transmitted intensity, which we depict in Figure 6.4.

The first measurement is that of the background intensity I_{BG}, which has to be measured when no vesicle is present in the microfluidic channel.

$$A_{BG} = \log_{10}\left(\frac{I_0}{I_{BG}}\right) = \varepsilon_{drug} \times c_{out} \times L + X \tag{6.3}$$

$$\rightarrow c_{out} = \frac{\log_{10}\left(\frac{I_0}{I_{BG}}\right) - X}{\varepsilon_{drug} \times L} \tag{6.4}$$

Where $\varepsilon_{drug} \times c_{out} \times L$ is the absorbance of the drug solute in the channel. Unknown elements such as the absorbance of the quartz cover slip and the rest of the PDMS are contained in the variable X and will later cancel out.

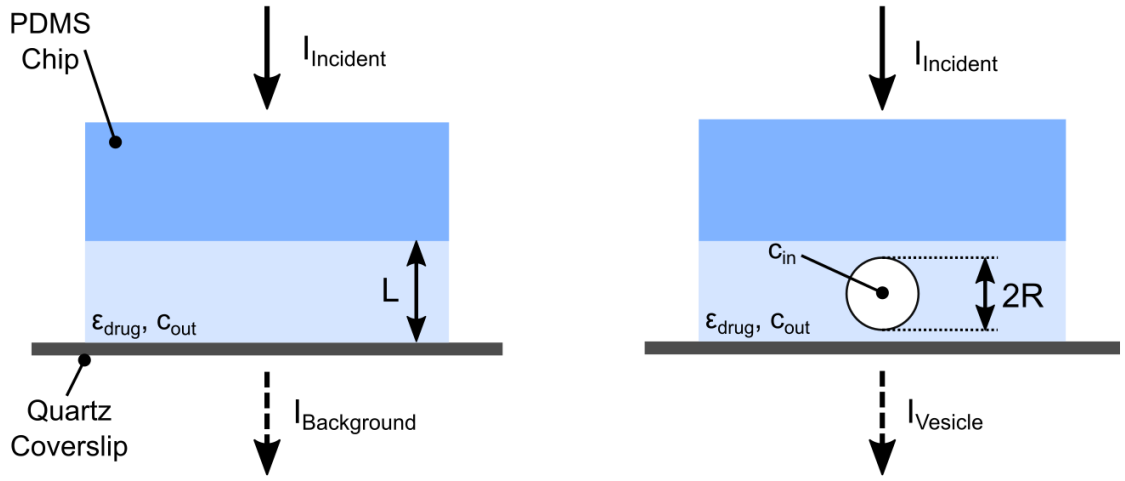

Fig. 6.4. Illustration of the intensity values that have to be obtained in order to determine the drug concentration inside the vesicles. The background intensity I_{BG} is measured when no vesicle is present in the channel. The transmitted intensity values of the vesicles $I_{Vesicle}$ have to be taken at two distinct time points. The microfluidic channel has a height of L and is filled with a drug solute of concentration c_{out} and attenuation coefficient ε_{drug}. The drug concentration in the inside of the vesicle at a given time point t is c_{in}.

The other two transmitted intensities are that of the vesicle $I_{Vesicle}$. The intensity must be measured at two distinct time points. We will call the intensity measurement at these time points I_1 and I_2. As in our previous diffusion model, we perform the first intensity measurement of a vesicle I_1 immediately after mixing with the drug solute (time point t_1) and the second measurement I_2 after several seconds when the vesicle appears in the field of view again (time point t_2).

$$A_1 = \log_{10}\left(\frac{I_0}{I_1}\right) = \varepsilon_{drug} \times c_1 \times 2R + \varepsilon_{drug} \times c_{out} \times (L-2R) + X \tag{6.5}$$

$$\rightarrow c_1 = \frac{\log_{10}\left(\frac{I_0}{I_1}\right) - \varepsilon_{drug} \times c_{out} \times (L-2R) - X}{2R \times \varepsilon_{drug}} \tag{6.6}$$

$$A_2 = \log_{10}\left(\frac{I_0}{I_2}\right) = \varepsilon_{drug} \times c_2 \times 2R + \varepsilon_{drug} \times c_{out} \times (L-2R) + X \tag{6.7}$$

$$\rightarrow c_2 = \frac{\log_{10}\left(\frac{I_0}{I_2}\right) - \varepsilon_{drug} \times c_{out} \times (L-2R) - X}{2R \times \varepsilon_{drug}} \tag{6.8}$$

The summands $\varepsilon_{drug} \times c_1 \times 2R$ and $\varepsilon_{drug} \times c_2 \times 2R$ express the absorbance of the drug within the vesicle at the time points t_1 and t_2, respectively. The absorbance of the drug solute

surrounding the vesicle in the channel is expressed by $\varepsilon_{drug} \times c_{out} \times (L-2R)$. The unknown parameters are again substituted for X.

We can assume that $c(t_1 = 0) = 0$, as the initial concentration of drug within the vesicle is zero. We can then solve Equation 6.5 for the unknown parameter X.

$$X = \log_{10}\left(\frac{I_0}{I_1}\right) - \varepsilon_{drug} \times c_{out} \times (L-2R) \tag{6.9}$$

Inserting Equation 6.9 into Equation 6.4 gives us for c_{out}

$$c_{out} = \frac{\log_{10}\left(\frac{I_0}{I_{BG}}\right) - \log_{10}\left(\frac{I_0}{I_1}\right)}{2R \times \varepsilon_{drug}} = \frac{\log_{10}(I_1) - \log_{10}(I_{BG})}{2R \times \varepsilon_{drug}} \tag{6.10}$$

We remember from our permeability model in Chapter 4 that

$$P = -\frac{R}{3t} \times \ln\left(\frac{c_{out} - c_{in}(t)}{c_{out}}\right) \tag{6.11}$$

For $c(t)$ in Equation 6.11, we can assume that $c(t) = c_2 - c_1$ and receive from inserting Equation 6.6 and Equation 6.8

$$c(t) = c_2 - c_1 = \frac{\log_{10}\left(\frac{I_0}{I_2}\right) - \log_{10}\left(\frac{I_0}{I_1}\right)}{2R \times \varepsilon_{drug}} = \frac{\log_{10}(I_1) - \log_{10}(I_2)}{2R \times \varepsilon_{drug}} \tag{6.12}$$

The expressions for c_{out} and $c_1 - c_2$ can now be inserted into Equation 6.11. For the expression in the brackets we receive

$$\frac{c_{out} + c_1 - c_2}{c_{out}} = 1 - \frac{c_2 - c_1}{c_{out}} = \frac{\frac{\log_{10}(I_1) - \log_{10}(I_2)}{2R \times \varepsilon_{drug}}}{\frac{\log_{10}(I_1) - \log_{10}(I_{BG})}{2R \times \varepsilon_{drug}}} \tag{6.13}$$

$$\Leftrightarrow \frac{c_{out} + c_1 - c_2}{c_{out}} = 1 - \frac{\log_{10}(I_1) - \log_{10}(I_2)}{\log_{10}(I_1) - \log_{10}(I_{BG})} \tag{6.14}$$

For our final formula of the permeability coefficient we get

$$P = -\frac{R}{3t}\ln\left(1 - \frac{\log_{10}(I_1) - \log_{10}(I_2)}{\log_{10}(I_1) - \log_{10}(I_{BG})}\right) \tag{6.15}$$

The diffusion model in the absorbance assay therefore requires the same parameters that we needed to calculate the permeability coefficient using autofluorescence. These are intensities I_1 and I_2 of a vesicle at two time points, the background intensity I_{BG}, as well as the vesicles radius R and the time t between the two measurement points.

6.3 Validation Experiments

6.3.1 Materials and Methods

Microfluidic Chip Design and Fabrication

The microfluidic chips were made of polydimethylsiloxane (PDMS) following the protocol presented in Sections 2.4.2 and 4.4.2. The silicon master chip was designed by J. Cama as previously described [37]. The design of the microfluidic chip is depicted in the Appendix Figure D.1.

Since standard glass coverslips are not transparent to UV radiation at 280 nm, we used quartz cover slips (Type 2, UQG Optics, UK) for our experiments in the absorbance assay. For the purpose of reusability, we coated the quartz cover slips with a thin PDMS layer as we described in Section 2.4.2. The microfluidic chip was then bonded onto the PDMS layer, rather than to the glass itself. This way the PDMS chip could be removed from the cover slip and the quartz slide reused.

Solution Composition

The vesicles were obtained via the electroformation method, according to the protocol we presented in Section 3.1.1. The lipid suspensions consisted of 80 µL DPhPC lipid (1,2-diphytanoyl-sn-glycero-3-phosphocholine, 5 mg/mL in chloroform) and were prepared in a 5 mM acetic acid, 200 mM sucrose buffer at pH 5. After electroformation, the vesicles were stored in an Eppendorf tube and used within one week.

The drug solute was prepared by dissolving fleroxacin powder (Sigma Aldrich, USA) in the same pH 5 acetic acid buffer (200 mM sucrose, 5 mM acetic acid) as used for vesicle formation. The drug concentration in the drug solute used for the absorbance setup was 8 mM, which leads to an overall concentration of 4 mM in the channel, if we assume equal mixing with the vesicle flow. The pH value of the buffer was adjusted using a digital pH meter (Hana Instruments, UK) by adding several µL of KOH (10 %) and HCl (10 %).

All chemicals were obtained from Sigma-Aldrich unless stated otherwise.

MATLAB Analysis Routine

After the system has been setup as described above, the field of view is moved to a recording position and image acquisition started using µManager. Frames are recorded at 100 fps and stored on external hard drives. After the data acquisition, the videos are analysed using a MATLAB routine. Among other values, this script extracts the area, the major and minor axis lengths, the weighted centroid and the intensity values of the vesicles passing through the channel for every frame. Based on the extracted data, the permeability values according to the model above are calculated.

Due to the low signal-to-noise ratio (SNR), intensive image processing has to be performed to reliably detect vesicles passing through the channel. The processing consists of 4 steps, illustrated in Figure 6.5. First, an image of the background is taken without vesicles being present in the channels. This background image is subtracted from each frame of the video. Vesicles that are present in the channel therefore appear much clearer than in the original image, similar to a dark field image. In a next step, a contrast enhancement algorithm from the MATLAB Image Processing Toolbox is used to further enhance the contrast of the image. Third, the enhanced image is converted into a binary image. A binary image is necessary in order to specify which pixel shows part of a vesicle and which pixel shows background. In this script, pixels with the value 1 show part of the vesicle, pixels with the value 0 show the background. The 1-pixels thus define the contour of the vesicle and we can use this information to extract the vesicle's properties that we are interested in, such as the area or the intensity values. Yet, before these properties can be extracted, several filters have to be applied to the binary image in the final step of image processing.

Two filters are applied to remove isolated noise pixels. Using the *bwmorph('clean')* and the *bwmorph('fill')* functions, false positive and false negative pixels are removed, respectively. In the binary image, false positive pixels are fields in the picture matrix with the value of 1 that are surrounded by fields with a value of 0. Similarly, false negatives are fields with a

value of 0 that are surrounded by fields of the value 1. Next, the *bwmorph('majority')* filter is used to smoothen the edges of the vesicle. It sets a pixel to 1 if five or more pixels in its 3-by-3 neighbourhood are 1. Finally, the *bwareaopen* function is used to eliminate small objects from the image that show the value of 1 that consist of less than 30 pixels. These are usually bright specs of lipid aggregates that otherwise would be detected as a vesicle.

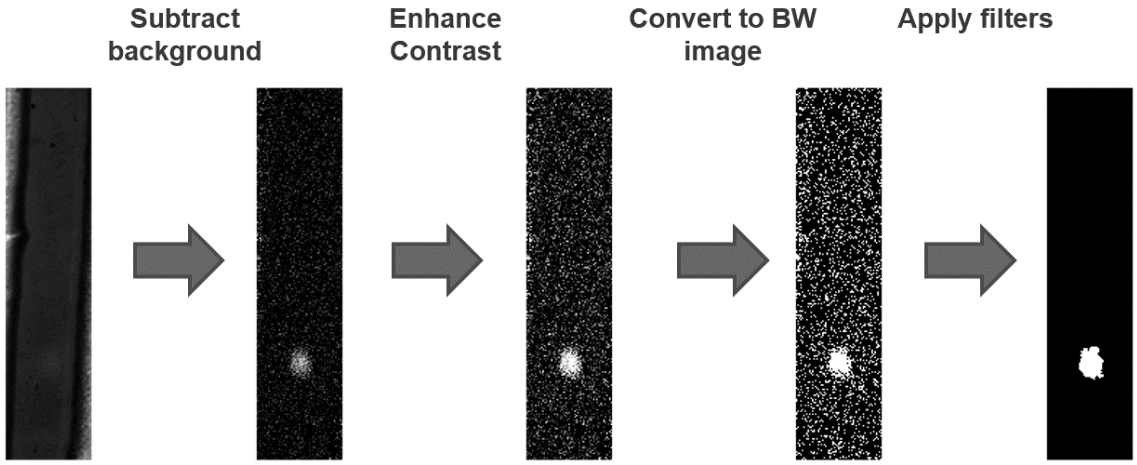

Fig. 6.5. Four step image processing to detect vesicles: First, a background image is subtracted from the acquired frames. Next, a contrast enhancing algorithm is applied to the images in order to increase the vesicle's contour. In a third step, the image is converted into a binary image. Finally, several filters are applied to the black-white image in order to remove noise pixels and remove false positives.

6.3.2 Results and Discussion

Scatter plots of our measurements are depicted in Figure 6.6. The x-axis displays the vesicle radius and the y-axis the transmitted intensity, normalised to the background intensity. Every scatter point represents a single vesicle measurement. The dark scatter points were obtained at the time point $t_1 \approx 0$ s, just after the vesicle entered the mixing channel. The coloured data points show the vesicle intensity after the time given inset.

As we did for our permeability assay in Chapter 4, we did not compare the intensity levels of one and the same vesicle at the two time points. Instead, we fitted a linear function to the scatter points we obtained for I_1 as a function of the radius. For every measurement at the second recording position (red scatter points), we recalculated the corresponding I_1 value according to the function.

The gap between the dark scatter points and the coloured points visualise the drug transport from the outside into the inside of the vesicle. Initially, the vesicle is bright on a dark background, represented by a high intensity to background ratio $\frac{I_1}{I_{BG}}$. As the light absorbing drug molecules permeate through the membrane, the transmitted intensity decreases and the vesicle appears darker. The intensity ratio at the second measurement position $\frac{I_2}{I_{BG}}$ is therefore closer to the baseline. Calculation of the permeability coefficient according to the diffusion model above reveals a permeability value of $14.4 \pm 2.1 \times 10^{-6}$ cm/s (mean ± standard error, N = 29) for fleroxacin at pH 5 through DPhPC vesicle membranes.

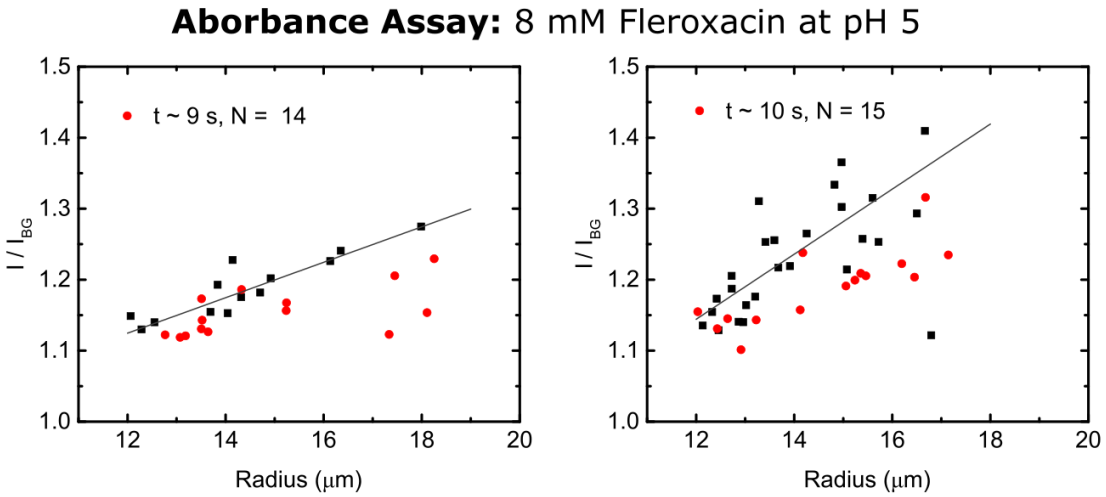

Fig. 6.6. Scatter plots of two fleroxacin experiments using the absorbance assay. The y-axis shows the intensity value of the vesicle normalised to the background intensity. The two graphs show the results of two individual experiments with the same drug. Every scatter point represents an individual vesicle measurement. The dark data points are taken at $t_1 \approx 0$ s. A linear function is fitted through these points and shown as solid line. The individual measurement points at t_2 are depicted in red. The time difference between the two measurement points, as well as the number of vesicles is shown in the top left corner.

The easiest way to assess the results we obtained from the absorbance assay is to directly compare them to a measurement we performed under the same conditions using the autofluorescence imaging mode. We performed such measurements on fleroxacin in a previous publication [153]. Two scatter plots of these permeability measurements are shown in Figure 6.7. It should be noted that the concentration of the drug solute in the autofluorescence measurements was 2 mM, instead of the 8 mM we use in the absorbance assay. All other chemical parameters between the experiments, such as the buffer or the lipid type were identical.

We can interpret the scatter plots shown in Figure 6.7 in a similar manner to the scatter plots we discussed in Chapter 4, as they follow the same imaging principle. If we remember, in the autofluorescence assay, we normalised the intensity inside the vesicle I_{in} to the intensity of the outside I_{out} in order to obtain $\Delta I = \frac{I_{out} - I_{in}}{I_{out}}$. The ΔI value for the vesicles was obtained at two time points. The dark scatter points were measured just after the vesicle encountered the drug solute ($t_1 \approx 0$ s) and the coloured data points after the time difference given inset. The permeability coefficient could then be calculated according to Equation 4.14. Our measurements in 2015 yielded a permeability value of $4.1 \pm 0.2 \times 10^{-6}$ cm/s (mean ± standard error, N = 283) [153]. In Table 6.1, we compare that value to the permeability coefficient we obtained with the absorbance assay.

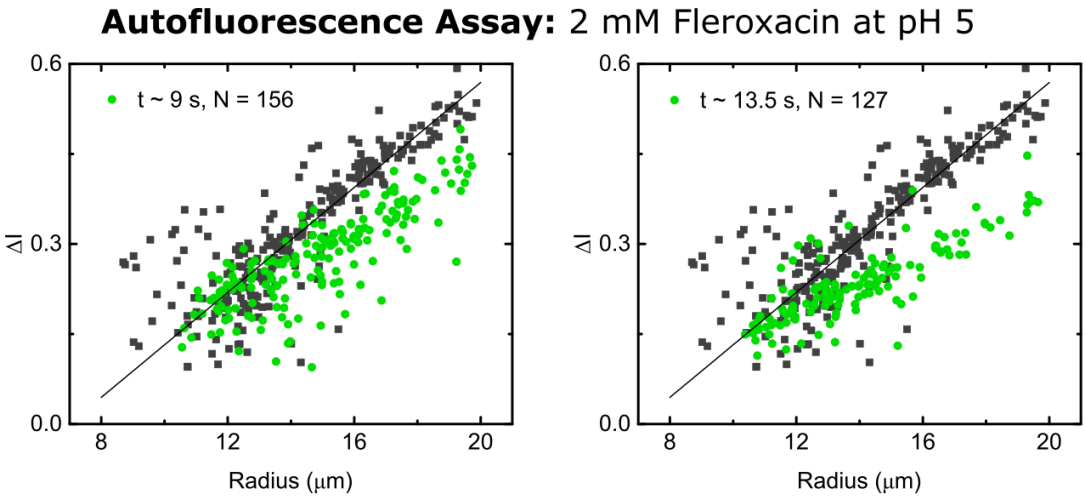

Fig. 6.7. Scatter plots of fleroxacin measurements using the autofluorescence assay. We calculate the y-axis value according to the formula $\Delta I = \frac{I_{out} - I_{in}}{I_{out}}$. The radius is given in the x-axis. Every scatter point represents an individual vesicle measurement. The dark data points are taken at $t_1 \approx 0$ s. A linear function is fitted through these points and shown as solid line. The individual measurement points at t_2 are depicted in green. The time difference between the two measurement points, as well as the number of vesicles is shown in the top left corner. The downward shift in ΔI results from an increase in autofluorescence within the vesicles, as the drug diffuses across the membrane. Image modified from [153].

Table 6.1. Permeability coefficient (mean ± standard error) of fleroxacin measured at pH 5 with the respective setups in 10^{-6} cm/s

Autofluoresence Assay	Absorbance Assay
4.1 ± 0.2	14.4 ± 2.1

The most evident difference when comparing the scatter plots obtained with the two techniques is the difference in the number of lipid vesicles in the experiments. While we detected a total of 283 vesicles with the two experiments conducted with the autofluorescence assay, this number is only 29 for our two experiments using absorbance. Even though the vesicle yield of the electroformation technique can vary from batch to batch, such a large deviance is unusual. It is in fact highly likely that more vesicles were present in the absorbance experiment, but we were not able to detect these. The reason for this is most likely the difference in signal to noise ratio (SNR) between the two assays. In the autofluorescence assay, the drug molecule itself emits the fluorescent signal we measure. Elements of the chip where no drug is present therefore appear dark in the image with a strong contrast to the fluorescing drug. The signal intensities of the vesicles and the background typically lie 60% - 100% apart, making it easy to detect the vesicles in the autofluorescence assay. In the absorbance assay, on the other hand, we measure the intensity of transmitted light from the UV LED. The mechanism that provides contrast is the difference in absorbance of the UV rays, which, however, is a very small effect. The signal of a vesicle often lies only 10% - 20% above that of the background level. As the drug permeates into the vesicle, that difference decreases even more, making it hard to detect the vesicles.

The low signal to noise ratio of the absorbance assay is also the reason why we used a drug concentration of 8 mM fleroxacin in these experiments, compared to 2 mM when relying on autofluorescence. As we discussed above, the absorbance is described as the product of the optical path length L, the attenuation coefficient ε and the concentration c. Since the path length is limited by the chip geometry (channel height) and the attenuation coefficient is a material constant, the only way for us to improve the signal to noise ratio was by increasing the drug concentration. The high drug concentration also forced us to conduct the experiments at pH 5, instead of at neutral pH levels. This is due to the fact that fluoroquinolones such as fleroxacin show their lowest aquesous solubility at neutral pH levels [181]. We were therefore only able to increase the fleroxacin concentration to 8 mM by usinga pH 5 acetic acid buffer.

Our optical resolution was further impeded by the available hardware suitable for deep UV measurements. Our autofluorescence setup is equipped with a 60× water immersion objective (UPLSAPO Olympus) with a numerical aperture (N.A.) of 1.2, whereas the absorbance setup uses a 0.5 N.A. air objective (LMU-40×-UVB, Thorlabs). The water immersion objective captures more light and enables finer specimen resolution than the air objective, but is not suitable for the deep UV experiments, due to the low UV transmittance of its constituent borosilicate glass. Furthermore, the EMCCD camera used for our experiments is

not optimised for use in the deep UV. According to the manufacturer, the quantum efficiency of the optical sensor lies between 50% - 95% in the optical range. This values drops to below 10% in the deep UV, further reducing our signal to noise ratio.

Finally, it is obvious from Table 4 that we obtain slightly different values for the permeability coefficient with the two setups. The value (mean ± S.E.) acquired with the autofluorescence assay is $4.1 \pm 0.2 \times 10^{-6}$ cm/s, whereas the permeability coefficient acquired with the absorbance assay is $14.4 \pm 2.1 \times 10^{-6}$ cm/s. This is a factor of 3.5 between the values. We explain this difference with the limiting factors of the absorbance measurement listed above: low SNR, lower optical resolution and a low number of vesicles. Another factor that might have contributed to the higher permeability value we observe in the absorbance assay is the higher drug concentration in these experiments. While the absolute concentration is accounted for in the diffusion model and should not influence the measured permeability coefficient, the vesicles might experience a higher osmotic pressure, which could alter the membrane tension and enhance the observed molecule flux through the membrane.

After discussing the differences between the two optical assays, we briefly want to comment on the fact that we were able to observe membrane permeation at pH 5 for fleroxacin in this chapter, while we did not observe norfloxacin permeation at pH 5 in Chapter 4 over the time scale of 40 seconds. The reason for this can be found in the chemical structure of the two compounds. As we see marked blue in Figure 6.7, fleroxacin carries two additional fluorine atoms, compared to norfloxacin. One fluoride atom is attached to the aromatic ring while the other is connected to an ethyl group. Furthermore, we see that both molecules have an amine in their piperazin-1-yl group. However, in norfloxacin, this amine is secondary, while it is a tertiary amine in fleroxacin. The secondary amine of norfloxacin is marked in red in the figure below.

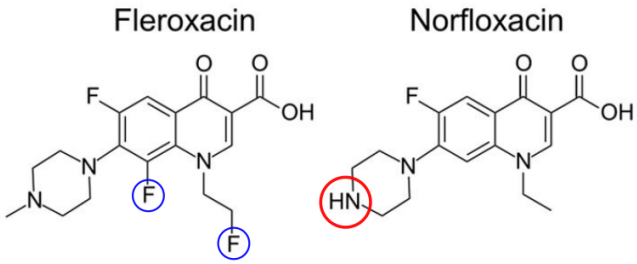

Fig. 6.8. Chemical structures of fleroxacin and norfloxacin. The two additional fluoride atoms of fleroxacin are marked in blue. The secondary amine in the norfloxacin molecule is marked in red.

In our 2015 publication, we showed that the secondary amine is responsible for the decreased lipophilicity of norfloxacin compared to fleroxacin [153, 263]. This manifests itself in the comparatively reduced permeability coefficient of norfloxacin, which lies one to two orders of magnitude below that of fleroxacin, depending on the pH [153]. The difference in lipophilicity between the compounds is also expressed in their respective octanol partition coefficients. According to the DrugBank database, calculated log P values for norfloxacin lie between 0.47 and -0.92, while experiments show a log P of -1.03 [182]. For fleroxacin, the calculated log P values lie between 0.3 and 1.12 with an experimental value of 0.24 [182]. For a detailed analysis of the permeability coefficients of the different compounds, we refer to our 2015 publication, where we measured and compare the permeability value of four fluoroquinolone antibiotics over a pH range from pH 5 – 7 using the autofluorescence assay [153].

Our results show that permeability measurements using the molecule's absorbance property are possible and could be a potential alternative for the label-free measurement of membrane transport. However, our validation experiments showed a significant difference in the obtained permeability coefficient compared to measurements using autofluorescence, which we attribute to the low signal to noise ratio, as well as to the lower optical resolution and number of vesicles in the absorbance measurements.

6.4 Conclusion

In this chapter, we investigated whether or not exploiting a molecule's absorbance property in the deep UV is a viable alternative to autofluorescence for the label-free measurement of membrane permeability. We developed a new optical setup and combined it with an established T-junction microfluidic chip assay, where we can expose electroformed vesicles to a drug solute, or a different molecule of interest, in a controlled manner. Furthermore, we derived a diffusion model from Beer-Lambert's law that allows for the calculation of the permeability coefficient.

We performed validation experiments on the new absorbance assay and measured the permeability coefficient of the fluoroquinolone drug fleroxacin through DPhPC lipid membranes. We compared these results with previous measurements that we performed with an established technique using autofluorescence. The permeability coefficient we obtained with the new method lies 3.5$\times$ above the value we measured previously. We attribute this disagreement in the values to the low signal to noise ratio and lower optical resolution of the UV-C

grade components that are necessary in the absorbance assay, compared to the assay based on autofluorescence.

Our experiments show that it is indeed possible to use the UV absorbance of a molecule as a tool to measure membrane permeation. However, our studies also reveal that the low signal to noise ratio of the absorbance method hinders us from achieving the same degree of sensitivity in our measurements that we were able to obtain using a molecules autofluorescence. In order to truly expand the scope of the possible molecule's that can be measured with the absorbance technique, the issue of low signal to noise must be addressed in future studies.

The two elements that make up the absorbance assay can be broken down into the optics part and the microfluidics part. Both areas have potential to improve the signal to noise ratio of the assay.

As we pointed out above, the deep UV radiation forced us to use a fused silica objective (LMU-40×-UVB, Thorlabs) that is capable of transmitting the 280 nm light. However, this objective features a lower numerical aperture, as well as a lower magnification (0.5 N.A., 40× magnification) compared to the autofluorescence setup (1.2 N.A., 60× magnification) leading to a substantially decreased image quality and overall signal in the absorbance setup. Future modification of the absorbance setup should therefore include a higher N.A. and higher magnification objective. A possible example is the Zeiss Ultrafluar series of objectives. These objectives use quartz lenses and are therefore able to transmit deep UV light. An objective with a 100× magnification and a numerical aperture of N.A. 1.25 is available which should provide better specimen resolution and enhanced signal, compared to the objective used by us. Further enhancement of the signal and image quality could also be provided by a different camera. While the EMCCD camera used by us (Evolve 512 Delta, Photometrics, UK) only has a quantum yield of 10% at wavelengths of 280 nm, there exist cameras such as the Prime 95B UV (Photometrics, UK) which are optimised for use between 250-310 nm and have a quantum yield of up to 80% in this range.

A look at the equation of the absorbance $A = \sum_{i=1}^{N} = \varepsilon_i \times c_i \times L_i$ can help us identify potential changes of the microfluidic design that could lead to a stronger absorbance contrast and hence a better signal to noise ratio. From the equation above, we see that the absorbance A scales directly with the optical path length L. Running the assay with larger vesicles would increase the relevant path length and therefore directly enhance the absorbance contrast between a GUV and the background. The microfluidic channels currently have a height of 40 µm, which also sets the upper boundary for the size of the GUVs. The redesign of the microfluidic chip with a larger channel height would allow us to perform the experiment with larger vesicles and obtain a better contrast. In our work with the permeability assay

presented in Chapter 4, we aimed to produce vesicles between ∅ 20-30 µm. However, in these experiments we observed that is possible to form GUVs with diameters of up to 60 µm, with the OLA permeability platform. The combination of this microfluidic chip with the absorbance assay might thus provide a possibility to enhance the absorbance contrast by up to 50%.

The other elements contributing to the absorbance are the molar attenuation coefficient and the drug concentration. Both the aqueous solubility (determining the maximal possible drug concentration) and the attenuation coefficient ε are material properties of the compound. We used fleroxacin in our studies presented here, as it shows both autofluorescence upon excitation at λ = 340 nm, as well as an absorbance peak λ = 280 nm and can therefore be measured with both the absorbance, and the autofluorescence assays. However, we did not screen and compare the absorbance of fleroxacin to that of other compounds. It is likely that other antibiotics with an absorbance peak in the range of our Deep UV LED, such as rifampicin, isoniazid, or pyrazinamide [264] have a greater attenuation coefficient and thus show a stronger overall absorbance. In future studies the antibiotic classes that the afore mentioned compounds belong to (rifamycins, hydrazides or pyrazine derivatives) could systematically be screened in order to determine whether they express a stronger UV absorbance than fluoroquinolones, and correspondingly whether they are more promising candidates for the absorbance assay.

Chapter 7

Summary and Outlook

The aim of this thesis was to use microfluidics for the investigation of passive transport processes through lipid membranes. We used the lipid bilayer of giant unilamellar vesicles as model for biological cell membranes. These membranes consist of a single lipid bilayer of a well-defined lipid composition and, unlike natural cell membranes, do not contain any membrane proteins. They therefore provide an ideal system for the isolated study of passive transport processes.

A novel microfluidic method called Octanol-Assisted Liposome Assembly (OLA) was the primary source of GUVs in our studies. Presented in 2016, this method has great potential for the study of membrane transport processes. Other microfluidic methods to generate GUVs on chip use alkanes or fatty acids as carrier phase for the lipid. In many cases, the vesicles made with these methods contain residual solvent in the membrane which has to be removed from the GUV in a subsequent washing step [54]. In contrast to that, OLA used the aliphatic alcohol 1-octanol as carrier phase for the lipids. The developers of the OLA technique have found that the use of octanol diminished the need for a second washing step, as the octanol separates from the GUV automatically due to a combination of surface tension minimisation as well as shear forces from the fluid flow and PDMS channel wall [56]. This property of OLA makes it an ideal candidate to be incorporated into microfluidic transport platforms to measure membrane permeability.

Before turning to microfluidic transport studies on the GUVs, we wanted to gain a better understanding of the properties of the GUVs made with the novel OLA technique. For this purpose, we compared vesicles generated with OLA to those obtained using the established electroformation method. Using confocal microscopy, we showed that OLA vesicles are highly homogeneous and have a very narrow size distribution upon production. Furthermore,

we observed the absence of any multivesicular or multilamellar vesicles among the OLA vesicles. We also tested the unilamellarity of the OLA vesicles quantitatively via a dithionite bleaching assay. In this assay, the membrane impermeable anion sodium dithionite is added to a population of vesicles labelled with the fluorophore NBD. While the inner leaflet remains unaffected, the dithionite reduces and quenches the fluorophore in the outer leaflet of the membrane [120]. A drop to in vesicle fluorescence to half of the initial value, like we observed it for the OLA vesicles, therefore quantitatively shows a lamellar structure consisting of a single lipid bilayer.

Previous research has shown that the lipid headgroup has substantial influence on the properties of the membrane [124, 150]. It is therefore important to know the precise lipid composition of the vesicles when conducting biophysical studies. However, there exists evidence suggesting that different lipid types have a different affinity to octanol [123]. We wanted to rule out the possibility of a demixing of the lipids in the Lipid-Octanol (LO) phase in OLA and tested whether or not the lipid mixture we add to the octanol translates directly into the lipid composition of the GUVs. For this purpose, we combined the lipids DOPC, DOPG and DOPE in the mixing ratios 1:3, 3:1 and 1:1 each. One of the lipid components in every binary lipid mixture was doped with a fluorescent tracer. From the scaling of the fluorescence intensity between the generated liposomes, we were able to show that the GUVs indeed maintain the lipid composition we add to the octanol. However, we were unable to form stable GUVs made from the DOPE-DOPG mixture in the 1:3 ratio, which we attribute to the high charge density as well as to the lipid polymorphism which makes it energetically unfavourable for PE lipids to form lamellar structures [126].

Next, we compared the lateral diffusion coefficient of DOPC and POPC vesicles obtained with electroformation and OLA by means of fluorescence recovery after photobleaching (FRAP). The lateral diffusion coefficient is an important biophysical property of membranes and the lateral mobility of lipids and proteins has been found to be rate limiting for many cellular processes [148–150]. Our results showed quantitatively similar lateral diffusion coefficients for vesicles obtained with the two techniques. Importantly, we found that the presence of the Poloxamer P-188, which is necessary for the formation of vesicles with OLA, does not affect the lateral lipid mobility. This finding is in line with other studies that have not found the alteration of membrane properties due to the presence of P-188 [81, 82]. Among the tested vesicles were also GUVs that had an octanol pocket attached to them. These vesicles were not subjected to enough shear force within the microfluidic chip for the octanol pocket to separate from it. Interestingly, we found no difference in lateral diffusion between the vesicles with and without visible octanol pocket. Similar results have been found

by Karamdad *et al.* who used a different microfluidic method to form vesicles and likewise found no difference in the mechanical properties between vesicles with and without residue solvent attached to them [52].

After the investigating of the membrane properties of OLA vesicles, we turned to the development of a microfluidic platform that enables the measurement of membrane permeability coefficients. We combined the OLA technique with a T-junction design that allows for the controlled exposure of GUVs to a substance of interest [37, 68]. The interaction between the vesicle and the target molecule can be observed as the vesicles flows along a microfluidic channel, engulfed in the solute. The microfluidic chip is operated on a custom-built epifluorescence setup that allows the excitation of the molecule whose transport is to be studied with a target wavelength. We performed permeation studies on vesicles made from a DOPC-DOPG lipid mixture on the fluoroquinolones norfloxacin and ciprofloxacin, exploiting the autofluorescence these antibiotics show upon excitation in the UV (λ_{ex} = 350 nm). As the autofluorescing drug diffuses across the lipid membrane, the vesicles increase in brightness over time. By measuring the intensity of the vesicles at two well-defined time points, we can calculate the permeability coefficient of the respective drug to the vesicle membrane.

We measured a median permeability coefficient of 3.57×10^{-6} cm/s for norfloxacin and 4.83×10^{-6} cm/s for ciprofloxacin in a PBS buffer at pH 7.4, respectively. These values agree with the partition coefficients of the drugs, as well as previous studies on lipid vesicles [68, 98]. In addition to the permeability value at pH 7.4, we showed that norfloxacin does not permeate the PGPC membrane over a time period of 40 seconds in an acidic pH 5 environment. The reason for this is the fact that at pH 5, the zwitterionic norfloxacin molecules are predominantly in their charged form which cannot easily permeate the hydrocarbon layer of the membrane [37]. Importantly, the pH 5 measurements revealed that the observed membrane permeability is indeed due to passive diffusion and does not stem from leakage caused by shear or other forms of mechanical stress on the membrane.

The presented microfluidic platform is an advancement to previous liposome-based permeability assays, due to its incorporation of the OLA technique. OLA allows for the reliable liposome formation in a wide range of buffers and at salt concentrations that prove difficult for other methods of GUV formation [56, 23]. Vesicle formation is furthermore possible with various lipid types, as we showed in our analysis of the lipid mixtures. Another advantage of the technique is its ability to effectively encapsulate substances inside the vesicles. By encapsulating fluorescent tracers or other biomarkers, compounds can be studied that do not express fluorescence themselves [69].

We used the capability of OLA to encapsulate substance inside the vesicles in the study of proton flux through vesicle membranes [121, 228]. Charged molecules and ions typically do not cross lipid membranes via passive diffusion. Instead, their transport is mediated via transmembrane proteins that span the lipid bilayer [4]. The recreation of such channel proteins is an active field of research in disciplines like synthetic biology. One promising approach for the creation of artificial ion channels is DNA nanotechnology. Using a DNA nanostructure that has previously shown ion conductance in electrophysiological measurements [228], we attempted to measure proton transport through the pore using microfluidics. We conducted the measurements on a novel microfluidic platform that enables the GUV formation with OLA and their subsequent capture on chip using vesicle traps [69]. The immobilised vesicles can then be perfused with a substance of interest. Importantly, the vesicle are trapped in up to eight separate perfusion chambers, which allowed us to expose vesicles created in identical chemical environment to different substances.

We trapped DOPC vesicles and performed two perfusion steps on them. In the first perfusion step, half of the perfusion chambers were flushed with the DNA nanopore, whereas the other half was flushed with a simple buffer solution. In the second perfusion step, we exposed all trapped vesicles to a low pH solution. Vesicle formation, as well as the first perfusion step for all vesicles occurred at pH 7.4, the second perfusion step at pH 5.9. Importantly, we encapsulated the fluorescent pH indicator HPTS inside the vesicles. HPTS is strongly fluorescent at neutral pH, but the signal is effectively quenched at lower pH values [235]. Since the pH is defined as the negative decadic logarithm of the proton concentration, the fluorescence is a direct readout of the number of protons inside the GUVs.

To our surprise, we observed a drop in fluorescence and therefore a significant proton transport in both, the vesicles that were incubated with the DNA pore, as well as for the control group. Moreover, the fluorescent traces of both sets of vesicles showed a similar, distinct biexponential decay curve. Our analysis revealed that the initial drop in fluorescence, to about 70% of the initial value, coincides with the pH shift inside the perfusion chamber. This first decay is completed after approximately 20-40 minutes. After that, the vesicle fluorescence exponentially decreases steadily at a lower rate until the observation was terminated, 400 minutes after exposure to the low pH solution. Our analysis of the decay parameters of the secondary decrease did not show significant differences between the vesicles that were exposed to the DNA pore or the buffer solution.

It turns out that proton transport represents a special form of membrane transport, whose mechanism is still an intensively debated topic [241, 243]. While lipid membranes provide an effective barrier for the ions of basic salts, hydrogen ions (protons) are able to cross

the membrane without the assistance of transmembrane proteins. Two main theories are proposed to explain this anomaly. According to one model, proton permeation occurs along transient hydrogen-bonded chains. These act similar to an electrical wire, which is why they are termed "water wires" [241]. The second model explains the unusually high proton permeability with the presence of contaminants that act as a protonophore and thereby mediate the proton transport [243]. Furthermore, the proton permeability spans over a large range of permeability values and depends strongly on the chemical environment [241]. It is possible that this behavior of proton transport, as well as potential counter ion movement, is responsible for the distinct biexponential shape we observe in our fluorescence decay curves [247].

The high passive permeation impeded our capability to detect substantial enhancement of proton flux through the DNA pore. Although overall we observed a slightly greater decrease in fluorescence for the vesicles incubated with the DNA structures, we cannot rule out the possibility that this is an artefact stemming from differences in perfusion speed between the different experiments. Different ions such as sodium or potassium might be more suited to assess the ion translocation through the DNA nanopores, as no substantial passive transport of these ions should occur over our observation period. Advances in the development of photo stable indicators for these ions could open up the possibility for further experiments in this direction.

In a last series of experiments, we looked into a different optical method which can be combined with our microfluidic transport assays. Instead of relying on autofluorescence or fluorescent tracers to visualise the target molecules, we used Beer-Lambert's law and exploit the absorbance peak that many organic molecules express in the deep UV to visualise the transport [256]. We designed and constructed an optical setup in which we collimated UV light from a 280 nm light source and radiated it on a microfluidic T-junction chip. The deep UV light is absorbed and therefore strongly attenuated by the target molecule. Because the absorbance scales linearly with the concentration, the transmitted intensity can be used as metric for the presence of the absorbing substance.

We conducted initial validation experiments on electroformed DPhPC vesicles on the fluoroquinolone antibiotic fleroxacin. This drug expresses both an absorbance peak at the wavelength of our deep UV LED (λ_{LED}= 280 nm) and can also be imaged using its autofluorescence upon excitation at 340 nm. The microfluidic chip design we used for the absorbance experiments consists of a simple T-junction design. As before, a stream of GUVs encounters and mixes with a stream of drug solute in the microfluidic chip. The vesicles in this assay initially appear bright on a dark background, as no absorbing drug is present within the lipid

vesicle initially. As the drug permeates through the membrane, the transmitted brightness of the vesicles decreases. By comparing the transmitted intensities of GUVs at two distinct time points, we can calculate the permeability coefficient.

Using the novel assay, we obtained a mean permeability coefficient (mean $\pm$ SE) for flerofloxacin molecules through DPhPC vesicle membranes of $14.4 \pm 2.1 \times 10^{-6}$ cm/s (N = 29) in a 5 mM acetic acid buffer at pH 5. In an earlier publication, we measured the drug permeability in the same buffer using autofluorescence. In these experiments, we obtained a value of $4.1 \pm 0.2 \times 10^{-6}$ cm/s (N = 283). The two measurements hence differ by a factor of 3.5. We attribute this deviation to two main factors. The first is the fact that we were bound to lower resolution optics in the absorbance assay. We were not able to use the same objective in both experiments. The 60$\times$ water immersion objective (N.A. 1.2) used for the autofluorescence measurements does not transmit light in the deep UV. Therefore, we had to use a 40$\times$ air objective (N.A. 0.5) made of fused silica to measure the transmitted deep UV rays. However, due to its lower magnification and numeric aperture, this objective does not provide the same degree of specimen resolution and captures less light than the objective used for the autofluorescence assay. The second element impeding our measurements with the absorbance assay was the low signal to noise ratio of this method. While the detected intensity contrast between a vesicle and the background lies in the order of 60% – 100% in the autofluorescence assay, this difference is only 10% – 20% in the absorbance assay. This is despite the fact that we used a 4-fold higher drug concentration in the latter method. We also attribute the low number of detected vesicles in the absorbance assay to its low signal to noise ratio. The smaller number of data points further contributes to the deviation in measured permeability coefficient. All in all, however, our measurements show that it is possible to determine the membrane permeability exploiting a molecules absorbance property in the deep UV. Yet, in order for the absorbance experiments to match the preciseness of our permeability measurements based on autofluorescence, modifications of the setup are needed. Optical hardware more suitable for measurements in the deep UV could be introduced. Further, adjustments of the microfluidic chip design that increase absorbance contrast, such as the use of larger GUVs, are possible.

In this thesis, we worked on the development and validation of new microfluidic methods to measure passive membrane permeation. The microfluidic OLA technique is an ideal platform for this purpose, as it allows us to generate vesicles and perform transport measurements in a wide range of chemical environments and at physiologically relevant pH and salt concentrations. Due to their microfluidic characters, we only require small reagent volumes in the platforms presented here. This makes our tools suitable for use in the early stages of drug development, when only small quantities of compounds are available for experimentation [69].

Another main advantage of OLA is its ability to encapsulate substances inside the vesicle upon formation. This enables us to work with fluorescent tracers and biomarkers in our transport studies. In our experiments on proton permeation, we already made use of this property of the technique to encapsulate the pH indicator HPTS inside the GUVs. However, fluorescent biosensors are available for a large number of other molecules. In recent years, there has been particularly strong progress in the development of biosensors based on DNA aptamers [265]. DNA aptamers are short, single DNA strands that selectively bind to a target substance [266]. For example, an aptamer that is known to bind to the broad-spectrum antibiotic kanamycin A, was used by Ma *et al.* for the development of fluorescent biosensors to this drug [267]. The mechanism of the biosensor is schematically drawn in Figure 7.1.

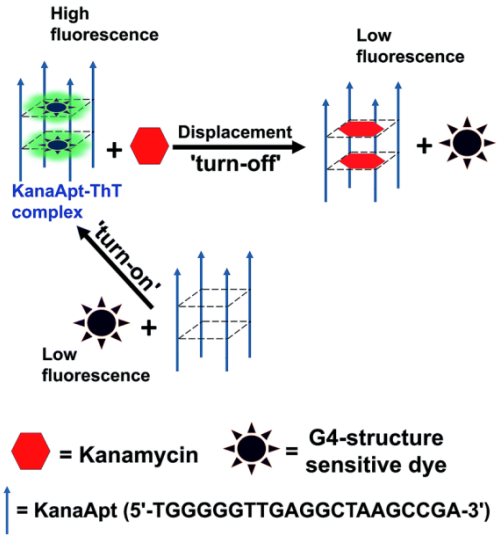

Fig. 7.1. Mechanism of fluorescent aptamer biosensor for kanamycin A. Four aptamers form a G-quadruplex (G4) structure which can bind to G4-sensitive dyes as well as the antibiotic. If bound to the fluorescent dye Thioflavin T (ThT), the aptamers form a complex that expresses a higher fluorescence than the unbound dye. The displacement of the dye with kanamycin A therefore leads to a drop in fluorescence signal, an effect which can be used to assess the presence of kanamycin molecules. Image from [267].

In solution, four kanamycin aptamer strands associate into a G-quadruplex (G4) structure. As such, both the antibiotic, as well as G4 sensitive dyes like Thioflavin T (ThT) can bind to the structure. If bound to the aptamer, the Aptamer-ThT complex expresses a stronger fluorescence than the unbound dye. The biosensor makes use of this effect, as well as of the fact that the aptamer has a higher affinity to bind to kanamycin than to the dye. If the Aptamer-ThT complex encounters a kanamycin molecule, its fluorescence is therefore effectively "turned off". It is likely that biosensors with such fluorescence properties can be used with our microfluidic tools.

Another example of a highly debated transport process that can be explored with our tools is that of free fatty acids (FFAs) permeation. Fatty acids are carboxylic acids with aliphatic chain of different lengths. Examples of three fatty acids are shown in Figure 7.2.

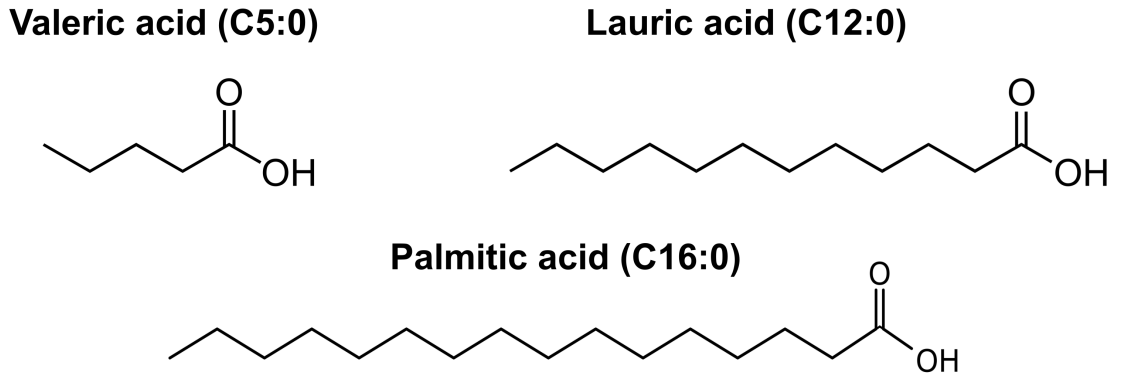

Fig. 7.2. Three examples of fatty acid molecules. The name of the acid and the number of carbon atoms are indicated.

Fatty acids are an important component in the human body and serve different structural, functional or biological roles [268]. For instance, as we know from our discussion in Chapter 1, they are a component of the lipids that make up the cell membrane [4]. However, the elevated circulation and cellular uptake of FFAs is also linked to a number of diseases such as diabetes, hypertension, atherosclerosis and non-alcoholic fatty liver disease [269]. Despite its severe medical implications, the process of membrane permeation is still not well understood. While short chained FFAs with five carbon atoms or less seem to follow the same diffusion mechanism as the small antibiotic molecules we investigated in this thesis, medium and long chained FFAs with more than 6 carbon atoms, are believed to cross the membrane via a flip-flop mechanism, as well as mediated by transporter proteins [157].

Further elements of controversy are the magnitude of the transport rate and the rate-limiting kinetic step of the transport [270].

Importantly, there exist fluorescent conjugates of the FFAs as well as fluorescent biomarkers such as the Acrylodan labeled Intestinal Fatty Acid Binding Protein (ADIFAB) that serve as indicators for FFAs [271]. Free fatty acids are therefore a promising candidate that we can study with our microfluidic assays. A possible experiment could be, for instance, to encapsulate the fluorescent biomarker ADIFAB inside GUVs using OLA and use it as a readout for the transport of FFA molecules into the vesicles. Alternatively, the fluorescently tagged version of the FFA molecules can be exposed to vesicle membranes directly using our permeability platform. In the latter case, however, it would be necessary to also investigate the effect of the fluorescent label on the transport properties of the molecule.

While the different mechanisms of passive diffusion are far from fully understood, a worthwhile aim for the further development of the microfluidic tools could be to enable the investigation of facilitated diffusion or even active transport. It is a well-known fact that many molecules do not cross cellular membranes via passive diffusion, but are mediated by porins or active transporters [4, 272]. The expansion of the OLA technique for the on-chip formation of proteoliposomes, could provide greater insight into the transport processes and the interplay between these proteins and other membrane components.

Membrane transport is fundamental for all living cells. Gaining a better understanding of the laws that govern membrane processes is not just important for the fields of drug discovery or cell signalling, but across a wide range of biological and biophysical questions. The methods presented in this thesis opens this field up to further investigation and provide a useful tool to improve our knowledge of this fundamental aspect of cellular life.

References

[1] Howard Gest. The discovery of microorganisms by robert hooke and antoni van leeuwenhoek, fellows of the royal society. *Notes and records of the Royal Society of London*, 58(2):187–201, 2004.

[2] Paolo Mazzarello. A unifying concept: the history of cell theory. *Nature Cell Biology*, 1(1):E13–E15, 1999.

[3] Nina Parker, Mark Schneegurt, Anh-Hue Thi Tu, Philip Lister, and Brian M Forster. *Microbiology*. OpenStax, 2016.

[4] Bruce Alberts, Alexander Johnson, Julian Lewis, Martin Raff, Keith Roberts, and Peter Walter. *Molecular Biology of the Cell*. Garland Science, 4th edition, 2002.

[5] Wilhelm Pfeffer. *Osmotische Untersuchungen: Studien zur Zellmechanik*. W. Engelmann, 1877.

[6] Thomas Heimburg. *Thermal Biophysics of Membranes*. John Wiley & Sons, 2008.

[7] Jonathan Lombard. Once upon a time the cell membranes: 175 years of cell boundary research. *Biology Direct*, 9(1):32, 2014.

[8] Steven H Zeisel. A brief history of choline. *Annals of Nutrition and Metabolism*, 61(3):254–258, 2012.

[9] Mary Ann Clark, Matthew Douglas, and Jung Choi. *Biology*. OpenStax, 2nd edition, 2018.

[10] E Gorter and F Grendel. On bimolecular layers of lipoids on the chromocytes of the blood. *Journal of Experimental Medicine*, 41(4):439–443, 1925.

[11] Gheorghe Benga. *Structure and Properties of Cell Membranes: Volume I*. CRC Press, 2018.

[12] David J Robertson. The ultrastructure of cell membranes and their derivatives. In *Biochemical Society Symposium*, volume 16, pages 3–43, 1959.

[13] Jonathan S Singer and Garth L Nicolson. The fluid mosaic model of the structure of cell membranes. *Science*, 175(4023):720–731, 1972.

[14] Garth L Nicolson. The fluid—mosaic model of membrane structure: Still relevant to understanding the structure, function and dynamics of biological membranes after more than 40 years. *Biochimica et Biophysica Acta (BBA)-Biomembranes*, 1838(6):1451–1466, 2014.

[15] Nicole J Yang and Marlon J Hinner. Getting across the cell membrane: an overview for small molecules, peptides, and proteins. In *Site-Specific Protein Labeling*, pages 29–53. Springer, 2015.

[16] Abhirup Mandal, Vibhuti Agrahari, Varun Khurana, Dhananjay Pal, and Ashim K Mitra. Transporter effects on cell permeability in drug delivery. *Expert Opinion on Drug Delivery*, 14(3):385–401, 2017.

[17] Hannah Sunshine and M Luisa Iruela-Arispe. Membrane lipids and cell signaling. *Current Opinion in Lipidology*, 28(5):408–413, 2017.

[18] Inchul Cho, Mark R Jackson, and Joe Swift. Roles of cross-membrane transport and signaling in the maintenance of cellular homeostasis. *Cellular and Molecular Bioengineering*, 9(2):234–246, 2016.

[19] Huseyin Demirbilek, Sonya Galcheva, Dogus Vuralli, Sara Al-Khawaga, and Khalid Hussain. Ion transporters, channelopathies, and glucose disorders. *International Journal of Molecular Sciences*, 20(10):2590, 2019.

[20] Anne H Delcour. Outer membrane permeability and antibiotic resistance. *Biochimica et Biophysica Acta (BBA)-Proteins and Proteomics*, 1794(5):808–816, 2009.

[21] Jehangir Cama, Harsha Bajaj, Stefano Pagliara, Theresa Maier, Yvonne Braun, Mathias Winterhalter, and Ulrich F Keyser. Quantification of fluoroquinolone uptake through the outer membrane channel ompf of escherichia coli. *Journal of the American Chemical Society*, 137(43):13836–13843, 2015.

[22] Demetri Psaltis, Stephen R Quake, and Changhuei Yang. Developing optofluidic technology through the fusion of microfluidics and optics. *Nature*, 442(7101):381–386, 2006.

[23] Dirk van Swaay and Andrew DeMello. Microfluidic methods for forming liposomes. *Lab Chip*, 13(5):752–767, 2013.

[24] Abolfazl Akbarzadeh, Rogaie Rezaei-Sadabady, Soodabeh Davaran, Sang Woo Joo, Nosratollah Zarghami, Younes Hanifehpour, Mohammad Samiei, Mohammad Kouhi, and Kazem Nejati-Koshki. Liposome: classification, preparation, and applications. *Nanoscale Research Letters*, 8(1):102, 2013.

[25] Alec D Bangham and RW Horne. Negative staining of phospholipids and their structural modification by surface-active agents as observed in the electron microscope. *Journal of Molecular Biology*, 8(5):660–668, 1964.

[26] David W Deamer. From "banghasomes" to liposomes: a memoir of alec bangham, 1921–2010. *The FASEB Journal*, 24(5):1308–1310, 2010.

[27] AD Bangham, Malcolm M Standish, and Jeff C Watkins. Diffusion of univalent ions across the lamellae of swollen phospholipids. *Journal of Molecular Biology*, 13(1):238–252, 1965.

[28] AD Bangham, MM Standish, and G Weissmann. The action of steroids and streptolysin s on the permeability of phospholipid structures to cations. *Journal of Molecular Biology*, 13(1):253–259, 1965.

[29] Grazia Sessa and Gerald Weissmann. Phospholipid spherules (liposomes) as a model for biological membranes. *Journal of Lipid Research*, 9(3):310–318, 1968.

[30] Rumiana Dimova. Giant vesicles and their use in assays for assessing membrane phase state, curvature, mechanics, and electrical properties. *Annual Review of Biophysics*, 48:93–119, 2019.

[31] Mehmet E Solmaz, Roshni Biswas, Shalene Sankhagowit, James R Thompson, Camilo A Mejia, Noah Malmstadt, and Michelle L Povinelli. Optical stretching of giant unilamellar vesicles with an integrated dual-beam optical trap. *Biomedical Optics Express*, 3(10):2419–2427, 2012.

[32] John P Reeves and Robert M Dowben. Formation and properties of thin-walled phospholipid vesicles. *Journal of Cellular Physiology*, 73(1):49–60, 1969.

[33] Miglena I Angelova and Dimiter S Dimitrov. Liposome electroformation. *Faraday Discussions of the Chemical Society*, 81:303–311, 1986.

[34] Omar Mertins, Nádya P da Silveira, Adriana R Pohlmann, André P Schröder, and Carlos M Marques. Electroformation of giant vesicles from an inverse phase precursor. *Biophysical Journal*, 96(7):2719–2726, 2009.

[35] Sarah L Veatch and Sarah L Keller. Seeing spots: complex phase behavior in simple membranes. *Biochimica et Biophysica Acta (BBA)-Molecular Cell Research*, 1746(3):172–185, 2005.

[36] Hammad A Faizi, Shelli L Frey, Jan Steinkühler, Rumiana Dimova, and Petia M Vlahovska. Bending rigidity of charged lipid bilayer membranes. *Soft Matter*, 15(29):6006–6013, 2019.

[37] J Cama, C Chimerel, S Pagliara, A Javer, and UF Keyser. A label-free microfluidic assay to quantitatively study antibiotic diffusion through lipid membranes. *Lab Chip*, 14(13):2303–2308, 2014.

[38] Jonas Korlach, Petra Schwille, Watt W Webb, and Gerald W Feigenson. Characterization of lipid bilayer phases by confocal microscopy and fluorescence correlation spectroscopy. *Proceedings of the National Academy of Sciences*, 96(15):8461–8466, 1999.

[39] Rumiana Dimova, Pasquale Stano, Carlos M Marques, and Peter Walde. Preparation methods for giant unilamellar vesicles. In Rumiana Dimova and Carlos M Marques, editors, *The Giant Vesicle Book*, chapter 1, pages 3–20. CRC Press, 2019.

[40] Marie Breton, Mooud Amirkavei, and Lluis M Mir. Optimization of the electroformation of giant unilamellar vesicles (guvs) with unsaturated phospholipids. *The Journal of Membrane Biology*, 248(5):827–835, 2015.

[41] Jan Steinkühler, Philippe De Tillieux, Roland L Knorr, Reinhard Lipowsky, and Rumiana Dimova. Charged giant unilamellar vesicles prepared by electroformation exhibit nanotubes and transbilayer lipid asymmetry. *Scientific Reports*, 8(1):11838, 2018.

[42] Eda Baykal-Caglar, Ebrahim Hassan-Zadeh, Bahar Saremi, and Juyang Huang. Preparation of giant unilamellar vesicles from damp lipid film for better lipid compositional uniformity. *Biochimica et Biophysica Acta (BBA)-Biomembranes*, 1818(11):2598–2604, 2012.

[43] M Gertrude Gutierrez, Shotaro Yoshida, Noah Malmstadt, and Shoji Takeuchi. Photolithographic patterned surface forms size-controlled lipid vesicles. *APL Bioengineering*, 2(1):016104, 2018.

[44] Peter Walde, Katia Cosentino, Helen Engel, and Pasquale Stano. Giant vesicles: preparations and applications. *ChemBioChem*, 11(7):848–865, 2010.

[45] Michel Wautelet. Scaling laws in the macro-, micro-and nanoworlds. *European Journal of Physics*, 22(6):601, 2001.

[46] Jake J Abbott, Zoltan Nagy, Felix Beyeler, and Bradley J Nelson. Robotics in the small, part i: microbotics. *IEEE Robotics & Automation Magazine*, 14(2):92–103, 2007.

[47] Edward M Purcell. Life at low reynolds number. *American Journal of Physics*, 45(1):3–11, 1977.

[48] David J Beebe, Glennys A Mensing, and Glenn M Walker. Physics and applications of microfluidics in biology. *Annual Review of Biomedical Engineering*, 4(1):261–286, 2002.

[49] Eric K Sackmann, Anna L Fulton, and David J Beebe. The present and future role of microfluidics in biomedical research. *Nature*, 507(7491):181–189, 2014.

[50] Dorothee Krafft, Sebastian Lopez-Castellanos, Rumiana Dimova, Ivan Ivanov, and Kai Sundmacher. Compartments for synthetic cells: Osmotically assisted separation of oil from double emulsions in microfluidic chip. *ChemBioChem*, 20(20):2604–2608, 2019.

[51] Shia-Yen Teh, Ruba Khnouf, Hugh Fan, and Abraham P Lee. Stable, biocompatible lipid vesicle generation by solvent extraction-based droplet microfluidics. *Biomicrofluidics*, 5(4):044113, 2011.

[52] K Karamdad, RV Law, JM Seddon, NJ Brooks, and O Ces. Preparation and mechanical characterisation of giant unilamellar vesicles by a microfluidic method. *Lab Chip*, 15(2):557–562, 2015.

[53] Sandro Matosevic and Brian M Paegel. Stepwise synthesis of giant unilamellar vesicles on a microfluidic assembly line. *Journal of the American Chemical Society*, 133(9):2798–2800, 2011.

[54] Yung-Chieh Tan, Kanaka Hettiarachchi, Maria Siu, Yen-Ru Pan, and Abraham Phillip Lee. Controlled microfluidic encapsulation of cells, proteins, and microbeads in lipid vesicles. *Journal of the American Chemical Society*, 128(17):5656–5658, 2006.

[55] Antoine Vian, Valentine Favrod, and Esther Amstad. Reducing the shell thickness of double emulsions using microfluidics. *Microfluidics and Nanofluidics*, 20(12):159, 2016.

[56] Siddharth Deshpande, Yaron Caspi, Anna EC Meijering, and Cees Dekker. Octanol-assisted liposome assembly on chip. *Nature Communications*, 7:10447, 2016.

[57] Laura R Arriaga, Sujit S Datta, Shin-Hyun Kim, Esther Amstad, Thomas E Kodger, Francisco Monroy, and David A Weitz. Ultrathin shell double emulsion templated giant unilamellar lipid vesicles with controlled microdomain formation. *Small*, 10(5):950–956, 2014.

[58] Justin L MacCallum and D Peter Tieleman. Structures of neat and hydrated 1-octanol from computer simulations. *Journal of the American Chemical Society*, 124(50):15085–15093, 2002.

[59] Andréas Manz, N Graber, and H áM Widmer. Miniaturized total chemical analysis systems: a novel concept for chemical sensing. *Sensors and Actuators B: Chemical*, 1(1-6):244–248, 1990.

[60] Gina S Fiorini and Daniel T Chiu. Disposable microfluidic devices: fabrication, function, and application. *BioTechniques*, 38(3):429–446, 2005.

[61] Younan Xia and George M Whitesides. Soft lithography. *Annual Review of Materials Science*, 28(1):153–184, 1998.

[62] George M Whitesides, Emanuele Ostuni, Shuichi Takayama, Xingyu Jiang, and Donald E Ingber. Soft lithography in biology and biochemistry. *Annual Review of Biomedical Engineering*, 3(1):335–373, 2001.

[63] Yujie Ma, Julian Thiele, Loai Abdelmohsen, Jinge Xu, and Wilhelm TS Huck. Biocompatible macro-initiators controlling radical retention in microfluidic on-chip photopolymerization of water-in-oil emulsions. *Chemical Communications*, 50(1):112–114, 2014.

[64] Siddharth Deshpande and Cees Dekker. On-chip microfluidic production of cell-sized liposomes. *Nature Protocols*, 13(5):856, 2018.

[65] Shohei Kaneda, Koichi Ono, Tatsuhiro Fukuba, Takahiko Nojima, Takatoki Yamamoto, and Teruo Fujii. Modification of the glass surface property in pdms-glass hybrid microfluidic devices. *Analytical Sciences*, 28(1):39–44, 2012.

[66] Tatiana Trantidou, Yuval Elani, Edward Parsons, and Oscar Ces. Hydrophilic surface modification of pdms for droplet microfluidics using a simple, quick, and robust method via pva deposition. *Microsystems & Nanoengineering*, 3:16091, 2017.

[67] JM Gohil and P Ray. Studies on oxalic acid as a crosslinker of polyvinyl alcohol. *Polymers and Polymer Composites*, 17(7):403–410, 2009.

[68] Michael Schaich, Jehangir Cama, Kareem Al Nahas, Diana Sobota, Hannah Sleath, Kevin Jahnke, Siddharth Deshpande, Cees Dekker, and Ulrich F Keyser. An integrated microfluidic platform for quantifying drug permeation across biomimetic vesicle membranes. *Molecular Pharmaceutics*, 2019.

[69] Kareem Al Nahas, Jehangir Cama, Michael Schaich, K Hammond, S Deshpande, Cees Dekker, MG Ryadnov, and UF Keyser. A microfluidic platform for the characterisation of membrane active antimicrobials. *Lab Chip*, 19(5):837–844, 2019.

[70] Siddharth Deshpande, Anthony Birnie, and Cees Dekker. On-chip density-based purification of liposomes. *Biomicrofluidics*, 11(3):034106, 2017.

[71] Siddharth Deshpande, Willem Kasper Spoelstra, Marleen van Doorn, Jacob Kerssemakers, and Cees Dekker. Mechanical division of cell-sized liposomes. *ACS Nano*, 12(3):2560–2568, 2018.

[72] Daniel J Estes and Michael Mayer. Giant liposomes in physiological buffer using electroformation in a flow chamber. *Biochimica et Biophysica Acta (BBA)-Biomembranes*, 1712(2):152–160, 2005.

[73] Thomas H Vaughn, HR Suter, Lester G Lundsted, and Marc G Kramer. Properties of some newly developed nonionic detergents. *Journal of the American Oil Chemists' Society*, 28(7):294–299, 1951.

[74] Joseph G Moloughney and Noah Weisleder. Poloxamer 188 (p188) as a membrane resealing reagent in biomedical applications. *Recent Patents on Biotechnology*, 6(3):200–211, 2012.

[75] Irving R Schmolka. A review of block polymer surfactants. *Journal of the American Oil Chemists' Society*, 54(3):110–116, 1977.

[76] Françoise Bonneté. Macromolecular crystallization controlled by colloidal interactions: the case of urate oxidase. In Marcello Rubens and Barsi Andreeta, editors, *Crystallization - Science and Technology*, chapter 13, pages 349–378. InTech Open, 2012.

[77] Martin Emanuele and Balu Balasubramaniam. Differential effects of commercial-grade and purified poloxamer 188 on renal function. *Drugs in R&D*, 14(2):73–83, 2014.

[78] Patricia Adams-Graves, Amos Kedar, Mabel Koshy, Martin Steinberg, Robert Veith, Daniel Ward, Rebekah Crawford, Suzanne Edwards, James Bustrack, and Martin Emanuele. Rheothrx (poloxamer 188) injection for the acute painful episode of sickle cell disease: a pilot study. *Blood*, 90(5):2041–2046, 1997.

[79] Eugene P Orringer, James F Casella, Kenneth I Ataga, Mabel Koshy, Patricia Adams-Graves, Lori Luchtman-Jones, Ted Wun, Masayo Watanabe, Frank Shafer, Abdullah Kutlar, et al. Purified poloxamer 188 for treatment of acute vaso-occlusive crisis of sickle cell disease: a randomized controlled trial. *Jama*, 286(17):2099–2106, 2001.

[80] Raphael C Lee, L Philip River, Fu-Shih Pan, Li Ji, and Robert L Wollmann. Surfactant-induced sealing of electropermeabilized skeletal muscle membranes in vivo. *Proceedings of the National Academy of Sciences*, 89(10):4524–4528, 1992.

[81] Stacey A Maskarinec, Jürgen Hannig, Raphael C Lee, and Ka Yee C Lee. Direct observation of poloxamer 188 insertion into lipid monolayers. *Biophysical Journal*, 82(3):1453–1459, 2002.

[82] Colette Weingarten, Nereide S Santos Magalhaes, Adam Baszkin, Simon Benita, and Monique Seiller. Interactions of a non-ionic aba copolymer surfactant with phospholipid monolayers: possible relevance to emulsion stabilization. *International Journal of Pharmaceutics*, 75(2-3):171–179, 1991.

[83] Chi-Yuan Cheng, Jia-Yu Wang, Ravinath Kausik, Ka Yee C Lee, and Songi Han. Nature of interactions between peo-ppo-peo triblock copolymers and lipid membranes:(ii) role of hydration dynamics revealed by dynamic nuclear polarization. *Biomacromolecules*, 13(9):2624–2633, 2012.

[84] Goran T Vladisavljević, Ruqaya Al Nuumani, and Seyed Ali Nabavi. Microfluidic production of multiple emulsions. *Micromachines*, 8(3):75, 2017.

[85] HW Tan, AR Abdul Aziz, and MK Aroua. Glycerol production and its applications as a raw material: A review. *Renewable and Sustainable Energy Reviews*, 27:118–127, 2013.

[86] Kelly M Schultz and Eric M Furst. High-throughput rheology in a microfluidic device. *Lab Chip*, 11(22):3802–3809, 2011.

[87] Evangelia Roumpea, Nina M Kovalchuk, Maxime Chinaud, Emilia Nowak, Mark JH Simmons, and Panagiota Angeli. Experimental studies on droplet formation in a flow-focusing microchannel in the presence of surfactants. *Chemical Engineering Science*, 195:507–518, 2019.

[88] S ten Klooster, S Sahin, and K Schroën. Monodisperse droplet formation by spontaneous and interaction based mechanisms in partitioned edge microfluidic device. *Scientific Reports*, 9(1):7820, 2019.

[89] Nian-Sheng Cheng. Formula for the viscosity of a glycerol- water mixture. *Industrial & Engineering Chemistry Research*, 47(9):3285–3288, 2008.

[90] Bo-Bi Tzeng and Yung-Shin Sun. Design and fabrication of a microfluidic viscometer based on electrofluidic circuits. *Micromachines*, 9(8):375, 2018.

[91] Agnieszka Nowacka, Stephane Douezan, L Wadsö, Daniel Topgaard, and Emma Sparr. Small polar molecules like glycerol and urea can preserve the fluidity of lipid bilayers under dry conditions. *Soft Matter*, 8(5):1482–1491, 2012.

[92] Abraham D Stroock, Stephan KW Dertinger, Armand Ajdari, Igor Mezić, Howard A Stone, and George M Whitesides. Chaotic mixer for microchannels. *Science*, 295(5555):647–651, 2002.

[93] Peter Westh. Unilamellar dmpc vesicles in aqueous glycerol: preferential interactions and thermochemistry. *Biophysical Journal*, 84(1):341–349, 2003.

[94] Witold K Surewicz. Membrane actions of water-soluble fusogens: effect of dimethyl sulfoxide, glycerol and sucrose on lipid bilayer order and fluidity. *Chemistry and Physics of Lipids*, 34(4):363–372, 1984.

[95] Albert Leo, Corwin Hansch, and David Elkins. Partition coefficients and their uses. *Chemical Reviews*, 71(6):525–616, 1971.

[96] Younggil Kwon. *Handbook of essential pharmacokinetics, pharmacodynamics and drug metabolism for industrial scientists*. Springer Science & Business Media, 2001.

[97] Dong-Sun Lee, Hee-Jung Han, Kun Kim, Won-Bong Park, Jung-Kil Cho, and Jae-Hyun Kim. Dissociation and complexation of fluoroquinolone analogues. *Journal of Pharmaceutical and Biomedical Analysis*, 12(2):157–164, 1994.

[98] Sowmya Purushothaman, Jehangir Cama, and Ulrich F Keyser. Dependence of norfloxacin diffusion across bilayers on lipid composition. *Soft Matter*, 12(7):2135–2144, 2016.

[99] Gregor Cevc, Ida Berts, Stefan F Fischer, Joachim O Radler, and Bert Nickel. Nanostructures in n-octanol equilibrated with additives and/or water. *Langmuir*, 34(21):6285–6295, 2018.

[100] Bin Chen and J Ilja Siepmann. Microscopic structure and solvation in dry and wet octanol. *The Journal of Physical Chemistry B*, 110(8):3555–3563, 2006.

[101] NP Franks, MH Abraham, and WR Lieb. Molecular organization of liquid n-octanol: An x-ray diffraction analysis. *Journal of Pharmaceutical Sciences*, 82(5):466–470, 1993.

[102] Kaarlo Sakari Vahvaselkä, RITVA Serimaa, and Mika Torkkeli. Determination of liquid structures of the primary alcohols methanol, ethanol, 1-propanol, 1-butanol and 1-octanol by x-ray scattering. *Journal of Applied Crystallography*, 28(2):189–195, 1995.

[103] Michael J Pringle, Kenneth B Brown, and Keith W Miller. Can the lipid theories of anesthesia account for the cutoff in anesthetic potency in homologous series of alcohols? *Molecular Pharmacology*, 19(1):49–55, 1981.

[104] Beate Griepernau, Simon Leis, Matthias F Schneider, Martin Sikor, Daniel Steppich, and Rainer A Böckmann. 1-alkanols and membranes: a story of attraction. *Biochimica Et Biophysica Acta (BBA)-Biomembranes*, 1768(11):2899–2913, 2007.

[105] JD Whitby. Alcohol in anaesthesia and surgical resuscitation. *Anaesthesia*, 35(5):502–505, 1980.

[106] Andreas Missner and Peter Pohl. 110 years of the meyer–overton rule: predicting membrane permeability of gases and other small compounds. *ChemPhysChem*, 10(9-10):1405–1414, 2009.

[107] Marieke Kranenburg and Berend Smit. Phase behavior of model lipid bilayers. *The Journal of Physical Chemistry B*, 109(14):6553–6563, 2005.

[108] Thomas Heimburg and Andrew D Jackson. The thermodynamics of general anesthesia. *Biophysical Journal*, 92(9):3159–3165, 2007.

[109] Frank K Hui and Peter G Barton. Mesomorphic behaviour of some phospholipids with aliphatic alcohols and other non-ionic substances. *Biochimica et Biophysica Acta (BBA)-Lipids and Lipid Metabolism*, 296(3):510–517, 1973.

[110] AW Eliasz, D Chapman, and DF Ewing. Phospholipid phase transitions. effects of n-alcohols, n-monocarboxylic acids, phenylalkyl alcohols and quatenary ammonium compounds. *Biochimica et Biophysica Acta (BBA)-Biomembranes*, 448(2):220–233, 1976.

[111] Martyn W Hill. The effect of anaesthetic-like molecules on the phase transition in smectic mesophases of dipalmitoyllecithin i. the normal alcohol up to c= 9 and three inhalation anaesthetics. *Biochimica et Biophysica Acta (BBA)-Biomembranes*, 356(1):117–124, 1974.

[112] AG Lee. Interactions between anesthetics and lipid mixtures. normal alcohols. *Biochemistry*, 15(11):2448–2454, 1976.

[113] Elizabeth L Godden, R Adron Harris, and Thomas V Dunwiddie. Correlation between molecular volume and effects of n-alcohols on human neuronal nicotinic acetylcholine receptors expressed in xenopus oocytes. *Journal of Pharmacology and Experimental Therapeutics*, 296(3):716–722, 2001.

[114] Thomas H Aagaard, Mette N Kristensen, and Peter Westh. Packing properties of 1-alkanols and alkanes in a phospholipid membrane. *Biophysical Chemistry*, 119(1):61–68, 2006.

[115] Helgi I Ingólfsson and Olaf S Andersen. Alcohol's effects on lipid bilayer properties. *Biophysical Journal*, 101(4):847–855, 2011.

[116] Lewen Yang and James T Kindt. Simulation study of the permeability of a model lipid membrane at the fluid–solid phase transition. *Langmuir*, 31(7):2187–2195, 2015.

[117] Andreas Blicher, Katarzyna Wodzinska, Matthias Fidorra, Mathias Winterhalter, and Thomas Heimburg. The temperature dependence of lipid membrane permeability, its quantized nature, and the influence of anesthetics. *Biophysical Journal*, 96(11):4581–4591, 2009.

[118] Michael Schaich, Diana Sobota, Hannah Sleath, Jehangir Cama, and Ulrich F Keyser. Characterization of lipid composition and diffusivity in ola generated vesicles. *Biochimica et Biophysica Acta (BBA)-Biomembranes*, page 183359, 2020.

[119] Su Li, Peichi Hu, and Noah Malmstadt. Confocal imaging to quantify passive transport across biomimetic lipid membranes. *Analytical Chemistry*, 82(18):7766–7771, 2010.

[120] Jonathan C McIntyre and Richard G Sleight. Fluorescence assay for phospholipid membrane asymmetry. *Biochemistry*, 30(51):11819–11827, 1991.

[121] Alexander Ohmann, Chen-Yu Li, Christopher Maffeo, Kareem Al Nahas, Kevin N Baumann, Kerstin Göpfrich, Jejoong Yoo, Ulrich F Keyser, and Aleksei Aksimentiev. A synthetic enzyme built from dna flips 10 7 lipids per second in biological membranes. *Nature Communications*, 9(1):2426, 2018.

[122] Elizabeth S Rowe, Fengli Zhang, Tina Wu Leung, James S Parr, and Peter T Guy. Thermodynamics of membrane partitioning for a series of n-alcohols determined by titration calorimetry: role of hydrophobic effects. *Biochemistry*, 37(8):2430–2440, 1998.

[123] Robert S Cantor. Bilayer partition coefficients of alkanols: predicted effects of varying lipid composition. *The Journal of Physical Chemistry B*, 105(31):7550–7553, 2001.

[124] Kui Yang and Xianlin Han. Lipidomics: techniques, applications, and outcomes related to biomedical sciences. *Trends in Biochemical Sciences*, 41(11):954–969, 2016.

[125] Paul A Beales, Barbara Ciani, and Alexa J Cleasby. Nature's lessons in design: nanomachines to scaffold, remodel and shape membrane compartments. *Physical Chemistry Chemical Physics*, 17(24):15489–15507, 2015.

[126] Vadim A Frolov, Anna V Shnyrova, and Joshua Zimmerberg. Lipid polymorphisms and membrane shape. *Cold Spring Harbor Perspectives in Biology*, 3(11):a004747, 2011.

[127] Els van den Brink-van der Laan, J Antoinette Killian, and Ben de Kruijff. Nonbilayer lipids affect peripheral and integral membrane proteins via changes in the lateral pressure profile. *Biochimica et Biophysica Acta (BBA)-Biomembranes*, 1666(1-2):275–288, 2004.

[128] Ben de Kruijff. Lipid polymorphism and biomembrane function. *Current Opinion in Chemical Biology*, 1(4):564–569, 1997.

[129] Philippe F Devaux. Static and dynamic lipid asymmetry in cell membranes. *Biochemistry*, 30(5):1163–1173, 1991.

[130] Ana Tari and Leaf Huang. Structure and function relationship of phosphatidylglycerol in the stabilization of phosphatidylethanolamine bilayer. *Biochemistry*, 28(19):7708–7712, 1989.

[131] Krzysztof Murzyn, Tomasz Róg, and Marta Pasenkiewicz-Gierula. Phosphatidylethanolamine-phosphatidylglycerol bilayer as a model of the inner bacterial membrane. *Biophysical Journal*, 88(2):1091–1103, 2005.

[132] Wei Zhao, Tomasz Róg, Andrey A Gurtovenko, Ilpo Vattulainen, and Mikko Karttunen. Atomic-scale structure and electrostatics of anionic palmitoyloleoylphosphatidylglycerol lipid bilayers with na+ counterions. *Biophysical Journal*, 92(4):1114–1124, 2007.

[133] Paulo FF Almeida, Winchil LC Vaz, and TE Thompson. Lateral diffusion in the liquid phases of dimyristoylphosphatidylcholine/cholesterol lipid bilayers: a free volume analysis. *Biochemistry*, 31(29):6739–6747, 1992.

[134] Begona Ugarte-Uribe, Kushal Kumar Das, and Ana J. Garcia-Saez. Lipid and protein mobility in giant unilamellar vesicles. In Rumiana Dimova and Carlos M Marques, editors, *The Giant Vesicle Book*, chapter 21, pages 455–471. CRC Press, 2019.

[135] Eric AJ Reits and Jacques J Neefjes. From fixed to frap: measuring protein mobility and activity in living cells. *Nature Cell Biology*, 3(6):E145–E147, 2001.

[136] Anne K Kenworthy. Fluorescence recovery after photobleaching studies of lipid rafts. In *Lipid Rafts*, pages 179–192. Springer, 2007.

[137] Daniel Axelrod, DE Koppel, J Schlessinger, Elliot Elson, and Watt W Webb. Mobility measurement by analysis of fluorescence photobleaching recovery kinetics. *Biophysical Journal*, 16(9):1055–1069, 1976.

[138] DM Soumpasis. Theoretical analysis of fluorescence photobleaching recovery experiments. *Biophysical Journal*, 41(1):95–97, 1983.

[139] Yun Chen, B Christoffer Lagerholm, Bing Yang, and Ken Jacobson. Methods to measure the lateral diffusion of membrane lipids and proteins. *Methods*, 39(2):147–153, 2006.

[140] Jean-François Tocanne, Laurence Dupou-Cézanne, and André Lopez. Lateral diffusion of lipids in model and natural membranes. *Progress in Lipid Research*, 33(3):203–237, 1994.

[141] Lin Guo, Jia Yi Har, Jagadish Sankaran, Yimian Hong, Balakrishnan Kannan, and Thorsten Wohland. Molecular diffusion measurement in lipid bilayers over wide concentration ranges: a comparative study. *ChemPhysChem*, 9(5):721–728, 2008.

[142] Radek Macháň, Yong Hwee Foo, and Thorsten Wohland. On the equivalence of fcs and frap: simultaneous lipid membrane measurements. *Biophysical Journal*, 111(1):152–161, 2016.

[143] Andrey Filippov, Greger Orädd, and Göran Lindblom. Influence of cholesterol and water content on phospholipid lateral diffusion in bilayers. *Langmuir*, 19(16):6397–6400, 2003.

[144] Frédéric Pincet, Vladimir Adrien, Rong Yang, Jérôme Delacotte, James E Rothman, Wladimir Urbach, and David Tareste. Frap to characterize molecular diffusion and interaction in various membrane environments. *PLoS One*, 11(7):e0158457, 2016.

[145] Greger Orädd, Göran Wikander, Göran Lindblom, and Lennart B-Å Johansson. Effect of glycerol on the translational and rotational motions in lipid bilayers studied by pulsed-field gradient 1 h nmr, epr and time-resolved fluorescence spectroscopy. *Journal of the Chemical Society, Faraday Transactions*, 90(2):305–309, 1994.

[146] Peter Jönsson, Magnus P Jonsson, Jonas O Tegenfeldt, and Fredrik Höök. A method improving the accuracy of fluorescence recovery after photobleaching analysis. *Biophysical Journal*, 95(11):5334–5348, 2008.

[147] Simona Rifici, Giovanna D'Angelo, Cristina Crupi, Caterina Branca, Valeria Conti Nibali, Carmelo Corsaro, and Ulderico Wanderlingh. Influence of alcohols on the lateral diffusion in phospholipid membranes. *The Journal of Physical Chemistry B*, 120(7):1285–1290, 2016.

[148] Anna L Duncan, Tyler Reddy, Heidi Koldsø, Jean Hélie, Philip W Fowler, Matthieu Chavent, and Mark SP Sansom. Protein crowding and lipid complexity influence the nanoscale dynamic organization of ion channels in cell membranes. *Scientific Reports*, 7(1):16647, 2017.

[149] Fen Zhang, Greta M Lee, and Ken Jacobson. Protein lateral mobility as a reflection of membrane microstructure. *Bioessays*, 15(9):579–588, 1993.

[150] Ken Jacobson, Ping Liu, and B Christoffer Lagerholm. The lateral organization and mobility of plasma membrane components. *Cell*, 177(4):806–819, 2019.

[151] WD Stein. The molecular basis of diffusion across cell membranes. *The movement of molecules across cell membranes*, pages 65–125, 1967.

[152] Begona Ugarte-Uribe, Ana J. Garcia-Saez, and Mireille M.A.E. Claessens. Membrane permeability measurements. In Rumiana Dimova and Carlos M Marques, editors, *The Giant Vesicle Book*, chapter 20, pages 437–451. CRC Press, 2019.

[153] Jehangir Cama, Michael Schaich, Kareem Al Nahas, Silvia Hernández-Ainsa, Stefano Pagliara, and Ulrich F Keyser. Direct optofluidic measurement of the lipid permeability of fluoroquinolones. *Scientific Reports*, 6:32824, 2016.

[154] Massimiliano Pio Di Cagno, Fabrizio Clarelli, Jon Vabeno, Christina Lesley, Sokar Darsim Rahman, Jennifer Cauzzo, Erica Franceschinis, Nicola Realdon, and Paul C Stein. Experimental determination of drug diffusion coefficients in unstirred aqueous environments by temporally resolved concentration measurements. *Molecular Pharmaceutics*, 15(4):1488–1494, 2018.

[155] AM Kleinfeld. Lipid phase fatty acid flip-flop, is it fast enough for cellular transport? *The Journal of membrane biology*, 175(2):79–86, 2000.

[156] JA Hamilton. Transport of fatty acids across membranes by the diffusion mechanism. *Prostaglandins, Leukotrienes and Essential Fatty Acids*, 60(5-6):291–297, 1999.

[157] Frits Kamp and James A Hamilton. How fatty acids of different chain length enter and leave cells by free diffusion. *Prostaglandins, Leukotrienes and Essential Fatty Acids*, 75(3):149–159, 2006.

[158] H Ti Tien and A Louise Diana. Bimolecular lipid membranes: a review and a summary of some recent studies. *Chemistry and Physics of Lipids*, 2(1):55–101, 1968.

[159] John Gutknecht and DC Tosteson. Diffusion of weak acids across lipid bilayer membranes: effects of chemical reactions in the unstirred layers. *Science*, 182(4118):1258–1261, 1973.

[160] Mathias Winterhalter. Black lipid membranes. *Current Opinion in Colloid & Interface Science*, 5(3-4):250–255, 2000.

[161] John Gutknecht, MA Bisson, and FC Tosteson. Diffusion of carbon dioxide through lipid bilayer membranes. effects of carbonic anhydrase, bicarbonate, and unstirred layers. *The Journal of General Physiology*, 69(6):779, 1977.

[162] Manfred Kansy, Frank Senner, and Klaus Gubernator. Physicochemical high throughput screening: parallel artificial membrane permeation assay in the description of passive absorption processes. *Journal of Medicinal Chemistry*, 41(7):1007–1010, 1998.

[163] Phillip Kuhn, Klaus Eyer, Steffen Allner, Dario Lombardi, and Petra S Dittrich. A microfluidic vesicle screening platform: monitoring the lipid membrane permeability of tetracyclines. *Analytical Chemistry*, 83(23):8877–8885, 2011.

[164] D Galinis-Luciani, L Nguyen, and M Yazdanian. Is pampa a useful tool for discovery? *Journal of Pharmaceutical Sciences*, 96(11):2886–2892, 2007.

[165] Yang Jun Kang and Sung Yang. Fluidic low pass filter for hydrodynamic flow stabilization in microfluidic environments. *Lab Chip*, 12(10):1881–1889, 2012.

[166] Arthur D Edelstein, Mark A Tsuchida, Nenad Amodaj, Henry Pinkard, Ronald D Vale, and Nico Stuurman. Advanced methods of microscope control using μmanager software. *Journal of Biological Methods*, 1(2):E10, 2014.

[167] Maryn McKenna. Antibiotic resistance: the last resort. *Nature News*, 499(7459):394, 2013.

[168] European Centre for Disease Prevention and Control. Surveillance of antimicrobial resistance in europe 2016. *Annual Report of the European Antimicrobial Resistance Surveillance Network (EARS-Net)*, 2017.

[169] Jessica MA Blair, Mark A Webber, Alison J Baylay, David O Ogbolu, and Laura JV Piddock. Molecular mechanisms of antibiotic resistance. *Nature Reviews Microbiology*, 13(1):42–51, 2015.

[170] Lynn L Silver. A gestalt approach to gram-negative entry. *Bioorganic & Medicinal Chemistry*, 24(24):6379–6389, 2016.

[171] Jean-Marie Pagès, Chloë E James, and Mathias Winterhalter. The porin and the permeating antibiotic: a selective diffusion barrier in gram-negative bacteria. *Nature Reviews Microbiology*, 6(12):893–903, 2008.

[172] David A Six, Thomas Krucker, and Jennifer A Leeds. Advances and challenges in bacterial compound accumulation assays for drug discovery. *Current Opinion in Chemical Biology*, 44:9–15, 2018.

[173] Mariano Andrea Scorciapino, Silvia Acosta-Gutierrez, Dehbia Benkerrou, Tommaso D'Agostino, Giuliano Malloci, Susruta Samanta, Igor Bodrenko, and Matteo Ceccarelli. Rationalizing the permeation of polar antibiotics into gram-negative bacteria. *Journal of Physics: Condensed Matter*, 29(11):113001, 2017.

[174] Imrich Barák and Katarína Muchová. The role of lipid domains in bacterial cell processes. *International Journal of Molecular Sciences*, 14(2):4050–4065, 2013.

[175] Susanne F Fenz and Kheya Sengupta. Giant vesicles as cell models. *Integrative Biology*, 4(9):982–995, 2012.

[176] Hannah Stein, Susann Spindler, Navid Bonakdar, Chun Wang, and Vahid Sandoghdar. Production of isolated giant unilamellar vesicles under high salt concentrations. *Frontiers in Physiology*, 8:63, 2017.

[177] Maxim G Ryadnov, Galina V Mukamolova, Ayman S Hawrani, James Spencer, and Roscoe Platt. Re coil: an antimicrobial peptide regulator. *Angewandte Chemie International Edition*, 48(51):9676–9679, 2009.

[178] Anthony G Vecchiarelli, Min Li, Michiyo Mizuuchi, and Kiyoshi Mizuuchi. Differential affinities of mind and mine to anionic phospholipid influence min patterning dynamics in vitro. *Molecular Microbiology*, 93(3):453–463, 2014.

[179] Paulina D Rakowska, Haibo Jiang, Santanu Ray, Alice Pyne, Baptiste Lamarre, Matthew Carr, Peter J Judge, Jascindra Ravi, Ulla IM Gerling, Beate Koksch, et al. Nanoscale imaging reveals laterally expanding antimicrobial pores in lipid bilayers. *Proceedings of the National Academy of Sciences*, 110(22):8918–8923, 2013.

[180] H Nikaido and DG Thanassi. Penetration of lipophilic agents with multiple protonation sites into bacterial cells: tetracyclines and fluoroquinolones as examples. *Antimicrobial Agents and Chemotherapy*, 37(7):1393, 1993.

[181] Valentina Uivarosi. Metal complexes of quinolone antibiotics and their applications: an update. *Molecules*, 18(9):11153–11197, 2013.

[182] David S Wishart, Yannick D Feunang, An C Guo, Elvis J Lo, Ana Marcu, Jason R Grant, Tanvir Sajed, Daniel Johnson, Carin Li, Zinat Sayeeda, et al. Drugbank 5.0: a major update to the drugbank database for 2018. *Nucleic Acids Research*, 46(D1):D1074–D1082, 2018.

[183] M Rhia L Stone, Mark S Butler, Wanida Phetsang, Matthew A Cooper, and Mark AT Blaskovich. Fluorescent antibiotics: new research tools to fight antibiotic resistance. *Trends in Biotechnology*, 36(5):523–536, 2018.

[184] Sunil Shah, Anjali Chandra, Amanjot Kaur, Nirupama Sabnis, Andras Lacko, Zygmunt Gryczynski, Rafal Fudala, and Ignacy Gryczynski. Fluorescence properties of doxorubicin in pbs buffer and pva films. *Journal of Photochemistry and Photobiology B: Biology*, 170:65–69, 2017.

[185] Anas Allam, Laure Maigre, Julia Vergalli, Estelle Dumont, Bertrand Cinquin, Rodolphe Alves de Sousa, Jelena Pajovic, Elizabeth Pinet, Nikaia Smith, Jean-Philippe Herbeuval, et al. Microspectrofluorimetry to dissect the permeation of ceftazidime in gram-negative bacteria. *Scientific Reports*, 7(1):986, 2017.

[186] Kittichoat Tiyanont, Thierry Doan, Michael B Lazarus, Xiao Fang, David Z Rudner, and Suzanne Walker. Imaging peptidoglycan biosynthesis in bacillus subtilis with fluorescent antibiotics. *Proceedings of the National Academy of Sciences*, 103(29):11033–11038, 2006.

[187] Kamilia Abdelraouf, Kai-Tai Chang, Taijun Yin, Ming Hu, and Vincent H Tam. Uptake of polymyxin b into renal cells. *Antimicrobial Agents and Chemotherapy*, 58(7):4200–4202, 2014.

[188] M Rhia L Stone, Muriel Masi, Wanida Phetsang, Jean-Marie Pagès, Matthew A Cooper, and Mark AT Blaskovich. Fluoroquinolone-derived fluorescent probes for studies of bacterial penetration and efflux. *MedChemComm*, 10(6):901–906, 2019.

[189] Alexander P Demchenko, Yves Mély, Guy Duportail, and Andrey S Klymchenko. Monitoring biophysical properties of lipid membranes by environment-sensitive fluorescent probes. *Biophysical Journal*, 96(9):3461–3470, 2009.

[190] Alex Avdeef, Stefanie Bendels, Li Di, Bernard Faller, Manfred Kansy, Kiyohiko Sugano, and Yukinori Yamauchi. Pampa—critical factors for better predictions of absorption. *Journal of Pharmaceutical Sciences*, 96(11):2893–2909, 2007.

[191] Aaron M Streets and Yanyi Huang. Chip in a lab: Microfluidics for next generation life science research. *Biomicrofluidics*, 7(1):011302, 2013.

[192] Jia Zeng, Heather M Eckenrode, Susan M Dounce, and Hai-Lung Dai. Time-resolved molecular transport across living cell membranes. *Biophysical Journal*, 104(1):139–145, 2013.

[193] Trang T Nguyen, Kelvin Rembert, and John C Conboy. Label-free detection of drug-membrane association using ultraviolet- visible sum-frequency generation. *Journal of the American Chemical Society*, 131(4):1401–1403, 2009.

[194] José B A Custódio, Leonor M Almeida, and Vitor MC Madeira. A reliable and rapid procedure to estimate drug partitioning in biomembranes. *Biochemical and Biophysical Research Communications*, 176(3):1079–1085, 1991.

[195] Christopher B Fox, Robert A Horton, and Joel M Harris. Detection of drug- membrane interactions in individual phospholipid vesicles by confocal raman microscopy. *Analytical Chemistry*, 78(14):4918–4924, 2006.

[196] Tsutomu Watanabe. Infective heredity of multiple drug resistance in bacteria. *Bacteriological Reviews*, 27(1):87–115, 1963.

[197] Ida Louise Jørgensen, Gerdi Christine Kemmer, and Thomas Günther Pomorski. Membrane protein reconstitution into giant unilamellar vesicles: a review on current techniques. *European Biophysics Journal*, 46(2):103–119, 2017.

[198] June-Bum Kim. Channelopathies. *Clinical and Experimental Pediatrics*, 57(1):1–18, 2014.

[199] Jane C Davies, Eric W F W Alton, and Andrew Bush. Cystic fibrosis. *BMJ*, 335(7632):1255–1259, 2007.

[200] John R Riordan, Johanna M Rommens, Bat-sheva Kerem, Noa Alon, Richard Rozmahel, Zbyszko Grzelczak, Julian Zielenski, Si Lok, Natasa Plavsic, Jia-Ling Chou, et al. Identification of the cystic fibrosis gene: cloning and characterization of complementary dna. *Science*, 245(4922):1066–1073, 1989.

[201] William A Catterall. Dravet syndrome: a sodium channel interneuronopathy. *Current Opinion in Physiology*, 2:42–50, 2018.

[202] Arsalan Anwar, Sidra Saleem, Urvish K Patel, Kogulavadanan Arumaithurai, and Preeti Malik. Dravet syndrome: An overview. *Cureus*, 11(6):e5006, 2019.

[203] Claire Edmondson and Jane C Davies. Current and future treatment options for cystic fibrosis lung disease: latest evidence and clinical implications. *Therapeutic Advances in Chronic Disease*, 7(3):170–183, 2016.

[204] Thomas E DeCoursey. Voltage and ph sensing by the voltage-gated proton channel, hv1. *Journal of the Royal Society Interface*, 15(141):20180108, 2018.

[205] Margaret Fogel and JW Hastings. Bioluminescence: mechanism and mode of control of scintillon activity. *Proceedings of the National Academy of Sciences*, 69(3):690–693, 1972.

[206] RC Thomas and RW Meech. Hydrogen ion currents and intracellular ph in depolarized voltage-clamped snail neurones. *Nature*, 299(5886):826–828, 1982.

[207] Thomas E DeCoursey. The voltage-gated proton channel: a riddle, wrapped in a mystery, inside an enigma. *Biochemistry*, 54(21):3250–3268, 2015.

[208] Thomas E DeCoursey. Voltage-gated proton channels: molecular biology, physiology, and pathophysiology of the hv family. *Physiological Reviews*, 93(2):599–652, 2013.

[209] Thomas E DeCoursey and Jonathan Hosler. Philosophy of voltage-gated proton channels. *Journal of The Royal Society Interface*, 11(92):20130799, 2014.

[210] Berton C Pressman. Biological applications of ionophores. *Annual Review of Biochemistry*, 45(1):501–530, 1976.

[211] Catalin Chimerel, Andrew J Murray, Enno R Oldewurtel, David K Summers, and Ulrich F Keyser. The effect of bacterial signal indole on the electrical properties of lipid membranes. *ChemPhysChem*, 14(2):417–423, 2013.

[212] Catalin Chimerel, Christopher M Field, Silvia Piñero-Fernandez, Ulrich F Keyser, and David K Summers. Indole prevents escherichia coli cell division by modulating membrane potential. *Biochimica et Biophysica Acta (BBA)-Biomembranes*, 1818(7):1590–1594, 2012.

[213] Nagendran Tharmalingam, Elamparithi Jayamani, Rajmohan Rajamuthiah, Dawilmer Castillo, Beth Burgwyn Fuchs, Michael J Kelso, and Eleftherios Mylonakis. Activity of a novel protonophore against methicillin-resistant staphylococcus aureus. *Future Medicinal Chemistry*, 9(12):1401–1411, 2017.

[214] Jai Moo Shin, Keith Munson, Olga Vagin, and George Sachs. The gastric hk-atpase: structure, function, and inhibition. *Pflügers Archiv-European Journal of Physiology*, 457(3):609–622, 2009.

[215] Jeremy M Berg, John L Tymoczko, and Lubert Stryer. *Biochemistry*. W. H. Freeman, 5th edition, 2002.

[216] Peter Mitchell. Coupling of phosphorylation to electron and hydrogen transfer by a chemi-osmotic type of mechanism. *Nature*, 191(4784):144–148, 1961.

[217] Philip Shapira, Seokbeom Kwon, and Jan Youtie. Tracking the emergence of synthetic biology. *Scientometrics*, 112(3):1439–1469, 2017.

[218] Kerstin Göpfrich, Ilia Platzman, and Joachim P Spatz. Mastering complexity: towards bottom-up construction of multifunctional eukaryotic synthetic cells. *Trends in Biotechnology*, 36(9):938–951, 2018.

[219] Nadrian C Seeman. Nucleic acid junctions and lattices. *Journal of Theoretical Biology*, 99(2):237–247, 1982.

[220] James D Watson and Francis HC Crick. Molecular structure of nucleic acids. *Nature*, 171(4356):737–738, 1953.

[221] Paul WK Rothemund. Folding dna to create nanoscale shapes and patterns. *Nature*, 440(7082):297–302, 2006.

[222] Fan Hong, Fei Zhang, Yan Liu, and Hao Yan. Dna origami: scaffolds for creating higher order structures. *Chemical Reviews*, 117(20):12584–12640, 2017.

[223] Nicholas AW Bell, Christian R Engst, Marc Ablay, Giorgio Divitini, Caterina Ducati, Tim Liedl, and Ulrich F Keyser. Dna origami nanopores. *Nano Letters*, 12(1):512–517, 2012.

[224] Martin Langecker, Vera Arnaut, Thomas G Martin, Jonathan List, Stephan Renner, Michael Mayer, Hendrik Dietz, and Friedrich C Simmel. Synthetic lipid membrane channels formed by designed dna nanostructures. *Science*, 338(6109):932–936, 2012.

[225] Jonathan R Burns, Eugen Stulz, and Stefan Howorka. Self-assembled dna nanopores that span lipid bilayers. *Nano Letters*, 13(6):2351–2356, 2013.

[226] Jonathan R Burns, Kerstin Göpfrich, James W Wood, Vivek V Thacker, Eugen Stulz, Ulrich F Keyser, and Stefan Howorka. Lipid-bilayer-spanning dna nanopores with a bifunctional porphyrin anchor. *Angewandte Chemie International Edition*, 52(46):12069–12072, 2013.

[227] Kerstin Göpfrich, Thomas Zettl, Anna EC Meijering, Silvia Hernández-Ainsa, Samet Kocabey, Tim Liedl, and Ulrich F Keyser. Dna-tile structures induce ionic currents through lipid membranes. *Nano Letters*, 15(5):3134–3138, 2015.

[228] Alexander Ohmann. *A synthetic lipid scramblase built from DNA*. PhD thesis, The University of Cambridge, 2019.

[229] Kevin Jahnke. Dna nanotechnology for bottom-up synthetic cell assembly. Master's thesis, University of Heidelberg, 2018.

[230] Alexander Ohmann, Kerstin Göpfrich, Himanshu Joshi, Rebecca F Thompson, Diana Sobota, Neil A Ranson, Aleksei Aksimentiev, and Ulrich F Keyser. Controlling aggregation of cholesterol-modified dna nanostructures. *Nucleic Acids Research*, 47(21):11441–11451, 2019.

[231] Thomas Gutsmann, Thomas Heimburg, Ulrich Keyser, Kozhinjampara R Mahendran, and Mathias Winterhalter. Protein reconstitution into freestanding planar lipid membranes for electrophysiological characterization. *Nature Protocols*, 10(1):188–198, 2015.

[232] Kerstin Göpfrich and Ulrich F Keyser. Dna nanotechnology for building sensors, nanopores and ion-channels. In *Biological and Bio-inspired Nanomaterials*, pages 331–370. Springer, 2019.

[233] Nicholas AW Bell and Ulrich F Keyser. Nanopores formed by dna origami: A review. *FEBS Letters*, 588(19):3564–3570, 2014.

[234] Oksana Iamshanova, Pascal Mariot, V'Yacheslav Lehen'Kyi, and Natalia Prevarskaya. Comparison of fluorescence probes for intracellular sodium imaging in prostate cancer cell lines. *European Biophysics Journal*, 45(7):765–777, 2016.

[235] Helmut Offenbacher, Otto S Wolfbeis, and Eva Fürlinger. Fluorescence optical sensors for continuous determination of near-neutral ph values. *Sensors and Actuators*, 9(1):73–84, 1986.

[236] Björn Finkler, Christian Spies, Michael Vester, Frederick Walte, Kathrin Omlor, Iris Riemann, Manuel Zimmer, Frank Stracke, Markus Gerhards, and Gregor Jung. Highly photostable "super"-photoacids for ultrasensitive fluorescence spectroscopy. *Photochemical & Photobiological Sciences*, 13(3):548–562, 2014.

[237] Yuki Kazayama, Tetsuhiko Teshima, Toshihisa Osaki, Shoji Takeuchi, and Taro Toyota. Integrated microfluidic system for size-based selection and trapping of giant vesicles. *Analytical Chemistry*, 88(2):1111–1116, 2016.

[238] Paul Flowers, Klaus Theopold, Richard Langley, and William R Robinson. *Chemistry*. OpenStax, 2nd edition, 2019.

[239] Jon V Thomas, Megan R Brimijoin, Thomas R Neault, and Richard F Brubaker. The fluorescent indicator pyranine is suitable for measuring stromal and cameral ph in vivo. *Experimental Dye Research*, 50(3):241–249, 1990.

[240] Yasuhiko Nozaki and Charles Tanford. Proton and hydroxide ion permeability of phospholipid vesicles. *Proceedings of the National Academy of Sciences*, 78(7):4324–4328, 1981.

[241] David W Deamer. Proton permeation of lipid bilayers. *Journal of Bioenergetics and Biomembranes*, 19(5):457–479, 1987.

[242] J Wylie Nichols, Martyn W Hill, Alec D Bangham, and David W Deamer. Measurement of net proton-hydroxyl permeability of large unilamellar liposomes with the fluorescent ph probe, 9-aminoacridine. *Biochimica et Biophysica Acta (BBA)-Biomembranes*, 596(3):393–403, 1980.

[243] John Gutknecht. Proton/hydroxide conductance through phospholipid bilayer membranes: effects of phytanic acid. *Biochimica et Biophysica Acta (BBA)-Biomembranes*, 898(2):97–108, 1987.

[244] HO Hauser, D Oldani, and MC Phillips. Mechanism of ion escape from phosphatidylcholine and phosphatidylserine single bilayer vesicles. *Biochemistry*, 12(22):4507–4517, 1973.

[245] John Gutknecht and Anne Walter. Hydrofluoric and nitric acid transport through lipid bilayer membranes. *Biochimica et Biophysica Acta (BBA)-Biomembranes*, 644(1):153–156, 1981.

[246] DB Spry, Alexei Goun, and Michael D Fayer. Deprotonation dynamics and stokes shift of pyranine (hpts). *The Journal of Physical Chemistry A*, 111(2):230–237, 2007.

[247] Walter F Boron. Transport of h+ and of ionic weak acids and bases. *The Journal of Membrane Biology*, 72(1-2):1–16, 1983.

[248] AP Sharp and RC Thomas. The effects of chloride substitution on intracellular ph in crab muscle. *The Journal of Physiology*, 312(1):71–80, 1981.

[249] Noga Barrash-Shiftan, Brina Brauer, and Ehud Pines. Solvent dependence of pyranine fluorescence and uv-visible absorption spectra. *Journal of Physical Organic Chemistry*, 11(10):743–750, 1998.

[250] TE Redelmeier, LD Mayer, KF Wong, MB Bally, and PR Cullis. Proton flux in large unilamellar vesicles in response to membrane potentials and ph gradients. *Biophysical Journal*, 56(2):385–393, 1989.

[251] Alireza Mashaghi, Samaneh Mashaghi, Ilya Reviakine, Ron MA Heeren, Vahid Sandoghdar, and Mischa Bonn. Label-free characterization of biomembranes: from structure to dynamics. *Chemical Society Reviews*, 43(3):887–900, 2014.

[252] Juan M Bueno, Francisco J Ávila, and Pablo Artal. Second harmonic generation microscopy: a tool for quantitative analysis of tissues. In *Microscopy and Analysis*, chapter 5, pages 99–120. InTech Open, 2016.

[253] Xiyi Chen, Oleg Nadiarynkh, Sergey Plotnikov, and Paul J Campagnola. Second harmonic generation microscopy for quantitative analysis of collagen fibrillar structure. *Nature Protocols*, 7(4):654–669, 2012.

[254] Murali Krishna Ghatkesar, Hans-Peter Lang, Christoph Gerber, Martin Hegner, and Thomas Braun. Comprehensive characterization of molecular interactions based on nanomechanics. *PloS One*, 3(11):e3610, 2008.

[255] Gary A Shaw, Andrew M Siegel, Joshua Model, Adam Geboff, Stanislav Soloviev, Alexey Vert, and Peter Sandvik. Deep uv photon-counting detectors and applications. In *Advanced Photon Counting Techniques III*, volume 7320, page 73200J. International Society for Optics and Photonics, 2009.

[256] RE Stuckey. The applications of ultra-violet absorption spectrophotometry in pharmaceutical analysis. *Journal of Pharmacy and Pharmacology*, 4:345–365, 1952.

[257] Gilbert N Lewis and Melvin Calvin. The color of organic substances. *Chemical Reviews*, 25(2):273–328, 1939.

[258] DF Swinehart. The beer-lambert law. *Journal of Chemical Education*, 39(7):333–335, 1962.

[259] August Beer. Bestimmung der absorption des rothen lichts in farbigen flüssigkeiten. *Annalen der Physik und Chemie*, 86:78–88, 1852.

[260] Thomas G Mayerhöfer, Harald Mutschke, and Jürgen Popp. Employing theories far beyond their limits—the case of the (boguer-) beer–lambert law. *ChemPhysChem*, 17(13):1948–1955, 2016.

[261] Günter Gauglitz and Tuan Vo-Dinh. *Handbook of Spectroscopy*, volume 1000. Wiley Online Library, 2003.

[262] Nadine Barrie Smith and Andrew Webb. *Introduction to Medical Imaging: Physics, Engineering and Clinical Applications*. Cambridge University Press, 2010.

[263] Thomas E Renau, Joseph P Sanchez, Jeffrey W Gage, Julie A Dever, Martin A Shapiro, Stephen J Gracheck, and John M Domagala. Structure- activity relationships of the quinolone antibacterials against mycobacteria: Effect of structural changes at n-1 and c-7. *Journal of Medicinal Chemistry*, 39(3):729–735, 1996.

[264] Kagisha Védaste, Kayitare Egide, Kayumba Pierre Claver, and Eliangiringa Kaale. Development and validation of high-performance thin-layer chromatographic method for the simultaneous determination of rifampicin, isoniazid, and pyrazinamide in a fixed dosage combination tablet. *Journal of Planar Chromatography*, 27(5):392–397, 2014.

[265] Asol Mehlhorn, Parvaneh Rahimi, and Yvonne Joseph. Aptamer-based biosensors for antibiotic detection: a review. *Biosensors*, 8(2):E54, 2018.

[266] Yang Zhang, Bo Shiun Lai, and Mario Juhas. Recent advances in aptamer discovery and applications. *Molecules*, 24(5):941, 2019.

[267] Long Ma, Nana Sun, Chunhao Tu, Qian Zhang, and Aipo Diao. Design of an aptamer–based fluorescence displacement biosensor for selective and sensitive detection of kanamycin in aqueous samples. *RSC Advances*, 7(61):38512–38518, 2017.

[268] Katalin Nagy and Ioana-Daria Tiuca. Importance of fatty acids in physiopathology of human body. In *Fatty Acids*, chapter 1, pages 3–22. InTech Open, 2017.

[269] Guenther Boden. Obesity and free fatty acids. *Endocrinology and Metabolism Clinics of North America*, 37(3):635–646, 2008.

[270] J Patrick Kampf and Alan M Kleinfeld. Is membrane transport of ffa mediated by lipid, protein, or both? *Physiology*, 22(1):7–14, 2007.

[271] Serena Faggiano, Luca Ronda, Samanta Raboni, and Andrea Mozzarelli. Adifab fluorescence data used for the quantification of free fatty acids in media at different ph. *Data in Brief*, 22:158–163, 2019.

[272] RW Albers. Biochemical aspects of active transport. *Annual Review of Biochemistry*, 36(1):727–756, 1967.

Appendix A

Biophysical Characterisation of OLA Vesicles

A.1 Microfluidic Chip Design

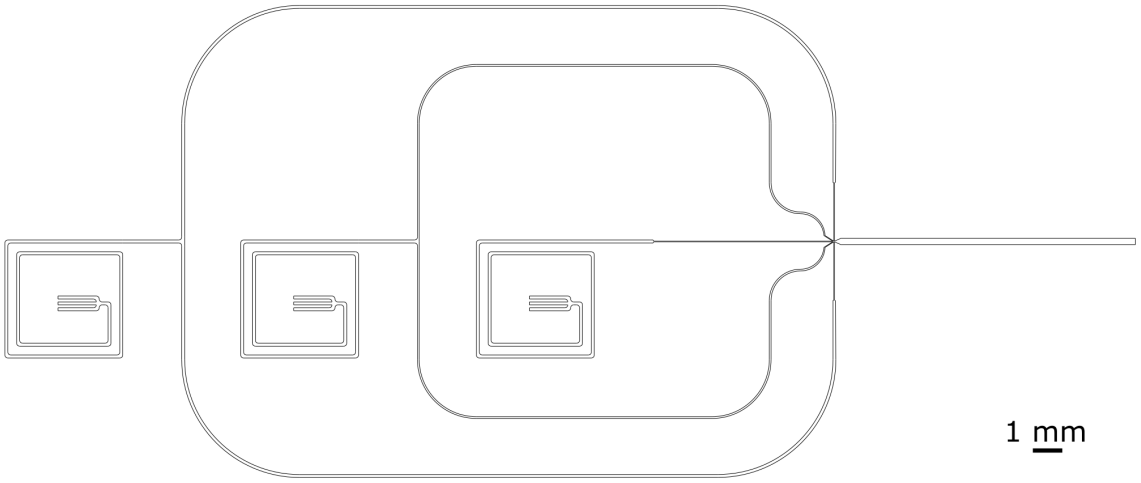

Fig. A.1. Design of the microfluidic chip used for the experiments in Chapter 3

A.2 Validation of Membrane Unilamellarity

The solution compositions for the membrane unilamellarity experiments are given below.

Table A.1. Solution composition for confocal micrographs of OLA and electroformed vesicles.

Solution	Composition
Inner Aqueous (IA)	- 200 mM sucrose - 15% v/v glycerol in milli-Q water
Outer Aqueous (OA)	- 200 mM sucrose - 15% v/v glycerol - 50 mg/mL P-188 in milli-Q water
Lipid-Octanol (LO)	- 4 mg/mL DOPC - 0.5% m/m 18:1 NBD-PC in 1-octanol
Low-density dilution stock	- 200 mM glucose - 15% v/v glycerol in milli-Q water
Electroformation	- 200 mM sucrose - 15% v/v glycerol in milli-Q water

Table A.2. Solution composition for dithionite bleaching assay.

Solution	Composition
Inner Aqueous (IA)	- 200 mM sucrose - 15% v/v glycerol in PBS
Outer Aqueous (OA)	- 200 mM sucrose - 15% v/v glycerol - 50 mg/mL P-188 in PBS
Lipid-Octanol (LO)	- 2 mg/mL DOPC-DOPG (3:1 ratio mixture) - 0.5% m/m 16:0 NBD-PC in 1-octanol
Low-density dilution stock	- 200 mM glucose - 15% v/v glycerol in PBS
Dithionite stock solution	1 M $Na_2S_2O_4$ in Tris buffer (pH 10)

A.3 Lipid Composition Experiments

A.3.1 Solution Composition

Table A.3. Solution composition for lipid mixture experiments.

Solution	Composition
Inner Aqueous (IA)	- 200 mM sucrose - 15% v/v glycerol in PBS
Outer Aqueous (OA)	- 200 mM sucrose - 15% v/v glycerol - 50 mg/mL P-188 in PBS
Lipid-Octanol (LO)	- 3.6 mg/mL of respective lipid mixture in 1-octanol
Low-density dilution stock	- 200 mM glucose - 15% v/v glycerol in PBS

A.3.2 Preparation of Lipid Stocks

The binary lipid mixtures for the liposome composition experiments were obtained as follows:

- **PGPC (DOPG – DOPC):** DOPC and DOPG lipid powder was dissolved in 100% ethanol to a final concentration of 100 mg/mL in separate vials. Furthermore, 18:1-12:0 NBD-PC was dissolved in ethanol to a final concentration of 1 mg/mL. An aliquot of fluorescently doped DOPC lipid was made by mixing the DOPC and NBD-PC in a 9:1 ratio, resulting in a total concentration of 90 mg/mL DOPC lipid. Similarly, a DOPG aliquot was obtained by mixing it in a 9:1 ratio with pure ethanol, resulting in a total concentration of 90 mg/mL DOPG lipid. The 90 mg/mL DOPG and DOPC/NBD-PC aliquots were further mixed in 1:3, 2:2 and 3:1 volume ratios and used as lipid stocks for the OLA experiments. The lipid stocks were stored in the freezer at -20°C. The binary lipid stocks were further diluted to 3.6 mg/mL in 1-octanol before each experiment.
- **PCPE (DOPC - DOPE):** DOPC and DOPE lipid powder was dissolved in 100% ethanol to a final concentration of 100 mg/mL in separate vials. Furthermore, 16:0 Liss Rhod PE was dissolved in ethanol to a final concentration of 0.5 mg/mL. An aliquot of

fluorescently doped DOPE lipid was made by mixing the DOPE and Liss Rhod PE in a 9:1 ratio, resulting in a total concentration of 90 mg/mL DOPE lipid. Similarly, a DOPC aliquot was obtained by mixing it in a 9:1 ratio with pure ethanol, resulting in a total concentration of 90 mg/mL DOPC lipid. The 90 mg/mL DOPC and DOPE/Liss Rhod PE aliquots were further mixed in 1:3, 2:2 and 3:1 volume ratios and used as lipid stocks for the OLA experiments. The lipid stocks were stored in the freezer at -20°C. The binary lipid stocks were further diluted to 3.6 mg/mL in 1-octanol before each experiment.

- **PGPE (DOPG - DOPE):** DOPG and DOPE lipid powder was dissolved in 100% ethanol to a final concentration of 100 mg/mL in separate vials. Furthermore, 16:0 Liss Rhod PE was dissolved in ethanol to a final concentration of 0.5 mg/mL. An aliquot of fluorescently doped DOPE lipid was made by mixing the DOPE and Liss Rhod PE in a 9:1 ratio, resulting in a total concentration of 90 mg/mL DOPE lipid. Similarly, a DOPC aliquot was obtained by mixing it in a 9:1 ratio with pure ethanol, resulting in a total concentration of 90 mg/mL DOPG lipid. The 90 mg/mL DOPG and DOPE/Liss Rhod PE aliquots were further mixed in 1:3, 2:2 and 3:1 volume ratios and used as lipid stocks for the OLA experiments. The lipid stocks were stored in the freezer at -20°C. The binary lipid stocks were further diluted to 3.6 mg/mL in 1-octanol before each experiment.

All chemicals were acquired from Sigma-Aldrich, unless stated otherwise.

A.3.3 Optical Parameters

The confocal images were obtained using the following optical parameters:

- **PGPC (DOPG – DOPC):** The images were acquired on a Leica TCS SP5 confocal microscope, equipped with a 488 nm Argon laser. The laser output power was set to 10%. Images were recorded via a 40× oil immersion objective (HCX PL APO CS 40.0, NA 1.25) with a scan speed of 400 Hz. Pinhole Diameter 67.93 µm, Laser Acousto-Optic Tunable Filter (AOTF) 40%, Smart Gain (HyD) 302% and Smart Offset disabled. The microscope was controlled via the Leica Microsystems LAS AF software.
- **PGPE (DOPG – DOPE):** The images were acquired in an Olympus FV 1000 confocal microscope, equipped with a LD559 laser (559 nm, 15 mW). The laser output power was set to 1%. Images were recorded via a 40× oil immersion objective (UPFLN 40×, NA 1.3) with a scan speed of 2 µs/pixel. Pinhole diameter 80 µm, PMT offset voltage

645 V and analog PMT offset 0. The microscope was controlled via the Olympus microscope Fluoview software.

- **PCPE (DOPC – DOPE):** The images were acquired in an Olympus FV 1000 confocal microscope, equipped with a LD559 laser (559 nm, 15 mW). The laser output power was set to 1%. Images were recorded via a 40× oil immersion objective (UPFLN 40×, NA 1.3) with a scan speed of 2 µs/pixel. Pinhole diameter 80 µm, PMT offset voltage 645 V and analog PMT offset 0. The microscope was controlled via the Olympus microscope Fluoview software.

A.3.4 Image Panels of Binary Lipid Systems

Representative images of GUVs obtained for the different binary lipid systems are shown in Figures A.2, A.3 and A.4, along with boxplots of their corresponding mean fluorescence intensity analyses. A clear increase in intensity of the vesicles for the different lipid mixtures can be observed. In the analysis, we performed a linear regression on the fluorescence intensities of each lipid system and then normalised the fluorescence values to the slope of the linear function we obtained. This results in a gradient of +1 for the normalised intensity values with increasing relative concentrations of fluorescently doped lipid. For the 3:1, 2:2 and 1:3 lipid mixtures this translates into values of 1, 2 and 3, respectively, if the lipid composition of the LO phase is maintained in the vesicle.

For the PGPC and PCPE systems, the normalised intensity shows a linear 1-2-3 increase, as expected. Stable PGPE vesicles could only be formed in the 2:2 and 1:3 ratio.

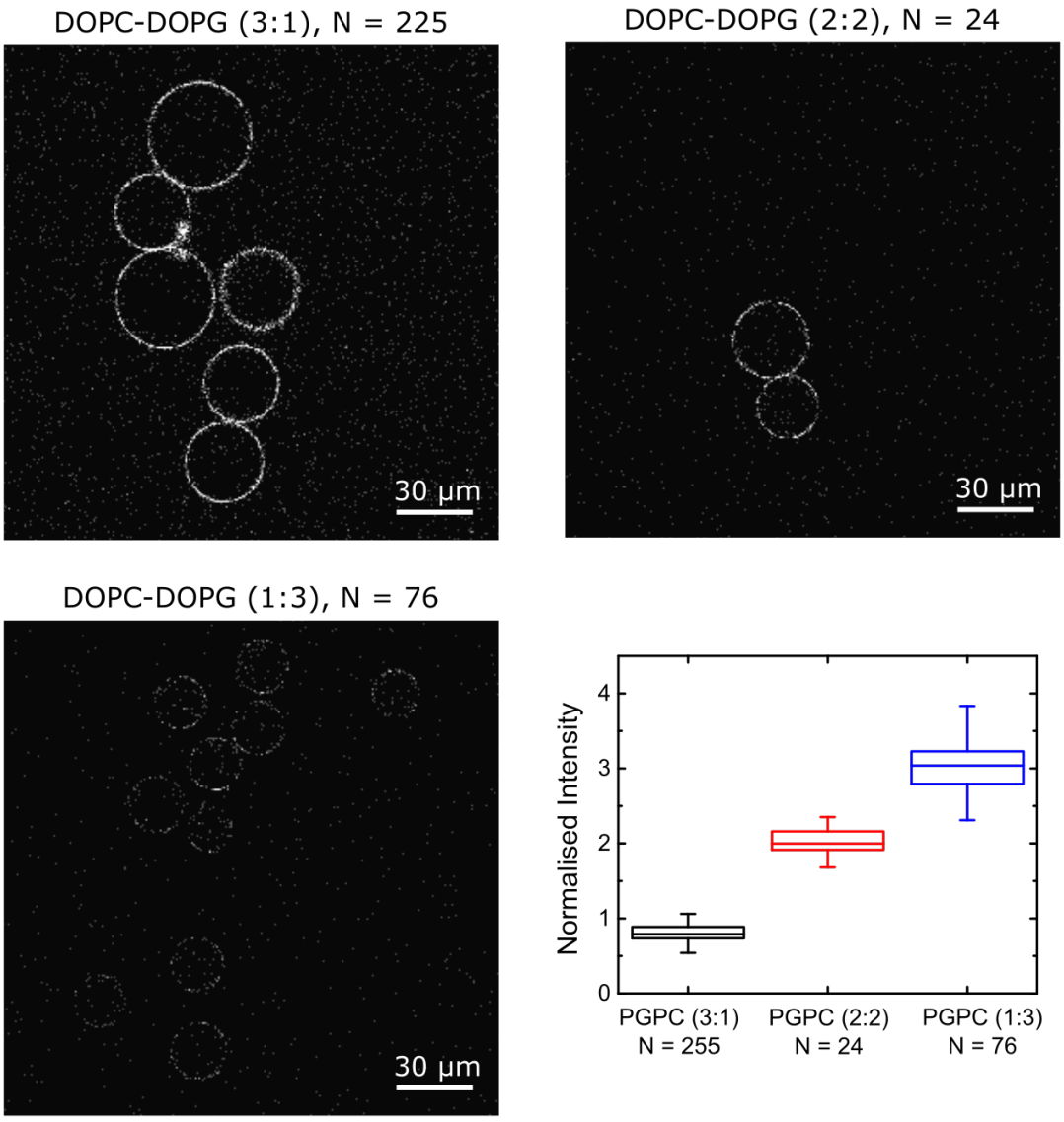

Fig. A.2. Panel showing representative confocal images of PGPC liposomes. The 1:3 ratio vesicles show the highest fluorescence intensity, whereas the 3:1 vesicles show the lowest fluorescence intensity. The vesicles with a 2:2 lipid ratio lie between the two. The boxplot shows the results of the mean fluorescence intensity analysis. The intensity scales in a linear manner in accordance with the relative concentration of fluorescently labelled NBD-PC in the LO phase.

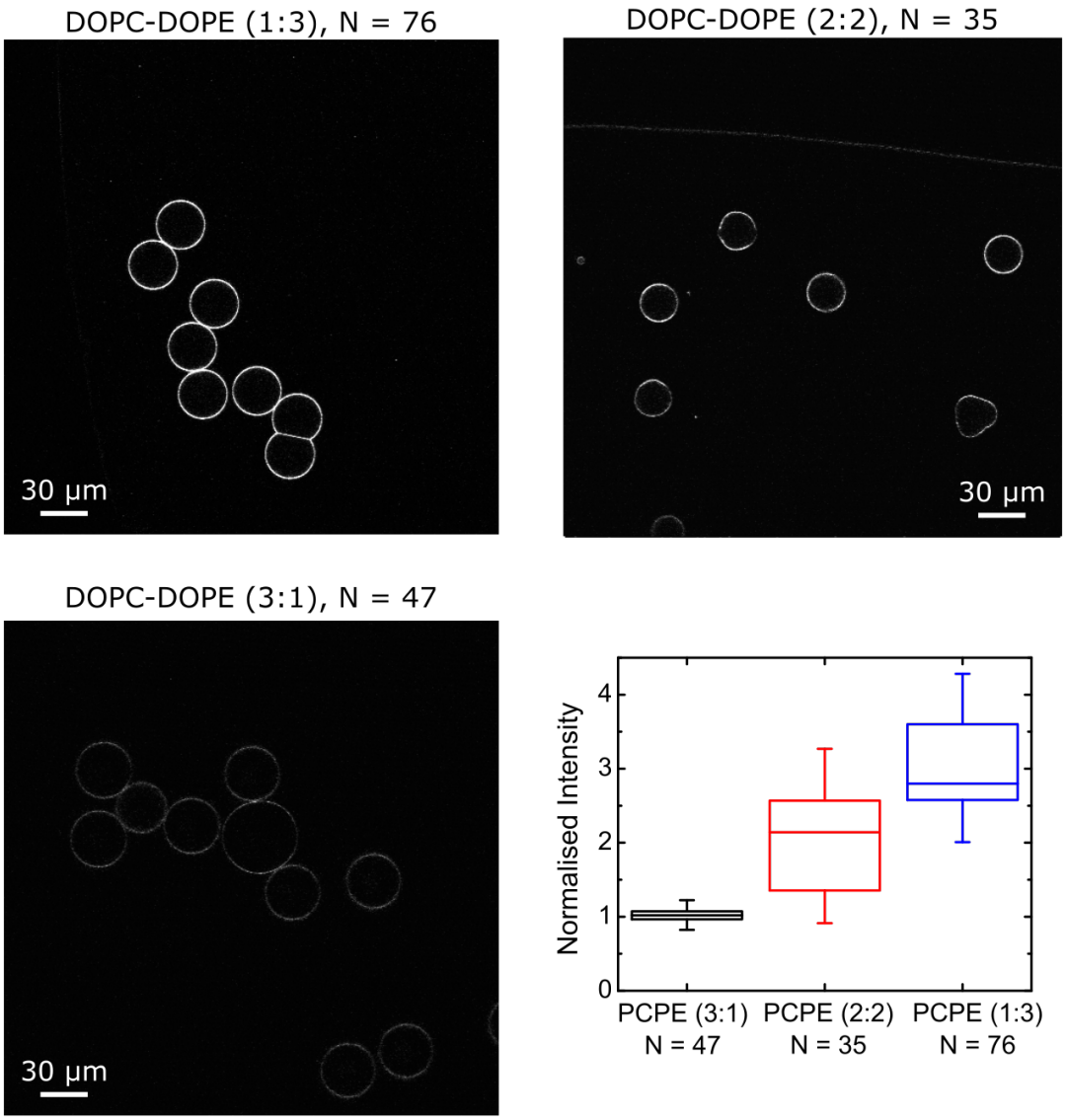

Fig. A.3. Panel showing representative confocal images of PCPE liposomes. The 1:3 ratio vesicles show the highest fluorescence intensity, whereas the 3:1 vesicles show the lowest fluorescence intensity. The vesicles with a 2:2 lipid ratio lie between the two. The boxplot shows the results of the mean fluorescence intensity analysis. The intensity scales in a linear manner in accordance with the relative concentration of fluorescently labelled Liss Rhod PE in the LO phase.

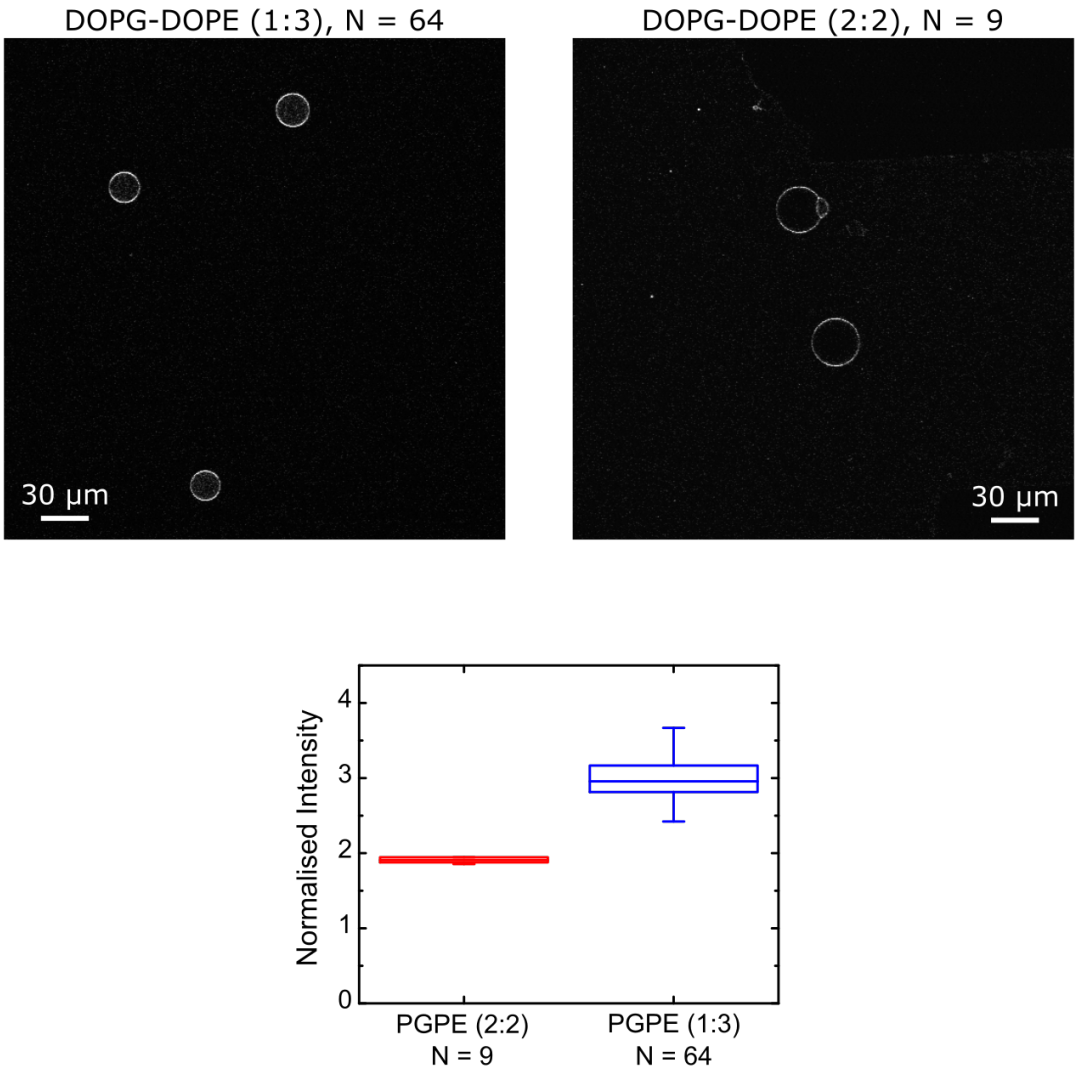

Fig. A.4. Panel showing representative confocal images of PGPE liposomes. The 1:3 ratio vesicles show the highest fluorescence intensity, whereas the 2:2 vesicles show lower fluorescence intensity. We were not able to form stable PGPE vesicles in 3:1 ratio. However, the fluorescence intensity of the other two lipid mixtures scales in a linear manner in accordance with the relative concentration of fluorescently labelled Liss Rhod PE in the LO phase.

A.4 Lateral Diffusion Experiments

A.4.1 Comparison of GUV Production Technique at Varying P-188 Concentrations

The composition of the solutions used to prepare the vesicles are listed in Table A.4. We formed GUVs via electroformation in two chemical environments. One environment was devoid of the poloxamer P-188 in the vesicle solution ('no P-188 environment'), and one environment contained 50 mg/mL P-188 ('high P-188 environment'). Similarly, we formed OLA vesicles in two chemical environments with varying P-188 concentrations. In one case, we prepared GUVs with 50 mg/mL P-188 encapsulated within (IA) and outside (OA) of the vesicles ('high P-188 environment'). However, since OLA vesicles cannot be formed without the presence of P-188 we were not able to create an environment completely devoid of P-188. Instead we formed the OLA GUVs in a 'low P-188 environment' where the inner aqueous (IA) solution contained no P-188 and the outside solution contained 50 mg/mL. The vesicle aliquots had to be further diluted for imaging. The exact solution compositions in which the FRAP measurements were performed are listed in Table A.4.

Table A.4. Solution compositions used for GUV formation. After production, 20 µL of the vesicle stock solution is extracted and diluted in 50 µL of glucose solution. The lower density of the surrounding medium causes the GUVs to sink to the bottom of the incubation chamber which facilitates confocal imaging. The components were mixed in ion free milli-Q water, as this increases liposome yield during electroformation.

	Inner Aqueous (IA)	**Outer Aqueous (OA)**	**Dilution Stock**
Electroformation 'no P-188'	-200 mM sucrose -15% v/v glycerol	-200 mM sucrose -15% v/v glycerol	-200 mM glucose -15% v/v glycerol
Electroformation 'high P-188'	-200 mM sucrose - 15% v/v glycerol -50 mg/mL P-188	- 200 mM sucrose -15% v/v glycerol - 50 mg/mL P-188	-200 mM glucose -15% v/v glycerol
OLA 'low P-188'	-200 mM sucrose -15% v/v glycerol	-200 mM sucrose -15% v/v glycerol	-200 mM glucose -15% v/v glycerol
OLA 'high P-188'	-200 mM sucrose -15% v/v glycerol -50 mg/mL P-188	-200 mM sucrose -15% v/v glycerol - 50 mg/mL P-188	-200 mM glucose -15% v/v glycerol

For visualisation, we mixed 20 µL of the vesicle stock with 50 µL of the low-density dilution stock in an incubation chamber (Grace Bio-Labs FlexWell, Sigma-Aldrich) with a wide bore pipette. The density mismatch causes the GUVs to sink to the bottom of the chamber, where they could be imaged. However, by diluting the vesicle stock with P-188 free glucose solution, we reduced the effective P-188 concentration in the outside of the vesicles. The effective solution compositions that the FRAP measurements were carried out in are summarised in Table A.5.

Table A.5. Effective solution composition encapsulated within the vesicles and outside at which the FRAP measurements were performed. We measure the lateral lipid diffusion coefficients in a high and a low P-188 environment for both GUV formation techniques. P-188 could not be completely removed from the outside solution for the OLA sets, as this technique requires a certain amount of P-188 for successful liposome formation.

	Encapsulated solution	**Outside solution**
Electroformation 'no P-188 environment'	- 200 mM sucrose - 15% v/v glycerol	- 200 mM sucrose - 15% v/v glycerol
Electroformation 'high P-188 environment'	- 200 mM sucrose - 15% v/v glycerol - 50 mg/mL P-188	- 200 mM sucrose - 15% v/v glycerol - 14 mg/mL P-188
OLA 'low P-188 environment'	- 200 mM sucrose - 15% v/v glycerol	- 200 mM sucrose - 15% v/v glycerol - 14 mg/mL P-188
OLA 'high P-188 environment'	- 200 mM sucrose - 15% v/v glycerol - 50 mg/mL P-188	- 200 mM sucrose - 15% v/v glycerol - 14 mg/mL P-188

Table A.6. Summary of measured lateral lipid diffusion coefficients (mean ± std. dev.) for the GUVs investigated. All measured lateral diffusion coefficients are on the order of 1 $\mu m^2/s$.

	DOPC	**POPC**
Electroformation 'no P-188 environment'	1.0 ± 0.2 $\mu m^2/s$ N = 17	0.8 ± 0.2 $\mu m^2/s$ N = 28
Electroformation 'high P-188 environment'	1.0 ± 0.2 $\mu m^2/s$ N = 14	1.3 ± 0.4 $\mu m^2/s$ N = 20
OLA 'low P-188 environment'	1.1 ± 0.2 $\mu m^2/s$ N = 34	1.0 ± 0.3 $\mu m^2/s$ N = 49
OLA 'high P-188 environment'	1.0 ± 0.3 $\mu m^2/s$ N = 30	0.9 ± 0.3 $\mu m^2/s$ N = 27

A.4.2 Effect of Glycerol and Temperature on Lipid Lateral Diffusion

In order to determine the effect of glycerol and temperature on the lateral lipid diffusion coefficient, we conducted FRAP experiments on electroformed DOPC vesicles with varying glycerol content and at two different temperatures. Sucrose/glucose solutions similar to the 'no P-188 environment' with and without 15% glycerol were prepared. FRAP measurements were conducted at room temperature (approx. 20°C) as well as at 37°C, but with the same optical parameters. Temperature control was performed with the cellVivo incubation system. The obtained values are presented in Table A.7.

Table A.7. Lateral diffusion coefficients (mean ± std. dev) of electroformed DOPC vesicle membranes at different temperatures and varying glycerol concentrations. The diffusion coefficient increases from 1.0 ± 0.2 $\mu m^2/s$ (mean ± std. dev, N = 17) at 20°C and 15% glycerol to 1.6 ± 0.2 $\mu m^2/s$ (N = 12) without the presence of glycerol. At 37°C, the coefficients rise to 1.9 ± 0.6 $\mu m^2/s$ (N = 19) with 15% glycerol and 2.2 ± 0.5 $\mu m^2/s$ without glycerol.

	DOPC (electroformation)
Room temperature (approx. 20°C) 15% v/v glycerol	1.0 ± 0.2 $\mu m^2/s$ N = 17
Room temperature (approx. 20°C) 0 % v/v glycerol	1.6 ± 0.2 $\mu m^2/s$ N = 12
37°C 15% v/v glycerol	1.9 ± 0.6 $\mu m^2/s$ N = 19
37°C 0% v/v glycerol	2.2 ± 0.5 $\mu m^2/s$ N = 7

A.4.3 Statistical Tests

The following tables show the results of the statistical tests performed on the lateral diffusion coefficients of the vesicles in different chemical environments (Tables A.8, A.9, A.13 and A.14), as well as with and without a visible octanol pocket attached (Tables A.10, A.11, A.12, A.15, A.16 and A.17).

DOPC

Table A.8. ANOVA on lateral lipid diffusion coefficients of DOPC vesicles in the different chemical environments. At the 0.01 level, the population means are not significantly different.

	N Analysis	N Missing	Mean	Standard Deviation	SE of Mean
Electroformation ‘’‘no P-188’	17	0	1.0066	0.18878	0.04579
Electroformation ‘high P-188’	14	0	1.2347	0.40438	0.10807
OLA ‘low P-188’	34	0	1.10313	0.21012	0.03604
OLA ‘high P-188’	30	0	0.9801	0.25758	0.04703

	DF	Sum of Squares	Mean Square	F Value	Prob >F
Model	3	0.72666	0.24222	3.62715	0.01593
Error	91	6.077	0.06678		
Total	94	6.80366			

R-square	Coeff Var	Root MSE	Data Mean
0.1068	0.24233	0.25842	1.06639

Table A.9. Two sample t-tests comparing lateral lipid diffusion coefficients of DOPC vesicles in 'no/low' and 'high' P-188 environments. At the 0.01 level, the means are not significantly different from one another.

Comparison of lateral diffusion coefficent	**p-value** (2 sample t-test with Welch's correction)
Electroformation 'no P-188' vs. Electroformation 'high P-188'	0.06812
Electroformation 'no P-188' vs. OLA 'low P-188'	0.10644
Electroformation 'no P-188' vs. OLA 'high P-188'	0.68838
Electroformation 'no P-188' vs. OLA 'high P-188'	0.04441
Electroformation 'no P-188' vs. OLA 'low P-188'	0.26509
OLA 'low P-188' vs. OLA 'high P-188'	0.04244

Table A.10. ANOVA on lateral lipid diffusion coefficients of DOPC vesicles in a 'high' P-188 environment with and without a visible octanol pocket attached. At the 0.05 level, the population means are not significantly different.

	N Analysis	**N Missing**	**Mean**	**Standard Deviation**	**SE of Mean**
Octanol pocket 'high P-188'	13	1	0.87757	0.17093	0.04741
No Octanol pocket 'high P-188'	17	2	1.0585	0.28856	0.06999

	DF	**Sum of Squares**	**Mean Square**	**F Value**	**Prob >F**
Model	1	0.24115	0.24115	4.01219	0.05494
Error	28	1.68289	0.0601		
Total	29	1.92404			

R-square	**Coeff Var**	**Root MSE**	**Data Mean**
0.12533	0.25014	0.24516	0.9801

Table A.11. ANOVA on lateral lipid diffusion coefficients of DOPC vesicles in a 'low' P-188 environment with and without a visible octanol pocket attached. At the 0.05 level, the population means are not significantly different.

	N Analysis	N Missing	Mean	Standard Deviation	SE of Mean
Octanol pocket 'low P-188'	15	3	1.06813	0.20468	0.05285
No Octanol pocket 'low P-188'	19	2	1.13075	0.21572	0.04949

	DF	Sum of Squares	Mean Square	F Value	Prob >F
Model	1	0.03287	0.03287	0.73853	0.39652
Error	32	1.42411	0.0445		
Total	33	1.45697			

R-square	Coeff Var	Root MSE	Data Mean
0.02256	0.19124	0.21096	1.10313

Table A.12. Two sample t-test comparing lateral lipid diffusion coefficients of DOPC vesicles with and without a visible octanol pocket attached. At 0.01 level, the means are not significantly different from one another.

Comparison of lateral diffusion coefficent	p-value (2 sample t-test with Welch's correction)
OLA octanol pocket attached vs. OLA octanol poclet separated ('low P-188')	0.39379
OLA octanol pocket attached vs. OLA octanol pocket separated ('high P-188')	0.04166

POPC

Table A.13. ANOVA on lateral lipid diffusion coefficients of POPC vesicles in the different chemical environments. At the 0.001 level, the difference in the population means are statistically significant.

	N Analysis	N Missing	Mean	Standard Deviation	SE of Mean
Electroformation 'no P-188'	28	0	0.79702	0.20225	0.03822
Electroformation 'high P-188'	28	0	1.34993	0.43119	0.09642
OLA 'low P-188'	49	0	0.97925	0.2719	0.03884
OLA 'high P-188'	27	0	0.93057	0.13276	0.02555

	DF	Sum of Squares	Mean Square	F Value	Prob >F
Model	3	0.72666	0.24222	3.62715	0.01593
Error	91	6.077	0.063378		
Total	94	6.80366			

R-square	Coeff Var	Root MSE	Data Mean
0.30166	0.27185	0.26839	0.98729

Table A.14. Two sample t-tests comparing lateral lipid diffusion coefficients of POPC vesicles in 'no/low' and 'high' P-188 environments. At the 0.001 level, the lateral lipid diffusion coefficient of electroformed vesicles in a 'high P-188' environment is significantly different from electroformed vesicles without P-188, as well as OLA vesicles with 'high P-188'. All remaining diffusion coefficients are not significantly different from one another.

Comparison of lateral diffusion coefficent	p-value (2 sample t-test with Welch's correction)
Electroformation 'no P-188' vs. Electroformation 'high P-188'	1.58549E-5
Electroformation 'no P-188' vs. OLA 'low P-188'	0.00133
Electroformation 'no P-188' vs. OLA 'high P-188'	0.00559
Electroformation 'no P-188' vs. OLA 'high P-188'	3.76001E-4
Electroformation 'no P-188' vs. OLA 'low P-188'	0.00147
OLA 'low P-188' vs. OLA 'high P-188'	0.29855

Table A.15. ANOVA on lateral lipid diffusion coefficients of POPC vesicles in a high P-188 environment with and without a visible octanol pocket attached. At the 0.05 level, the population means are not significantly different.

	N Analysis	**N Missing**	**Mean**	**Standard Deviation**	**SE of Mean**
Octanol pocket 'high P-188'	17	1	0.94456	0.13026	0.03159
No Octanol pocket 'high P-188'	9	2	0.88763	0.13453	0.04484

	DF	**Sum of Squares**	**Mean Square**	**F Value**	**Prob >F**
Model	1	0.01907	0.01907	1.09968	0.30478
Error	24	0.41627	0.01734		
Total	25	0.43534			

R-square	**Coeff Var**	**Root MSE**	**Data Mean**
0.30166	0.27185	0.26839	0.98729

Table A.16. ANOVA on lateral lipid diffusion coefficients of POPC vesicles in a low P-188 environment with and without a visible octanol pocket attached. At the 0.05 level, the population means are not significantly different.

	N Analysis	**N Missing**	**Mean**	**Standard Deviation**	**SE of Mean**
Octanol pocket 'low P-188'	32	11	0.93381	0.28302	0.05003
No Octanol pocket 'low P-188'	17	5	1.06477	0.23388	0.05672

	DF	**Sum of Squares**	**Mean Square**	**F Value**	**Prob >F**
Model	1	0.19039	0.19039	2.66451	0.10929
Error	47	3.35829	0.07145		
Total	48	3.54868			

R-square	**Coeff Var**	**Root MSE**	**Data Mean**
0.05365	0.27297	0.26731	0.97925

Table A.17. Two sample t-tests comparing lateral lipid diffusion coefficients of POPC vesicles with and without a visible octanol pocket attached. At 0.05 level, the means are not significantly different from one another.

Comparison of lateral diffusion coefficent	**p-value** (2 sample t-test with Welch's correction)
OLA octanol pocket attached vs. OLA octanol poclet separated ('low P-188')	0.09139
OLA octanol pocket attached vs. OLA octanol pocket separated ('high P-188')	0.25367

Appendix B

Permeability Measurements of Fluoroquinolone Antibiotics

B.1 Microfluidic Chip Designs

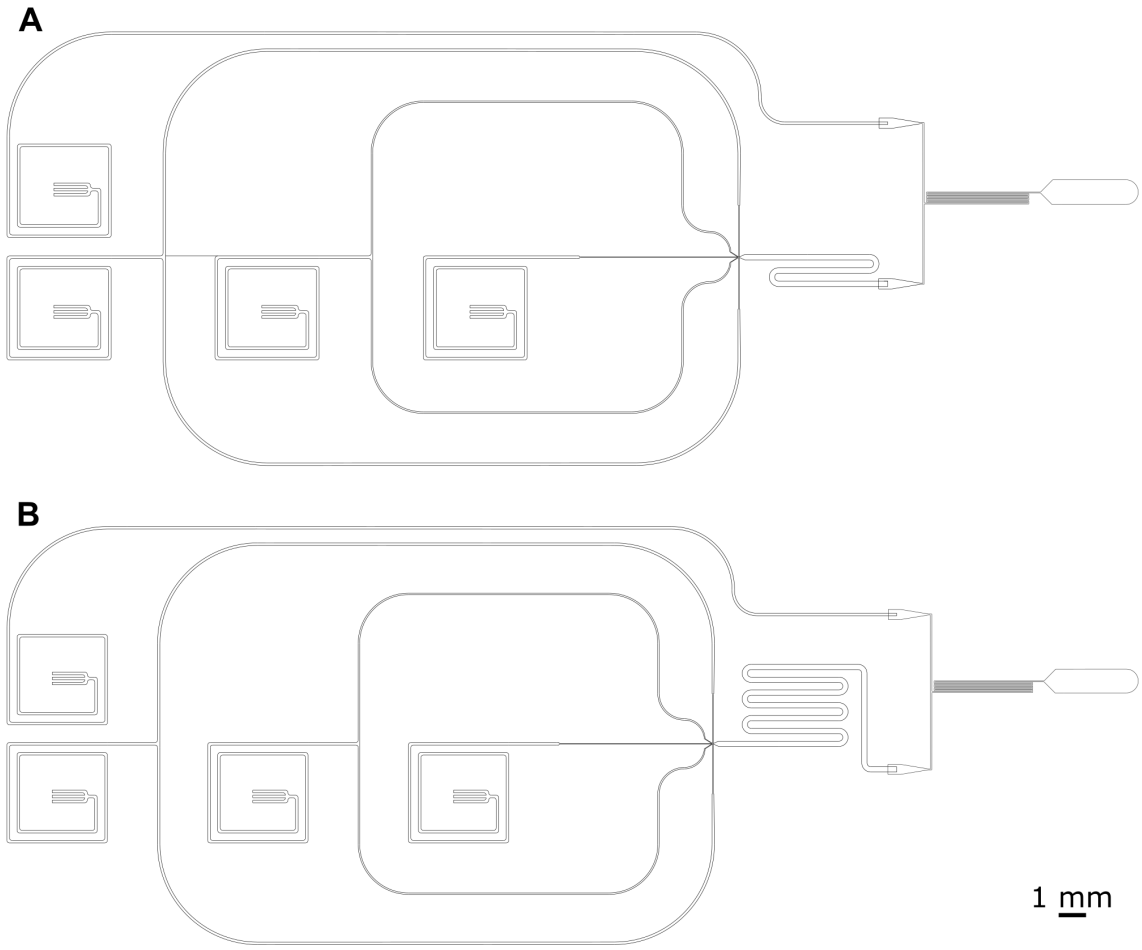

Fig. B.1. Chip design of microfluidic permeability assay. Two different chip designs were used for the measurements. Design B has a longer outlet, leading to the T-junction, which can be used as reservoir for more GUVs.

B.2 Scatter Plots of Permeability Measurements

The scatter plots of the individual permeability measurements obtained via the microfluidic platform are given below.

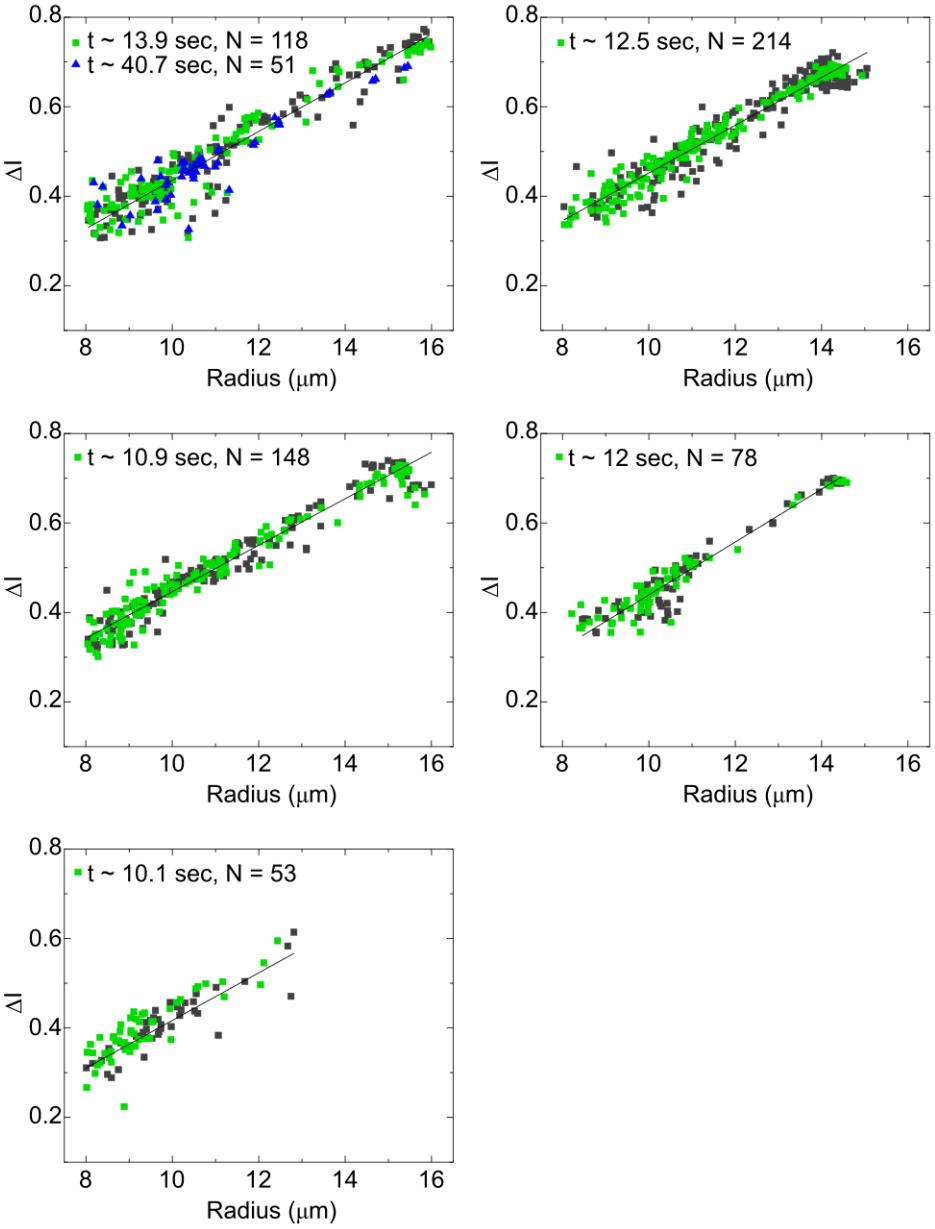

Fig. B.2. Scatter plots of ΔI vs R for norfloxacin in 5 mM acetic acid buffer with 200 mM sucrose at pH 5. No significant transport of the drug through the PGPC vesicles can be detected in any of the experiments, since no significant change of ΔI was detected between the different time points.

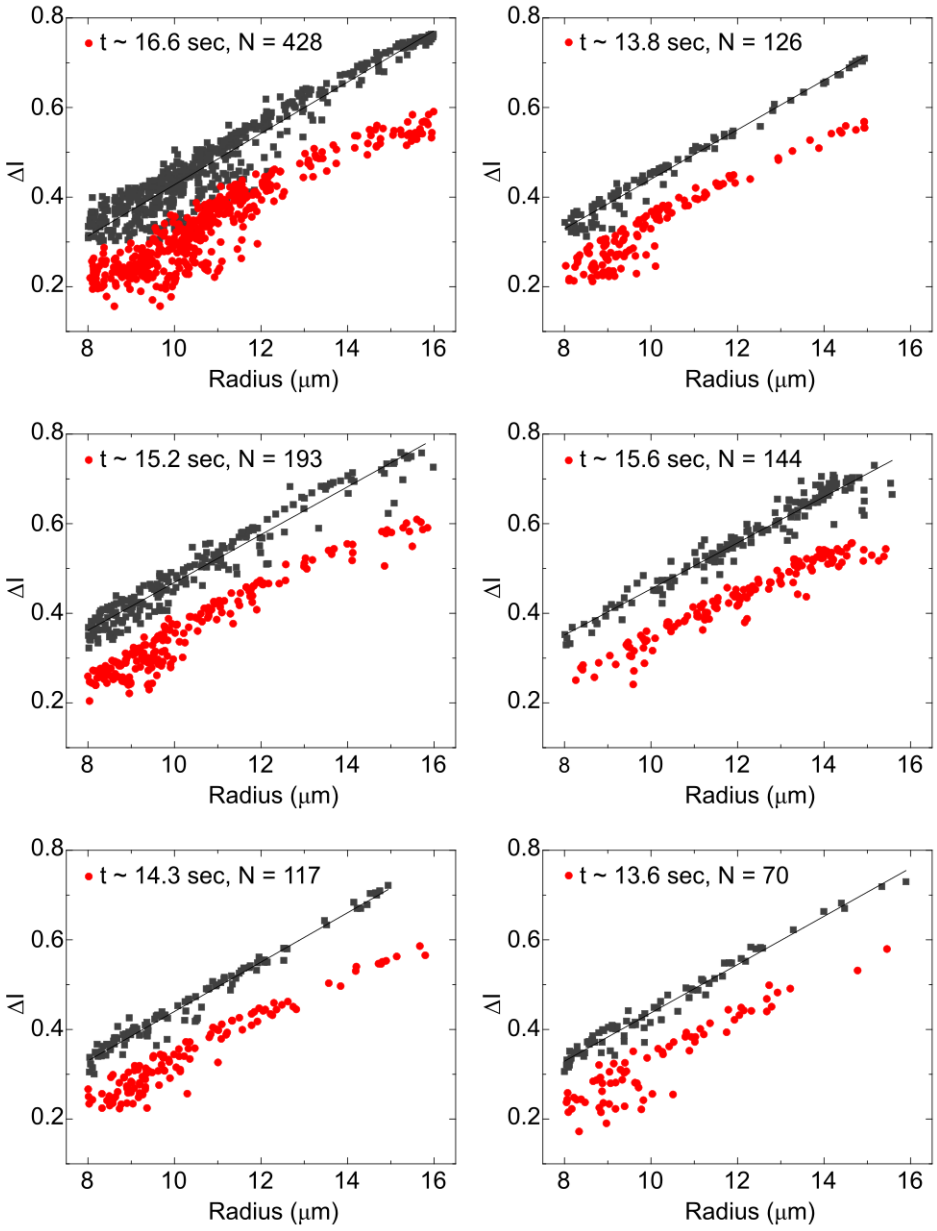

Fig. B.3. Scatter plots of ΔI vs R for norfloxacin in PBS with 200 mM sucrose at pH 7.4. Significant transport of the drug through the PGPC vesicles can be detected in all experiments, visible by the gap in ΔI between the two time points.

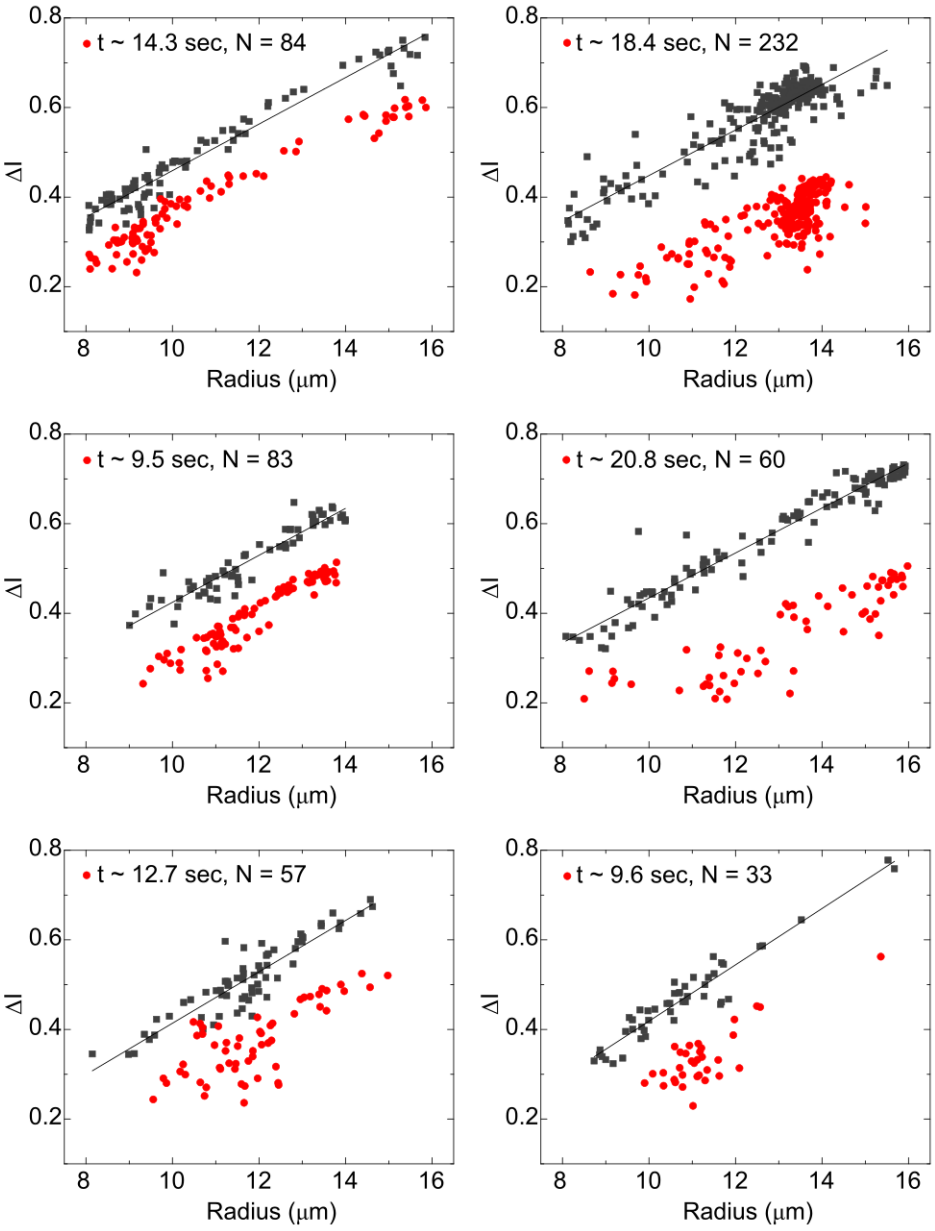

Fig. B.4. Scatter plots of ΔI vs R for norfloxacin in PBS with 200 mM sucrose at pH 7.4. Significant transport of the drug through the PGPC vesicles can be detected in all experiments, visible by the gap in ΔI between the two time points.

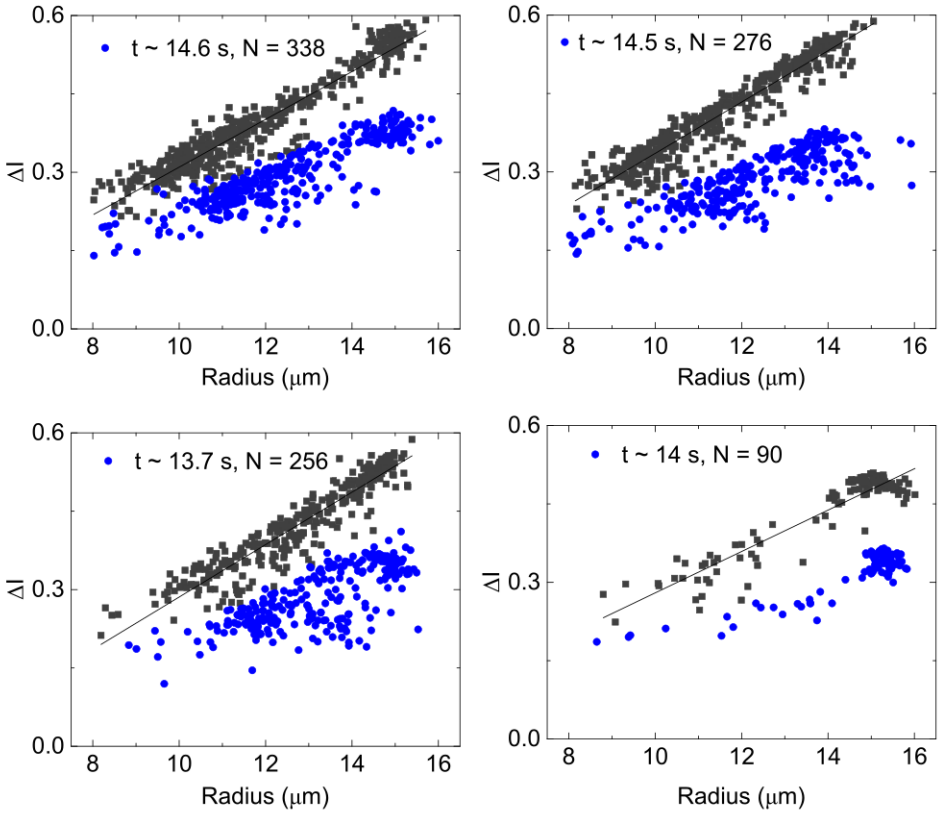

Fig. B.5. Scatter plots of ΔI vs R for ciprofloxacin in PBS with 200 mM sucrose at pH 7.4. Significant transport of the drug through the PGPC vesicles can be detected in all experiments, visible by the gap in ΔI between the two time points.

Appendix C

DNA Nanopores

C.1 Strand Sequence of the DNA Pore

The strand sequence of the DNA pore is given in Table C.1.

Table C.1. Sequence of individual DNA strands forming the nanopore.

Name	Sequence (5' to 3')	Length (nt)
Sc1	CCTTTCCACGAACACAGGGTTGTCCGATCCTATATTACGACTCCTTT	47
Sc2	TTTGGGAAGGGGTTCGCAAGTCGCACCCTAAACG	34
Sc3	TCTTATCCTGCATCGAAAGCTCAATCATGCATCTTT	36
Sc4	TTTATGTTGAAGGCTCAGGATGC	23
St1	TTTATCGGACATTCAACATGGAGTCGTGGTGCGACT	36
St2	TGCGAACAGGATAAGACGTTTAGAATATAGGTTT	34
St3	TTTTTCGATGCCCCTTCCCGATGCATGAAGGGCATCCTGAGCCACCC	47
St4	TGTGTTCGTGGAATTGAGCTTTT	23

C.2 Folding Protocol

All DNA strands were acquired from Integrated DNA Technology (IDT). The DNA strands were mixed to a final concentration of 1 µM in TE20 buffer (10 mM Tris, pH 8.0, 0.1 mM EDTA) containing an additional 20 mM $MgCl_2$ in an Eppendorf tube. The mixture of DNA strands then underwent a heating protcol using a ProFlex™ PCR thermal cycler (Thermo Fisher Scientific). The mixture was heated to 85°C for 5 minutes and subsequently cooled to 25°C over 18 hours. After assembly, the structures were stored at 4°C.

C.3 Polyacrylamide Gel Electrophoresis (PAGE) [1]

We used polyacrylamide gel electrophoresis (PAGE) to validate successful assembly of the DNA structures before every experiment, following an established protocol [228, 229]. In this technique, an electric field is applied across a gel of cross-linked polymers. The negatively charged DNA structures migrate against the direction of the electric field. The distance the DNA structures are able to travel depends primarily of the size and shape of the structure. By comparing the distances by which the nanostructures migrated to that of a known reference (DNA ladder), the correct assembly of the DNA pores can be assessed. Figure C.1 shows an example PAGE of correctly assembled DNA pores.

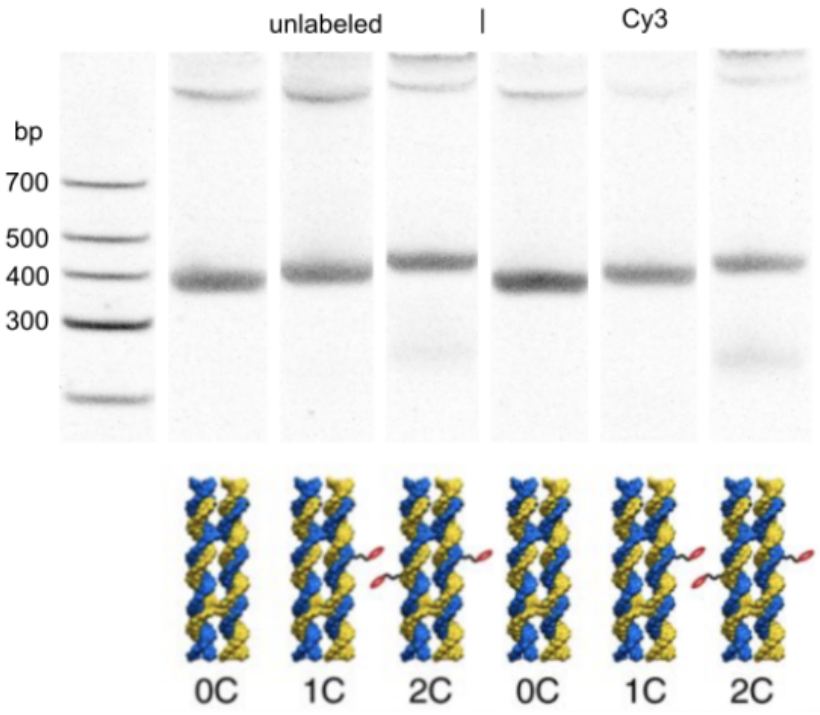

Fig. C.1. Polyacrylamide gel electrophoresis to validate the correct assembly of the DNA structures. The leftmost lane displays a DNA ladder of known base pairs which are used as the reference. The remaining lanes depict unlabelled as well as labelled 0C, 1C and 2C structures. The strong bands indicate the successful assembly of the pore. The small steps between the 0C, 1C and 2C structures stems from their additional mass due to the cholesterol tags, again suggesting successful assembly of the structure. Image from [229].

[1] PAGE was either performed by K. Jahnke or A. Ohmann.

C.4 Solution Composition

The base stock solution consisted of 200 mM sucrose, 15% v/v glycerol in PBS (pH 7.4). The OLA solutions were made up as follows:

- **IA:** Base stock + 50 µM HPTS
- **OA:** Base stock + 50 mg/mL P-188
- **LO:** 4 mg/mL DOPC in 1-Octanol

The solutions for the perfusion steps are listed in Tables C.2 and C.3.

Table C.2. Solutions used in the different perfusion steps in Experiment 1

Perfusion 1		**Perfusion 2**
DNA pore chamber Base stock (pH 7.4) *50 nM DNA pores* *20 mM MgCl2*	Buffer chamber *Base stock (pH 7.4)* *20 mM $MgCl_2$*	All chambers *Base stock (pH 5.9)* *20 µM HPTS* *20 mM $MgCl_2$*

Table C.3. Solutions used in the different perfusion steps in Experiment 2 and 3

Perfusion 1		**Perfusion 2**
DNA pore chamber Base stock (pH 7.4) *50 nM DNA pores* *20 mM MgCl2*	Buffer chamber *Base stock (pH 7.4)* *20 mM $MgCl_2$*	All chambers *Base stock (pH 5.9)* *5 µM HPTS* *20 mM $MgCl_2$*

C.5 Detailed Protocol of Chip Operation

The perfusion assay is operated using two pressure-driven pumps (MFCS, Fluigent SA, France), as well as one flow-driven syringe pump (neMESYS, Cetoni GmbH, Germany) equipped with a 250 µL glass syringe (ILS, Germany). One of the Fluigent pumps is needed to drive the flows at the OLA junction and enable vesicle production. The second Fluigent pump is needed to flush in a substance of interest via the perfusion inlets. The syringe pump is required for applying suction via the outlet A, thereby forcing the GUVs from the second-level connector chip into the perfusion chambers where the vesicle traps are located. Furthermore, one Fluigent switch (2-switch, Fluigent SA, France) connected to outlet B is necessary to control the open and close the outlet on demand.

The microfluidic device is initially filled with air and needs to be filled in a controlled manner in order to avoid the presence of air bubbles in the microfluidic chip that disturb the flow pattern. The following procedure enables successful chip operation:

1. The Fluigent containing the OLA solutions is connected to the OLA inlets. However, no pressure is applied yet. The perfusion inlets are left unconnected for now. The neMESYS syringe pump is filled with 100 µL of base stock solution and connected to outlet A. The 2-Switch is set the "open" state and connected to Outlet B.

2. The syringe pump is used to fill the microfluidic device with the base stock liquid via outlet A. For this, a positive flow rate (flow into the chip) of approximately 50 µL/h is applied. The chip fills with liquid via outlet A, pushing the air that is initially present in the perfusion chambers into the connector chip. Furthermore, the liquid will move towards the perfusion inlets and fill the biopsy punches that serve as fluid access ports. This process takes approximately 30 minutes.

3. When the trapping chambers and the perfusion access ports are filled with liquid, the positive flow from the syringe pump is reduced to 3-5 µL/h. The Fluigent pump containing the perfusion solutes is connected, however, no pressure is applied via these inlets yet. Since the fluid access ports are filled with liquid before the Fluigent is connected, no air bubbles are introduced to the system via the perfusion inlets once pressure is applied here. Furthermore, the connected Fluigent effectively blocks further fluid flow in the direction and the entire fluid flow stemming from the syringe pump is directed upwards into the connector chip.

4. The OLA pressures are applied using the Fluigent that is connected to the corresponding inlets. The fluid flows likewise push the air that is present in the OLA channels into the connector chip. Since both the fluid flows from the OLA junction, as well as the flow from the perfusion chambers are directed into the chip, all fluids and the remaining air bubbles in the connector chip are driven towards outlet B where they leave the microfluidic device.

5. The pressures at the OLA junction fine-tuned such that vesicle formation starts. Pressures vary from device to device, but typically the IA and LO flows are set to 10-15 mbar, while the OA flow is in the range of 100 mbar.

6. Once GUV formation at the OLA junction is established and all air bubbles are pushed out of the chip, the syringe pump is switched from pushing mode to suction. A negative flow rate of 10 µL/h is applied. The negative flow rate (suction of liquid out of the device via outlet A) drives the GUVs that are present in the connector chip down into

the perfusion chambers where the vesicle traps are located. The GUVs have typically lost their octanol pocket by this point, as described in Section 5.3.4.

7. Steady vesicle production and suction via Outlet A is maintained until the vesicle traps are sufficiently filled. We typically aimed to fill the chambers to at least 80% occupancy. Depending on the vesicle production and filling rate, this process can take up to 4-5 hours.

8. Once a sufficient number of vesicles are trapped, the GUV production is halted by reducing the OLA flows to 0 mbar. The 2-switch is set to the "blocked" state, which stops any fluid flow out of Outlet B. The syringe pump is disconnected from outlet A which is now the only open outlet.

9. The first perfusion step containing the DNA pores is started by applying pressure via the perfusion inlets. In the first experiment we applied perfusion pressures of 10 mbar per chamber. In the subsequent experiments we reduced this to 8 mbar and 4 mbar respectively, in order to avoid flushing vesicles out of the traps by applying too high a flow rate.

10. The solutes of the first perfusion are flushed for 1 h. After that the pressures are reduced to 0 mbar. The fluid vials containing the DNA pore solution are unscrewed from the Fluiwell system and replaced with the low pH solution which is to be flushed in the second perfusion step. After switching the vials, the perfusion is restarted by applying the same perfusion pressures as before.

11. The different recording positions are programmed into the piezo stage and recording is started. Every position is scanned either every 30 s or every minute (EM gain 100, 10 ms exposure, bin 1, 10% LED power).

C.6 Calcuation of Proton Flux through DNA Pore

In this secion, we provide a simple back of the envelope calculation of the proton flux through a DNA nanopore. Note that in the following calculations, we do not consider any effects of the PBS buffer used in the experiment. Furthermore, we assume that diffusion is solely driven by a concentration gradient and neglect the effect of any electric potential that arises from the separation of ions. Nevertheless, the following calculation gives us an idea of the number of ions and the time scales of the proton transport through the nanopore in our experiment.

According to Fick's law of diffusion, the flux between two reservoirs is determined by the diffusion coefficient D_H of the particle (in this case protons), as well as the concentration gradient Δc and the distance the ion has to travel L.

$$J_{Proton} \approx D_H \frac{\Delta c}{L} \tag{C.1}$$

If we remember the definition of pH:

$$pH = -\log_{10} c(H^+) \tag{C.2}$$

we obtain the proton concentration (in mol/l) from

$$c(H^+) = 10^{-pH} \tag{C.3}$$

A pH gradient from pH 5.9 to pH 7.4, hence results in

$$\Delta c = 10^{-5.9} - 10^{-7.4} = 1.2 \times 10^{-6}\ mol/l \tag{C.4}$$

Using Avogadros's number N_A, we see that this corresponds to:

$$1.2 \times 10^{-6}\ mol/l = 1.2 \times 10^{-6}\ \frac{N_A}{l} = 7.2 \times 10^{-7}\ \frac{protons}{nm^3} \tag{C.5}$$

With a bilayer thickness of L = 5 nm and a diffusion coefficient $D_H = 2.4 \times 10^{-3} cm^2/s$ we receive from Equation C.1

$$J_{Proton} \approx 3.5 \times 10^4\ \frac{protons}{nm^2} \tag{C.6}$$

With an area of the nanopores A_{Pore} = 0.5 nm^2 the number of protons passing through the pore is thus:

$$\frac{dN_{Proton}}{dt} = J_{Proton}A_{Pore} \approx 2 \times 10^4 \ \frac{protons}{s} \tag{C.7}$$

Under the assumption that proton transport occurs exclusively through one pore, we can calculate the time necessary to equlibrate the pH in a ∅ 25 µm vesicle.

From Equation C.5 we know

$$1.2 \times 10^{-6} \ mol/l = 722 \frac{protons}{\mu m^3} \tag{C.8}$$

Multiplied with the volume of the GUV, this gives us the necessary number of protons

$$722 \ \frac{protons}{\mu m^3} \times \frac{4}{3}\pi(12.5\mu m)^3 \approx 6 \times 10^6 protons \tag{C.9}$$

Using the number of protons passing through the pore per second we obtained in Equation C.7, we receive

$$\frac{6 \times 10^6 protons}{2 \times 10^4 protons/s} = 300s = 5min \tag{C.10}$$

C.7 Designs of Microfluidic Chip

The designs of the microfluidic perfusion platform are given below.

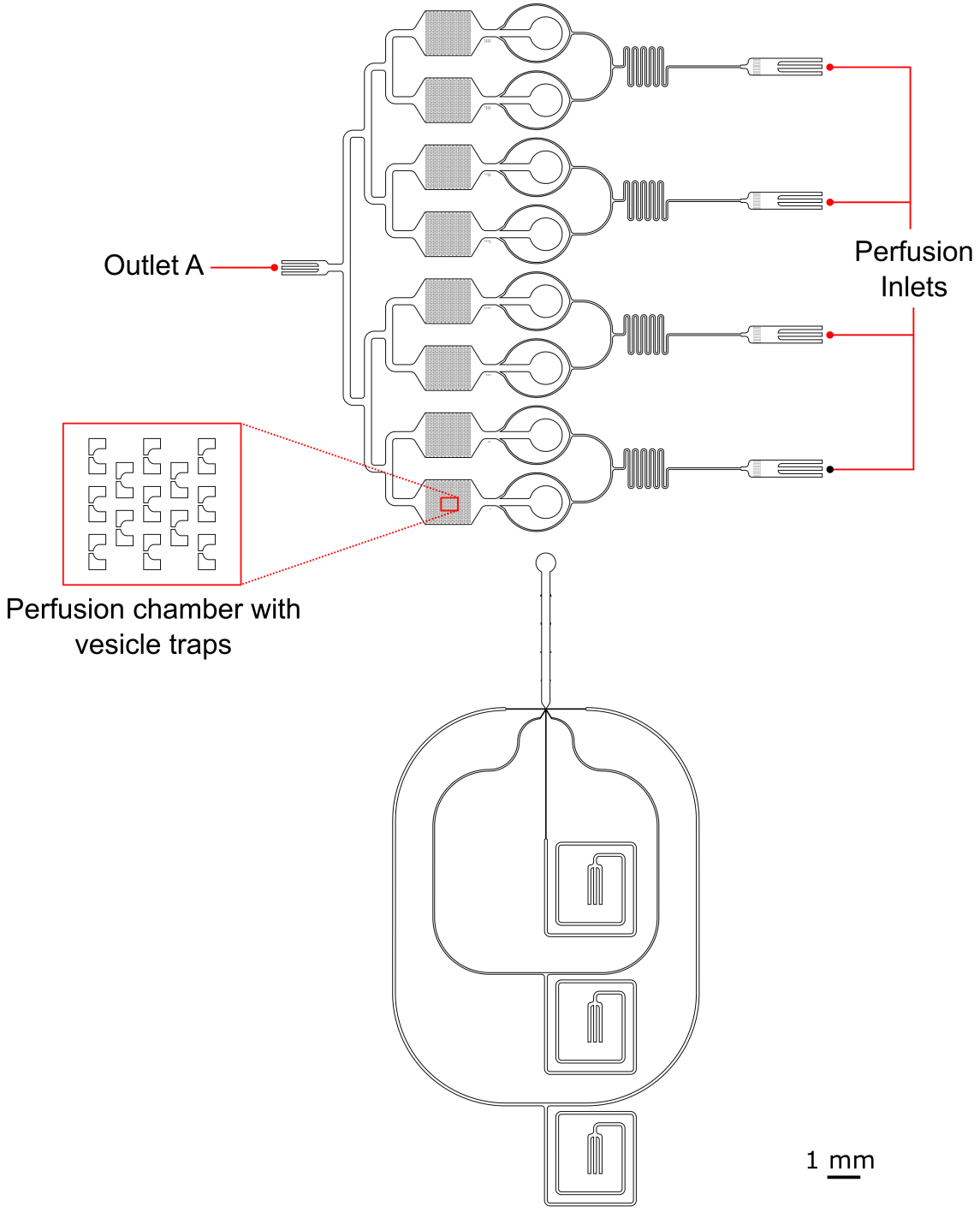

Fig. C.2. Chip design of the microfluidic perfusion platform used for Experiment 1. Connector chip not shown.

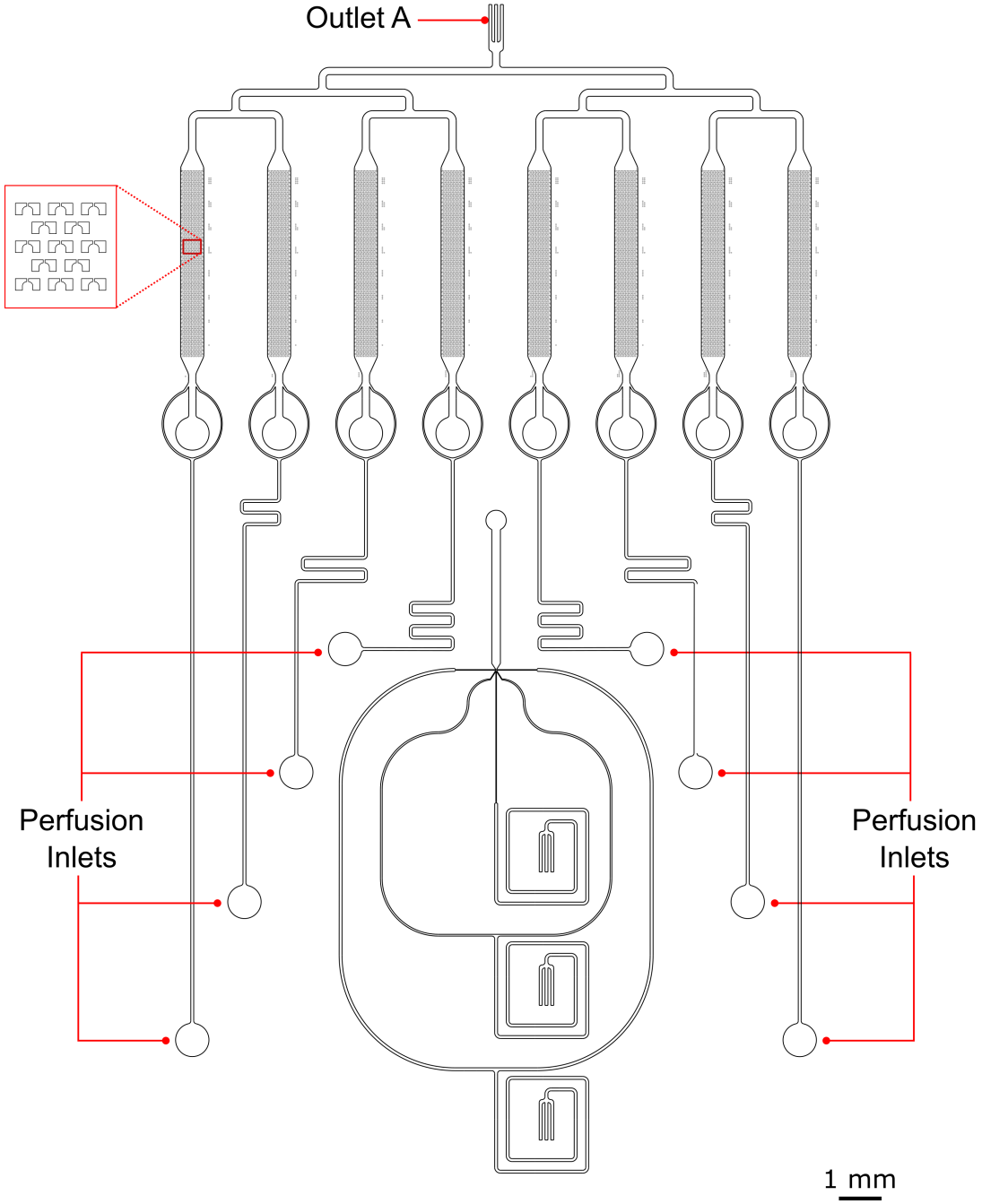

Fig. C.3. Chip design of the microfluidic perfusion platform used for Experiments 2 and 3. Connector chip not shown.

Appendix D

Deep UV Absorbance Assay

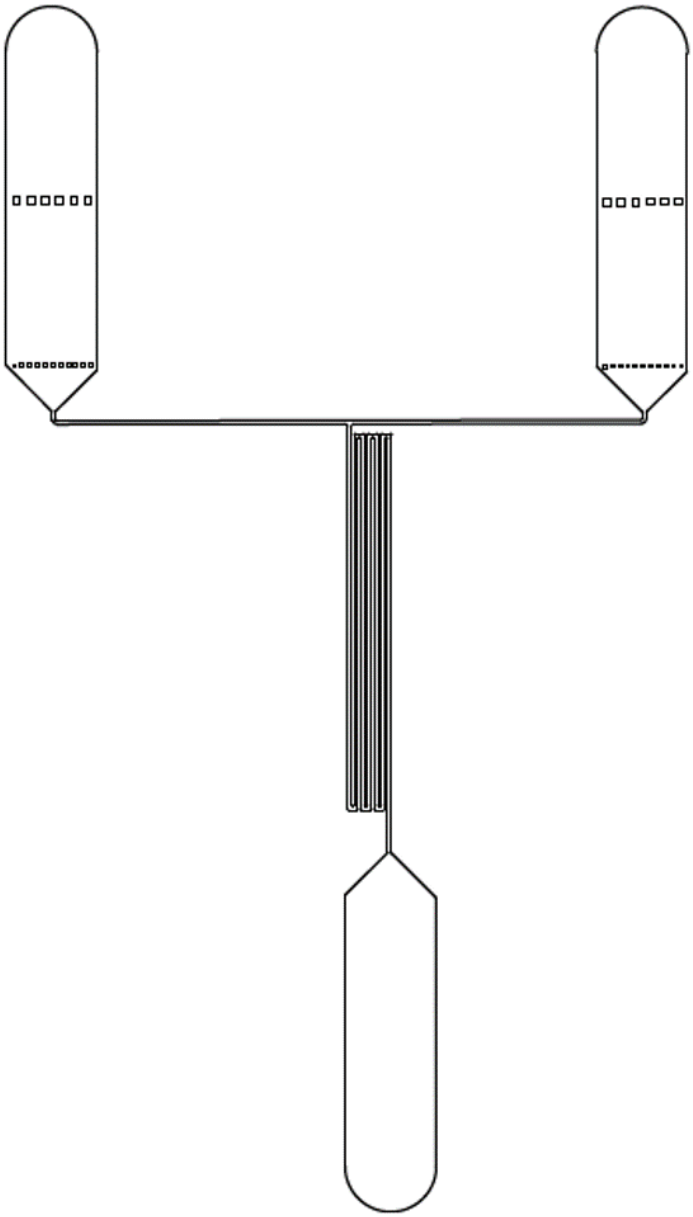

Fig. D.1. Design of the microfluidic chip used for the experiments with the UV absorbance assay. Image from [153]